Computational Analysis Of Viscoelastic Free Surface Flows

Suchitra Samanthi Edussuriya

Centre for Numerical Modelling and Process Analysis
School of Computing and Mathematical Sciences
the University of Greenwich
London

A thesis submitted in partial fulfillment of the requirements of the University of Greenwich for the Degree of Doctor of Philosophy

August 20, 2003

To Goddess Shakthi

Abstract

The demand for increasingly small and lightweight products require micro-scale components made of materials which are durable and light. Polymers have therefore become a popular choice since they can be used to produce materials which meet industrial requirements. Many of these polymers are viscoelastic fluids. The reduction in the sizes of components make physical experimentation difficult and costly. Therefore computational tools are being sought to replace old methods of testing.

This research has been concerned with the development of a finite volume algorithm for viscoelastic flow which can be readily applied to real world applications.

A major part of the research involved the implementation of the Oldroyd-B constitutive equations and associated solution methods, in the 3-D multi-physics software environment PHYSICA+. This provides an unstructured finite volume solution technique for viscoelastic flow. This algorithm is validated using the 4:1 planar contraction and results are reported.

The developed viscoelastic algorithm has also been coupled with two interface tracking techniques one of which includes surface tension effects. These techniques are the Scalar Equation Algorithm (SEA) and the Level Set Method (LSM). With both techniques the algorithms are able to take into account flow effects from both fluids (ie. air and polymer) in a two-fluid system. The LSM technique maintains a sharp interface overcoming the smearing of the interface which generally affects interface tracking techniques on Eulerian fixed grids, for example SEA, and enables the curvature of the interface to be calculated accurately to implement surface tension effects.

This integrated viscoelastic flow solver and free surface algorithm is then illustrated by predicting two industrial flow processes as used in the electronic packaging industry.

Acknowledgements

I would like to express my sincere gratitude to my supervisors Professor Christopher Bailey and Dr. Alison Williams for their invaluable advice and guidance during this project.

I thank Professor Mark Cross for offering me the PhD. position and for his encouraging comments on the progress of the work.

I would like to acknowledge the financial support provided by the University of Greenwich for this project and the University of Greenwich Accommodation Services for selecting me to be part of their team during the past three years.

My sincere thanks to all my teachers, friends and colleagues who have encouraged and helped me in my academic endeavours during the years.

Finally a very special thank you to my parents Das and Mano and my sisters Durga and Surekha for being my safety net and listening to all those long phone calls.

Contents

List of Figures

List of Tables

Chapter 1

Introduction

1.1 Introduction to Viscoelastic Fluids

The balance laws in solid and fluid mechanics usually define the relationship between externally applied forces and the resulting deformation of a given medium.

If the deformation of the medium is characterized by stress and strain, then in a Newtonian fluid under shear as shown in Figure 1.1 a), the shear stress τ_{yx} and strain rate $\dot{\varepsilon}_{yx}$ are related by Newton's law

$$\tau_{yx}(t) = \eta_0 \dot{\varepsilon}_{yx}(t), \tag{1.1}$$

since the force per unit area is proportional to shear rate $U(t)/H$ and $\dot{\varepsilon}_{yx} = U(t)/H$. The constant of proportionality η_0 is the viscosity of the fluid.

For a Hookean elastic solid if the upper plane undergoes an infinitesimal displacement $D(t_0, t)$ as shown in Figure 1.1 b), the displacement of the material may be assumed to be a linear function of the distance y. Then the displacement at any position $d_x(y, t_0, t)$ is given by

$$d_x(y, t_0, t) = \frac{D(t_0, t)}{H} y = \varepsilon_{yx}(t_0, t) y, \tag{1.2}$$

where ε_{yx} is the shear strain. The shear stress τ_{yx} is given by

$$\tau_{yx}(t) = G \varepsilon_{yx}(t_0, t), \tag{1.3}$$

where G is the rigidity modulus.

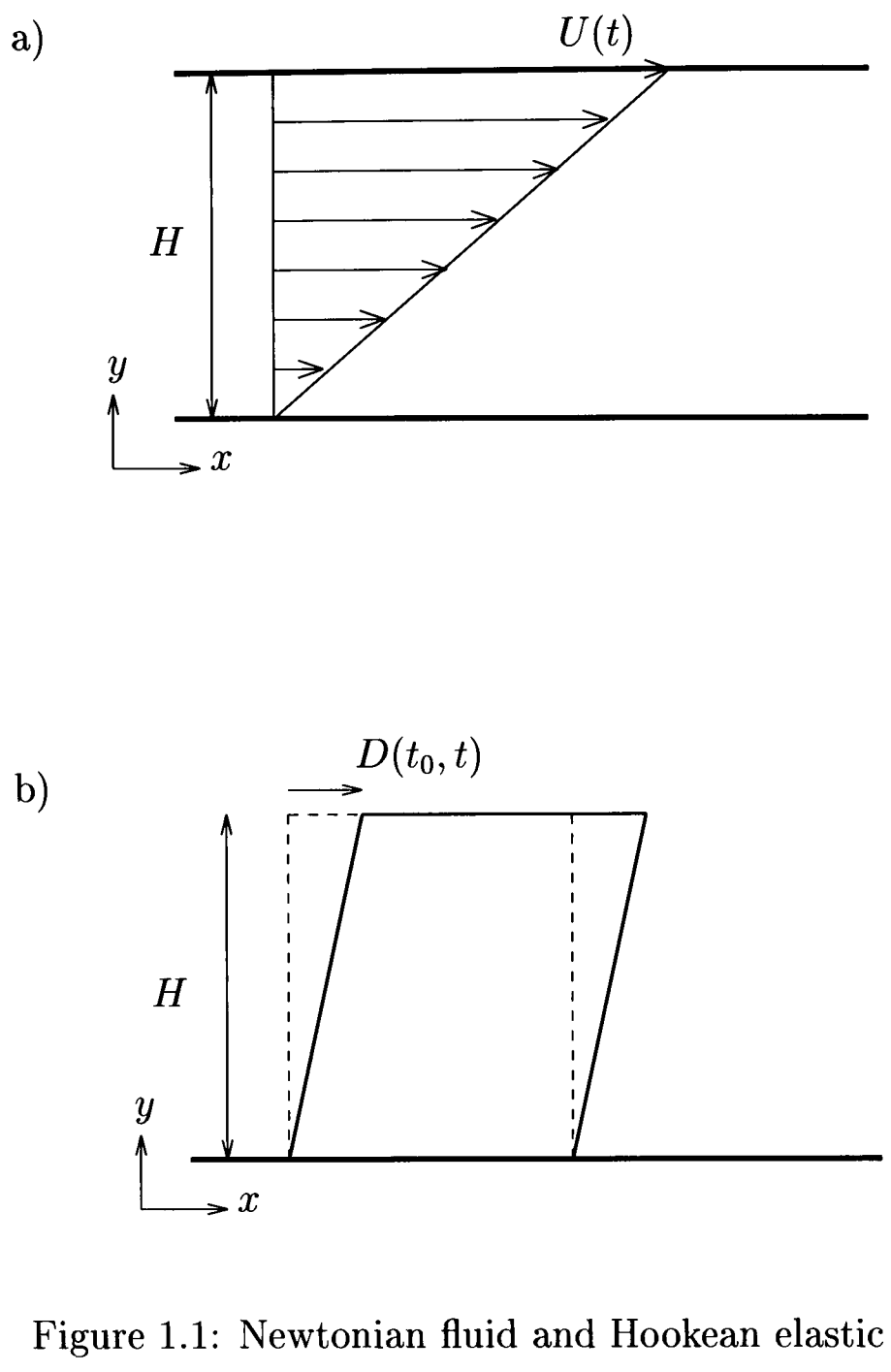

Figure 1.1: Newtonian fluid and Hookean elastic solid.

From Eqn(1.1) for a Newtonian fluid the stress at a given time t is proportional to the rate of strain at the same time. From Eqn(1.3) for a Hookean solid the stress at a given time t is proportional to strain at time t with reference to the isotropic stress at time t_0. Therefore a Hookean solid "remembers" where it was at a previous time whereas a Newtonian fluid has no memory of the past.

Substances which appear fluid like yet show the characteristics of a spring are an integral part of our lives. These materials whether natural or manmade cannot be classified as Newtonian fluids or elastic solids since their behaviour lies somewhere between the two extremes. Therefore they fall under the large umbrella of non-Newtonian materials.

The extrudate swell of a solution of polymethylmethacrylate in dimethylphthalate (when emerging from a capillary tube) and the elastic recoil of the upper half of

a falling column of Aluminium soap solution when the column is cut in midstream [1] are two examples which clearly demonstrate the peculiar behaviour of such fluids which depart from that of Newtonian fluids such as water. Rheometrical experiments have shown that this behaviour of polymers is a manifestation of fluid-memory effects. That is, even though the substances appear like viscous fluids, if a force is applied and then removed the material attempts to return to its original condition thereby exhibiting elastic solid like behaviour to a certain degree. Materials which display both viscous and elastic behaviour range from naturally occuring fluids such as blood, mineral oils, rubber fluids, etc., to manmade polymer compounds such as plastic fluids, underfill, etc. The applications which involve such materials are wide and increasingly growing. Polymer materials, for example, are used extensively in many complex industrial processes since their chemical composition enables the formation of new compounds which are stronger and lighter and therefore highly suitable for the manufacturing of articles which range from snowboards to microscale electronic components. Therefore the study of these types of non-Newtonian fluids is a very important area for investigation.

1.1.1 Non-Newtonian Fluids

For a Newtonian fluid the viscosity at a given temperature and pressure is a constant independent of rate of shear. The curve relating shear stress to rate of shear is therefore a straight line.

For non-Newtonian fluids the relationship between shear stress and rate of shear is non-linear. The viscosity is not only dependent upon temperature and pressure but also on factors such as rate of shear, the type of apparatus holding fluid, the previous history of the fluid etc.

Non-Newtonian fluids are broadly categorised as follows:

1. Time-independent fluids

   Fluids for which the shear rate at any point is some function of the shear stress at that point and nothing else.

   (a) Bingham plastics (eg. toothpaste, oil paints etc.)

(b) pseudo-plastic fluids (eg. 1% poly(ethylene-oxide) in water, Polystyrene at a temperature of $422K$)

(c) dilatant fluids (eg. starch pastes)

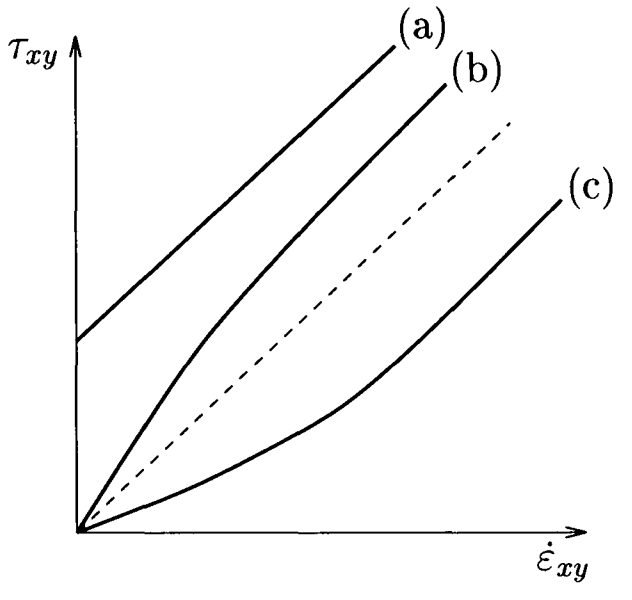

Figure 1.2: Flow curves for time-independent non-Newtonian fluids.

Figure 1.2 shows the flow curves for each type of fluid mentioned above. The dashed line shows the Newtonian flow curve. These fluids are modelled using the generalised Newtonian fluid model which is a modification of the Newtonian fluid through the use of models such as the Power-law model to express shear rate dependent viscosity.

2. Time-dependent fluids

   Fluids for which the relation between shear stress and shear rate depend on the time the fluid has been sheared.

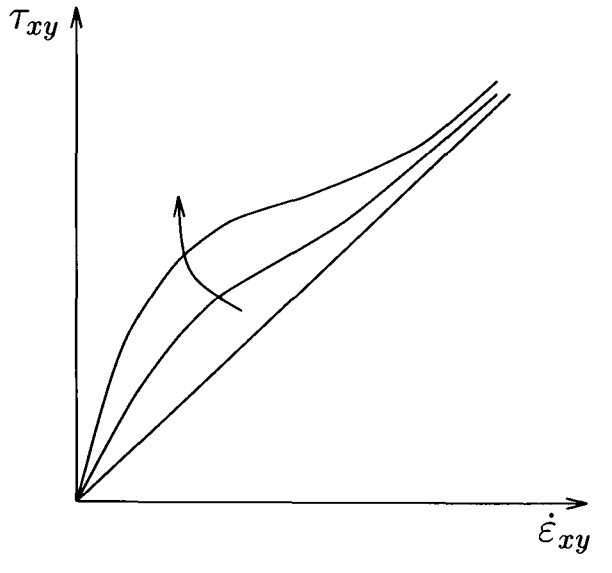

Figure 1.3: Flow curves for time-dependent non-Newtonian fluids.

(a) thixotropic fluids

Materials whose structure breaksdown with shear. Once the shearing is stopped the structure begins to reform over time. After shearing is stopped the material shows flow curves as shown in Figure 1.3 over time. The direction of the arrow indicates the direction of increasing time the material has been in recovery. The lowest curve corresponds to the time immediately after the shearing was stopped.

(b) rheopectic fluids

Material whose structure is gradually formed by shear. For example if 42% gypsum paste in water is shaken and left to rest then it takes 40 minutes to resolidify where as if the container is gently rolled between the hands then the material resolidifies in 20 seconds.

3. Viscoelastic fluids

Fluids which exhibit partial elastic recovery after deformation. Polymer materials mentioned in the previous section fall into this category. The behaviour of viscoelastic fluids may be illustrated through the stress relaxation and creep tests as shown in Figures 1.4 and 1.5 respectively.

In the stress relaxation experiment the material is subjected to a strain for time $t \geq 0$. If the material is a fluid then based on Newton's law it will show a response given in Figure 1.4 b). A viscoelastic material shows the response shown by Figure 1.4 c).

In the creep test if a step stress is applied for times $t \geq 0$ a Newtonian fluid will show a response as in Figure 1.5 b) and a viscoelastic fluid responds as shown in Figure 1.5 c).

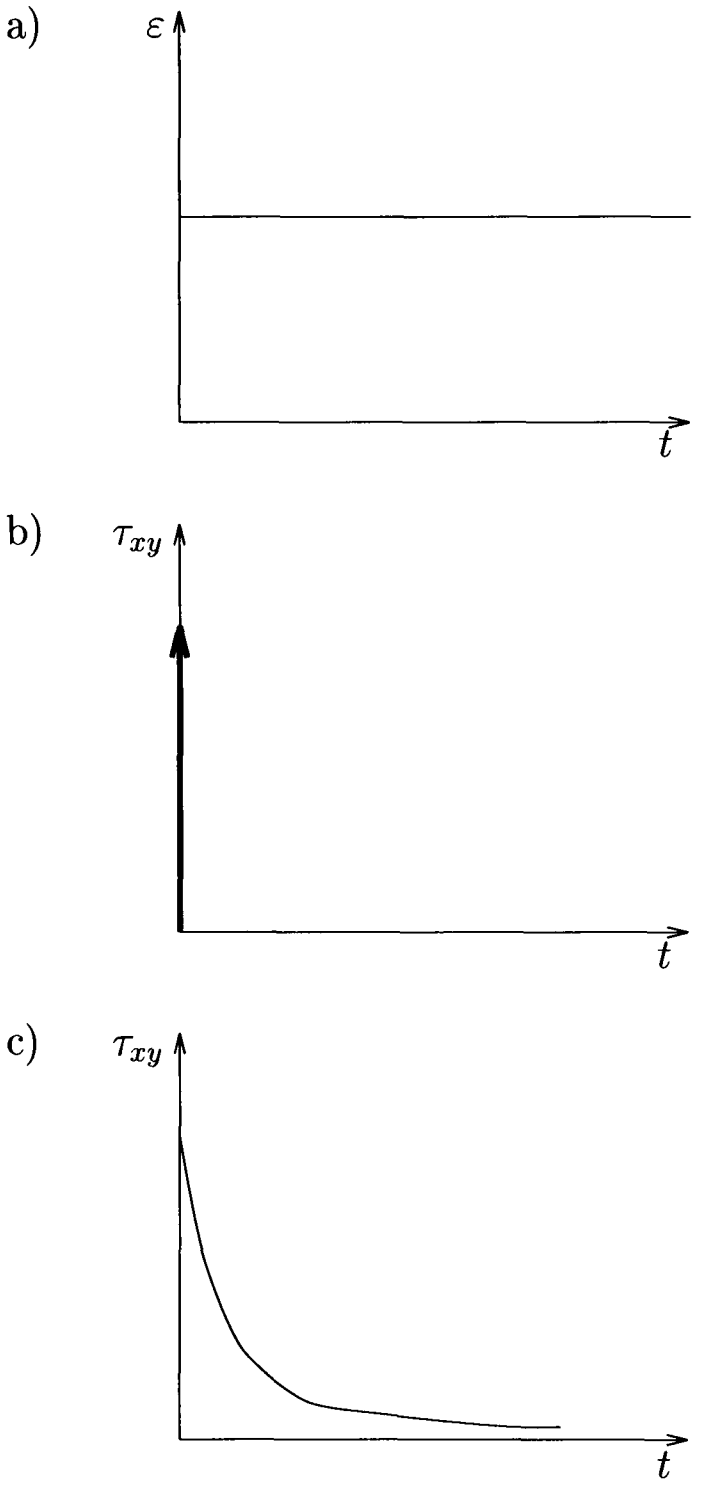

Figure 1.4: Step shear strain applied at $t = 0$.

1.1.2 Rheology and Viscoelasticity

Rheology is *the study of the deformation and flow of matter.* The term "Rheology" was proposed by Professor Bingham when the American Society of Rheology was founded in 1929 [2].

According to Newton's law a fluid is viscous and Hookes law states that a solid is elastic. As pointed out above polymer materials display both types of behaviour simultaneously. Rheometrical experiments have shown solids to have liquid-like properties and liquids to have solid-like properties, which point to the fact that viscous and elastic properties coexist in all materials and which property dominates is de-

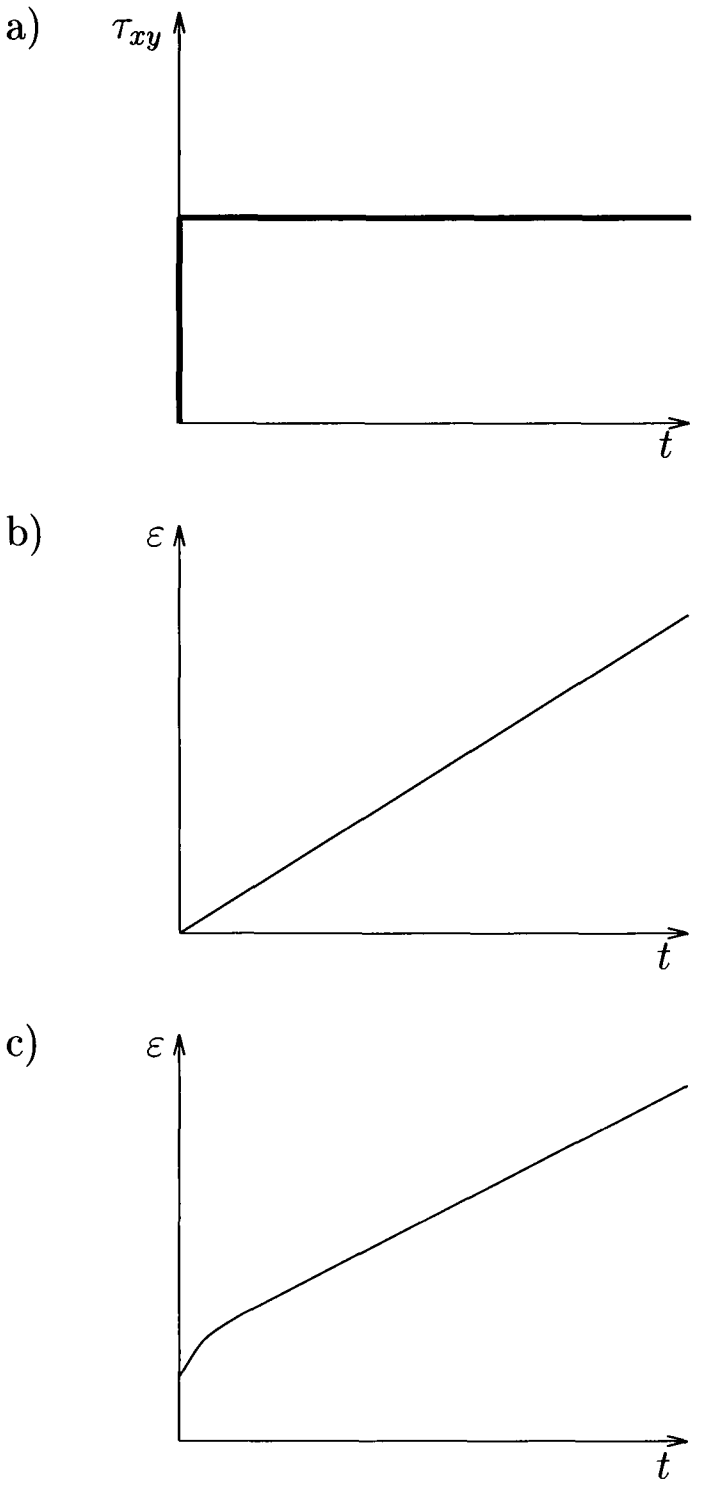

Figure 1.5: Creep test response with shear stress applied.

termined by the applied stress and duration of the experiment.

Therefore rheologists prefer to classify rheological behaviour. This allows a material to be included in more than one classification depending on experimental conditions and it also allows for the mathematical description of rheology as the mathematics of a set of behaviours rather than of a set of materials. Even though the definition of the discipline includes the classical extremes of Newtonian fluids and Hookean elastic solids, rheology is confined to the study of non-Newtonian materials.

As a means of determining the response a material displays, Reiner [3, 4] introduced a non-dimensional number called the "Deborah number" (De) which is the ratio of

characteristic time of a material to a characteristic time of observation of flow.

$$De = \frac{\lambda}{T_o}, \tag{1.4}$$

where λ is a characteristic time of the material and T_o is the time of observation. Given this assumption a material will display Newtonian or Hookean behaviour or a combination of both based on a given situation.

For a Newtonian fluid $\lambda = 0$ and for a Hookean solid $\lambda = \infty$. For a viscoelastic material $0 < \lambda < \infty$. Solid materials with viscoelasticity are called viscoelastic solids and liquids with viscoelastic behaviour are called viscoelastic fluids.

In section 2 of this chapter some of the constitutive models which have been developed to model viscoelastic effects in fluids will be discussed. The numerical methods which have been used to solve viscoelastic flow are reviewed in section 5. Section 6 presents a brief review of process modelling. The motivation for this research project and the objectives are presented in sections 7 and 8 followed by the research strategy and outline of this thesis in sections 9 and 10.

1.2 Linear Viscoelastic Models

1.2.1 Roots

Even though rheology is a relatively new discipline the recognition of the viscoelastic nature of materials and attempts at expressing such behaviour through a single equation can be traced back to the 19^{th} century.

In 1865 Thomson (who later became Lord Kelvin) did experiments on the damping of metals and introduced the term 'viscosity of metals' [5].

In 1867/68 James Clerk Maxwell presented an equation relating stress to strain which also involved the Young's modulus and a time constant and used it to study gases as he believed gases to be viscoelastic [5].

The next theoretical work combining viscous and elastic behaviour appears to have been in 1874 by Oskar E. Meyer who assumed that stress and strain may be represented by an equation which involved material constants such as the rigidity modulus

and viscosity [5]. The concept behind this equation was the same as implied by Lord Kelvin in his experiments on metals and in the years 1889-1892 Voigt generalised this theory to encompass anisotropic materials and it is now known has the Kelvin-Voigt body [5].

The most significant of contributions to the mathematical theory of linear viscoelasticity was made in 1874 by Ludwig Boltzmann who in an attempt to generalise Meyers theory presented a general theory for linear viscoelasticity which related stress at a given time not only to strain at that time but also to past times [5]. It was also assumed explicitly that the longer the time interval between the present and past time the smaller the contribution would be to the stress from the strain which presented the principle of *fading memory.* Boltzmann's theory was based on the assumption of linear superposition and he pointed out that the principle of superposition will only hold for small displacements.

1.2.2 The General Differential Equation

The linear viscoelastic models are based on the "superposition principle" mentioned in the section above which implies that the strain at any given time is directly proportional to the value of stress at that time. This leads to linear differential equations. The coefficients of the time differentials are material parameters such as the coefficient of viscosity and the rigidity modulus, etc., and they are independent of variables such as strain or strain rate. The time derivatives are ordinary partial derivatives. The general differential equation for linear viscoelasticity is therefore

$$\left(1+\alpha_1\frac{\partial}{\partial t}+\alpha_2\frac{\partial^2}{\partial t^2}+.....+\alpha_n\frac{\partial^n}{\partial t^n}\right)\tau(t)= \left(\beta_0+\beta_1\frac{\partial}{\partial t}+\beta_2\frac{\partial^2}{\partial t^2}+.....+\beta_m\frac{\partial^m}{\partial t^m}\right)\varepsilon(t_0,t), \tag{1.5}$$

where τ and ε are functions of time. Although Eqn (1.5) has been expressed in terms of shear stress τ and strain ε other types of deformation can be easily included with the stress and strain pertaining to the deformation process. Consequently the scalar variables τ and ε may be replaced by the tensors τ_{ij} $(\boldsymbol{\tau})$ and ε_{ij}

When β_0 is the only non-zero parameter Eqn(1.3) is obtained which is Hooke's law for an elastic solid. If β_1 is the only non-zero variable the equation for Newton's law

(Eqn 1.1) for a Newtonian viscous fluid is obtained.

In the following sections two models derived from Eqn(1.5) are used to illustrate how the ideas of lasticity and viscosity are displayed by a single constitutive equation.

1.2.3 The Maxwell Model

In the general equation (Eqn(1.5)) if $\alpha_1 = \eta_0/G$ and $\beta_1 = \eta_0$ while all other constants are zero, this gives the linear viscoelastic model called the Maxwell model mentioned in the section above given by

$$\tau + \frac{\eta_0}{G}\frac{\partial \tau}{\partial t} = \eta_0 \frac{\partial \varepsilon}{\partial t}. \tag{1.6}$$

If a particular stain $\bar{\varepsilon}$ is applied at $t = 0$ and held for $t > 0$ by integrating Eqn(1.6) and applying limits [4] it can be shown that

$$\tau_{xy} = \frac{\eta_0 \bar{\varepsilon}_{xy}}{\lambda_1} \exp\left(\frac{-t}{\lambda_1}\right), \tag{1.7}$$

where $\lambda_1 = \eta_0/G$. The result above indicates that the stress undergoes an exponential relaxation from its initial equilibrium value to zero as shown in Figure 1.6 (note this result is similar to stress behaviour shown in Figure 1.4 c)). The material constant λ_1 is therefore referred to as the "relaxation time". The relaxation time for water is about 10^{-12} seconds while for a low density polyethylene it is around 10 seconds and materials such as glass have relaxation times amounting to days [4]. Table 1.1 lists relaxation times for a few materials as given by Tanner [6].

1.2.4 The Kelvin Model

If β_0 and β_1 are non-zero while all the other constants are zero in the general linear equation (Eqn(1.5)) then the Kelvin-Voigt model is obtained which is of the form

$$\tau_{xy} = G\varepsilon_{xy} + \eta_0 \frac{\partial \varepsilon_{xy}}{\partial t}. \tag{1.8}$$

If a stress $\bar{\tau}_{xy}$ is applied at time $t = 0$ and held constant for $t > 0$ then by integrating the linear differential equation (1.8) the following result is obtained

$$\varepsilon_{xy} = \frac{\bar{\tau}_{xy}}{G}\left[1 - \exp\left(\frac{-t}{\lambda_2}\right)\right], \tag{1.9}$$

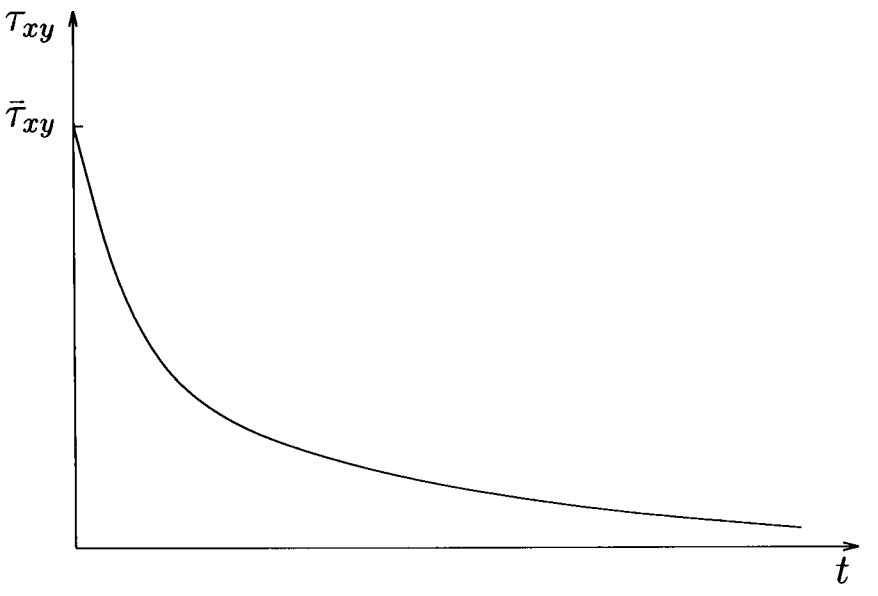

Figure 1.6: Relaxation of shear stress with the Maxwell model.

where the material parameter $\lambda_2 \equiv \eta_0/G$. From Eqn(1.9) it can be seen that, unlike an elastic solid the strain does not reach a value of $\bar{\tau}_{xy}/G$ instantaneously at $t = 0$, the time at which the constant stress $\bar{\tau}_{xy}$ is applied (see Figure 1.7). Instead the growth of the strain occurs over a longer period of time. The time taken by the material to reach a strain of $(1 - e^{-1})$ of its final value of $\bar{\tau}_{xy}/G$ is λ_2. Alternatively, if a constant stress $\bar{\tau}_{xy}$ which has been applied is suddenly removed then it can be shown that λ_2 is the time taken for the shear to reduce to e^{-1} of its original value. Since the growth or the decay of strain is retarded over time λ_2 it is called the "retardation time".

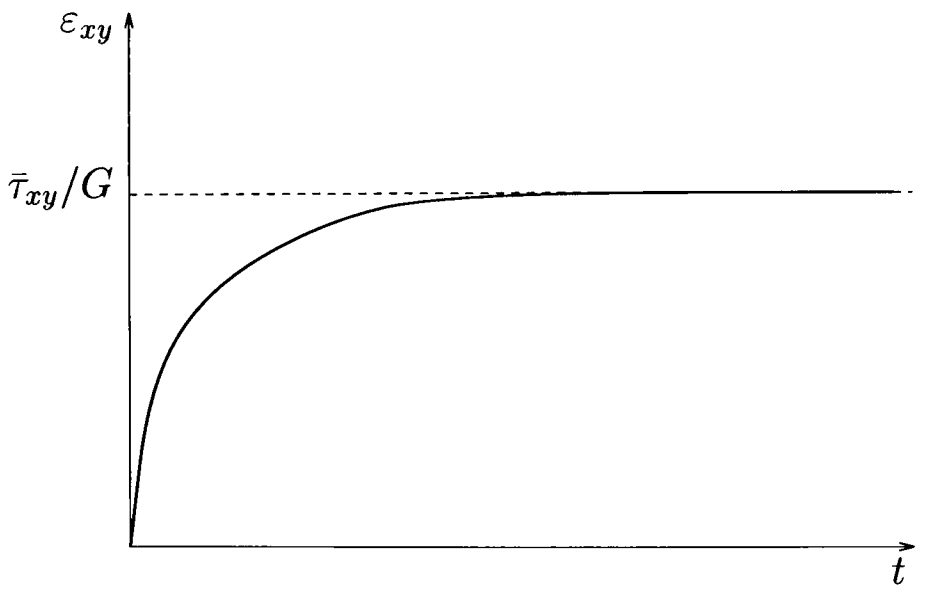

Figure 1.7: Growth of strain with the Kelvin model.

More complex linear viscoleastic models may be obtained from Eqn(1.5) by setting more material constants to non-zero. This would lead to constitutive equations

Material	Temperature(K)	λ_1(s)
Water	293	$\sim 10^{-12}$
Mineral oil	303	7×10^{-10}
Low-density polyethylene	388	10
	513	0.1
High-density polyethylene	453	0.07
	493	0.05
High-impact polystyrene	443	7
	483	3
0.5% Hydroxyethyl-cellulose in water	300	0.1
2% Polyisobutylene solution in Primol oil	300	100
Glass	300	$> 10^5$

Table 1.1: Relaxation times (λ_1) for some materials.

for materials with a *spectrum* of relaxation and retardation times and viscosities. However all of these models can be generalised as Maxwell or Kelvin type models.

1.3 Normal Stresses

Consider a Newtonian fluid under shear as shown in Figure 1.1 a). If the distance H is infinitesimally small and the viscosity η_0 is very large then the velocity distribution of the x-component $u_x(y,t)$ is a linear function of y given as

$$u_x(y,t) = \frac{U(t)}{H} y = \dot{\varepsilon}_{xy} y. \tag{1.10}$$

Then the velocity field is

$$\boldsymbol{u} = (\dot{\varepsilon}_{xy} y, 0, 0). \tag{1.11}$$

The stress distribution may be written as

$$\begin{aligned} &\sigma_{xy} = \eta_0 \dot{\varepsilon}_{xy}, \quad \sigma_{xz} = \sigma_{yz} = 0, \\ &\sigma_{xx} - \sigma_{yy} = 0, \\ &\sigma_{yy} - \sigma_{zz} = 0, \end{aligned} \tag{1.12}$$

where $\boldsymbol{\sigma}$ is the 3×3 Cauchy stress tensor. For a non-Newtonian fluid undergoing the same shear flow the components of the Cauchy stress tensor are such that

$$\begin{aligned} \sigma_{xy} &= \eta(\dot{\varepsilon})\dot{\varepsilon}_{xy}, \quad \sigma_{xz} = \sigma_{yz} = 0, \\ \sigma_{xx} - \sigma_{yy} &= N_1(\dot{\varepsilon}), \\ \sigma_{yy} - \sigma_{zz} &= N_2(\dot{\varepsilon}). \end{aligned} \tag{1.13}$$

It can be seen from Eqns(1.12) and (1.13) that the differences between the normal stresses are zero in the case of Newtonian fluids while they are functions of shear rate for non-Newtonian fluids. These functions denoted by N_1 and N_2 are *viscometric functions* which are referred to as the first and second normal stress differences respectively.

Experiments have shown that there are very high non-zero first and second normal stress differences when viscoelastic fluids exhibit phenomena such as "die swell" and rod climbing effects [2].

1.4 Oldroyd/Maxwell Type Models

In section 1.2 we discussed viscoelastic constitutive equations which model the elastic effects in viscoelastic fluids. These models are restricted to flows with very small displacement gradients since time derivatives are ordinary partial derivatives and they do not provide insight into behaviour induced by normal stress effects. Therefore non-linear constitutive models were developed which could explain non-linear behaviour and normal stress effects and be used to model high shear rate flows.

The "retarded-motion expansion" models for viscoelastic flow presented by Coleman and Noll [7, 4] are an example of such models. These equations are polynomial expansions about the Newtonian fluid which account for the deviations from the Newtonian behaviour due to elastic effects. Different constitutive equations are obtained by truncating the expansion. Although the models account for normal stress effects they have been found to be suitable only for slightly elastic fluids with very low Deborah numbers under slow and slowly varying conditions [4, 2].

Since retarded motion equations cannot be applied to arbitrary flows due to the limitations associated with them, constitutive equations were sought which could

model arbitrary flows. The Oldroyd/Maxwell type models were developed in an effort to generalise the linear viscoelastic models to be valid under varying conditions of stress and motion. The general Oldroyd model has a differential as well as integral representation. Here the differential model is presented as this study employs a model derived from this equation.

In rectangular Cartesian coordinates the general Oldroyd model is given by

$$\begin{aligned} \boldsymbol{\tau} + \lambda_1 \overset{\square}{\boldsymbol{\tau}} + \mu_0(\mathrm{tr}\,\boldsymbol{\tau})\boldsymbol{D} - \mu_1(\boldsymbol{\tau}\cdot\boldsymbol{D} + \boldsymbol{D}\cdot\boldsymbol{\tau}) \\ = 2\eta_0(\boldsymbol{D} + \lambda_2 \overset{\square}{\boldsymbol{D}} - \mu_2 \boldsymbol{D}\cdot\boldsymbol{D}), \end{aligned} \tag{1.14}$$

where $\boldsymbol{D}$ is the rate of deformation tensor given by

$$\boldsymbol{D} = \frac{1}{2}(\nabla\boldsymbol{u} + \nabla\boldsymbol{u}^T). \tag{1.15}$$

In the equation above $\boldsymbol{u}$ is the velocity vector and the symbol $\square$ above a tensor denotes a derivative of the form

$$\overset{\square}{\boldsymbol{b}} = (1 - \frac{a}{2})\overset{\nabla}{\boldsymbol{b}} + \frac{a}{2}\overset{\Delta}{\boldsymbol{b}}\,. \tag{1.16}$$

The coefficient a is a constant which governs whether the upper or lower-convected derivatives are recovered. For a tensor $\boldsymbol{b}$ the upper-convected derivative is

$$\overset{\nabla}{\boldsymbol{b}} = \frac{\partial \boldsymbol{b}}{\partial t} + \boldsymbol{u}\cdot\nabla\boldsymbol{b} - \nabla\boldsymbol{u}\cdot\boldsymbol{b} - \boldsymbol{b}\cdot(\nabla\boldsymbol{u})^T, \tag{1.17}$$

and the lower-convected derivative is

$$\overset{\Delta}{\boldsymbol{b}} = \frac{\partial \boldsymbol{b}}{\partial t} + \boldsymbol{u}\cdot\nabla\boldsymbol{b} + (\nabla\boldsymbol{u})^T\cdot\boldsymbol{b} + \nabla\boldsymbol{u}\cdot\boldsymbol{b}. \tag{1.18}$$

Many constitutive models used for modelling are derived from Eqn(1.14), some of which are listed in Table 1.2.

Apart from the constitutive models contained in this equation, various other differential, integral and kinetic theory constitutive equations have been developed in an attempt to produce constitutive models which can more accurately model material behaviour [1]. The Oldroyd-B model for example depicts a constant viscosity fluid and has very limited applications (eg. Boger fluids). The Phan-Thien−Tanner (PTT) model on the other hand has been found to be better suited to model low density fluids such as low density polyethylene melts [8]. Currently no one particular

a	λ_1	μ_0	μ_1	λ_2	μ_2	*Name*	*Constitutive equation*
0	λ_1	0	0	0	0	Upper-convected Maxwell	$\boldsymbol{\tau} + \lambda_1 \overset{\nabla}{\boldsymbol{\tau}} = 2\eta_0 \boldsymbol{D}$
2	λ_1	0	0	0	0	Lower-convected Maxwell	$\boldsymbol{\tau} + \lambda_1 \overset{\Delta}{\boldsymbol{\tau}} = 2\eta_0 \boldsymbol{D}$
2	λ_1	0	0	λ_2	0	Oldroyd liquid A	$\boldsymbol{\tau} + \lambda_1 \overset{\Delta}{\boldsymbol{\tau}} = 2\eta_0(\boldsymbol{D} + \lambda_2 \overset{\Delta}{\boldsymbol{D}})$
0	λ_1	0	0	λ_2	0	Oldroyd liquid B	$\boldsymbol{\tau} + \lambda_1 \overset{\nabla}{\boldsymbol{\tau}} = 2\eta_0(\boldsymbol{D} + \lambda_2 \overset{\nabla}{\boldsymbol{D}})$

Table 1.2: Some constitutive equations derived from the general Oldroyd model Eqn(1.14).

model is as yet valid for all viscoelastic flows. Therefore, the type of constitutive equation has to be chosen according to material properties and flow characteristics of the material being considered.

1.5 Numerical Modelling of Viscoelastic Materials

Having developed more advanced viscoelastic models they then need to be solved in order to find solutions to applications which involve viscoelastic fluids. Finding theoretical solutions to such problems has always been associated with difficulties. However, the development of faster computers with large memory capabilities in the recent years, has enabled the numerical prediction of viscoelastic flows in complex geometries through computational modelling.

To test the accuracy and capability of the numerical methods and to address the issue of difficulties which arise when viscoelastic fluids meet complex geometries, several benchmark test problems were proposed at the Fifth Workshop on Numerical Methods in Non-Newtonian Flow (1987) [5]. Among the benchmark problems proposed were the 4:1 planar contraction problem and the flow past a sphere or cylinder problem. The planar contraction problem for example is considered a difficult problem to model as the geometry contains a point of singularity at the re-entrant corner which is thought to cause many numerical methods to fail due to high stress build up in the region as elasticity is increased. This results in limiting the range of Weissenberg numbers for which stable numerical convergence may be achieved. Therefore proving

a good test for the robustness of any algorithm. The other benchmark problem which has raised considerable interest is the flow past cylinder in a channel. Even though the geometry has no point of singularity, the presence of steep stress boundary layers and the normal stress wake at high elasticity affect the convergence of numerical methods.

1.5.1 Numerical Techniques

Many of the solution algorithms which have been developed to solve viscoelastic flow are based on one of the commonly used numerical techniques: finite difference, finite element, finite volume and spectral methods. In some cases a hybrid of these techniques is used.

Finite difference method

This technique transforms a Partial Differential Equation (PDE) into a system of first-order algebraic equations by replacing the derivatives in the PDE by their finite difference approximations. The solution domain is covered by a rectangular grid and the unknowns are solved at the grid points which are distributed along families of non-intersecting lines. The finite difference approximations of the derivatives are obtained from truncated Taylor series expansions and form a stencil which relates the unknowns at each grid point to the neighbouring points. A detailed account of the method can be found in Smith [9] and Twizell [10].

The advantage of the method is in being able to use higher order approximations on structured grids. However the method is restricted to simple regular goemetries which is a drawback as most problems involve complex flows.

Finite element method

With this method the solution domain is discretized into elements of arbitrary shape and size. Since all polygonal elements can be reduced to triangular or quadrilateral shapes, these are used as the basis element shapes. The elements cannot overlap and they have to cover the whole computational domain. For each element a certain

number of points are defined either within the cell or on the sides. The unknown functions and their derivatives will be solved at these points. Simple piecewise functions are used to approximate the local variations of the unknown variables. The substitution of the piecewise approximations of the unknowns into the governing equation will give rise to an error. A residual is defined to measure the error and the residuals are minimised by means of multiplying by a set of weighting functions and integrating. This gives a set of algebraic equations for the unknown coefficients of the approximating functions. An in depth account of the technique is found in Zienkiewicz and Taylor [11].

The finite element method is a popular choice as it can accommodate irregular geometries and local mesh refinement.

Spectral method

Spectral methods are global methods. The interpolation functions are defined on the whole domain using trigonometric functions which lead to a Fourier or Chebyshev series. The functions can therefore be orthogonal polynomials of Legendre or Chebyshev types. The discrete equations consist of relationships between unknowns which may not be local. Once the approximation is done a weighted residual technique, as with finite elements, is carried out to obtain a set of algebraic equations for the coefficients of the unknowns. The advantage of the method is that it gives higher order approximations to the differentials than other discretization techniques. The reader is referred to Gottlieb and Orszag [12] for a comprehensive account.

Finite volume method

In this method the solution domain is discretized into control volumes and there are a large numbers of options for the definition of the control volume (ie. any type of polygonal shape). The conservation laws are expressed around these arbitrary control volumes. The technique consists of three main steps:

- The formal integration of the governing equations over all the control volumes.
- The conversion of the integrated equations into a set of algebraic equations

using finite difference type approximations.

- The solution of the system of algebraic equations by an iterative method.

The direct discretization of the integral forms of the conservation equations ensures that mass, momentum and energy is conserved at the discrete level. The method also has low storage requirements compared to other schemes. A detailed description of the technique is given by Patankar [13].

1.5.2 Weissenberg Number

An important dimensionless group in the non-dimensional analysis of viscoelastic flow is the "Weissenberg number" defined as

$$We = \frac{\lambda U}{L}, \tag{1.19}$$

where λ is a characteristic time of the material, U is a characteristic velocity and L is a characteristic length. The existence of this group was first demonstrated by White [5] and is the ratio of elastic to viscous effects. For a Newtonian liquid $We = 0$.

Sometimes in the non-dimensional analysis of viscoelastic fluids the ratio of elastic to viscous effects are defined as the Deborah number (De) instead of the Weissenberg number. A list of definitions used by different research groups for the 4:1 planar contraction benchmark problem are given in Table 1.3 (where the characteristic velocity U and length L are the downstream average velocity and half channel width and $\dot{\gamma}$ is the shear rate on the downstream wall).

1.5.3 High Weissenberg Number Problem

The earliest numerical algorithms for non-linear higher order numerical models (whether differential or integral) failed to converge beyond a relatively low range of elasticity. The range for which convergence was achieved was only marginally above the range for which the order-fluids were valid. This problem came to be known as the *high Weissenberg number problem.* The high Weissenberg number problem affects the numerical simulation of flow even in simple geometries. Therefore it is particularly

Paper	Definition of We or De
Sato and Richardson [14]	$We = \lambda_1 U/L$
Carew et al. [15]	$We = \lambda_1 U/L$
Matallah et al. [16]	$De = \lambda_1 \dot{\gamma}$
Marchal and Crochet[17]	$De = \lambda_1 \dot{\gamma}$
Yoo and Na [18]	$We = (\lambda_1 U/L)(1-\beta)$
Phillips and Williams [19]	$We = \lambda_1 U/L$
Aboubacar et al. [20]	$We = \lambda_1 U/L$
Oliveira et al. [21]	$De = \lambda_1 U/L$
Alves et al. [22]	$De = \lambda_1 U/L$

Table 1.3: Definitions of the We and De numbers for the 4:1 planar contraction.

difficult to model geometries which contain points of singularity or give rise to steep stress boundary layers. In the late 1980s Marchal and Crochet [17] introduced a finite element scheme based on Hermitian finite elements to model viscoelastic flow with which they were able to extend the range of convergence up to a Weissenberg number of 2.19 for creeping flow of a Oldroyd-B fluid in a 4:1 contraction geometry.

Various other stable numerical methods have since been developed to model viscoelastic flow which have been able to further increase the range of Weissenberg numbers for which converged solutions can be obtained. Matallah et al. [16] were able to achieve converged solutions for up to a De number of 24 using recovery and stress-splitting schemes within a finite element formulation. Phillips and Williams were able to achieve convergence up to a Weissenberg number of 2.5 for both creeping and inertial flows of the Oldroyd-B fluid in a 4:1 contraction geometry with a semi-Lagrangian finite volume method [19].

Alves et al. [22] used a semi-structured finite volume method for the Upper Convected Maxwell fluid in a contraction geometry. Their method proved to be stable up to $De = 3$ on meshes with very high refinement at the re-entrant corner. Aboubacar et al. [20, 23] introduced a cell-vertex hybrid finite volume/element scheme based on triangular meshes to solve both sharp and rounded re-entrant corner, planar contraction problems. For the Oldroyd-B model in the rounded corner geometry converged

solutions were obtained for Weissenberg numbers less than 4.4 whereas with the PTT model they were able to attain convergence of up to 20.

Hua-Shu Dou and Nhan Phan-Thien [24] used a parallel unstructured finite volume method to simulate the flow of an Oldroyd-B fluid past a cylinder and managed to achieve convergence up to Deborah number 1.8. Sun et al. [25] with their DAVSS-G/DG finite element scheme managed to achieve convergence for up to a Deborah number of 12.35 thereby exceeding previously attained values of elasticity for the benchmark of flow past a cylinder in a channel. Baaijens et al. [8] have used a variation of the discontinuous Galerkin method to study the capabilities of constitutive models such as the PTT and Giesekus models for the flow past a cylinder problem. With the Giesekus model they were able to obtain converged solutions up to a Deborah number of 4.6 while the PTT model converged up to Deborah number 8.9.

1.6 Process Modelling

Research into viscoelastic flow was initiated partly as a result of challenges encountered in industrial processes. Consequently a large amount of work has also been carried out on process modelling. A small selection of recently published work is presented below to highlight the type of processes that have been investigated, the complex physics which govern the processes and the computational methods used.

Optical fibers are used in numerous applications such as communications systems, imaging processes and medical science. Organic polymers are used to manufacture these fibres through process which involves momentum, heat and mass transfer and free surface flows. This is one of the processes which has been investigated using numerical techniques by Tsai and co-workers [26]. The computational method is based on the finite element method with the streamline upwind scheme for solution of momentum, mass and energy transfer and the spine method to track the free surface.

Cable coating is another industrial process that has been researched in a viscoelastic context. The simulation of viscoelastic flows on cable coating carried out by Mutlu

et al. [27] where changes in velocity, stress distribution and pressure loss are investigated using finite element techniques is an example of work carried out in this area.

The issue of natural convection heat transfer in enclosed spaces has been addressed by Demir and co-workers in their recent publications [28, 29] using viscoelastic flow and a finite difference formulation. This is a topic which has wide applications such as double glazed windows technology, solar collectors technology, cooling of radioactive waste containers etc..

The effects of viscous heating on the stability of a viscoelastic flow without externally imposed heating has been studied by Becker et al. [30] using a spectral method. The investigation was motivated by the fact that poor heat conductance in polymers cause significant temperature gradients within flowing polymers even in the absence of externally applied heat sources due to frictional dissipation and this exponentially reduces local viscosity and polymer elasticity.

Wachs et al. have also carried out nonisothermal viscoelastic flow computations [31]. In this particular paper they investigate the various effects that occur under thermal conditions related to external cooling operations particularly in the presence of geometrical singularities using a solution algorithm based on a velocity-pressure-stress-temperature finite volume method.

Other recent work includes a finite element code by Pillapakkam and Singh [32] based on the level-set method to model the motion of viscoelastic two-phase flows and a boundary element based algorithm by Khayat [33] where lubrication theory is extended to simulate the transient free surface flow of Oldroyd-B type fluids inside thin cavities.

The small sample of work detailed above show the diversity of applications involving viscoelastic flow.

In addition to algorithms of the type described above there are also commercial codes avialable for modelling polymers such as Polyflow [34] and CMOLD [35]. These codes are used widely by industry as well as researchers. For example Sun et al. [36] implemented a nonisothermal formulation for viscoelastic flow within Polyflow to model nonisothermal meltspinning with ongoing crystallization.

Both Polyflow and CMOLD use solution techniques based on finite element methods. CMOLD uses the Cross-exp model which is a modified Newtonian model to predict polymer behaviour. Polyflow has an extensive library of viscoelastic models to choose from ranging from differential to kinetic theory models. The free surfaces are tracked using mesh adapting techniques.

1.7 Motivation for this Project

Several sections in this chapter have focused on reviewing the complex nature of viscoelastic fluids, the challenges associated with finding numerical solutions to such flow, the complexity of the industrial processes which involve viscoelastic fluids and the algorithms that have been developed in an attempt to find accurate solutions. Even though great strides have been made in this field during the last 20 years it is clear that the work is by no means complete. In many industrial processes viscoelastic fluids are still being treated as Newtonian or modified Newtonian models to avoid the difficulties associated with solving viscoelastic constitutive equations when developing algorithms for process modelling. The following are a list of persisting issues surrounding the numerical modelling of viscoelastic fluids and gaps in currently available software.

- The high Weissenberg number problem.
- The lack of fully unstructured finite volume algorithms for viscoelastic flow in spite of the robustness of the technique with regard to conservation and low memory requirements.
- The lack of viscoelastic flow algorithms which can be used as a predictive tool with interface tracking capability on Eulerian fixed meshes that take into account effects from both fluids, maintains the interface as sharp front and takes surface tension effects into account.

This research project aims to address the issues identified above using a novel computational fluid dynamics algorithm for viscoelastic flow.

1.8 Objectives of the Project

The objectives of the work in this thesis are as follows:

- To develop a collocated unstructured finite volume algorithm for viscoelastic flow.
- To address the high Weissenberg number problem.
- To investigate latest trends reported on the behaviour of the salient corner vortex for the 4:1 planar contraction benchmark problem.
- To couple the viscoelastic algorithm with interface tracking techniques to simulate free surface flow with surface tension effects.

1.9 Research Strategy

In order to achieve the objectives listed in the section above

- The Oldroyd-B fluid is incorporated within the finite volume algorithm PHYSICA+.
- Simulations are carried out on the 4:1 planar contraction benchmark problem to test the sensitivity of the algorithm and to investigate salient corner vortex behaviour for increasing Weissenberg numbers.
- The viscoelastic algorithm is coupled with the Scalar Equation Algorithm and the Level Set Method. The LSM is used to capture surface tension effects.
- The viscoelastic free surface algorithm is validated using a planar channel flow test case and surface tension effects are tested using the square to circle test case.
- Simulations are then carried out for the real world problems of underfill encapsulation: injection flow and jetting.

1.10 Outline

This thesis consists of six chapters including this introductory chapter. This chapter began with a brief description of the nature of viscoelastic fluids and their applications. In sections 1.2 and 1.3 several constitutive models for viscoelastic fluids were outlined. Some of the difficulties associated with solving such constitutive equations were presented and a discussion of the advancement of numerical modelling during the last two decades for viscoelastic fluids was given. Towards the end of the chapter some of the demands of process modelling were discussed and the gaps in existing algorithms were identified. This was followed by the aims of the project and the research strategy.

In Chapter 2 the details of an unstructured finite volume method for the solution of a generic scalar variable are presented.

In Chapter 3 the implementation of the Oldroyd-B viscoelastic model in 3-D within the finite volume algorithm presented in Chapter 2 will be discussed. This algorithm provides a novel method to solve viscoelastic flow and is validated through simulations on flow through a planar channel and 4:1 planar contraction benchmark test case.

Chapter 4 presents the details of free surface algorithms within PHYSICA$^+$ and the coupling of the viscoelastic flow algorithm with these interface tracking techniques. The resulting viscoelastic free surface algorithm is a novel technique for viscoelastic fluids and numerical tests are carried out to validate the algorithm by simulating free surface flow through a planar channel.

In Chapter 5 the viscoelastic free surface algorithm is applied to two industrial applications on geometries which involve micro-scale dimensions.

Finally in Chapter 6 concluding remarks and suggestions for future work will be presented.

Chapter 2

An Unstructured CFD Algorithm

In this chapter a collocated finite volume technique for the solution of a generic scalar variable will be described. This will begin with a brief review of finite volume schemes and will be followed by the discretization of a general convection-diffusion equation on unstructured meshes. A description of the various differencing schemes which have been of interest in this present study will be presented. Finally the solution algorithm for the coupling between the momentum and pressure equations are discussed.

2.1 A Brief Introduction to FV Techniques

The Finite Volume (FV) technique has become a popular choice for Computational Fluid Dynamics (CFD) algorithms due to the clear relationship between the numerical algorithm and the underlying physical conservation principle and the low computational storage requirements. This technique where the integral formulation of the conservation laws are discretized directly in the physical space was introduced independently by McDonald [37] and MacCormack and Paullay [38] to solve 2-D, time dependent Euler equations and was extended to 3-D flows by Rizzi and Inouye [39]. This technique which can be viewed as a special finite difference formulation involves the formal integration of the governing equations of fluid flow over all the control volumes of the domain. The discretization is carried out by approximating the convection, diffusion and source terms in the integrated flow equation with finite

difference type approximations which converts the integral equations into a system of algebraic equations. The algebraic equations are solved by an iterative method. The direct discretization of the integral form of the governing equations ensures that mass, momentum and energy remain conserved at the discrete level.

This method can be used with arbitrary meshes which enable the definition of a large range of control volume types around which the conservation laws are expressed. Two types of meshes are used with the method:

- Structured meshes which are finite difference type meshes where the mesh points lie on the intersection of curvilinear coordinate lines.
- Unstructured meshes which are finite element type meshes which contain triangular, quadrilateral or even tetrahedral elements where the mesh points cannot be identified with coordinate lines. Therefore the points are identified by numbering them in a orderly manner. The unstructured meshes are important when the computational domains are irregular.

Once the type of mesh is selected, the next step is to locate the variables on the mesh. In the cell-centred method the variables are averaged over the cell to represent the value at a point within the cell. In the cell-vertex method the variables are located at the mesh points. Figure 2.1 shows the two grid arrangements.

Due to the irregular nature of real world computational domains unstructured, cell-centred finite volume methods are preferred by the CFD community. One of the earlier applications of the finite volume approach on unstructured meshes was by Thomadakis [40]. The algorithm was based on a staggered mesh approach, with the velocities being solved at the element centres and the pressure at the element vertices for low Reynolds number flows. Pan et al. [41] employed an unstructured mesh with triangular elements to solve a variety of laminar flow problems. Chow [42] employed the unstructured, cell-centred finite volume technique to solve simple flow and heat transfer problems in 2-D using polygonal elements ranging from triangles to octagons. This methodology was later extended to solve transport phenomena on 3-D unstructured meshes by Croft [43]. The finite volume algorithm presented in the following section is based on this method.

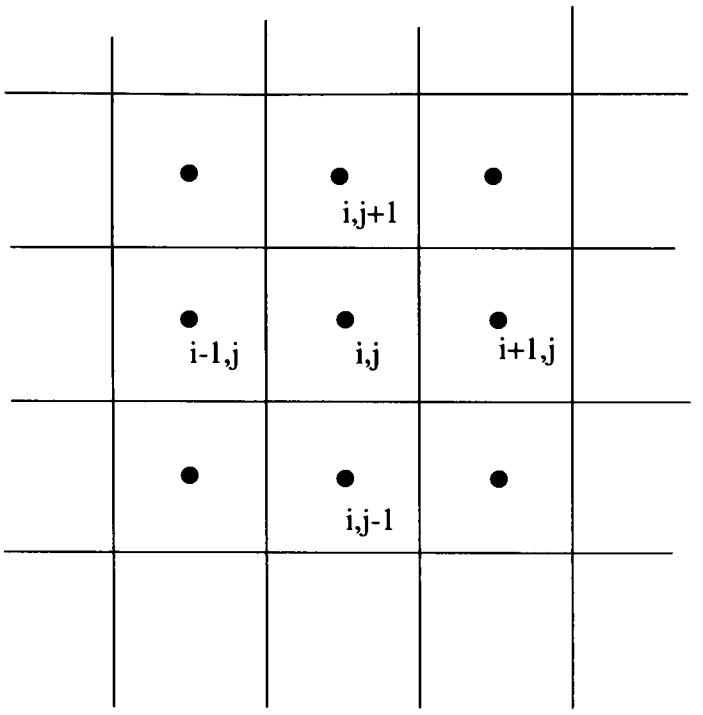

a) cell centred mesh

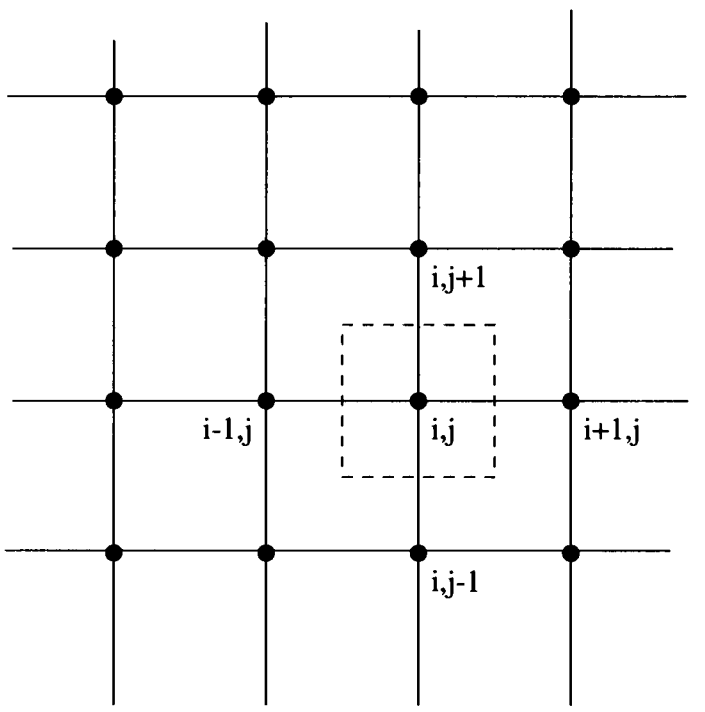

b) cell vertex mesh

control volume

• location of unkowns

Figure 2.1: cell centred and cell vertex grids.

2.2 FV Discretization of the Scalar Equation

The finite volume technique for the solution of a generic scalar variable presented in this section has been implemented within the multiphysics framework PHYSICA+ [44]. PHYSICA+ solves solid mechanics as well as fluid dynamics phenomena on unstructured meshes using finite volume techniques based on the methodology developed by Chow [42], Croft [43] and Taylor [45]. The CFD algorithm models Newtonian flow using a cell-centred arrangement. The cell-centred method places all variables such as velocity components, pressure, etc. at the centre of the control volume which is also the centre of the mesh elements which represent the flow domain.

The general conservation equation used in the CFD algorithm is given by

$$\frac{\partial(\delta\phi)}{\partial t} + \nabla \cdot (\theta \boldsymbol{u}\phi) = \nabla \cdot (\Gamma_\phi \nabla\phi) + S_\phi, \tag{2.1}$$

where δ, θ and Γ_ϕ are material properties and ϕ and S_ϕ are functions whose definitions depend on the equation being considered. The terms in Eqn (2.1) represent, from left to right, the transient, convective, diffusive and source contributions respectively.

To discretize Eqn(2.1) a grid which consists of non-overlapping polyhedral control volumes is placed on the computational domain. The point at which the value of ϕ is sought is at the centre of each control volume. Using the divergence theorem for the convection and diffusion terms the resulting equation is

$$\int_V \frac{\partial(\delta\phi)}{\partial t} dV + \int_S \theta(\boldsymbol{u}\cdot\boldsymbol{n})\phi ds = \int_S \Gamma_\phi \nabla\phi \cdot \boldsymbol{n} ds + \int_V S_\phi dv, \tag{2.2}$$

where $\boldsymbol{n}$ is the outwardly directed unit normal vector to a face of the control volume. Using a fully implicit approximation, and assuming the mesh does not move the transient term becomes

$$\int_V \frac{\partial(\delta\phi)}{\partial t} dV \simeq \frac{V_P(\delta_P\phi_P - \delta_P^o\phi_P^o)}{\Delta t}, \tag{2.3}$$

where the subscript P represents the average value in the centre of the control volume and the superscript o indicates the value at the previous time step. V_P is the volume of the control volume.

The source term is expressed in a linearised form as

$$S_\phi = S_C - S_P\phi_P, \tag{2.4}$$

where S_C and S_P can be functions of any stored values and $S_P < 0$ to ensure diagonal dominance. This leads to

$$\int_V S_\phi dV \simeq (S_C - S_P \phi_P) V_P. \tag{2.5}$$

The diffusive and convective terms are approximated at the faces of the control volume. The diffusive term becomes

$$\int_S \Gamma_\phi \Delta\phi \cdot \boldsymbol{n} ds = \sum_f (\Gamma_\phi)_f \frac{\partial \phi}{\partial n}|_f A_f \simeq \sum_f (\Gamma_\phi)_f \left(\frac{\phi_A - \phi_P}{d_{AP}} \right) A_f, \tag{2.6}$$

where the summation is over the number of faces. Here ϕ_A is the value of the variable at the centre of the neighbouring cell, d_{AP} is the distance between the centres of the neighbouring cells and A_f is the area of the face.

The value of Γ_ϕ is calculated using the harmonic mean where

$$(\Gamma_\phi)_f = \frac{(\Gamma_\phi)_A (\Gamma_\phi)_P}{\alpha_f (\Gamma_\phi)_P + (1 - \alpha_f)(\Gamma_\phi)_A}, \tag{2.7}$$

where

$$\alpha_f = \frac{d_{Af}}{d_{Af} + d_{fP}}. \tag{2.8}$$

Instead of using the harmonic mean the arithmetic mean could be used. However the second method suffers from the drawback that if for example $(\Gamma_\phi)_A$ is zero then it would approximate a value for $(\Gamma_\phi)_f$ between the nodes A and P instead of it being zero as it should. Similarly if $(\Gamma_\phi)_A$ is much less than $(\Gamma_\phi)_P$ then $(\Gamma_\phi)_f$ should depend on $(\Gamma_\phi)_A$ and inversely on α_f as the resistance to the flux of ϕ is less between the interface and the centroid of element A. Instead with the model based on arithmetic mean the value of $(\Gamma_\phi)_f$ is dominated by $(\Gamma_\phi)_P$ which is not correct. Therefore the approximation based on the harmonic mean is a much better model as it gives $(\Gamma_\phi)_f = 0$ if either $(\Gamma_\phi)_A$ or $(\Gamma_\phi)_P$ is zero and for $(\Gamma_\phi)_P >> (\Gamma_\phi)_A$

$$(\Gamma_\phi)_f \approx \frac{(\Gamma_\phi)_A}{\alpha_f}. \tag{2.9}$$

The quantity $A_f (\Gamma_\phi)_f / d_{AP}$ in Eqn(2.6) is the diffusion coefficient and will be referred to from here on as D_f.

The discretized convection term becomes

$$\int_S \theta (\boldsymbol{u} \cdot \boldsymbol{n}) \phi dS \simeq \sum_f \theta_f (\boldsymbol{u} \cdot \boldsymbol{n})_f \phi_f A_f. \tag{2.10}$$

The value of θ_f takes the value in the upwind element such that

$$\theta_f = \begin{cases} \theta_P & \text{if } (\boldsymbol{u}\cdot\boldsymbol{n})_f > 0, \\ \theta_A & \text{if } (\boldsymbol{u}\cdot\boldsymbol{n})_f < 0. \end{cases} \tag{2.11}$$

In an effort to avoid pressure checker boarding effects the Rhie-Chow [46] interpolation method is used to evaluate the normal component of velocity at the faces i.e. $(\boldsymbol{u}\cdot\boldsymbol{n})_f$. The value of ϕ at the face (ϕ_f) is calculated using an appropriate differencing scheme. In section 2.2.3 we present the differencing schemes which have been used during the course of this study. The term $A_f\theta_f(\boldsymbol{u}\cdot\boldsymbol{n})_f$ is the convection coefficient and will be represented by F_f in the rest of this thesis.

Once all terms in Eqn (2.1) are approximated, for any element P it is possible to derive a linear equation of the form

$$a_P\phi_P = \sum_{nb} a_{nb}\phi_{nb} + b_P. \tag{2.12}$$

For a finite number of points, Eqn (2.1) can be expressed as a linear matrix equation of the form

$$[\boldsymbol{A}]\boldsymbol{\phi} = \boldsymbol{b}, \tag{2.13}$$

where $\boldsymbol{\phi}$ is a vector of the values of ϕ. This matrix equation can now be solved to get an approximation as close as possible to the solution of Eqn (2.1).

2.2.1 Rhie-Chow Interpolation

The Rhie-Chow interpolation provides a method which overcomes the pressure and velocity checker boarding effects which occur if the arithmetic mean of values in the control volumes adjacent to a face is used to approximate the pressure or velocity on face of an element. Therefore, if the velocity component v is considered then the face velocity v_f in the coefficient $(v\cdot n_y)_f$ is approximated as

$$v_f = \overline{v_f} + \overline{d_f}(\overline{(\nabla_y p)_f} - (\nabla_y p)_f), \tag{2.14}$$

where

$$\overline{v_f} = \frac{v_P + v_A}{2}, \tag{2.15}$$

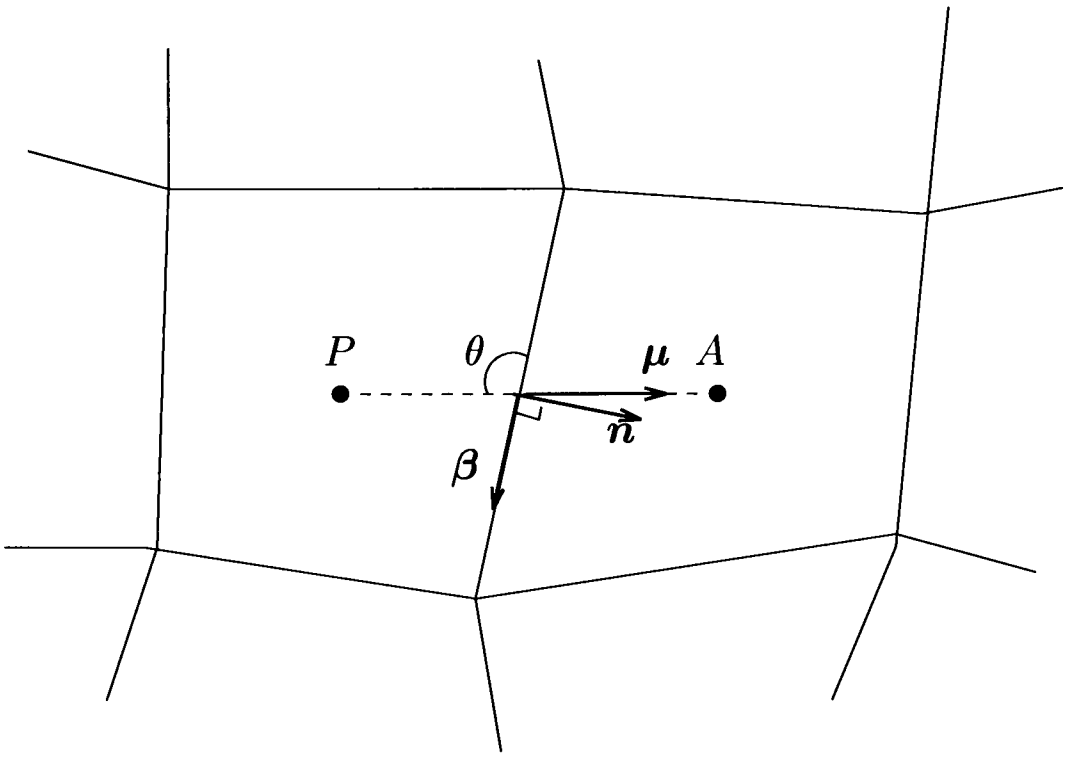

Figure 2.2: Non-orthogonal control volumes.

$$\overline{(\nabla_y p)_f} = \frac{(\nabla_y p)_P + (\nabla_y p)_A}{2}, \tag{2.16}$$

$$(\nabla_y p)_P = \sum_f n_y p_f A_f, \tag{2.17}$$

$$(\nabla_y p)_f = A_f n_y (p_A - p_P), \tag{2.18}$$

$$a_f = \frac{a_P + a_A}{2}, \tag{2.19}$$

$$\overline{d_f} = \frac{1}{a_f}. \tag{2.20}$$

2.2.2 The Cross Diffusion Terms

In Eqn(2.6) the normal gradient of two adjacent elements A and P were approximated as

$$\frac{\partial \phi}{\partial n} \simeq \frac{\phi_A - \phi_P}{d_{AP}}, \tag{2.21}$$

where d_{AP} is the distance between the centroids of elements A and P.

For the above approximation to be made the mesh has to be fully orthogonal. On unstructured meshes, the line connecting the centroids of the nodes is not parallel to the normal to the face (see Figure 2.2). This type of mesh skewness is referred to as non-orthogonality [43]. Therefore corrections are made when discretizing the diffusion term to prevent numerical error due to non-orthogonality by approximating

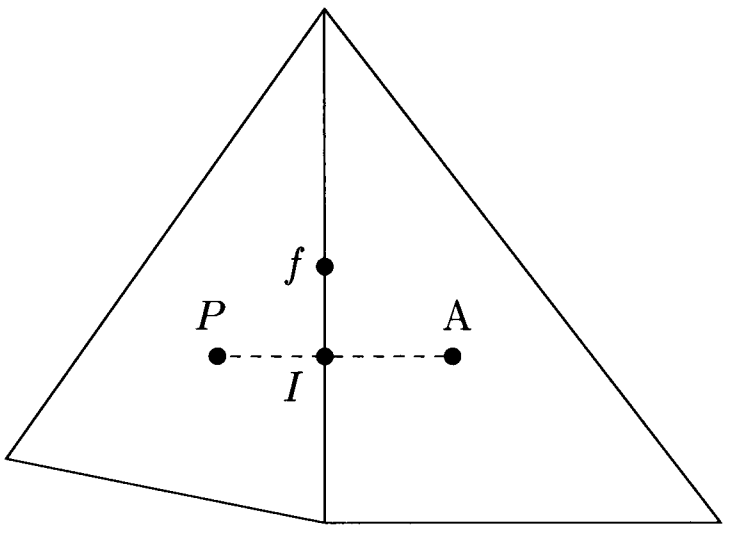

Figure 2.3: Non-conjunctional control volumes.

the normal gradient as

$$\frac{\partial \phi}{\partial n} = (\boldsymbol{\mu} \cdot \boldsymbol{n}) \frac{\partial \phi}{\partial \mu} + \boldsymbol{\beta} \frac{\partial \phi}{\partial \eta}. \tag{2.22}$$

In Eqn(2.22), $\boldsymbol{\mu}$ is vector along the line connecting two adjacent nodes, $\boldsymbol{\beta}$ is a tangential component of the normal vector $\boldsymbol{n}$ and $\boldsymbol{\eta}$ is a unit vector in the direction of $\boldsymbol{\beta}$.

Once the non-orthogonality terms are introduced, the diffusion coefficient in the discretized equation changes to

$$A_f \frac{(\Gamma_\phi)_f}{d_{AP}} (\boldsymbol{\mu} \cdot \boldsymbol{n})_f, \tag{2.23}$$

and the source term gains an extra term equal to

$$A_f (\Gamma_\phi)_f \left(\beta_x \frac{\partial \phi}{\partial x} + \beta_y \frac{\partial \phi}{\partial y} + \beta_z \frac{\partial \phi}{\partial z} \right), \tag{2.24}$$

where A_f is the area of any face f between two adjacent elements A and P.

Another form of mesh skewness occurs when the line connecting the centres of the two adjacent elements does not pass through the centroid of the face as depicted in Figure 2.3. This is referred to as non-conjuctionality [43].

The value at the face centre is estimated by extrapolating the value at the intersection point and its gradients. The value at the intersection is calculated by interpolating the nodal values. Therefore the non-conjunctionality correction for a face centre is

$$\phi_f = \phi_I + \boldsymbol{d}_{If} \cdot \nabla \phi. \tag{2.25}$$

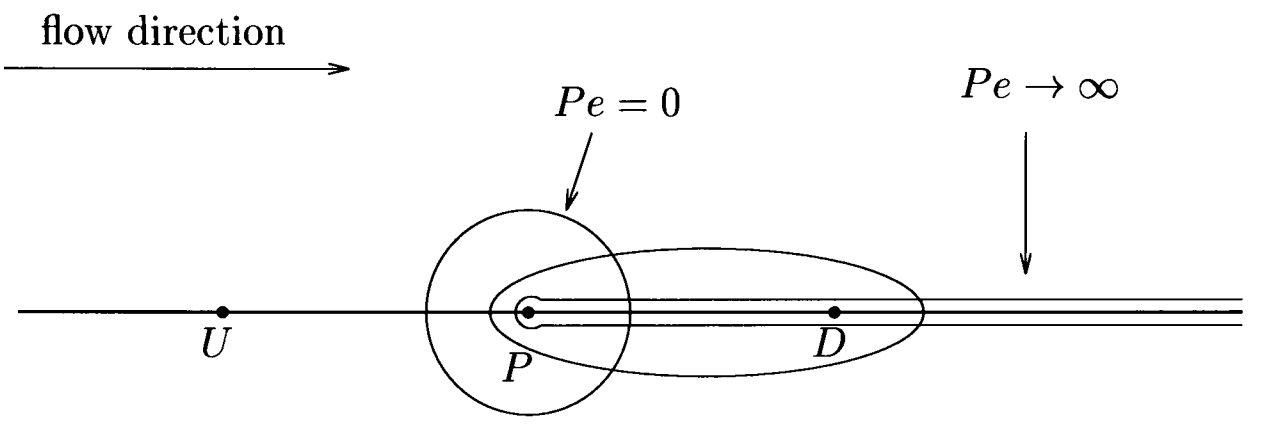

Figure 2.4: Convection and the Peclet number.

The term $\boldsymbol{d}_{If}$ is a vector from the intersection point to the face centre.

2.2.3 Differencing Schemes

Peclet number

The Peclet number is a non-dimensional number which is a measure of the relative strengths of convection and diffusion in a cell given as

$$Pe = \frac{F}{D} = \frac{\theta U}{\Gamma_\phi / L}, \tag{2.26}$$

where F is the convective mass flux per unit area and D is the diffusion conductance at cell faces. The values θ, Γ_ϕ are material functions, U is the characteristic velocity in the cell and L is the characteristic length.

When $Pe = 0$ we have pure diffusion. To illustrate this if we consider the contours of a variable ϕ they will be concentric circles around a source at node P (see Figure 2.4) since in the absence of convection, diffusion tends to spread ϕ equally in all directions. Now if Pe is gradually increased then the contours will gradually evolve into ellipses and get shifted in the direction of the flow. We also see that although the node D is influenced by both upstream and downstream conditions at this point there is more influence from upstream. Conditions at P will only be very weakly affected if at all by conditions at D. In the extreme case of there being only convection then ($P \to \infty$) the elliptical contours will become completely stretched out in the direction of the

flow which would mean that properties at P are directly transported downstream. Therefore point D will be influenced solely by upstream conditions and as there is no diffusion ϕ_D will have the same value as ϕ_P. The relationship between the value of the Peclet number and the direction from which there is the strongest influence is called the "transportiveness". It is very important that discretization schemes for convection account for transportiveness. The F_f and D_f which were introduced at the end of section 2.2 as the convection and diffusion coefficients of the discretized equation are the cell face values of F and D.

The central differencing scheme

To evaluate the variable ϕ_f on the face of the control volume we could use the central differencing scheme which would give

$$\phi_f = \frac{\phi_P + \phi_A}{2}. \tag{2.27}$$

Then

$$a_{nb} = D_f - 0.5F_f, \tag{2.28}$$

and

$$a_P = \sum_{nb} a_{nb} + \sum_f F_f. \tag{2.29}$$

where a_P is the coefficient of ϕ_P in the discretized equation.

One of the requirements of a differencing scheme to be bounded is that all coefficients of the discretized equation should have the same sign. However with the central differencing scheme some coefficients may become negative while others are positive if convection is dominant. This places an upper bound upon the Peclet number at 2 above which the scheme becomes unstable. Therefore this method is suitable for diffusion dominated flows or, since d_{PA} and $\boldsymbol{u}$ both appear in the numerator of the definition of the Peclet number, for flows with very small grid spacing or low Reynolds number flows where the velocity is very small.

The other drawback with this scheme is that it does not take into account the direction of the flow or the strength of the convection over diffusion thereby neglecting the transportiveness property.

The upwind differencing scheme

The main drawback with the central differencing scheme was its inability to account for transportiveness. The upwind scheme treats the diffusion term the same as in the central differencing scheme but is able to incorporate transportiveness into the discretization of the convection term. The face value of ϕ_f is approximated by setting it to the value of the upwind element such that

$$\phi_f = \begin{cases} \phi_P & \text{if} \quad (\boldsymbol{u} \cdot \boldsymbol{n})_f > 0, \\ \phi_A & \text{if} \quad (\boldsymbol{u} \cdot \boldsymbol{n})_f < 0. \end{cases} \tag{2.30}$$

Then

$$a_{nb} = D_f + \max(-F_f, 0), \tag{2.31}$$

$$a_P = \sum_{nb} a_{nb} + \sum_f F_f. \tag{2.32}$$

With this scheme the coefficients of the discretized equation are always positive therefore it is unconditionally bounded. Transportiveness of the flow is recognized as the formulation takes into account the direction of the flow. However the scheme is only first order accurate and is prone to false diffusion if the geometry contains regions where the flow direction is not aligned with the grid lines.

The hybrid differencing scheme

There have been many improved first-order schemes which have been developed to overcome the shortcomings of the upwind scheme. Several have been implemented within the PHYSICA+ framework. Here we discuss the hybrid scheme since it is the first-order scheme that has been employed during this work.

The hybrid scheme of Spalding [47] is based on a combination of central and upwind differencing schemes. The switching between the schemes is based on the value of the local Pe number. The scheme uses piecewise formulae based on the local Peclet number to evaluate the net flux through each control volume face, f. The local Peclet number evaluated at any face f of a control volume can be expressed as

$$Pe_f = \frac{F_f}{D_f}, \tag{2.33}$$

where F_f and D_f are the convection and diffusion coefficients of the discretized equation.

Therefore, using the hybrid differencing scheme for any element P, a_{nb} which is the coefficient of any neighbouring node in the discretized equation can be expressed as follows:

for $Pe_f < -2$

$$a_{nb}/D_f = -Pe_f, \tag{2.34}$$

for $-2 \leq Pe_f \leq 2$

$$a_{nb}/D_f = 1.0 - 0.5Pe_f, \tag{2.35}$$

for $Pe_f > 2$

$$a_{nb}/D_f = 0. \tag{2.36}$$

This can be rewritten as

$$a_{nb} = \max\left\{-F_f, D_f - \frac{F_f}{2}, 0\right\}, \tag{2.37}$$

and

$$a_P = \sum_{nb} a_{nb} + \sum_f F_f. \tag{2.38}$$

This scheme is fully conservative and unconditionally bounded since the coeficients of the discretized quation are always positive. By switching to the upwind scheme at high Pe numbers it accounts for the transportiveness of the flow. The scheme is very stable but is only first-order accurate which leads to numerical diffusion. Therefore higher order methods have been developed which possess transportiveness and better stability.

The QUICK scheme

The higher order scheme that is employed in this thesis is the Quadratic Upstream Interpolation for Convective Kinematics scheme (QUICK) of Leonard [48]. This three point scheme for convection is third-order accurate on uniform meshes and reduces to second order accuracy on non-uniform meshes. For any face, f, it uses a three-point upstream weighted quadratic interpolation.

The value of ϕ_f between two bracketing nodes i and $i-1$ is given by

$$\phi_f = \frac{6}{8}\phi_{i-1} + \frac{3}{8}\phi_i - \frac{1}{8}\phi_{i-2}, \tag{2.39}$$

where nodes $i-1$ and $i-2$, are upstream of node i. The formulation presented in Eqn (2.39), causes negative main coefficients to appear in the main diagonal which results in the scheme becoming unstable. Therefore, the expression is re-formulated in order to guarantee diagonal dominance which in turn overcomes the stability problems. The re-formulation of Eqn (2.39) used in PHYSICA+ [44] is

$$\phi_f = \phi_{i-1} + \frac{1}{8}(3\phi_i - 2\phi_{i-1} - \phi_{i-2}). \tag{2.40}$$

This formulation places the negative coefficients in the source term whilst retaining the positive main coefficients. This corresponds to the well known deferred-correction approach. The method introduces a contribution to the diagonal of the system matrix of the form

$$D_f + \max(-F_f, 0). \tag{2.41}$$

The negative of the value in (2.41) is placed in the off-diagonal position corresponding to the adjacent element and there is a contribution to the source term for both elements associated with any face, f, equal to

$$\max(-F_f, 0)0.125(3\phi_i - 2\phi_{i-1} - \phi_{i-2}). \tag{2.42}$$

Since this method uses quadratic functions to approximate the face values, it is second-order accurate and the use of two upstream nodes in the quadratic formulation ensures transportiveness. False diffusion has been found to be minimal with results on coarse grids being more accurate than with hybrid or upwind schemes. However the use of two upstream nodes causes difficulties when approximating nodes close to the boundaries of the domain. To overcome this Leonard [48] recommended the use of mirror nodes. The scheme has also been seen to produce slight undershoots and overshoots at discontinuities in the flow field.

2.2.4 Solution Algorithm

The pressure field is calculated within PHYSICA+ using the SIMPLE or SIMPLEC algorithms. The acronym SIMPLE stands for Semi-Implicit Method for Pressure-

Linked Equations and was presented by Patankar and Spalding [49]. The acronym SIMPLEC stands for SIMPLE-Consistent algorithm and was presented by van Doormal and Raithby [50].

SIMPLE algorithm

The SIMPLE algorithm uses the continuity equation

$$\frac{\partial \rho}{\partial t} + \nabla(\rho \boldsymbol{u}) = 0, \tag{2.43}$$

to predict the pressure field. This is done by expressing the continuity in terms of a pressure correction where the face velocity terms are redefined in terms of pressures by using Rhie-Chow interpolation. Starting with a guessed velocity field $\boldsymbol{u}^*$ and pressure field p^* the corrections to these fields, $\boldsymbol{u}'$, p', are sought so that the guessed pressure field p^* is improved and consequently $\boldsymbol{u}^*$ gets progressively closer to satisfying the continuity equation.

If p is the correct pressure and v is a component of the correct velocity field $\boldsymbol{u}$ then

$$p = p^* + p', \tag{2.44}$$

$$v = v^* + v'. \tag{2.45}$$

Based on the Rhie-Chow interpolation technique the face velocities and pressure must satisfy Eqn(2.14) upon convergence. Then for any guessed velocity and pressure values the face velocities can be given by

$$v_f^* = \overline{v_f^*} + \overline{d_f}(\overline{(\nabla_y p^*)_f} - (\nabla_y p^*)_f). \tag{2.46}$$

Subtracting Eqn(2.46) from Eqn(2.14) gives

$$v_f' = \overline{v_f'} + \overline{d_f}(\overline{(\nabla_y p_f')_f} - (\nabla_y p')_f). \tag{2.47}$$

Since the first two terms in Eqn(2.47) cancel upon convergence, the first two terms are dropped to simplify the resulting pressure equation. Therefore

$$v_f' = -\overline{d_f}(\nabla_y p')_f. \tag{2.48}$$

By approximating $(\nabla_y p')_f$ as in Eqn(2.18), the above equation can be rewritten as

$$v_f' = \overline{d_f} A_f \boldsymbol{n}(p_P' - p_{nb}'). \tag{2.49}$$

The discretized form of Eqn(2.43) is

$$\frac{\rho_P V_P - \rho_P^o V_P^o}{\Delta t} + \sum_f A_f(\rho \boldsymbol{u} \cdot \boldsymbol{n})_f = 0, \tag{2.50}$$

where the superscript, o, signifies the previous time step values and Δt is the time step. The summation is over all the faces of the control volume signified by the subscript P.

Then for the velocity component v substituting Eqn(2.45) and Eqn(2.49) into Eqn(2.50) gives

$$\sum_f \rho_f A_f^2 \boldsymbol{n} \cdot \boldsymbol{n}\overline{d_f}(p_P^{'} - p_A^{'})_f = \frac{\rho_P^o V_P^o - \rho_P V_P}{\Delta t} - \sum_f A_f \rho_f (v^* \cdot \boldsymbol{n})_f. \tag{2.51}$$

The above equation can be written in the form

$$a_P p_P^{'} + \sum_{nb} a_{nb} p_{nb}^{'} = b_P, \tag{2.52}$$

which is the discretized equation for the pressure corrections. In the above equation

$$a_{nb} = \rho_f A_f^2 \overline{d_f} \boldsymbol{n} \cdot \boldsymbol{n}, \tag{2.53}$$

$$a_P = \sum_f a_{nb}, \tag{2.54}$$

$$b_P = \frac{\rho_P^o V_P^o - \rho_P V_P}{\Delta t} - \sum_f A_f \rho_f (v^* \cdot \boldsymbol{n})_f. \tag{2.55}$$

Therefore by solving Eqn(2.52) the pressure corrections can be obtained. To derive the discretized form of the velocity correction equation, the discretized momentum equation is considered for the velocity component v, which is

$$a_P v_P = \sum_f a_{nb} v_{nb} + b_P - (\nabla_y p)_P. \tag{2.56}$$

The guessed pressure field is used to obtain the guessed velocity from Eqn(2.56) during the solution procedure which means

$$a_P v_P^{'} = \sum_f a_{nb} v_{nb}^{'} - (\nabla_y p^{'})_P. \tag{2.57}$$

An approximation is made to the above equation by dropping the summation term which gives a direct solution for the velocity corrections given by

$$v_P^{'} = -\sum_f \overline{d_f} \boldsymbol{n}_f A_f (\alpha_f p_P^{'} + (1 - \alpha_f) p_{nb}^{'}), \tag{2.58}$$

where

$$\alpha_f = \frac{d_{(nb)f}}{d_{(nb)f} + d_{fP}}. \tag{2.59}$$

In the equation above, d is the distance from the element centroids to the common face where A and P are adjacent control volumes.

SIMPLEC algorithm

The pressure correction equation in the SIMPLEC algorithm is calculated the same as in SIMPLE. The difference in the two schemes is in the calculation of v' the velocity correction. In SIMPLEC a term $v'_P \sum_{nb} a_{nb}$ is subtracted from both sides of Eqn(2.57). This changes the a_P term to

$$a_P - \sum_{nb} a_{nb}, \tag{2.60}$$

and the term dropped in obtaining Eqn(2.58) from Eqn(2.57) is

$$\sum a_{nb}(v'_{nb} - v'_P). \tag{2.61}$$

The solution sequence of SIMPLE/SIMPLEC

1. Initialise velocity field $\boldsymbol{u}$ and pressure field with initial guess $\boldsymbol{u}^*$ and p^*.
2. Solve for new velocities $\boldsymbol{u}^*_n$ using $\boldsymbol{u}^*$, p^* with Eqn(2.56).
3. Solve for pressure corrections p' using $\boldsymbol{u}^*_n$ with Eqn(2.52).
4. Solve for velocity corrections $\boldsymbol{u}'$ using p' and Eqn(2.58).
5. Velocity and pressure fields $\boldsymbol{u}$ and p are updated using $\boldsymbol{u}^*_n$, $\boldsymbol{u}'$, p^* and p' with Eqns(2.44)-(2.45).
6. Check for convergence. If converged then stop else set $\boldsymbol{u}$ and p to $\boldsymbol{u}^*$ and p^* and repeat steps 2 to 5 until convergence is achieved.

2.3 Conclusion

In this chapter a collocated unstructured finite volume discretization for the solution of a generic scalar variable was presented and the interpolation technique used to overcome pressure checkerboard effects was discussed. Several differencing schemes have been presented for convection and properties of each scheme were outlined. Finally the solution algorithm for the pressure velocity coupling was presented.

Chapter 3

Implementing The Oldroyd-B Model In PHYSICA+

The finite volume algorithm in PHYSICA+ for a Newtonian fluid was presented in the previous chapter. This algorithm is now extended to solve viscoelastic flow for the Oldroyd-B model. The resulting algorithm is validated using a planar channel test case and the 4:1 planar contraction benchmark test case.

3.1 Use of Finite Volume Techniques for Viscoelastic Flow

Recently there has been a renewed interest in the use of finite volume methods to model viscoelastic flow. This is mainly due to their economy of computational resources when compared to finite element methods. This renewal of interest began with Yoo and Na [18], Sasmal [51] and Xue et al. [52] who used orthogonal staggered meshes. The finite volume method presented by Yoo and Na [18] was also able to cope with non-uniform meshes and was used to simulate flow of an Oldroyd-B fluid. The constitutive equation was discretized using the deferred correction method and the equations were solved using the Semi-Implicit Method for Pressure Linked Equations-Revised(SIMPLER) algorithm [13].

The finite volume algorithm presented by Sasmal [51], was based on the stream

function-vorticity approach in the Elastic Viscous Split Stress (EVSS) form and was employed to solve steady creeping flow of an Upper Convected Maxwell (UCM) fluid through a 4:1 axisymmetric contraction. The discretized equations were solved by a semi-implicit line-to-line method using the Tri-Diagonal Matrix Algorithm (TDMA) and a pseudo-transient term was added to the stress constitutive equation to improve stability. The value of the pseudo-transient term was inversely proportional to elasticity. Since the initial value used was very small, it placed an upper-bound on the range of elasticity.

Xue et al. [52] introduced artificial diffusion terms to both sides of the discretized constitutive equations to improve stability and simulated the flow of a modified Phan-Thien−Tanner (MPTT) fluid. The Semi-Implicit Method for Pressure-Linked Equations with Splitting Technique (SIMPLEST) algorithm was developed to solve viscoelastic type flow by applying decoupled techniques. The solution process was split into a series of steps through which continuity of the flow field was maintained by solving Poisson's equation for the pressure and by ensuring both pressure and velocity fields satisfied the same momentum equation at the end of each timestep.

The above authors used the same staggered grid arrangement where the pressure and all three stress variables were located at the centre of the control volume. Through this arrangement they avoided placing any stresses at the re-entrant corner of the geometry and consequently were able to avoid the stress singularity. However, all schemes used first-order upwind approximations for the convection terms in the governing equations which tend to lose their accuracy when the flow is not aligned with the grid.

The use of higher-order differencing schemes along with a different staggered grid arrangement with finite volume techniques to solve viscoelastic type flow were explored by Darwish, Whiteman and Bevis [53] and Mompean and Deville [54]. This staggered grid placed the shear stress at the corners of the control volume while the normal stresses and pressure were placed at the same location. A similar mesh arrangement was used by others such as Gerritsma [55] and Phillips and Williams [19].

Darwish et al.[53] studied the flow of a Upper Convected Maxwell (UCM) fluid in

a sudden expansion geometry and an analytical solution was used as the solution to the value of the shear stress at the re-entrant corner. A Perera and Walters [56] type substitution was used to replace the extra-stress tensor in the momentum equation to enhance numerical stability and the Sharp and Monotonic Algorithm for Realistic Transport (SMART) scheme developed by Gaskell and Lau [57] was used to discretize the convection terms. Discretized equations were solved using the PRessure Implicit Momentum Explicit (PRIME) algorithm [58] with modifications to increase efficiency when solving viscoelastic flow.

Mompean and Deville [54] used the second-order QUICK scheme to approximate convection and extended the 2-D finite volume scheme to a 3-D algorithm in order to study the flow of Oldroyd-B fluids in 3-D domains.

Phillips and Williams introduced a semi-Lagrangian technique based on the work of Scroggs and Semazzi [59] to handle the convection terms. In order to handle the difficulty associated with calculating the shear stress at the re-entrant corner, an approximation was made using shear stress values located very close to the re-entrant corner, details of which can be found in Phillips and Williams [19]. The SIMPLER algorithm was used to solve the discretized equations.

The aforementioned algorithms clearly extended the boundaries on the application of finite volume techniques to the numerical modelling of viscoelastic flow. However, these methods can not be applied readily to real world problems as they require structured orthogonal meshes. Most industrial geometries contain irregular geometries. Therefore the modelling of such problems require numerical techniques which can be used along with unstructured meshes, preferably with a collocated grid arrangement.

A collocated finite volume technique for viscoelastic flow through structured meshes was published by Missirlis et al. [60]. A momentum interpolation technique was used by them to overcome pressure checkerboard effects. Simulation results were presented for a UCM fluid on a 4:1 planar expansion geometry. The stress conservation equations were expressed in total stresses which led to a faster algorithm than the PRIME algorithm used by Darwish et al. [53].

Work on unstructured finite volume techniques for viscoelastic flow was first published by Huang et al. [61] who used a non-structured method to simulate inertialess

flow of the PTT fluid in eccentric bearings. Dou and Phan-Thien [24] presented a parallel unstructured finite volume method to simulate the flow of an Oldroyd-B fluid in a planar channel past a stationary cylinder. The flow equations were treated using a discrete elastic viscous split stress (DEVSS) formulation along with an independent interpolation of the vorticity (DEVSS-ω). A collocated grid arrangement was used based on a control volume based finite element method. The discretized equations were solved using the SIMPLER algorithm.

Oliveira et al.[62] developed a fully collocated finite volume method for non-orthogonal block structured meshes using curvilinear coordinates. The basic equations used were the 3-D incompressible and isothermal laminar flow of a UCM. The UCM constitutive equation was used in conservative form, consequently, an ordinary diffusion term was added to both sides of the momentum equation to ensure numerical stability. Rhie and Chow [46] type interpolation was used to overcome pressure, velocity, stress decoupling. The SIMPLEC algorithm [50] is employed to solve the equations. A time-marching version of the algorithm is used to facilitate the solution of transient flows and to enable the use of under-relaxation in steady flows.

These unstructured finite volume algorithms of Huang et al. and Dou and Phan-Thien and the semi-structured collocated alogorithm of Oliveira et al. have been successful in predicting the latest numerical trends associated with specific constitutive models for the chosen benchmark test cases. However these results cannot be generalised as the challenges associated with modelling viscoelastic flow vary with constitutive models and type of benchmark test case. Therefore there is still considerable interest within the modelling comunity in developing stable numerical methods as there is no one method capable of providing stable solutions for a wide range of constitutive equations on different geometries which is not affected by the high Weissenberg number problem.

In the remainder of this chapter a fully unstructured cell-centred finite volume algorithm will be presented for the Oldroyd-B model. This technique uses Rhie-Chow interpolation and the hybrid and QUICK differencing schemes. The SIMPLEC algorithm is employed to solve the discretized equations.

3.2 The Oldroyd-B Model

The viscoelastic model that is implemented in this work is the Oldroyd-B differential model. A differential constitutive model is chosen since with differential models the evolution of the stress at a given time is only dependent on the velocity and stress fields of that particular moment in time. Therefore a knowledge of the deformation history for past times is not required. The system of PDE's for the flow of the Oldroyd-B fluid is elliptic, parabolic and hyperbolic in character. Even though it is one of the simplest of the non-linear models the hyperbolic nature affects the numerical solution around singularities with increasing elasticity. Therefore it is a good test for numerical algorithms.

3.3 Governing Equations

The governing equations for the Oldroyd-B fluid are given by the continuity and momentum equations of motion (neglecting gravitational forces)[63]

$$\nabla \cdot \boldsymbol{u} = 0, \tag{3.1}$$

$$\rho \frac{\partial \boldsymbol{u}}{\partial t} + \rho \boldsymbol{u} \cdot \nabla \boldsymbol{u} = -\nabla p + \nabla \cdot \boldsymbol{\tau}, \tag{3.2}$$

and the constitutive equation (refer Table 1.2)

$$\boldsymbol{\tau} + \lambda_1 \overset{\nabla}{\boldsymbol{\tau}} = 2\eta(\boldsymbol{D} + \lambda_2 \overset{\nabla}{\boldsymbol{D}}). \tag{3.3}$$

where λ_1 is the relaxation time, λ_2 is the retardation time, η is the zero shear rate viscosity and $\boldsymbol{\tau}$ is the extra-stress tensor. The terms $\overset{\nabla}{\boldsymbol{\tau}}$ and $\boldsymbol{D}$ are the upper convected derivative of the stress tensor and the rate of deformation tensor both of which are defined in Chapter 1 (Eqn(1.17) and (1.15)). When $\lambda_2 = 0$, Eqn(3.3) reduces to the constitutive equation for the UCM model and if $\lambda_1 = \lambda_2$ it simplifies to a Newtonian fluid with viscosity η.

The stress tensor $\boldsymbol{\tau}$ can be split into a viscoelastic component $\boldsymbol{\tau}_1$ and a purely viscous component $\boldsymbol{\tau}_2$. Then

$$\boldsymbol{\tau} = \boldsymbol{\tau}_1 + \boldsymbol{\tau}_2, \tag{3.4}$$

where

$$\boldsymbol{\tau}_1 + \lambda_1 \overset{\nabla}{\boldsymbol{\tau}}_1 = 2\eta_1 \boldsymbol{D}, \tag{3.5}$$

and

$$\boldsymbol{\tau}_2 = 2\eta_2 \boldsymbol{D}. \tag{3.6}$$

Here η_1 is the viscosity of the viscoelastic contribution and η_2 is the viscosity of Newtonian contribution. The relationship between the constants can be expressed as

$$\eta = \eta_1 + \eta_2, \tag{3.7}$$

and

$$\lambda_2 = \frac{\eta_2}{\eta}\lambda_1. \tag{3.8}$$

The constitutive equation for the Oldroyd-B fluid can now be expressed as

$$\boldsymbol{\tau}_1 + \lambda_1 \overset{\nabla}{\boldsymbol{\tau}}_1 = 2\eta_1 \boldsymbol{D}, \tag{3.9}$$

using only viscoelastic stresses.

The continuity and momentum equations can be written as

$$\rho\frac{\partial \boldsymbol{u}}{\partial t} + \rho\boldsymbol{u}\cdot\nabla\boldsymbol{u} = -\nabla p + \nabla\cdot\boldsymbol{\tau}_1 + \eta_2\nabla^2\boldsymbol{u}, \tag{3.10}$$

$$\nabla\cdot\boldsymbol{u} = 0. \tag{3.11}$$

Eqns(3.9) - (3.11) are nondimensionalized by introducing the non-dimensional variables:

$$\boldsymbol{u}^* = \frac{\boldsymbol{u}}{U},\ p^* = \frac{Lp}{\eta U},\ \boldsymbol{\tau}^* = \frac{L\boldsymbol{\tau}}{\eta U},\ x^* = \frac{x}{L},\ y^* = \frac{y}{L},\ t^* = \frac{Ut}{L}, \tag{3.12}$$

where U and L are the characteristic velocity and length respectively. The definition of these scales depend on the problem being considered. In dimensionless form the governing equations become

$$\nabla\cdot\boldsymbol{u} = 0. \tag{3.13}$$

$$Re\left(\frac{\partial \boldsymbol{u}}{\partial t} + \boldsymbol{u}\cdot\nabla\boldsymbol{u}\right) = -\nabla p + \nabla\cdot\boldsymbol{\tau}_1 + \beta\nabla^2\boldsymbol{u}, \tag{3.14}$$

$$\boldsymbol{\tau}_1 + We\,\overset{\nabla}{\boldsymbol{\tau}}_1 = 2(1-\beta)\boldsymbol{D}, \tag{3.15}$$

The parameter β is the ratio of the retardation and relaxation time and is defined by

$$\beta = \frac{\lambda_2}{\lambda_1}. \tag{3.16}$$

Equation	δ	θ	ϕ	Γ_ϕ	S_ϕ
momentum	Re	Re	$\boldsymbol{u}$	β	$-\nabla p + \nabla \cdot \boldsymbol{\tau}_1$
continuity	0	1	1	0	0
constitutive	We	We	$\boldsymbol{\tau}$	0	$2(1-\beta)\boldsymbol{D} + We(\nabla \boldsymbol{u}^T \cdot \boldsymbol{\tau}_1 + \boldsymbol{\tau}_1 \cdot \nabla \boldsymbol{u}) - \boldsymbol{\tau}_1$

Table 3.1: Definition of constants and variables in general equation (3.18).

The value β takes will depend on the problem being considered. The Reynolds and Weissenberg numbers are defined by

$$Re = \frac{\rho U L}{\eta}, We = \frac{\lambda_1 U}{L}. \tag{3.17}$$

3.4 Computational Approach

The governing equations (3.13)-(3.15) can each be expressed in general conservative form as

$$\frac{\partial(\delta\phi)}{\partial t} + \nabla \cdot (\theta \boldsymbol{u}\phi) = \nabla \cdot (\Gamma_\phi \nabla \phi) + S_\phi, \tag{3.18}$$

where δ, θ and Γ_ϕ are constants and the functions ϕ and S_ϕ are defined in Table 3.1. The terms in Eqn (3.18) represent, from left to right, the transient, convective, diffusive and source contributions respectively.

The discretization of the equations is carried out using the finite volume technique described in Chapter 2. The constitutive equations are implemented in 3-D. In three-dimensional Cartesian coordinates the governing equations become

$$\frac{\partial u}{\partial x} + \frac{\partial v}{\partial y} + \frac{\partial w}{\partial z} = 0, \tag{3.19}$$

$$\begin{aligned} Re\left(\frac{\partial u}{\partial t} + u\frac{\partial u}{\partial x} + v\frac{\partial u}{\partial y} + w\frac{\partial u}{\partial z}\right) &= -\frac{\partial p}{\partial x} + \frac{\partial \tau_1^{xx}}{\partial x} + \frac{\partial \tau_1^{xy}}{\partial y} + \frac{\partial \tau_1^{xz}}{\partial z} \\ &+ \beta\left(\frac{\partial^2 u}{\partial x^2} + \frac{\partial^2 u}{\partial y^2} + \frac{\partial^2 u}{\partial z^2}\right), \end{aligned} \tag{3.20}$$

$$\begin{aligned} Re\left(\frac{\partial v}{\partial t} + u\frac{\partial v}{\partial x} + v\frac{\partial v}{\partial y} + w\frac{\partial v}{\partial z}\right) &= -\frac{\partial p}{\partial y} + \frac{\partial \tau_1^{yy}}{\partial y} + \frac{\partial \tau_1^{xy}}{\partial x} + \frac{\partial \tau_1^{yz}}{\partial z} \\ &+ \beta\left(\frac{\partial^2 v}{\partial x^2} + \frac{\partial^2 v}{\partial y^2} + \frac{\partial^2 v}{\partial z^2}\right), \end{aligned} \tag{3.21}$$

$$Re\left(\frac{\partial w}{\partial t} + u\frac{\partial w}{\partial x} + v\frac{\partial w}{\partial y} + w\frac{\partial w}{\partial z}\right) = -\frac{\partial p}{\partial z} + \frac{\partial \tau_1^{zz}}{\partial z} + \frac{\partial \tau_1^{yz}}{\partial y} + \frac{\partial \tau_1^{xz}}{\partial x}$$

$$+ \quad \beta\left(\frac{\partial^2 w}{\partial x^2}+\frac{\partial^2 w}{\partial y^2}+\frac{\partial^2 w}{\partial z^2}\right), \tag{3.22}$$

$$We\left(\frac{\partial \tau_1^{xx}}{\partial t}+u\frac{\partial \tau_1^{xx}}{\partial x}+v\frac{\partial \tau_1^{xx}}{\partial y}+w\frac{\partial \tau_1^{xx}}{\partial z}\right) = 2(1-\beta)\frac{\partial u}{\partial x}+\left(2We\frac{\partial u}{\partial x}-1\right)\tau_1^{xx}$$
$$+ \quad 2We\tau_1^{xy}\frac{\partial u}{\partial y}+2We\tau_1^{xz}\frac{\partial u}{\partial z}, \tag{3.23}$$

$$We\left(\frac{\partial \tau_1^{yy}}{\partial t}+u\frac{\partial \tau_1^{yy}}{\partial x}+v\frac{\partial \tau_1^{yy}}{\partial y}+w\frac{\partial \tau_1^{yy}}{\partial z}\right) = 2(1-\beta)\frac{\partial v}{\partial y}+\left(2We\frac{\partial v}{\partial y}-1\right)\tau_1^{yy}$$
$$+ \quad 2We\tau_1^{xy}\frac{\partial v}{\partial x}+2We\tau_1^{yz}\frac{\partial v}{\partial z}, \tag{3.24}$$

$$We\left(\frac{\partial \tau_1^{zz}}{\partial t}+u\frac{\partial \tau_1^{zz}}{\partial x}+v\frac{\partial \tau_1^{zz}}{\partial y}+w\frac{\partial \tau_1^{zz}}{\partial z}\right) = 2(1-\beta)\frac{\partial w}{\partial z}+\left(2We\frac{\partial w}{\partial z}-1\right)\tau_1^{zz}$$
$$+ \quad 2We\tau_1^{xz}\frac{\partial w}{\partial x}+2We\tau_1^{yz}\frac{\partial w}{\partial y}, \tag{3.25}$$

$$We\left(\frac{\partial \tau_1^{xy}}{\partial t}+u\frac{\partial \tau_1^{xy}}{\partial x}+v\frac{\partial \tau_1^{xy}}{\partial y}+w\frac{\partial \tau_1^{xy}}{\partial z}\right) = (1-\beta)\left(\frac{\partial u}{\partial y}+\frac{\partial v}{\partial x}\right)+We\tau_1^{xx}\frac{\partial v}{\partial x}$$
$$+ \quad We\tau_1^{yy}\frac{\partial u}{\partial y}+\left(We\left(\frac{\partial u}{\partial x}+\frac{\partial v}{\partial y}\right)-1\right)\tau_1^{xy}$$
$$+ \quad We\tau_1^{xz}\frac{\partial v}{\partial z}+We\tau_1^{yz}\frac{\partial u}{\partial z}, \tag{3.26}$$

$$We\left(\frac{\partial \tau_1^{yz}}{\partial t}+u\frac{\partial \tau_1^{yz}}{\partial x}+v\frac{\partial \tau_1^{yz}}{\partial y}+w\frac{\partial \tau_1^{yz}}{\partial z}\right) = (1-\beta)\left(\frac{\partial w}{\partial y}+\frac{\partial v}{\partial z}\right)+We\tau_1^{yy}\frac{\partial w}{\partial y}$$
$$+ \quad We\tau_1^{zz}\frac{\partial v}{\partial z}+\left(We\left(\frac{\partial w}{\partial z}+\frac{\partial v}{\partial y}\right)-1\right)\tau_1^{yz}$$
$$+ \quad We\tau_1^{xz}\frac{\partial v}{\partial x}+We\tau_1^{xy}\frac{\partial w}{\partial x}, \tag{3.27}$$

$$We\left(\frac{\partial \tau_1^{xz}}{\partial t}+u\frac{\partial \tau_1^{xz}}{\partial x}+v\frac{\partial \tau_1^{xz}}{\partial y}+w\frac{\partial \tau_1^{xz}}{\partial z}\right) = (1-\beta)\left(\frac{\partial w}{\partial x}+\frac{\partial u}{\partial z}\right)+We\tau_1^{zz}\frac{\partial u}{\partial z}$$
$$+ \quad We\tau_1^{xx}\frac{\partial w}{\partial x}+\left(We\left(\frac{\partial w}{\partial z}+\frac{\partial u}{\partial x}\right)-1\right)\tau_1^{xz}$$
$$+ \quad We\tau_1^{yz}\frac{\partial u}{\partial y}+We\tau_1^{xy}\frac{\partial w}{\partial y}, \tag{3.28}$$

The unknowns of the 3-D equations above are solved at the cell centre. The source term S_ϕ of each of the constitutive equations is linearised according to Eqn (2.4) in Chapter 2. The S_C and S_P functions for the 3-D equations are given in Table 3.2.

Equation	ϕ	$-S_P$	S_C
continuity	1	0	0
u-momentum	u	0	$-\partial p/\partial x + \partial \tau_1^{xx}/\partial x + \partial \tau_1^{xy}/\partial y + \partial \tau_1^{xz}/\partial z$
v-momentum	v	0	$-\partial p/\partial y + \partial \tau_1^{yy}/\partial y + \partial \tau_1^{xy}/\partial x + \partial \tau_1^{yz}/\partial z$
w-momentum	w	0	$-\partial p/\partial z + \partial \tau_1^{zz}/\partial z + \partial \tau_1^{yz}/\partial y + \partial \tau_1^{xz}/\partial x$
τ_1^{xx} normal stress	τ_1^{xx}	1	$2(1-\beta)\partial u/\partial x + 2We(\partial u/\partial x)\tau_1^{xx}$ $+2We\tau_1^{xy}\partial u/\partial y + 2We\tau_1^{xz}\partial u/\partial z$
τ_1^{yy} normal stress	τ_1^{yy}	1	$2(1-\beta)\partial v/\partial y + 2We(\partial v/\partial y)\tau_1^{yy}$ $+2We\tau_1^{xy}\partial v/\partial x + 2We\tau_1^{yz}\partial v/\partial z$
τ_1^{zz} normal stress	τ_1^{zz}	1	$2(1-\beta)\partial w/\partial z + 2We(\partial w/\partial z)\tau_1^{zz}$ $+2We\tau_1^{xz}\partial w/\partial x + 2We\tau_1^{yz}\partial w/\partial y$
τ_1^{xy} shear stress	τ_1^{xy}	1	$(1-\beta)(\partial u/\partial y + \partial v/\partial x) + We\tau_1^{xx}\partial v/\partial x$ $+We\tau_1^{yy}\partial u/\partial y + We(\partial u/\partial x + \partial v/\partial y)\tau_1^{xy}$ $+We\tau_1^{xz}\partial v/\partial z + We\tau_1^{yz}\partial u/\partial z$
τ_1^{yz} shear stress	τ_1^{yz}	1	$(1-\beta)(\partial w/\partial y + \partial v/\partial z) + We\tau_1^{yy}\partial w/\partial y$ $+We\tau_1^{zz}\partial v/\partial z + We(\partial w/\partial z + \partial v/\partial y)\tau_1^{yz}$ $+We\tau_1^{xz}\partial v/\partial x + We\tau_1^{xy}\partial w/\partial x$
τ_1^{xz} shear stress	τ_1^{xz}	1	$(1-\beta)(\partial w/\partial x + \partial u/\partial z) + We\tau_1^{zz}\partial u/\partial z$ $+We\tau_1^{xx}\partial w/\partial x + We(\partial w/\partial z + \partial u/\partial x)\tau_1^{xz}$ $+We\tau_1^{yz}\partial u/\partial y + We\tau_1^{xy}\partial w/\partial y$

Table 3.2: The unknowns and the components of the linearised source terms of the 3-D governing equations.

3.4.1 Differencing Schemes

To evaluate the variable at the control volume face, ϕ_f, a differencing scheme which employs upwinding is used to ensure that the transportiveness of the fluid through convection is properly taken into account.

Previous results for viscoelastic flow have shown that accuracy is improved when higher order differencing schemes are used [22]. Therefore, for purposes of comparison, ϕ_f is calculated using two differencing schemes: the first order accurate hybrid scheme of Spalding [47] and the second order accurate (QUICK) scheme of Leonard [48]. The two schemes have been discussed in Chapter 2.

3.4.2 Flow Algorithm

The SIMPLEC [50] algorithm is used to solve the flow equations. The constitutive equation (3.15) is solved implicitly, ensuring that the flow and stress behaviour is fully coupled. Within the SIMPLEC loop, the stress equations are solved before the momentum equation. Once the stress values are calculated, the differentials of the stresses are calculated. These values are then fed into the flow equations as source terms. The flow algorithm is given below.

- Initialise variables
- Begin time-step
  - Set $\boldsymbol{\tau}^o = \boldsymbol{\tau}, \boldsymbol{u}^o = \boldsymbol{u}, p^o = p$
  - SIMPLEC
    - Solve constitutive equations
    - Solve momentum equations
    - Solve pressure correction equation
    - Correct pressure and velocity fields
    - Calculate convection fluxes
    - Iterate until convergence
- End time-step

- Advance time until steady-state
- Write result files

3.5 Model Validation

In order to validate the implementation of the Oldroyd-B model in PHYSICA+two test cases have been investigated. These are

1. Flow through a planar channel.
2. Flow through a 4:1 planar contraction.

In the following sections these test cases are described and results are presented.

3.6 Flow Through a Planar Channel

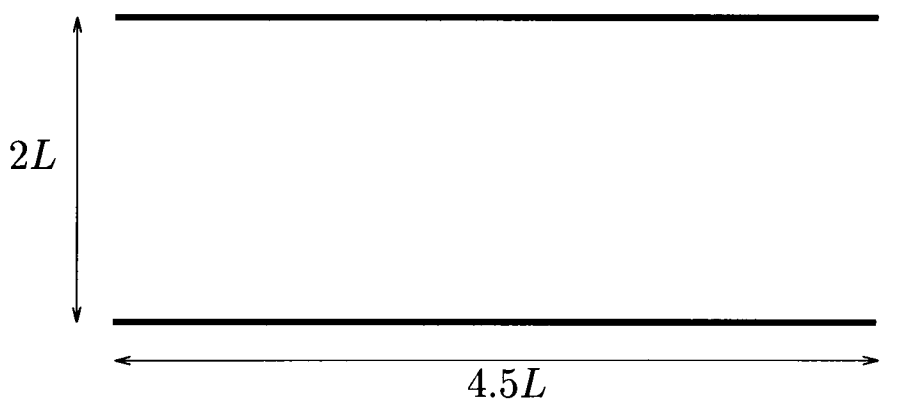

Figure 3.1: 2-D channel geometry in XY-plane.

In this section the flow of an Oldroyd-B fluid through a planar channel is modelled. This test case has been chosen as a means of checking the 3-D implementation of the model and to check the numerical accuracy of the model implementation over a range of We numbers. In order to check the 3-D implementation numerical simulations are carried out on the XY-plane, YZ-plane and the ZX-plane. If the 3-D model has been implemented correctly the numerical errors should be identical.

Figure 3.1 shows the 2-D geometry which has a channel length of $4.5L$ and width of $2L$. The length L is 4 and $U = 1$.

XY-plane	$u = \frac{3}{128}(16 - y^2)$	$v = 0$
YZ-plane	$v = \frac{3}{128}(16 - z^2)$	$w = 0$
ZX-plane	$w = \frac{3}{128}(16 - x^2)$	$u = 0$

Table 3.3: The velocity at the inlet.

XY-plane	$\tau_1^{xx} = 2\mathrm{We}(1-\beta)\left(\frac{\partial u}{\partial y}\right)^2$	$\tau_1^{xy} = (1-\beta)\frac{\partial u}{\partial y}$
YZ-plane	$\tau_1^{yy} = 2\mathrm{We}(1-\beta)\left(\frac{\partial v}{\partial z}\right)^2$	$\tau_1^{yz} = (1-\beta)\frac{\partial v}{\partial z}$
ZX-plane	$\tau_1^{zz} = 2\mathrm{We}(1-\beta)\left(\frac{\partial w}{\partial x}\right)^2$	$\tau_1^{xz} = (1-\beta)\frac{\partial w}{\partial x}$

Table 3.4: The analytical solutions for the 2-D planar channel.

Fully developed flow is imposed at the inlet given in Table 3.3. No-slip conditions are imposed on the solid boundaries. At outflow the pressure is set to zero and homogeneous Neumann boundary conditions are imposed for the stresses. Simulations are carried out on Mesh 1 (see Figure 3.2) and the equations are solved as a steady state problem for creeping flow. The hybrid differencing scheme is used for the constitutive equations. The solution to the corresponding Stokes problem is used as the initial condition and flow is simulated for $We = 0.1$ at $\beta = 0.11$ on each plane.

To test the accuracy of the results the normal and shear stresses at steady state are compared with the analytical solutions. The analytical solutions for stresses are given in Table 3.4

The steady state results of the normal stresses $\tau_1^{xx}, \tau_1^{yy}, \tau_1^{zz}$ and the shear stresses $\tau_1^{xy}, \tau_1^{yz}, \tau_1^{xz}$ along a cross section at $x = 10$ $(0 \leq x \leq 18)$ are plotted against the analytical solution in Figures 3.3 and 3.4. The steady state numerical stress profiles compare well with the analytical solutions. From these figures it can be seen that the numerical stress profiles agrees well with the analytical solution for each plane. In

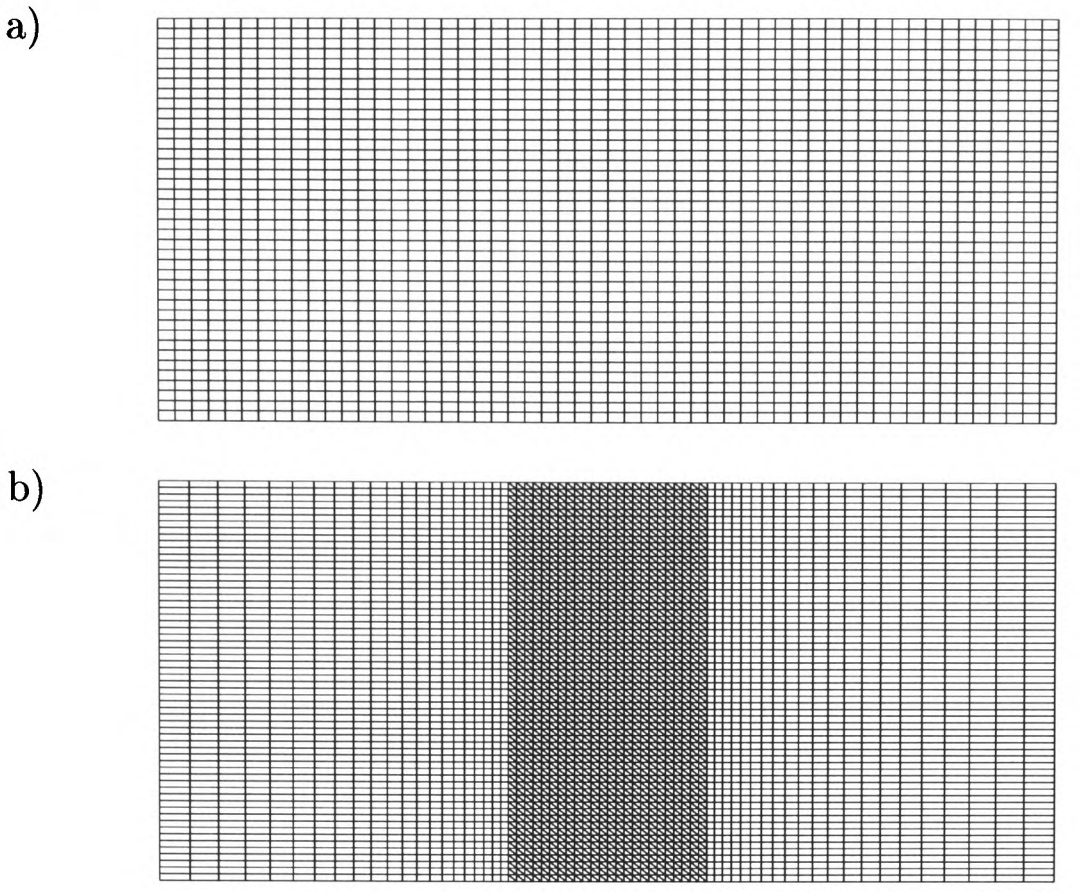

Figure 3.2: The 2-D untructured meshes a) Mesh 1: uniform mesh with rectangular elements, b) Mesh 2: non-uniform mesh with mixed elements.

order to quantify the agreements the l_2 error was calculated for each example where the l_2 error is defined as

$$E^{ij} = \frac{\sum(\tau^{ij}_{1(exact)} - \tau^{ij}_{1(numeric)})^2}{\sum(\tau^{ij}_{1(exact)})^2}, \tag{3.29}$$

where τ_1^{ij} is the normal or shear stress. The l_2 errors are presented in Table 3.5 where it can be seen that the errors for τ_1^{xx} and τ_1^{xy} are small and are almost identical on each plane. These results indicate that the model has been implemented similarly across each plane.

Simulations were then continued on the XY-plane in order to test the accuracy of the model implementation for higher We numbers. The We number was incremented by 0.5 for each consecutive run and the result from the previous simulation was used for the initial values.

The calculated normal and shear stress profiles along the cross section at $x = 10$ are plotted with the analytical solutions in Figure 3.5. From these it can be seen that there is close agreement between the calculated and analytical values for increasing We. For τ_1^{xy} the values superimpose each other which indicates excellent agreement. This is confirmed by the l_2 errors which are presented in Table 3.6.

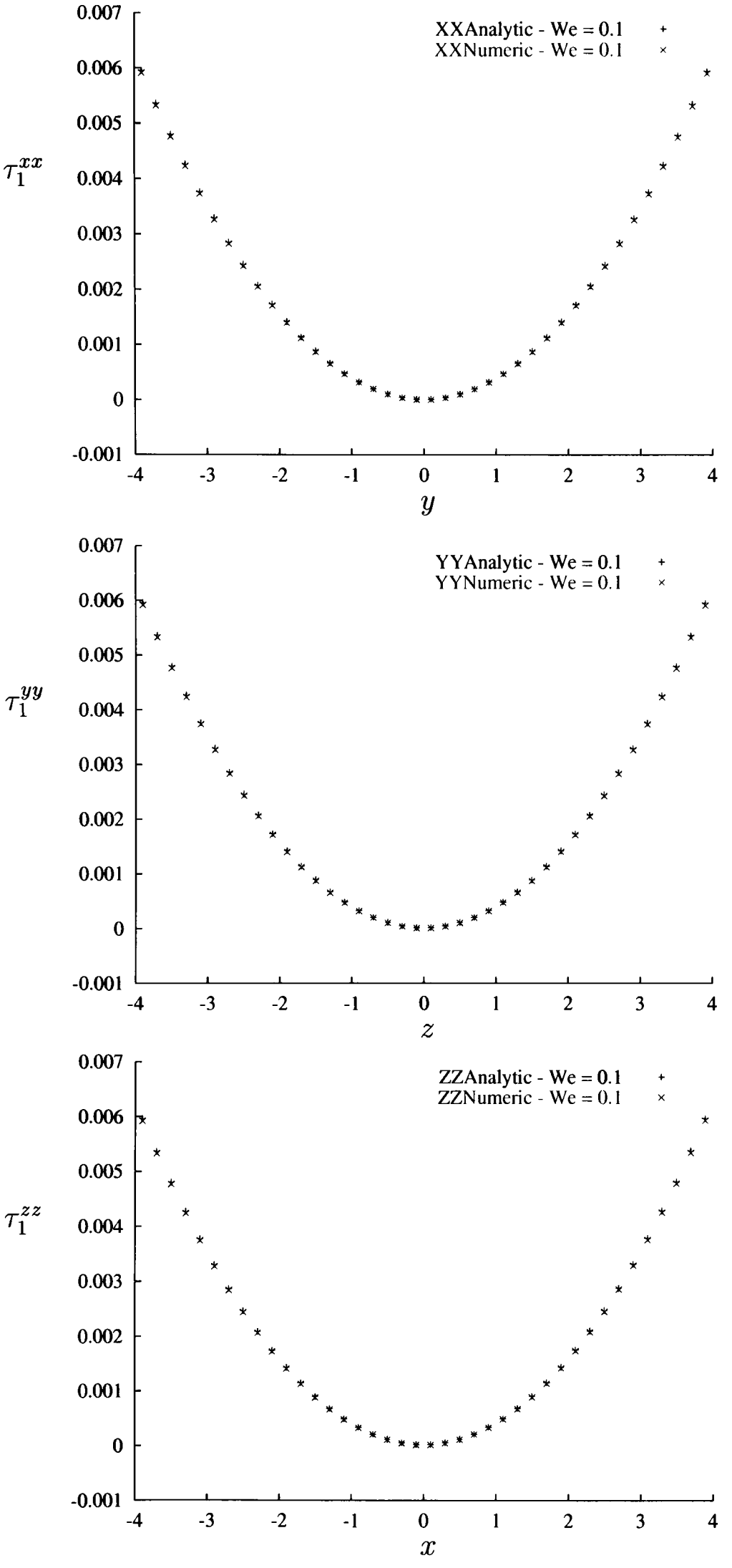

Figure 3.3: The analytical and numerical plots of τ_1^{xx},τ_1^{yy} and τ_1^{zz} normal stresses in XY,YZ and ZX planes respectively.

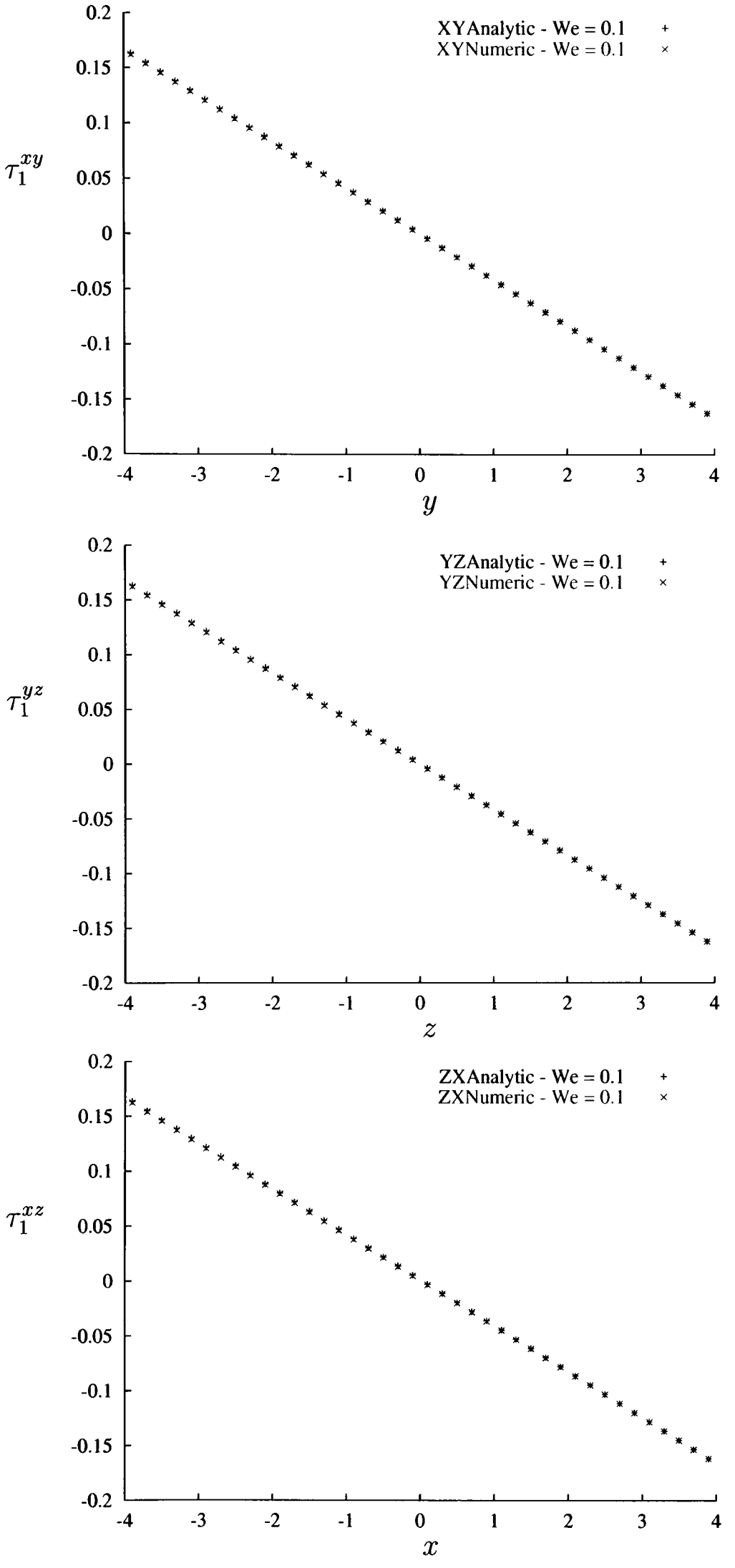

Figure 3.4: The analytical and numerical plots of τ_1^{xy}, τ_1^{yz} and τ_1^{zx} shear stresses in XY,YZ and ZX planes respectively.

XY-plane	$E^{xx} = 3.51\text{E}-05$	$E^{xy} = 7.35\text{E}-06$
YZ-plane	$E^{yy} = 3.51\text{E}-05$	$E^{yz} = 7.35\text{E}-06$
XZ-plane	$E^{zz} = 3.51\text{E}-05$	$E^{xz} = 7.35\text{E}-06$

Table 3.5: The l_2-norm values for the stresses on XY, YZ and XZ planes.

Stress	$We = 0.1$	$We = 0.5$	$We = 1.0$	$We = 1.5$	$We = 2.0$	$We = 2.5$
τ_1^{xx}	$3.51\text{E}-5$	$2.92\text{E}-5$	$2.94\text{E}-5$	$2.95\text{E}-5$	$3.10\text{E}-5$	$3.02\text{E}-5$
τ_1^{xy}	$7.35\text{E}-6$	$7.26\text{E}-6$	$7.21\text{E}-6$	$7.19\text{E}-6$	$7.18\text{E}-6$	$7.17\text{E}-6$

Table 3.6: The l_2 errors for the τ_1^{xx} and τ_1^{xy} stresses with increasing We numbers.

In order to test the capability of the algorithm further, simulations were carried out on Mesh 2 which is a non-uniform mesh consisting of rectangular as well as triangle elements (see Figure 3.2 b)). Simulations were carried out on the XY-plane and the initial and boundary conditions used were the same as for the orthogonal mesh, Mesh 1. In this test non-orthogonal corrections were used. The We number was incremented by 0.5 for each consecutive run and the result from the previous simulation was used as initial values. Figure 3.6 shows the calculated normal and shear stress profiles along the cross section at $x = 9$ which is the centre line and lies within the region where the triangular elements are at Weissenberg numbers $0.1, 1.0$ and 2.0. The plots show that the numerical values compare very well with the analytical solutions for increasing We. For τ_1^{xy} once again the results superimpose each other showing very good agreement with the analytical solution. The l_2 errors are presented in Table 3.7. The l_2 errors for Mesh 2 are larger than for Mesh 1. This may be due to the region of triangular elements in the mesh.

Having validated the accuracy of the implementation of the model through a planar channel, the algorithm is tested using the 4:1 planar contraction benchmark problem in the next section.

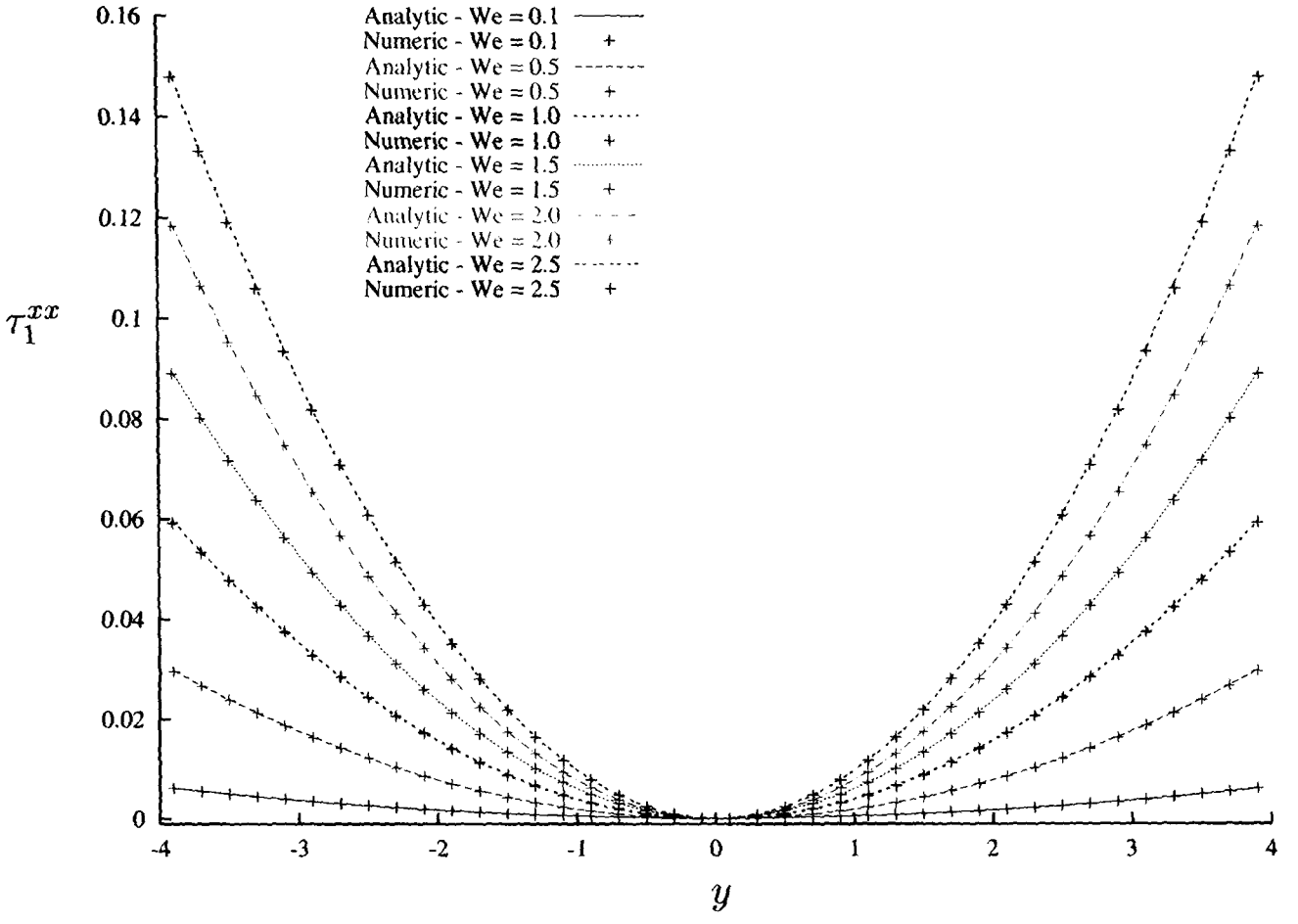

Figure 3.5: The analytical and numerical plots of τ_1^{xx} and τ_1^{xy} stresses in the XY plane with increasing Weissenberg number.

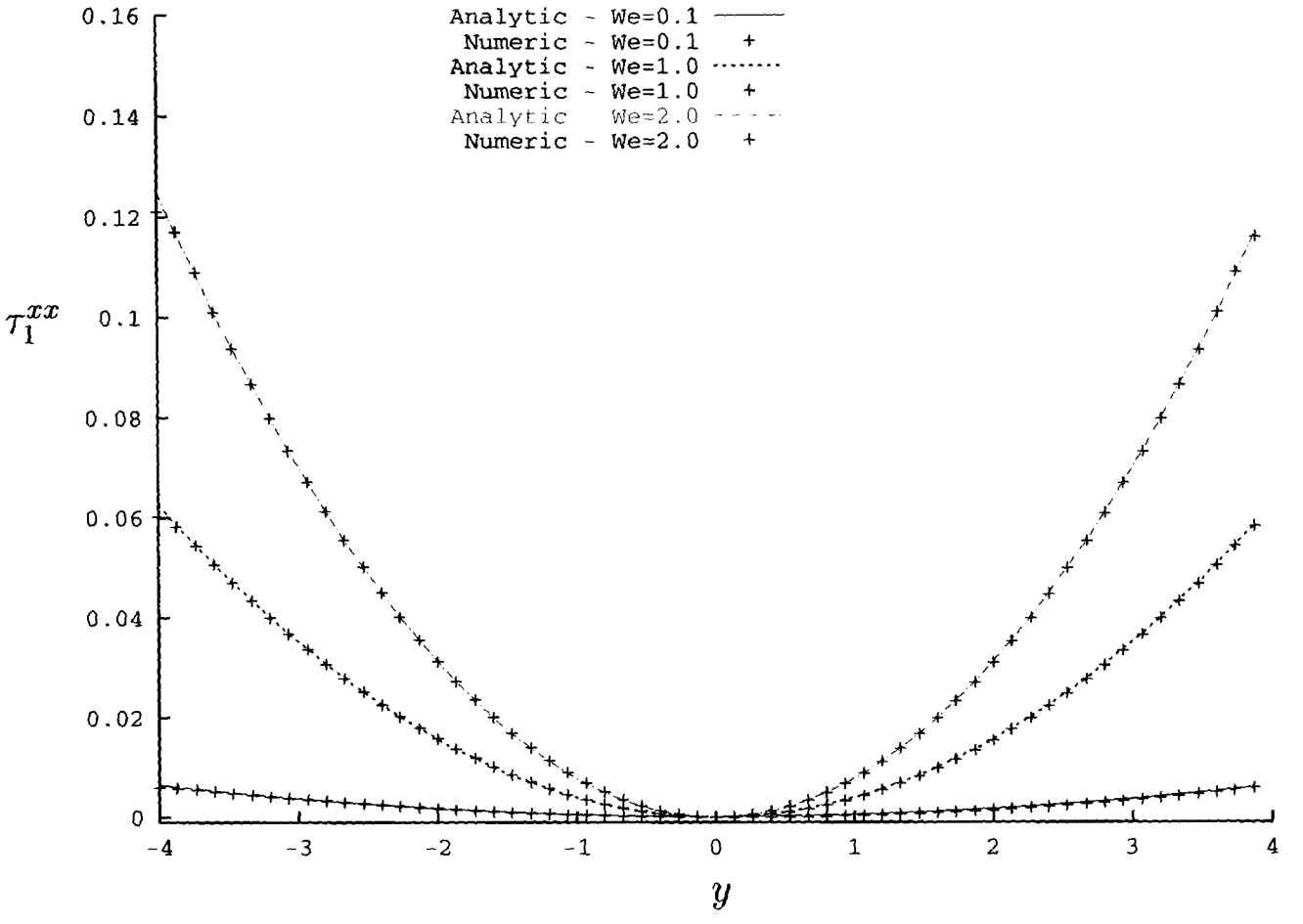

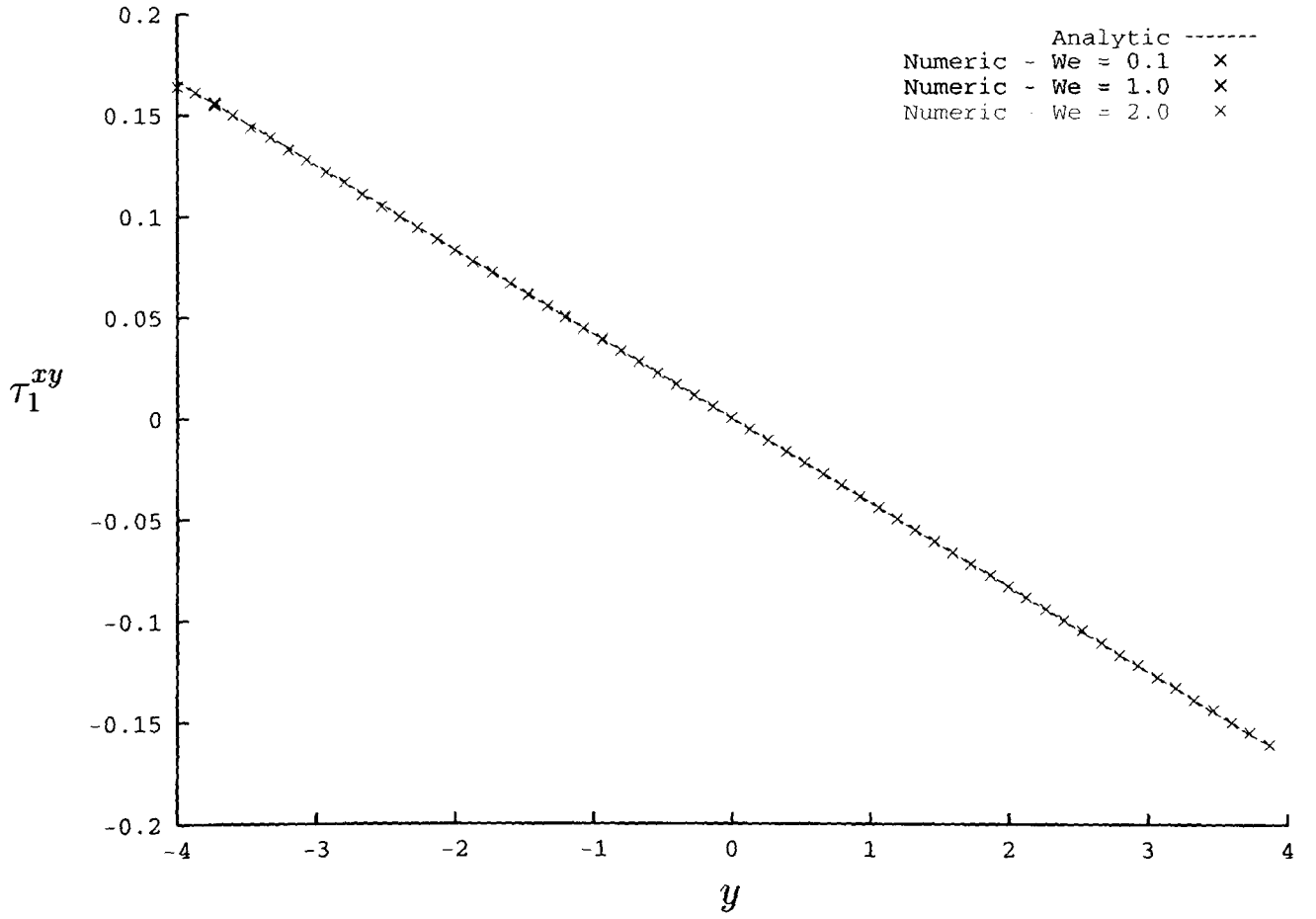

Figure 3.6: The analytical and numerical plots of τ_1^{xx} and τ_1^{xy} stresses in the XY plane with increasing Weissenberg number on mesh with mixed elements.

Stress	$We = 0.1$	$We = 1.0$	$We = 2.0$
τ_1^{xx}	2.29E − 3	3.28E − 3	1.22E − 4
τ_1^{xy}	2.02E − 5	1.92E − 5	1.80E − 5

Table 3.7: The l_2 errors for the τ_1^{xx} and τ_1^{xy} stresses with increasing We numbers on the mixed element mesh.

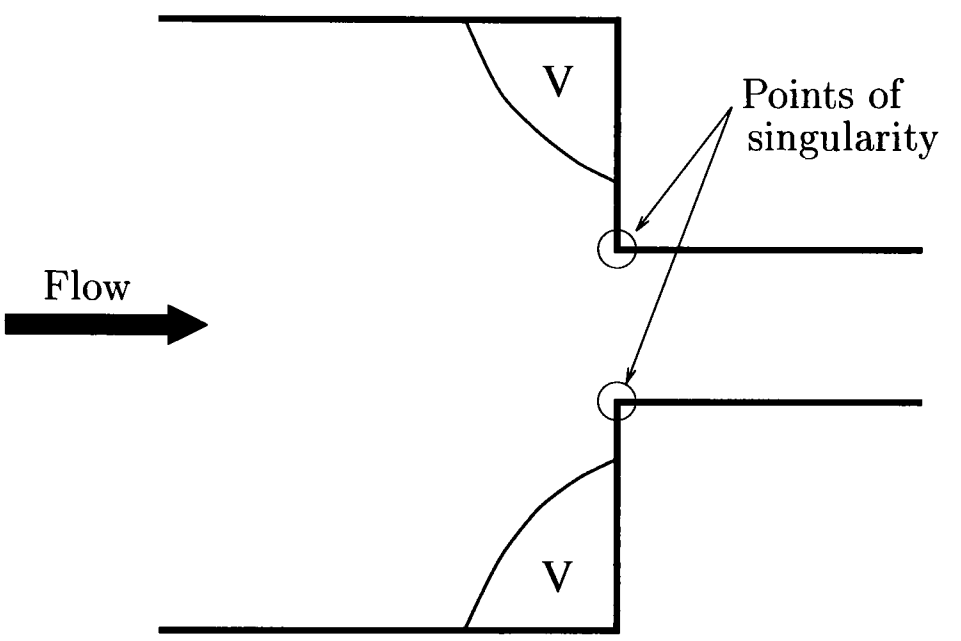

V - Vortex

Figure 3.7: The 4:1 planar contraction geometry.

3.7 Flow Through a 4:1 Planar Contraction

In this section creeping flow (ie $Re = 0$) of the Oldroyd-B fluid through a 4:1 planar contraction will be modelled. This is a challenging test case and there have been many papers published on it during the last two decades.

Although the geometry of the test case is relatively simple, see Figure 3.7, it has been found to be numerically challenging when modelling Oldroyd/Maxwell type fluids. The existence of a point of singularity in the geometry is believed to cause many numerical methods to fail for high We numbers mainly due to a high stress build up in this region. The presence of a vortex in the salient corner of the geometry is considered another important feature in terms of validation of numerical techniques.

The complexity of the flow of an Oldroyd-B fluid through a 4:1 planar contraction has made this problem an important benchmark test case for novel numerical methods for viscoelastic flow. In the following section a review of published numerical and experimental results for this test case is presented.

3.7.1 Review of Previous Numerical Work

The earliest work on the numerical modelling of the Oldroyd-B fluid through a 4:1 planar contraction using a finite volume technique is by Yoo and Na [18]. In their numerical study Yoo and Na investigated creeping flow. The results presented on the size and shape of the salient corner vortex clearly showed the development of a lip vortex with increasing We. It was also noted that the centre of rotation of the salient corner vortex shifted towards the re-entrant corner as We was increased. The shifting of the salient corner vortex was found to be qualitatively similar to experimental results of Boger et al. [64]. The size and shape of the vortex for creeping flow, was also found to be sensitive to the value of β.

Sato and Richardson [14] used a combined finite volume/finite element technique to model transient viscoelastic flow through a 4:1 planar contraction. Here the momentum equations were modelled using a finite element method and the finite-volume was used to solve the Oldroyd-B constitutive equation. The flow was modelled for $Re = 0.01, Re = 0.1$ and $Re = 1$ with $\beta = 1/9$. For $Re = 1$ a slight lip vortex was observed on the most refined mesh. Its absence in the less refined meshes, led the authors to suggest that it may be sensitive to mesh resolution. Simulations were stopped at $We = 2$ due to the computational time required to achieve a steady state solution being too long. Results for the detachment length proved to be independent of Re when $Re \leq 0.1$. It was also seen that a transient lip vortex appeared for $Re = 0.01$ when We was instantaneously increased from 1 to 2 which weakened in intensity and was enveloped by the salient corner vortex. The results presented for the salient corner vortex were in good agreement with other published numerical results and the experimental results of White and Baird [65].

Matallah et al. [16] used recovery and stress-splitting within a fractional-staged finite-element formulation for both $Re = 0$ and $Re = 1$. For $Re = 0$, with the

recovery scheme the size and strength of the salient corner vortex slightly decreased between $2 \leq We \leq 4$ and then increased as We reached 8. A lip vortex was detected at $We = 2$ which was larger in intensity than the salient corner vortex. As We was further increased the lip vortex grew in intensity dominating the salient corner vortex. The size of the salient corner vortex compared well with results produced by Sato and Richardson [14] and Yoo and Na [18] for creeping flow. For the coupled EVSS scheme the salient corner vortex was seen to grow with increasing We, but the lip vortex which appeared at $We = 0$ was seen to grow up to $We = 4$ and then decay as We was further increased. However the formulation produced large salient corner vortices which were over-exaggerated. This was attributed to inaccuracies resulting from the correction schemes employed.

Phillips and Williams [19], using a semi-Lagrangian finite volume method for the Oldroyd-B fluid, presented results for both creeping and inertial flows. It was observed that the length of the salient corner vortex decreased slightly with increasing We and that when $We = 2.0$ a lip vortex appeared, which grew in intensity as We was further increased. The lip vortex only appeared in their most refined mesh, and the authors suggested that the appearance of the lip vortex may be mesh dependent. Their results for creeping flow compared well with Matallah et al. [16].

The initial work by Oliveira et al. [62] using the collocated finite volume technique with the linear-upwind differencing scheme, involved the benchmark problems of a UCM fluid on the entry flow problem of Eggleton et al. [66] and the unbounded flows around a cylinder. In a subsequent publication Oliveira and Pinho [21] employed the same finite volume technique with the second-order Linear Upwinding Scheme(LUDS) to model the flow of UCM and Simplified Phan-Thien−Tanner (SPTT) fluids in a 4:1 planar contraction geometry in 2-D. Their $De = 1$ is equivalent to our $We = 1$. With the first-order differencing scheme(UDS), it was possible to achieve convergence up to $De = 8$ on their finest mesh. However with LUDS the De value for which convergence could be achieved decreased with mesh refinement. The range was as low as $De \leq 1$ on the finest mesh with LUDS. On the finest mesh with UDS,the salient corner vortex decreased both in size and intensity in the range $De \leq 2$ as elasticity was raised for $Re = 0.01$. A lip vortex was observed for elasticity as low as $De \approx 1$. As the Deborah number was increased from 1 to 2 the

lip vortex was seen to increase in size and strength while the salient corner vortex began to finger towards the re-entrant corner and gradually separating stream lines enveloped the two vortices. Alves et al. [22] modelled UCM fluid flow through a 4:1 planar contraction using the same finite volume technique as Oliveira et al. with the MINMOD differencing scheme. The MINMOD scheme which is a hybrid of upwind, linear upwind and central differencing was able to extend the range of Deborah numbers for which converged solutions could be obtained on extremely refined meshes. Using the most refined mesh of Oliveira et al. [21], the range of De was extended to 5 with the use of MINMOD. The plots of streamlines confirmed trends reported by Oliveira et al.[21]. The salient corner vortex decreased in both size and strength as elasticity was increased up to $De = 3$ and was followed by vortex enhancement with further increase in elasticity. A lip vortex appeared at $De = 1$. However, enveloping of the two vortices appeared to be delayed well beyond $De = 3$ whereas with UDS [21] it had already taken place when elasticity reached $De = 3$ for creeping flow.

More recently Aboubacar and Webster [20] published work on this problem for an Oldroyd-B fluid with creeping flow using a cell-vertex hybrid finite volume/element scheme with triangular meshes. Their results showed the existence of a lip vortex for $We > 1$ and the size of the lip vortex clearly showed mesh dependency. They observed a diminishing lip vortex with mesh refinement which nearly vanished at $We = 2$ and was similar to the observations by Matallah et al.[16] for the same problem and Alves et al. [22] for a UCM fluid. On their most refined mesh, they also noted the presence of a faint trailing edge vortex on the downstream wall close to the re-entrant corner. With increasing We the salient corner vortex decreased in size and strength while the lip vortex grew in intensity.

The latest work by Alves et al [67] on the 4:1 planar contraction includes results for the Oldroyd-B fluid using a new convection scheme specially designed to dampen oscillations in regions of high gradient in flow in the numerical solution of differential constitutive equations. With this new scheme they have been able to achieve convergence up to $De = 2.5$ on the their finest mesh where the minimum mesh spacing is $\Delta x_{min} = \Delta y_{min} = 0.0035$. The results confirm trends reported earlier by them for the UCM [22] fluid and by Aboubacar et al [20]. Lip vortex activity is observed at $De = 1.5$.

It can clearly be seen that modelling Oldroyd-B fluid in a 4:1 planar contraction geometry has been aimed at increasing the elasticity limit and capturing the flow behaviour in the region of the salient and re-entrant corners. The work of Sato and Richardson [14], Phillips and Williams [19] and Matallah et al. [16] indicated a constant salient vortex size for creeping flow of an Oldroyd-B fluid with increasing elasticity. However, recent work by Alves et al.[22, 67] and Aboubacar et al.[20] show that the size of the salient corner vortex in fact decreases with increasing elasticity for a UCM fluid at $Re = 0.01$ and creeping flow of an Oldroyd-B fluid. This presents a new trend in the numerical prediction of salient corner behaviour.

The appearance and behaviour of the lip-vortex mechanism tends to vary with elasticity, mesh refinement and type of differencing scheme used for the convection terms. Experiments carried out by Evans and Walters [68, 69] on planar flows point to the possibility of salient corner vortex enhancement and the existence of lip vortex mechanisms under certain conditions. The dominant mechanism has been found to depend on the material properties of the fluid and the contraction ratio of the geometry. In the experiments in [69], a solution of polyacrylamide gave rise to a lip vortex for a 4:1 contraction, while in [68] for a Boger fluid, the contraction ratio had to be increased to 80:1 in order to be able to even see a lip vortex. Therefore, the existence of a lip vortex mechanism is considered to be more likely for high contraction ratios while its existence in a 4:1 geometry has been quite elusive.

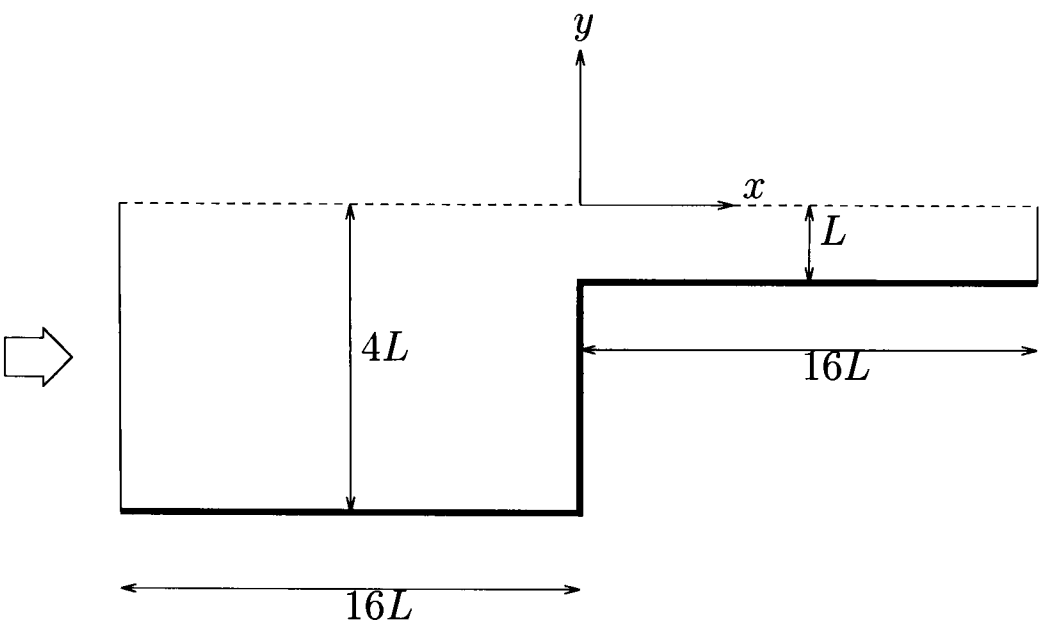

Figure 3.8: The contraction flow geometry.

3.7.2 Geometry

The flow geometry for the 4:1 planar contraction is presented in Figure 3.8. Since the flow is symmetric about $y = 0$, a solution is only sought for $y \leq 0$. Therefore, only the lower half of the geometry is considered. L is the downstream half channel width. At inflow the half channel width is $4L$. Up and downstream channel lengths are each $16L$. It is assumed that the downstream channel length is chosen long enough so that the exit flow has a fully developed parabolic profile.

3.7.3 Boundary Conditions

The dimensionless units U and L are chosen to be $U = 1$ and $L = 1$. Then

$$We = \lambda_1. \tag{3.30}$$

At inflow a fully developed parabolic Poiseuille flow is imposed given by

$$u = \frac{3}{128}(16 - y^2), \;\; v = 0. \tag{3.31}$$

No-slip conditions are imposed on solid boundaries for u, v. Symmetry conditions are specified on the axis of symmetry. At outflow, pressure is set to zero and homogeneous Neumann boundary conditions are imposed for the extra-stresses. No boundary conditions were imposed for the stresses. The parameter β is taken to be $1/9$ for purposes of comparison. The initial conditions are chosen to be either the

Mesh	Control volumes	Total degrees of freedom	Δx_{min}	Δy_{min}
Mesh 1	6560	39360	0.0342	0.0750
Mesh 2	7392	44352	0.0250	0.0190
Mesh P3	19857	119142	0.0076	0.0127
Mesh 3	37248	223488	0.0057	0.0085

Table 3.8: Mesh characteristics of the 4:1 contraction problem.

solution to the corresponding Stokes problem or the solution obtained for a smaller We number.

3.7.4 Numerical Results

Mesh characteristics

To study the effects of mesh refinement on the algorithm relative to elasticity, simulations were carried out on several meshes for the 4:1 planar contraction geometry. All meshes are non-uniform and have a greater concentration of cells in the region of the salient and re-entrant corners. The meshes were refined towards the salient corner in an attempt to capture the salient corner vortex behaviour as accurately as possible, while the refinement in the region of the re-entrant corner was aimed at picking up lip vortex mechanisms and testing the robustness of the algorithm in coping with the high stress build up at the point of singularity. The mesh characteristics of four of the meshes used are presented in Table 3.8. Figure 3.9 shows the mesh distribution in the region of the salient and re-entrant corners of Meshes 1 to 3. On Mesh 1, the smallest element is at the salient corner. On Meshes 2,P3 and 3, the smallest element is at the re-entrant corner. The four meshes are also consecutively refined towards the salient and re-entrant corners to investigate the mesh dependency of the vortex behaviour as elasticity is increased for creeping flow. For purposes of validation and to pick up the latest trends observed in salient corner vortex behaviour, the mesh refinement is also such that Mesh 3 is similar to the most refined mesh of Alves et al. [22]. The timestep used for the transient runs is $\Delta t = 1 \times 10^{-3}$.

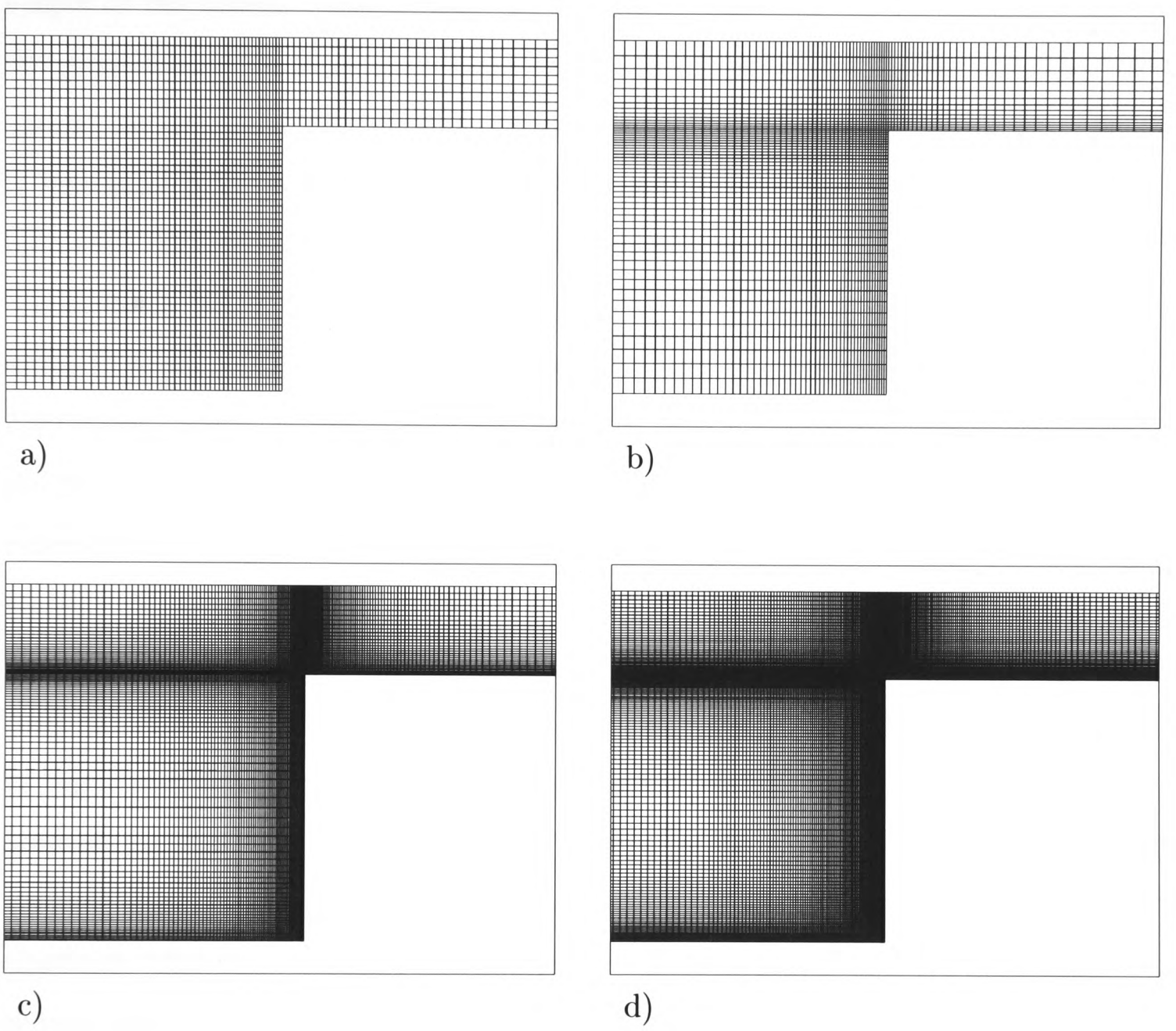

Figure 3.9: The mesh in the region of the salient and re-entrant corners for a) Mesh 1, b) Mesh 2, c) Mesh P3 and d) Mesh 3.

Streamlines and vortex behaviour

Simulations were carried out on Mesh 1 for a series of Weissenberg numbers, using the hybrid differencing scheme which is a first-order scheme for convection. The length of the salient corner vortex L_1, which is defined to be the distance between the point where the separation line meets the bottom of the channel and the salient corner, is tabulated against the corresponding We number in Table 3.9. As We is increased from 0 to 0.1 the length increases and as the Weissenberg number is increased further the size of the salient corner vortex decreases and remains fairly constant for $We \leq 1.5$. Beyond $We = 2.0$ we observe vortex enhancement. The strength of the vortex ($\psi_{max} - 1$) also increases with elasticity (see Table 3.10). Figure 3.10 shows salient corner vortex behaviour as We is increased. The streamlines are plotted at increasing intervals of 2.0E-4 starting with the separation line which has a value of 1.0. At $We = 1.0$ a very weak lip-vortex appears slightly below the re-entrant corner. Aboubacar et al. [20] and Matallah et al. [16] reported similar lip-vortex behaviour for $We > 1$. The L_1 values are plotted against results of Yoo and Na [18], Sato and Richardson [14], Matallah et al. [16] and Phillips and Williams[19] in Figure 3.11. The results compare well with the other published results. However according to recent trends reported by Alves et al. [22, 67] and Aboubacar [20] the length and strength of the salient corner vortex should decrease with increasing elasticity. Therefore simulations were carried out on Mesh 2 which has a higher mesh refinement in the salient and re-entrant corners.

Figure 3.12 shows the streamlines obtained using the hybrid differencing scheme on Mesh 2. The streamlines have been plotted using the same intervals as in Figure 3.10. With the hybrid scheme, the lip-vortex appears at $We = 1.5$, which is at a higher elasticity than on Mesh 1. As with Mesh 1 the length of the salient corner vortex increases between $We = 0$ and $We = 0.1$ (see Table 3.9. This then gradually decreases and settles to a near constant value for higher elasticity. However the vortex enhancement which occured at $We \geq 2.0$ on Mesh 1 is not observed on Mesh 2. The $\psi_{max} - 1$ values are listed in Table 3.10. There is a sudden increase in the salient corner vortex intensity at $We = 0.1$ which then settles down to a near constant value with increasing elasticity.

Simulations were also carried out on Mesh 2 using the QUICK differencing scheme. The vortex length and intensity is tabulated in Tables 3.9 and 3.10. The $\psi_{max} - 1$ values are similar to the hybrid scheme and length L_1 appears to follow the same trend as with the hybrid scheme. However, the lip-vortex appears at $We = 1.0$ which is a lower elasticity (see Figure 3.12).

For Mesh 1 and Mesh 2 there is no indication of the trends reported by Alves et al. [22] and Aboubacar et al. [20]. Therefore, simulations were carried out on Mesh 3 for the same range of Weissenberg numbers using the QUICK differencing scheme. Vortex behaviour with increasing elasticity is presented in Figure 3.13 and the L_1 and $\psi_{max} - 1$ values are listed in Tables 3.9 and 3.10. The scale for the streamlines is the same as in Figure 3.12. It can clearly be seen that as elasticity is increased the size and intensity of the salient corner vortex decreases and the lip-vortex only appears at $We = 1.5$. These results compare well with the trends reported by Alves et al. [22, 67] and Aboubacar et al. [20] as shown in Figure 3.14. In the initial phase of this project computational resources were restricted to a 433MHz Dec Alpha EV5.6 64-bit CPU. Therefore simulations on Mesh 3 were not carried out beyond $We = 3.0$ due to calculation times of the order of up to six weeks to achieve convergence.

Since the continuous decrease in L_1 with increasing We was only seen on the most refined mesh, Mesh 3, a series of simulations were then carried out on Mesh P3 which has local refinement patterns similar to Mesh 3 in the salient and re-entrant corners but with less refinement than Mesh 3. The L_1 values for increasing We numbers for Mesh P3 are listed in Table 3.9. It is clear from the L_1 values that with Mesh P3 the vortex length also decreases significantly with increasing We up to $We = 2.0$. This confirms that the trend observed on Mesh 3 is not unique to Mesh 3, but is behaviour observed on suitably refined meshes for viscoelastic flow. However, it is interesting to note that with Mesh P3 the vortex length remains constant for $We > 2.0$.

The CPU times for increasing We numbers on Meshes P3 and 3 are given in Table 3.12.

	Mesh 1	Mesh 2		Mesh P3	Mesh 3
We	hybrid	hybrid	QUICK	QUICK	QUICK
0.0	1.391	1.391	1.391	1.391	1.391
0.1	1.582	1.617	1.617	1.582	1.530
0.5	1.547	1.582	1.617	1.530	1.478
1.0	1.530	1.582	1.582	1.460	1.408
1.5	1.530	1.478	1.478	1.408	1.391
2.0	1.582	1.478	1.478	1.356	1.304
2.5	1.652	1.408	1.460	1.356	1.269
3.0	-	-	-	1.356	1.217

Table 3.9: The dependence of L_1 on We for the meshes based on the differencing scheme.

	Mesh 1	Mesh 2		Mesh P3	Mesh 3
We	hybrid	hybrid	QUICK	QUICK	QUICK
0.0	0.001	0.001	0.0011	0.0011	0.0011
0.1	0.0017	0.0021	0.0021	0.0016	0.0015
0.5	0.0015	0.0019	0.0019	0.0014	0.0013
1.0	0.0015	0.0016	0.0017	0.0012	0.0011
1.5	0.0017	0.0015	0.0015	0.001	0.0009
2.0	0.0024	0.0015	0.0015	0.0009	0.0007
2.5	0.0041	0.0016	0.0016	0.0009	0.0007
3.0	-	-	-	0.001	0.0007

Table 3.10: The dependence of $\psi_{max} - 1$ on We for the meshes based on the differencing scheme.

We	Max τ^{xx}	Max τ^{yy}	Max τ^{xy}
0.1	91.9954	8.4007	22.7339
0.5	1377.9746	6.6538	39.3483
1.0	4506.2676	5.4870	50.3151
1.5	8281.7031	4.8365	55.6935
2.0	12254.9961	4.4014	58.6721
2.5	16397.4590	4.1382	60.7027
3.0	20827.3711	4.0126	62.4520

Table 3.11: The peak values of shear and normal total stresses as a function of We when $\mathrm{Re} = 0$.

Stress contours

In Figures 3.15 and 3.16 the stress contours for Mesh 3 are presented for Weissenberg numbers 1.0 and 2.0. While the contours are smooth around the corner singularity, downstream of the re-entrant corner there is a build up of stress boundary layers. Just beyond the re-entrant corner on the down-stream channel wall, there is a region of high stress concentration for the τ_1^{xx} and τ_1^{xy} stresses. This feature compares qualitatively with the work of Aboubacar et al.[20] where a similar behaviour for the τ_{xx} and τ_{xy} stresses is observed at $We = 1.0$ and $We = 2.0$. In Figure 3.17, the τ stresses (i.e. $\tau = \tau_1 + \tau_2$) are plotted along the line $y = -1$ and it can be seen clearly that all stresses hit a peak at the point of singularity. The τ^{xx} stress continues to rise with increasing elasticity and slight oscillations begin to appear in the stress values just past the re-entrant corner. Similar behaviour is observed for the τ^{xy} stress, however the oscillations are more pronounced leading to negative τ^{xy} values. The τ^{yy} stress decreases with increasing elasticity. The peak values are presented in Table 3.11. Figure 3.17 show that the stress values settle down to their fully developed values along the downstream wall.

	Mesh P3		Mesh 3	
We	time-steps	CPU-time(h)	time-steps	CPU-time(h)
0.0	1000	36.95	1000	58.37
0.1	3000	151.91*	3000	220.16*
0.5	6000	65.86	6000	142.99
1.0	8000	88.09	8000	186.22
1.5	10000	114.26	10000	232.38
2.0	12000	133.22	10000	240.53
2.5	14000	153.77	14000	330.99
3.0	14000	144.59	14000	333.99

Table 3.12: The CPU times for increasing We numbers on Meshes P3 and 3. The CPU times are for serial simulations carried out on a single node of a 5 Alpha server E545 system with each system containing four, 1GHz CPUs and 4Gb of memory (1Gb per CPU) on operating system Tru645.1. The CPU times with * are on a 466MHz Dec Apha EV5.6 with 1Gb memory.

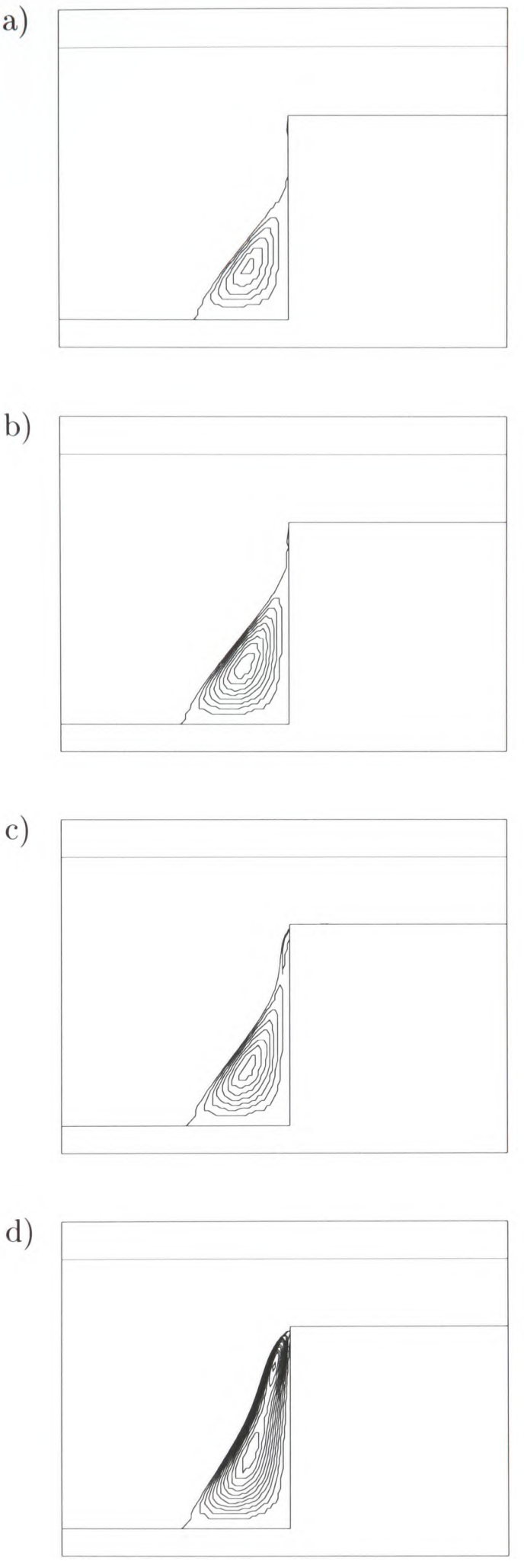

Figure 3.10: The streamlines for a) $We = 0$, b) $We = 0.1$, c) $We = 1.0$ and d) $We = 2.0$ when $Re = 0$ with hybrid on Mesh 1.

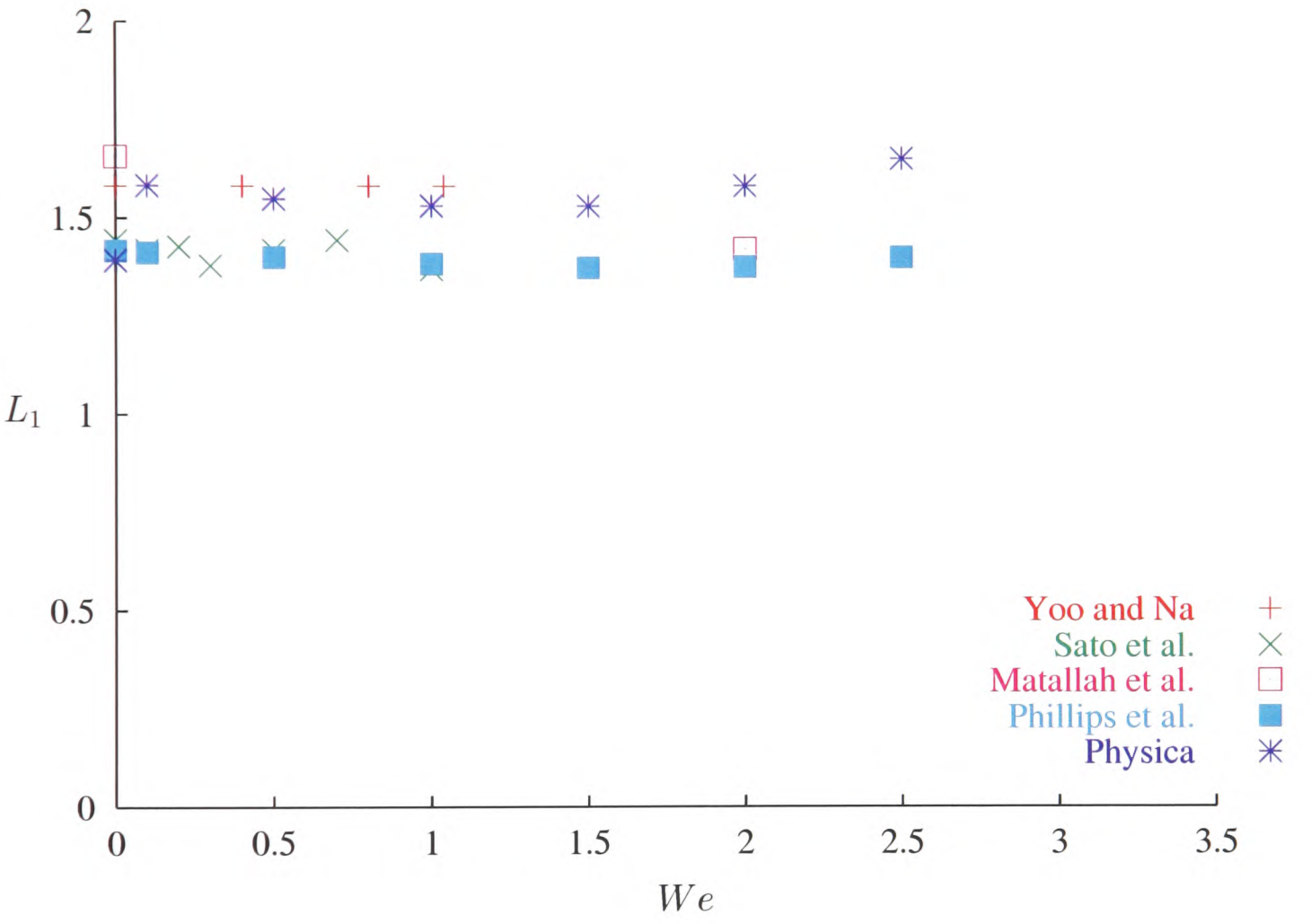

Figure 3.11: The length of the vortex L_1 on Mesh 1 with hybrid when $Re = 0$.

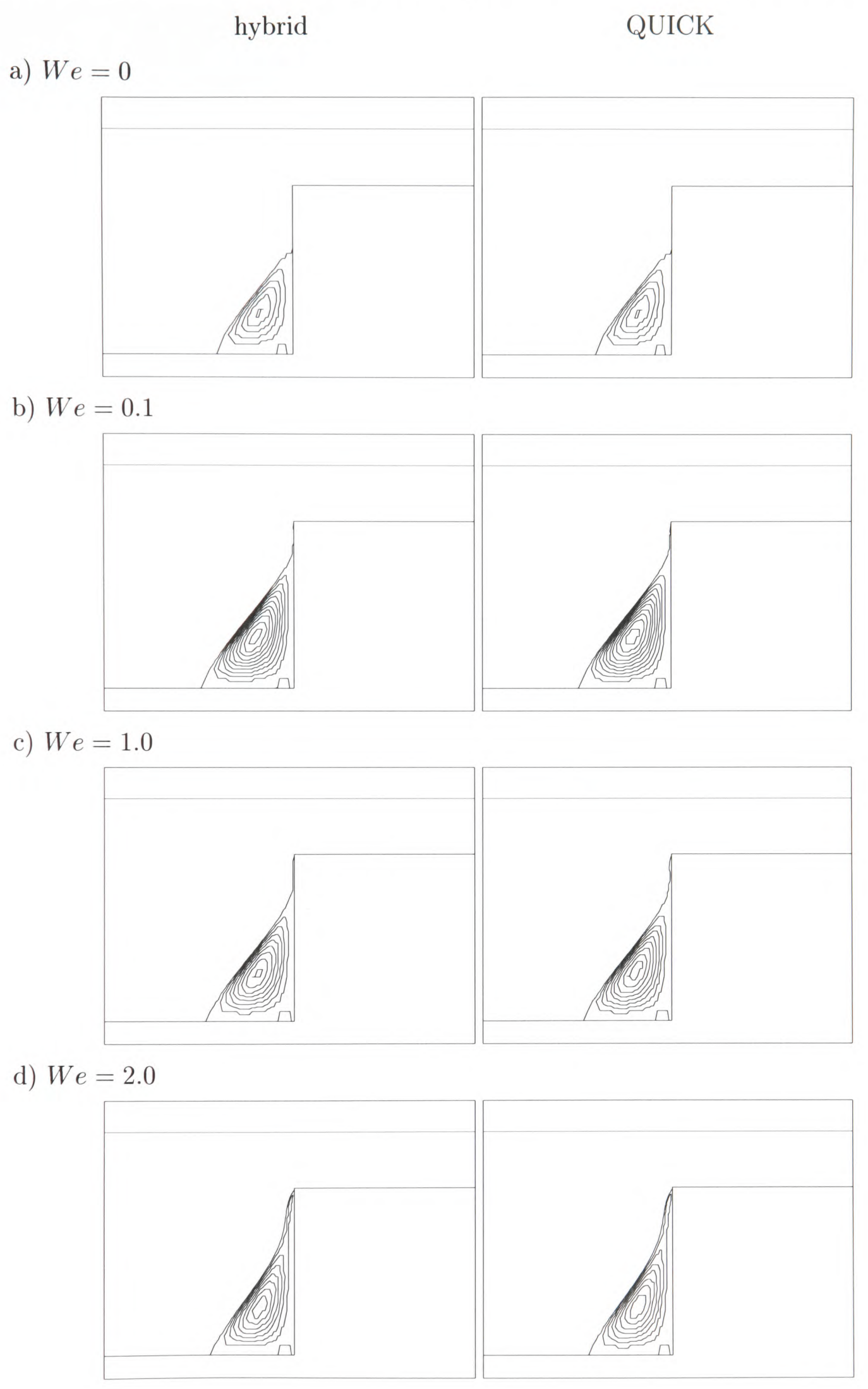

Figure 3.12: The streamlines for Mesh 2 with increasing We for hybrid and QUICK schemes.

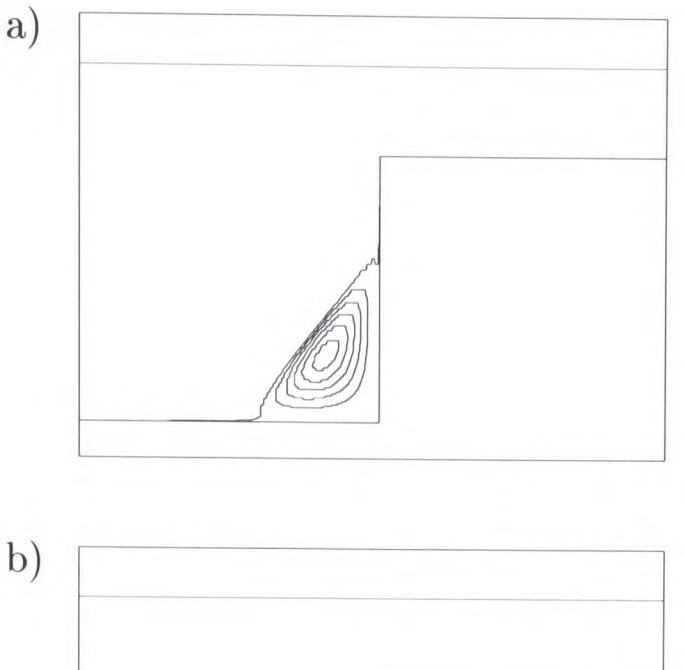

Figure 3.13: The streamlines for a) $We = 0$, b) $We = 0.1$, c) $We = 1.0$ and d) $We = 2.0$ when $Re = 0$ with QUICK on Mesh 3.

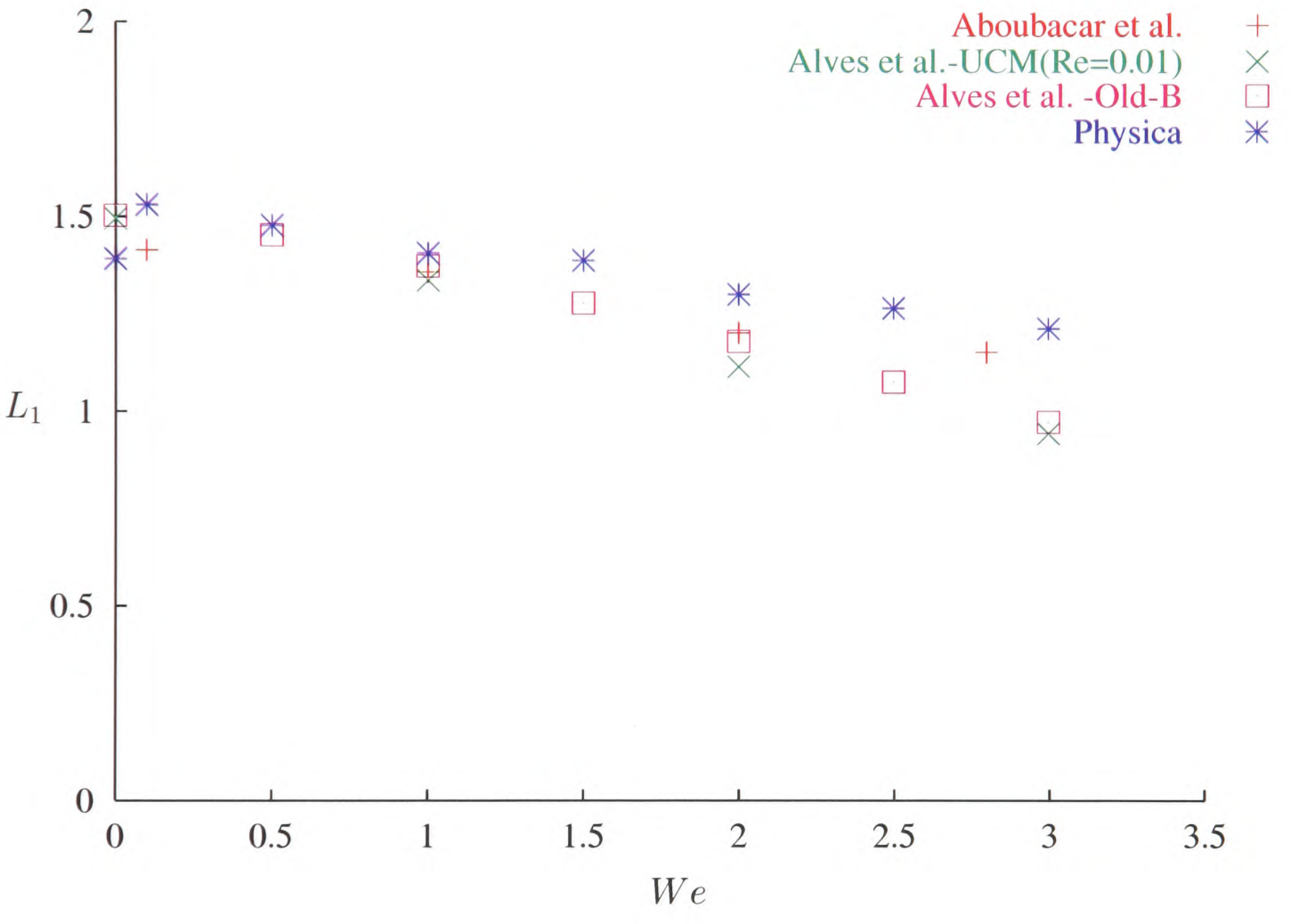

Figure 3.14: The length of the vortex L_1 when $Re = 0$.

a)

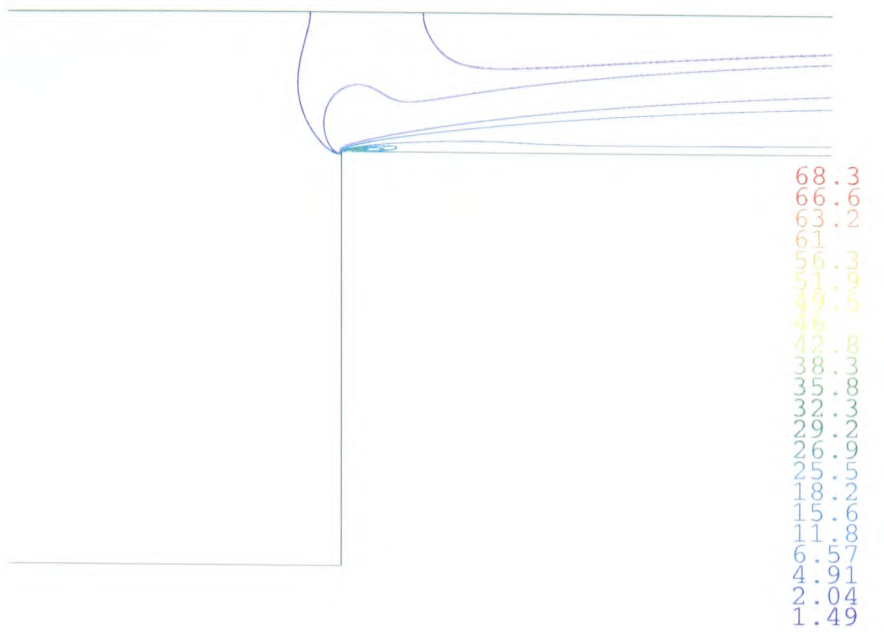

b)

c)

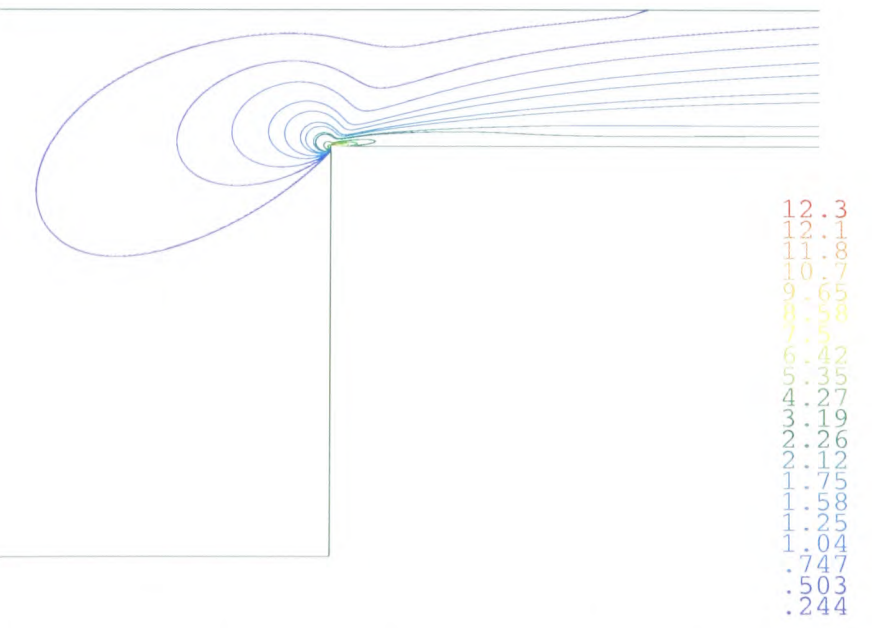

Figure 3.15: The a) τ_1^{xx}, b) τ_1^{yy} and c) τ_1^{xy} contours for $We = 1.0$ on Mesh 3 when $Re = 0$.

a)

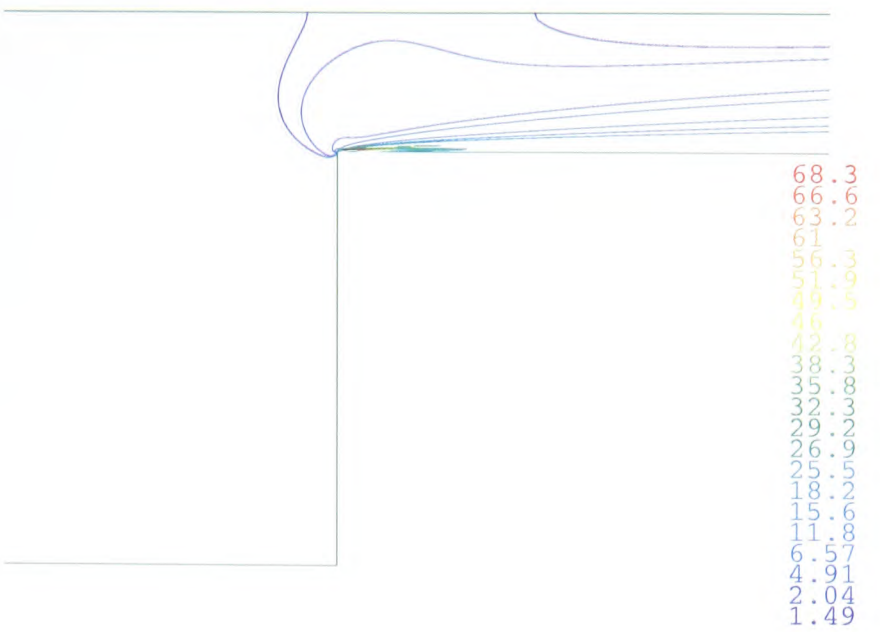

b)

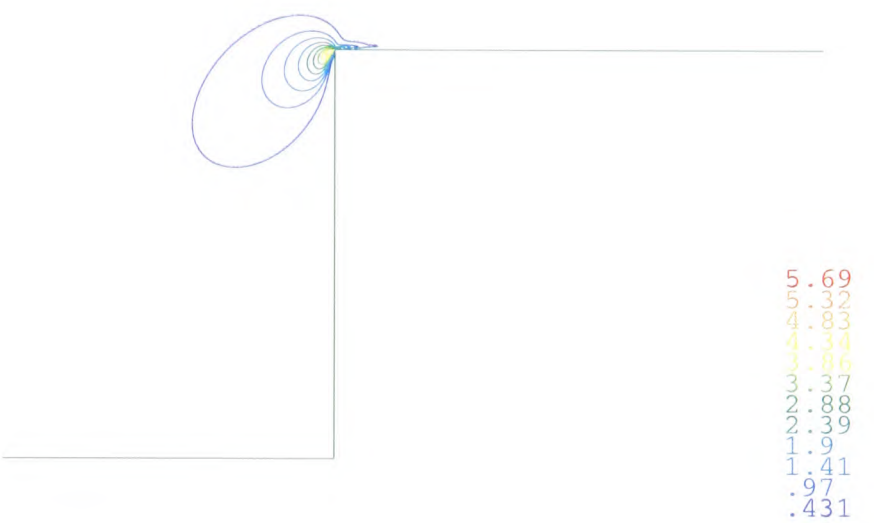

c)

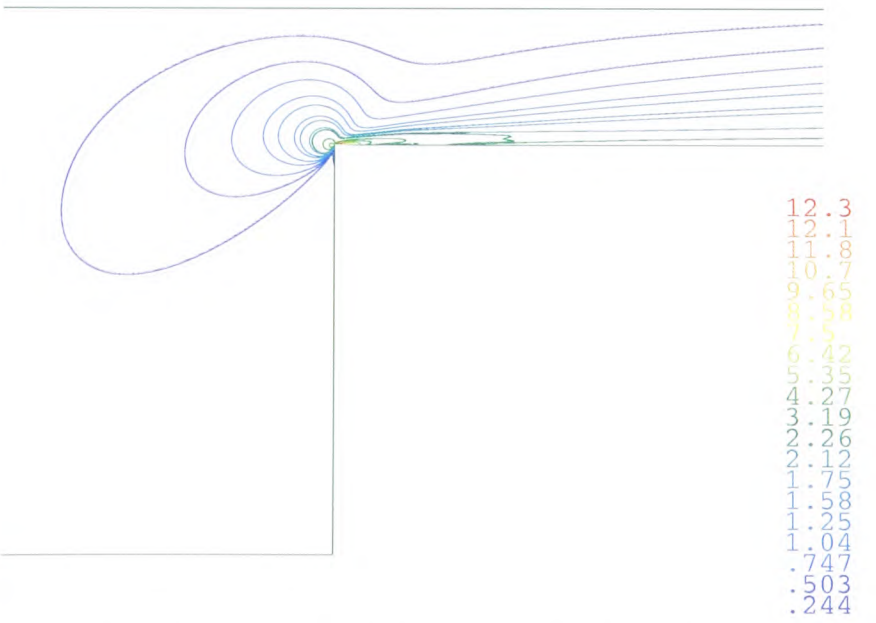

Figure 3.16: The a) τ_1^{xx}, b) τ_1^{yy} and c) τ_1^{xy} contours for $We = 2.0$ on Mesh 3 when $Re = 0$.

a)

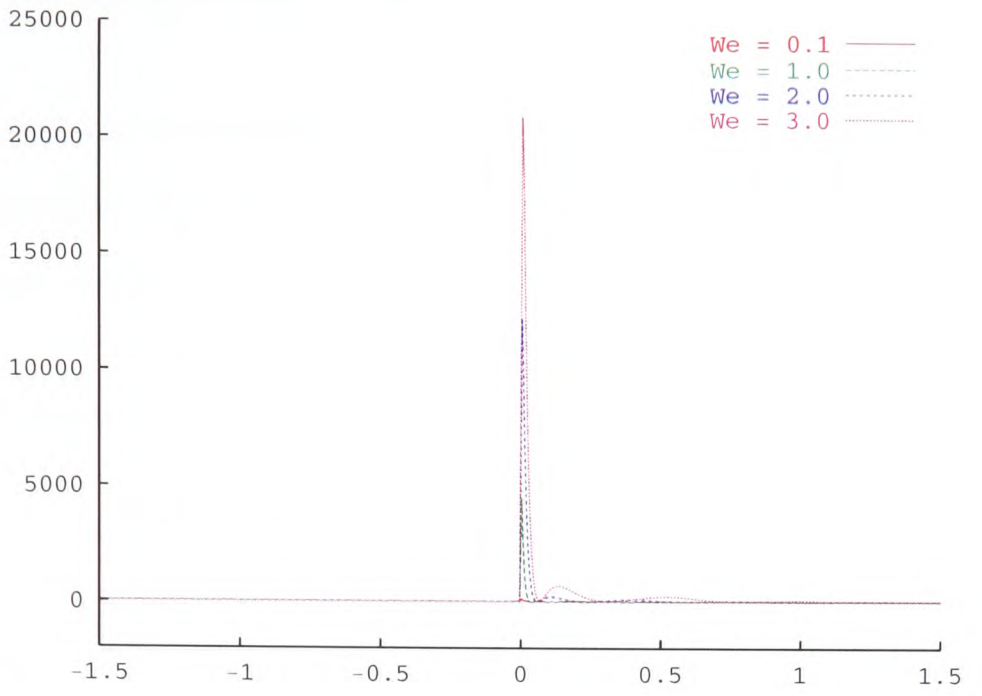

b)

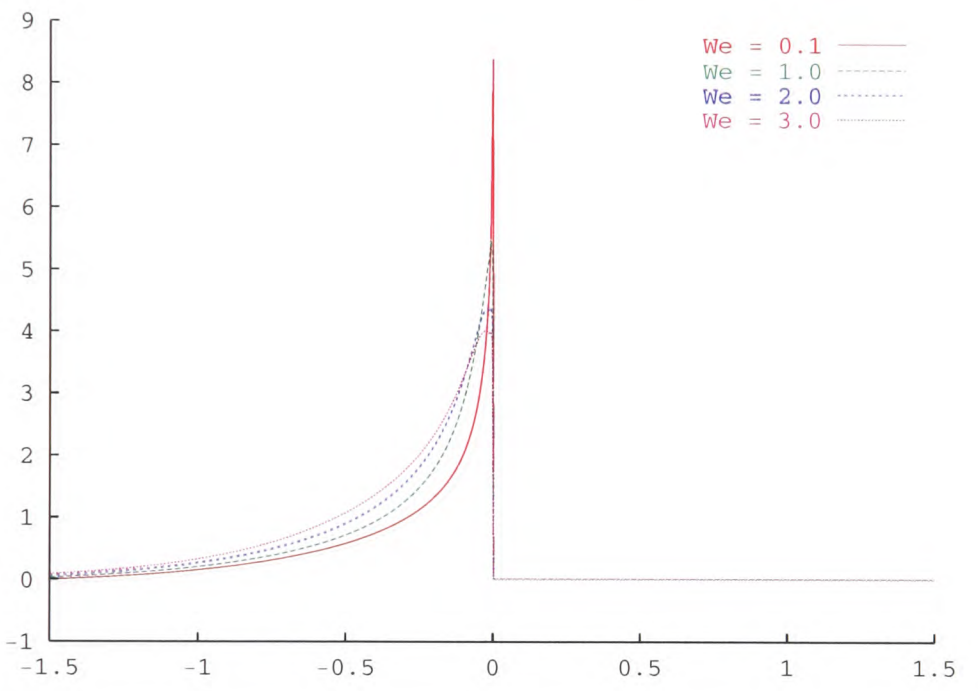

c)

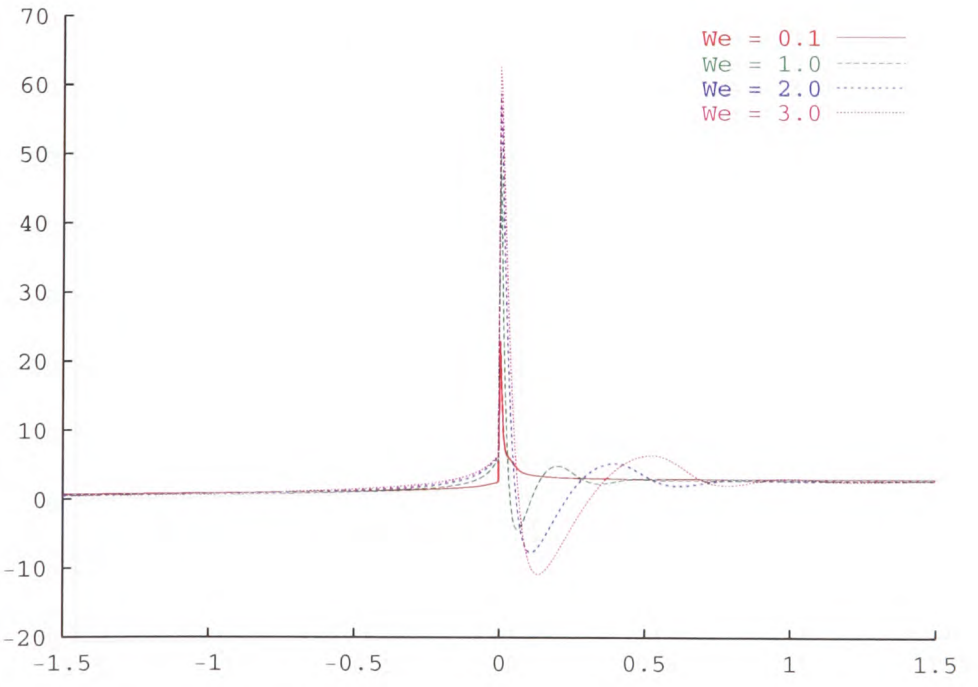

Figure 3.17: The values of the stresses a) τ^{xx},b) τ^{yy} and c) τ^{xy} along $y = -1$ for $Re = 0$.

3.8 Conclusion

The 3-D constitutive equations for the Oldroyd-B viscoelastic model have been implemented within the PHYSICA+ framework. The implementation of the 3-D model was validated using two test cases:

1. Flow through a planar channel.

2. Flow through a 4:1 planar contraction.

For the planar channel test viscoelastic flow was solved as a steady state problem in the XY,YZ and XZ planes respectively using a uniform mesh. The numerical stress profiles at steady state were compared with the analytical solutions and the l_2 errors were calculated to quantify the results. In all three planes the l_2 errors were found to be exact indicating accurate implementation. Simulations were then continued on the XY plane for increasing We numbers and the stress profiles and the l_2 errors at steady state once again indicated that the algorithm was able predict stress behaviour accurately for increasing We numbers. Finally a test was carried out for increasing values of We using a non-uniform mesh consisting of mixed elements (ie. rectangular as well as triangular elements). A comparison of the numerical stress profiles with the respective analytical solutions proved the algorithm to be able to accurately model viscoelastic flow on irregular unstructured meshes.

On the 4:1 planar contraction benchmark problem flow was solved as a transient problem for creeping flow. Several meshes with increased refinement were used to examine the vortex behaviour in the salient corner of the goemetry for increasing Weissenberg numers.

On the least refined mesh, Mesh 1, with the least accurate scheme, hybrid, the size, shape and strength of the salient corner vortex compares well with the results of Phillips and Williams [19], Matallah et al. [16] and Sato and Richardson [14] which all predicted a constant vortex size. The appearance of a lip-vortex at $We = 1.0$ indicates a similarity to observations of Aboubacar and Webster [20] on a reasonably coarse mesh.

However, on the most refined mesh, Mesh 3, a sharp decrease in vortex length is observed for increasing Weissenberg number - a trend which has been recently observed by Alves et al. [22] and Aboubacar et al. [20] on very refined meshes with higher order differencing schemes. The growth of the stress in the region of the re-entrant corner displays a similar behaviour to that reported in Aboubacar et al. [20] and the algorithm is stable for the range of Weissenberg numbers tested. In order to confirm the trend on the reduction of vortex sizes for increasing Weissenberg numbers, a further test was carried out on Mesh P3. Mesh P3 has local refinement patterns similar to Mesh 3 in the salient and re-entrant corners, but is less refined than Mesh 3. The simulation results for increasing Weissenberg numbers confirmed the trend seen on Mesh 3 up to a Weissenberg number of 2.0. Even though simulations have not been carrried out beyond $We = 3.0$ on Mesh 3, this is due to time constraints on this project and therefore $We = 3.0$ is not the Weissenberg number limit for this algorithm on this benchmark problem for this particular mesh. Further simulations will have to be carried out in order to establish the Weissenberg number limit for this algorithm for this problem.

The research presented in this chapter has demonstrated for the first time the use of a cell centred finite volume, fully unstructured mesh algorithm using hybrid and QUICK differencing schemes for the Oldroyd-B model through a 4:1 planar contraction. The results also emphasise the importance of using good quality and suitably refined, meshes when developing numerical models for viscoelastic flows. Although mesh refinement can be very expensive in computation time for structured meshes, this can potentially be overcome by using unstructured mesh techniques such as this one.

In the next chapter the algorithm developed and validated in this chapter is extended to solve viscoelastic free surface flows.

Chapter 4

Viscoelastic Free Surface Algorithms

This chapter presents two novel interface tracking methods for viscoelastic fluids based on the collocated finite volume algorithm presented in Chapter 2. The free surface algorithms are based on the Scalar Equation Algorithm (SEA) and the Level Set Method (LSM) to model two phase flow. The LSM algorithm models surface tension phenomena.

To validate the free surface viscoelastic algorithms results are presented for flow in a 2-D planar channel. The effect of surface tension is shown through the square to circle test case.

4.1 Free Surface Algorithms

Free surface motion is an integral feature of many natural phenomena. Therefore there is great interest especially in the CFD community in developing algorithms which can accurately model the motion of interfaces. However the numerical modelling of interface dynamics has proved to be quite challenging. Two main methods are employed at present to capture the interface dynamics:

- The first technique involves modifying the computational grid in a Lagrangian manner to match the distortion of the interface.

- With the second technique the interface has to be tracked through an Eulerian fixed grid.

The Lagrangian technique is commonly used for solid mechanics applications and is particularly suitable for problems involving small deformations. However problems involving large scale deformations result in highly distorted meshes which require frequent remeshing of the domain. This can be computationally expensive.

The Eulerian technique is more commonly used in fluid mechanics applications, particularly those which involve large deformations as it avoids the problem of mesh distortion. However, this technique is prone to numerical diffusion which causes the interface to spread over a number of cells as it moves through the domain. Therefore the numerical solution may not be realistic as in reality free surfaces remain sharp due to the action of gravity which separates immiscible fluids of differing density and surface tension. Techniques have been developed with solutions to overcome this problem on a Eulerian framework.

The Volume Of Fluid (VOF) [70] method is a popular method with fixed grids as it maintains the interface as a sharp front when used with the donor-acceptor [71] flux approximation technique. The method is based on the distribution of a scalar field which obeys an advection equation. The calculated scalar variable specifies the volume fraction occupied by the fluid in any particular cell in the computational domain. Thus the scalar will have a value of 1 if a cell contains only liquid and 0 if a cell is void of liquid. At the interface the scalar will have a value between 0 and 1. The method is computationally expensive in 3-D due to the Courant criterion limitation. It is also limited to modelling interface dynamics of a single fluid. In physical space all fluid systems are governed by two phase flows where when one fluid moves into a domain it displaces another (eg. air). Therefore the displacement of the second fluid has an effect on the interface. The VOF method does not take these effects into account.

The two-fluid technique has been developed to study the flow of two interpenetrating phases. As a result the method is able to take into account the effects from both fluids. The technique involves the coupled solution of two Navier-Stokes equations (one for each fluid). It also employs volume conservation and the interface is pre-

vented from smearing through the use of a donor acceptor flux approximation. The ISPA algorithm of Spalding is based on this method [72]. An important feature of the method is in being able to include wave-breaking and atomization phenomena. However the interphase momentum, heat and mass transfer are correlations which are specified implicitly tend to increase the complexity of the method.

Another method which is used to model two-phase flow and takes into account effects from both fluids is the Scalar Equation Algorithm (SEA) [73]. With this technique a scalar marker is employed to track the position of the interface and the equations governing flow cover both fluids. The scalar marker takes a value of 1 in Fluid 1 and 0 in Fluid 2. Then at the interface the scalar marker has a value between 0 and 1. This method too tends to suffer from the smearing of the interface, therefore to maintain the interface as a sharp front higher order schemes such as the van Leer TVD differencing scheme are employed for the solution of the advection equation.

A technique which has become very popular recently is the Level Set Method (LSM) [74]. With LSM it is possible to overcome the smearing of the interface encountered with other methods. In this method too, the equations governing flow cover both fluids in two-phase flow and the position of the interface is tracked through the advection of a scalar marker through the flow field. However the values of the scalar are distances which are calculated relative to the position of the interface where it takes a value of zero. Since it is not prone to numerical smearing low order differencing schemes can be used for the advection equation.

The techniques discussed above have been used extensively by the Newtonian fluid mechanics community. As already mentioned in Chapter 1 free surfaces are an inherent feature of many processes involving viscoelastic flow. Therefore numerical algorithms that have been developed to model viscoelastic flow in industrial applications consists of some form of interface tracking techniques. Existing viscoelastic free surface algorithms too can be classified as mesh adapting or fixed grid methods.

Of the two techniques, Lagrangian type mesh modifying methods are the more widely used. Recent work include a finite element code for the simulation of optical fiber spinning using the spine method to track the free surface [26], a finite elment algorithm for 3-D simulations of die swell based on a streamline free surface technique

[75] and a free surface algorithm to model Hele-Shaw and slot coating flow based on the fininte element method coupled with a pseudo-solid domain mapping technique [76]. Khayat employs integral equations to model the flow front with the boundary element technique [77].

Recent publications on fixed grid tracking techniques include the use of a non-linear differential equation to model the flow front based on the lubrication theory [33], a finite element formulation coupled with the level set method for viscoelastic flow by Pillapakkam and Singh [32], a lattice Bolzmann method with free energy functional based interphase tracking method [78] and a Marker-And-Cell(MAC) method based finite difference formulation by Tomè et al.[79].

At present there are no finite volume algorithms for viscoelastic flow using the level set method on Eulerian fixed grids. Due to the computational advantages of finite volume techniques such an algorithm is desirable.

4.2 Free Surface Algorithms Within PHYSICA+

There are two free surface algorithms currently implemented within PHYSICA+- The Scalar Equation Algorithm [73] and the Level Set Method [74].

In both free surface algorithms the flow field is solved using one momentum equation for both fluids. Thus the governing equations for continuity and velocity are

$$\frac{\partial \rho_m}{\partial t} + \nabla \cdot (\boldsymbol{u}\rho_m) = 0, \tag{4.1}$$

and

$$\rho_m \frac{\partial \boldsymbol{u}}{\partial t} + \rho_m \boldsymbol{u} \nabla \cdot \boldsymbol{u} = -\nabla p + \mu_m \nabla^2 \boldsymbol{u} + \boldsymbol{S}, \tag{4.2}$$

where ρ_m and μ_m are the density and viscosity of the fluid mixture.

4.3 Scalar Equation Algorithm (SEA)

In the SEA algorithm [80] the interface of the two fluids is tracked using a scalar marker variable which is advected with the velocity field through the solution of the

scalar equation

$$\frac{\partial \phi}{\partial t} + \nabla \cdot (\boldsymbol{u}\phi) = 0, \tag{4.3}$$

based on the assumption that the motion of the scalar ϕ is governed solely by convection. The scalar ϕ takes the value 1 in fluid 1 and 0 in fluid 2. The movement of ϕ in the flow field is obtained through the solution of the advection equation (4.3) and at the interface ϕ will have a value between 0 and 1. This technique is similar to the VOF method except that the equations for fluid flow cover both the air and liquid region. For the momentum equation (4.2) the fluid mixture material properties in an element P are calculated as a function of the proportion of each fluid in the element using the equation

$$\nu_m = \nu_2 + \phi(\nu_1 - \nu_2), \tag{4.4}$$

where ν_m is the fluid mixture density ρ_m or mixture viscosity μ_m and ν_1 and ν_2 are the material property values in fluid 1 and 2 respectively.

4.3.1 GALA Algorithm

The GALA algorithm developed by Spalding [81] for flows with large changes in density across the interface of two phase flows is used to conserve volume rather than mass. The mass continuity equation (Eqn 4.1) is rewritten to conserve volume by assuming incompressibility and immiscibility. Substituting Eqn(4.4) in Eqn(4.1) gives

$$\frac{\partial \rho_2}{\partial t} + \frac{\partial \phi(\rho_1 - \rho_2)}{\partial t} + \nabla \cdot (\boldsymbol{u}\rho_2) + \nabla \cdot (\boldsymbol{u}\phi(\rho_1 - \rho_2)) = 0. \tag{4.5}$$

When the two fluids have constant density the above equation becomes

$$(\rho_1 - \rho_2)\frac{\partial \phi}{\partial t} + (\rho_1 - \rho_2)\nabla \cdot (\boldsymbol{u}\phi) + \rho_2 \nabla \cdot \boldsymbol{u} = 0. \tag{4.6}$$

Using Eqn(4.3) the above equation becomes

$$\nabla \cdot \boldsymbol{u} = 0. \tag{4.7}$$

4.3.2 The Discretization of the Scalar Equation

The finite volume discretization of Eqn(4.3) is carried out by applying the divergence theorem and integrating the equation over a control volume. This leads to

$$\int_t \int_V \frac{\partial \phi}{\partial t} dV dt + \int_S (\boldsymbol{n} \cdot \boldsymbol{u}) \phi dS = 0, \tag{4.8}$$

which is then approximated at the faces of the control volume as

$$\frac{\phi_P - \phi_P^o}{\Delta t} + \sum_f (\boldsymbol{n} \cdot \boldsymbol{u})_f A_f \phi_f = 0. \tag{4.9}$$

where f is a subscript for values on the face of a control volume. Eqn(4.9) can be rewritten as

$$\phi_P + \sum_f \sigma_f \phi_f = \phi_P^o, \tag{4.10}$$

where σ_f is known as the Courant-Friedrichs-Lewy(CFL) stability number which is given by

$$\sigma_f = \frac{(\boldsymbol{n} \cdot \boldsymbol{u})_f A_f \Delta t}{V_P}. \tag{4.11}$$

In order to achieve stable explicit solutions for Eqn(4.10) the value of σ_f must lie within the range $|\sigma_f| \leq 1/\sqrt{N}$ where N is the number of spatial dimensions. The approximation of ϕ_f is carried out through the use of a differencing scheme.

4.3.3 Smearing of the Fluid Interface

In the solution of Eqn(4.10), ϕ is calculated for each element. Therefore for an element which contains a mixture of the two fluids ϕ will have a value indicating the proportion of each fluid in the element. This leads to numerical smearing of the interface as a fluid entering an element on one side has an immediate effect on the value of ϕ which leaves through any other face of the control volume. Therefore ϕ_f in Eqn(4.10) has to be approximated using a differencing scheme which would minimise the smearing of the interface. In PHYSICA+ there are several differencing schemes which can be used to calculate ϕ_f.

The first of the techniques is the upwind method. For an element P with a neighbouring element A with $\boldsymbol{n}$ being the outward normal to the current face the value of

ϕ_f is given by

$$\phi_f = \begin{cases} \phi_A & \text{if } (\boldsymbol{n} \cdot \boldsymbol{u})_f < 0, \\ \phi_P & \text{if } (\boldsymbol{n} \cdot \boldsymbol{u})_f > 0. \end{cases} \tag{4.12}$$

First-order schemes such as the upwind method are highly prone to numerical diffusion which causes the interface to smear and become less distinct. Therefore higher order schemes such as van Leer [82] TVD and donor-acceptor scheme [71] have been implemented within PHYSICA+.

The van Leer scheme uses the equation

$$\phi_f = \phi_U + \frac{1}{2}\frac{\Delta\phi}{\Delta\boldsymbol{n}}(d_{UD} - |(\boldsymbol{n} \cdot \boldsymbol{u})_f|\delta t), \tag{4.13}$$

where the subscripts U and D indicate the values in the upwind and downwind elements respectively. The distance between the upwind and downwind element centroids is given by d_{UD} and δt is the time step size. The term $\Delta\phi/\Delta\boldsymbol{n}$ is calculated using the equation

$$\frac{\Delta\phi}{\Delta\boldsymbol{n}} = \begin{cases} 0 & \text{if} \quad \phi_{DU} * \phi_{UC} < 0, \\ \min(|\phi_{DU}|, |\phi_{UC}|, 0.5(|\phi_{DU}| + |\phi_{UC}|)) & \text{if} \quad \phi_{UC} > 0, \\ \text{-min}(|\phi_{DU}|, |\phi_{UC}|, 0.5(|\phi_{DU}| + |\phi_{UC}|)) & \text{if} \quad \phi_{UC} < 0, \end{cases} \tag{4.14}$$

where

$$\phi_{DU} = \frac{\phi_D - \phi_U}{d_{UD}}, \tag{4.15}$$

and

$$\phi_{UC} = \frac{\phi_U - \phi_C}{d_{UC}}. \tag{4.16}$$

The subscript C indicates the upwind, upwind element. For an internal face without an upwind, upwind element associated with it, ϕ_f is given by

$$\phi_f = \phi_U. \tag{4.17}$$

4.3.4 Pressure Gradients

The pressure gradient between the two fluids is discontinuous across the interface. Consequently care has to be taken when calculating the integrated gradient for an element. The technique is based on the standard approach for calculating the pressure

gradient used in PHYSICA+ which is

$$(\nabla_y p)_P \approx \sum_f n_f A_f p_f, \tag{4.18}$$

where

$$p_f = \alpha p_P + (1.0 - \alpha) p_A. \tag{4.19}$$

In the equation above P and A are adjacent element with the common face f and α is a weighting factor given by

$$\alpha = \frac{d_{Af}}{d_{Af} + d_{Pf}}, \tag{4.20}$$

where d_{Af} and d_{Pf} are the normal distances from the element centre to the common face. When the free surface algorithm is being used the value of α is calculated as

$$\alpha = \frac{d_{Af}(\rho_A - \rho_{ref})}{d_{Af}(\rho_A - \rho_{ref}) + d_{Pf}(\rho_P - \rho_{ref})}, \tag{4.21}$$

where ρ_A,ρ_P and ρ_{ref} are the densities in elements A, P and a reference density. When the above expression is used to calculate α the value may not lie between zero and 1.0 which means that the face value of pressure may not be bounded by the pressure values in the elements either side of the face. This could lead to stability problems in which case ρ_{ref} is set to the minimum density value expected or to zero.

4.3.5 SEA Viscoelastic Algorithm

In this coupled algorithm fluid 1 is a viscoelastic material and fluid 2 is a Newtonian fluid. The interface is assumed to be at $\phi = 0.5$.

The governing equations are

$$\frac{\partial \rho_m}{\partial t} + \nabla \cdot (\boldsymbol{u}\rho_m) = 0, \tag{4.22}$$

$$\rho_m \frac{\partial u}{\partial t} + \rho_m \boldsymbol{u} \nabla \cdot \boldsymbol{u} = -\nabla p + \mu_m \nabla^2 \boldsymbol{u} + \boldsymbol{S}, \tag{4.23}$$

and

$$\boldsymbol{\tau}_1 + \lambda_1 \overset{\nabla}{\boldsymbol{\tau}}_1 = 2\eta_1 \boldsymbol{D} \tag{4.24}$$

where the equations for continuity, flow and constitutive model respectively. The term $\boldsymbol{S}$ represents the source terms such as $\nabla \cdot \boldsymbol{\tau}_1$, surface tension terms etc. The subscript m indicates mixture properties which are calculated using Eqn(4.4). In

this case for the mixture viscosity μ_m, $\mu_1 = \eta_2$ (dynamic viscosity of the Newtonian contribution of the viscoelastic fluid) and μ_2 will take the dynamic viscosity of the Newtonian fluid. In Eqn(4.24) η_1 is the dynamic viscosity of the viscoelastic contribution of the viscoelastic fluid.

The constitutive equation for the viscoleastic fluid is solved across the whole domain using the condition that if $\phi_P < 0.5$ the a_P coefficient is assigned a very large value which ensures the value of the viscoelastic contribution is negligible at P. In addition no stress source term contributions are made to the momentum equations at P if $\phi_P < 0.5$.

The advection equation (4.3) is solved explicitly at the end of the time step. The solution sequence is given below.

1. Initialise variables
2. Update material properties
3. Begin time-step
   - Set $\boldsymbol{\tau}^o = \boldsymbol{\tau}, \boldsymbol{u}^o = \boldsymbol{u}, p^o = p$
   - SIMPLEC
     - Solve constitutive equation
     - Solve momentum equation
     - Solve pressure correction equation
     - Correct pressure and velocity fields
     - Calculate convection fluxes
     - Iterate until convergence
   - Solve advection equation
4. End time-step
5. Repeat steps 2-4 for time-step advancement

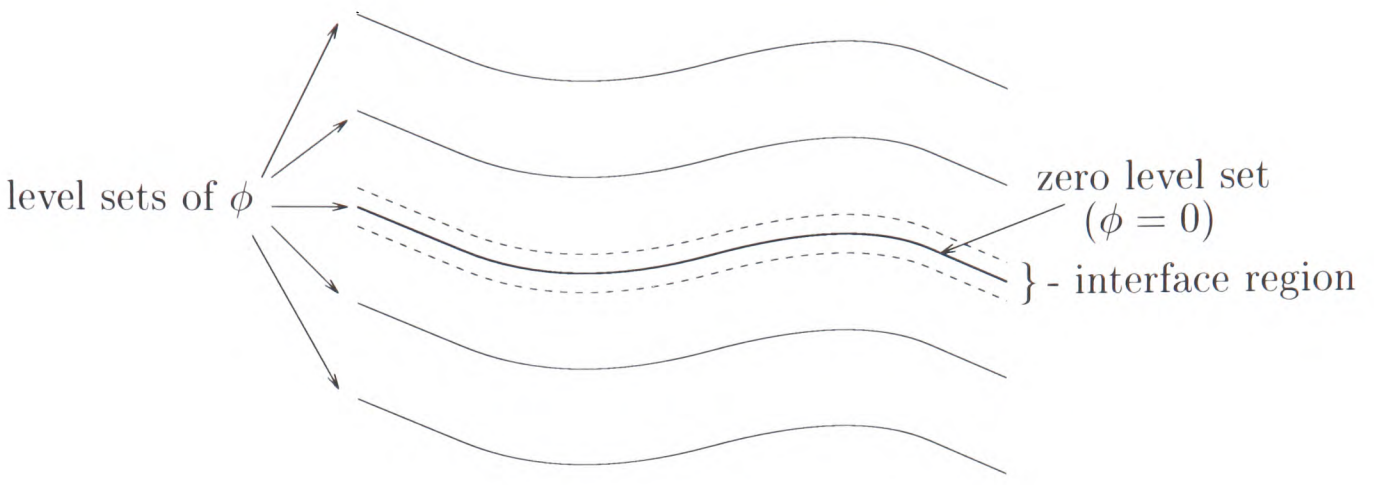

Figure 4.1: Level sets of ϕ.

4.4 Level Set Method (LSM)

In the level set method [74] the scalar ϕ is a distance function and the values of ϕ are called level sets (see Figure 4.1). The interface between the two fluids is represented by the zero level set ($\phi = 0$) and ϕ is calculated as the normal distance from the zero level set. The position of the interface is such that

$$\phi(\boldsymbol{r}) > 0 \quad \text{in fluid 1,} \tag{4.25}$$

$$\phi(\boldsymbol{r}) = 0 \quad \text{interface,} \tag{4.26}$$

$$\phi(\boldsymbol{r}) < 0 \quad \text{in fluid 2,} \tag{4.27}$$

where $\boldsymbol{r}$ is a position vector. The variable ϕ is continuous, smooth and monotonic in the direction normal to the interface.

To predict the evolution of the interface, ϕ is advected through the velocity field using an advection equation and the calculated velocity field. Eqn(4.3) is used to advect the distance function ϕ and the velocity field is calculated using Eqns(4.2) and (4.7). Once ϕ is advected through the velocity field the values of ϕ are reinitialised as a distance function from the zero level set, without disturbing the position of the interface, using the reinitialisation equation

$$\frac{\partial \phi}{\partial \tau} = S(\phi_0)(1 - |\nabla \phi|). \tag{4.28}$$

In Eqn(4.28) ϕ_0 is the value of ϕ at the beginning of the reinitialisation and τ is a

pseudo timestep. $S(\phi_0)$ is a sign function given by

$$S(\phi_0) = \frac{\phi_0}{\sqrt{(\phi_0)^2 + (d_{AP}^{max})^2}} \tag{4.29}$$

where d_{AP}^{max} is the maximum distance between the centre of element, P and the centre of adjacent element, A. Therefore the value of the sign function is such that

$$S(\phi) > 0 \quad \text{if} \quad \phi > 0, \tag{4.30}$$

$$S(\phi) < 0 \quad \text{if} \quad \phi < 0, \tag{4.31}$$

$$S(\phi) = 0 \quad \text{if} \quad \phi = 0. \tag{4.32}$$

Equation(4.28) may be recast as

$$\frac{\partial \phi}{\partial \tau} + S(\phi_0)\frac{\nabla\phi \cdot \nabla\phi}{|\nabla\phi|} = S(\phi_0). \tag{4.33}$$

from which the characteristics are given by

$$\boldsymbol{w} = S(\phi_0)\frac{\nabla\phi}{|\nabla\phi|}. \tag{4.34}$$

The gradient over a control volume is evaluated at the surface by expressing it as a surface integral such that

$$\int_V \nabla\phi dV = \int_S \boldsymbol{n}\phi dS, \tag{4.35}$$

which is then discretized and divided on both sides by the cell volume, V_P, to give

$$\nabla\phi = \sum_f \frac{A_f}{V_P}\boldsymbol{n}_f\phi_f, \tag{4.36}$$

where A_f is the area of the control volume face and $\boldsymbol{n}_f$ is the outward normal to the control volume face. Upwinding is used to determine ϕ_f which gives

$$\phi_f = \phi_P \quad \text{if} \quad \boldsymbol{w} \cdot \boldsymbol{n} \geq 0, \tag{4.37}$$

$$\phi_f = \phi_A \quad \text{if} \quad \boldsymbol{w} \cdot \boldsymbol{n} < 0. \tag{4.38}$$

The following modification is used for the gradient

$$\nabla\phi = \frac{\boldsymbol{\Delta\Phi}}{V_P}, \tag{4.39}$$

where

$$\Delta_i\Phi = \text{maxmag}(\delta_i^+, \delta_i^-, \delta_i), \tag{4.40}$$

with

$$\begin{aligned} \delta_i^+ &= \sum_{f+}(A_f n_i \phi_P) + \sum_{f-}(A_f n_i \phi_f), \\ \delta_i^- &= \sum_{f+}(A_f n_i \phi_f) + \sum_{f-}(A_f n_i \phi_P), \\ \delta_i &= \sum_{f}(A_f n_i \phi_f), \end{aligned} \tag{4.41}$$

where $f+$ is summed over all positive terms and for $f-$ over the negative terms. This form of discretizing the re-initialisation equation allows information to be conveyed from the interface while not allowing the extremities to be smoothed.

The magnitude of the gradient is therefore calculated from

$$|\nabla\phi| = \sqrt{\sum_i \left(\frac{\Delta_i \Phi}{V_P}\right)^2}. \tag{4.42}$$

Any material property is calculated using the expressions

$$\begin{aligned} \nu &= \nu_1 && \text{if } \phi > \alpha, \\ \nu &= \nu_2 && \text{if } \phi < -\alpha, \\ \nu &= \frac{\nu_1 + \nu_2}{2} + \frac{\nu_1 - \nu_2}{2}\sin\left(\frac{\pi\phi}{2\alpha}\right) && \text{if } |\phi| \leq \alpha. \end{aligned} \tag{4.43}$$

In order to prevent instabilities at the interface the material properties are smoothed by defining a finite interface thickness 2α. Here α is defined by

$$\alpha = \frac{N d_{AP}^{max}}{2}, \tag{4.44}$$

where N is the number of elements across the thickness of the interface. This definition of α ensures that the thickness of the interface is dependant on the mesh size thereby minimizing smearing of the interface.

The discretized version of the re-initialisation equation Eqn(4.28) is

$$\phi_P^{i+1} = \phi_P^i + \Delta\tau S(\phi_0)(1 - |\nabla\phi_P|), \tag{4.45}$$

where $i+1$ and i denote the current and previous iterations and $\Delta\tau$ is the time step which is chosen such that

$$\Delta\tau = \min\left(\frac{d_{AP}^{min}}{10}\right). \tag{4.46}$$

4.4.1 Volume Reinitialisation

The level set method does not automatically preserve volume. If volume conservation is required a volume reinitialisation technique is employed. This is done after the

level set reinitialisation. The equation used to reinitialise the volume is

$$\frac{\partial \phi}{\partial \tau} = (V_0 - V(\tau)), \tag{4.47}$$

where V_0 is the volume of the fluid with $\phi > 0$ at $\tau = 0$, $V(\tau)$ is the volume of fluid with $\phi > 0$ at a later time and τ is the pseudo time step as defined by Eqn(4.46).

The discretization of Eqn(4.47) is

$$\phi_P^{i+1} = \phi_P^i + \Delta\tau(V_0 - V(\tau)), \tag{4.48}$$

where $i+1$ and i denote the current and previous iterations of volume reinitialization.

The volume is calculated using

$$\begin{aligned} \text{vol} = \ & V_P && \text{if} \quad \phi_P > \alpha, \\ \text{vol} = \ & 0 && \text{if} \quad \phi_P < \alpha, \\ \text{vol} = \ & V_P\left(1 + \sin\left(\frac{\pi\phi_P}{2\alpha}\right)\right) && \text{if} \quad |\phi_P| \leq \alpha, \end{aligned} \tag{4.49}$$

where α is the interface thickness.

4.4.2 LSM Viscoelastic Algorithm

In this coupled algorithm fluid 1 is viscoelastic and fluid 2 is Newtonian. The governing equations are Eqns(4.22) - (4.24). The mixture material properties are calculated using the expressions in Eqn(4.43). For the mixture viscosity μ_m, $\mu_1 = \eta_2$ (dynamic viscosity of the Newtonian contribution of the viscoelastic fluid) and μ_2 will take the dynamic viscosity of the Newtonian fluid. In Eqn(4.24) η_1 is the dynamic viscosity of the viscoelastic contribution of the viscoelastic fluid.

The contitutive equation for the viscoelastic fluid is solved across the whole domain as in the SEA coupled algorithm. The condition under which the a_P term is assigned a large value and no stress source term contribution is made to the momentum equations is $\phi_P < -\alpha$. The interface thickness is given by $-\alpha < \phi < \alpha$. The advection equation (4.3) is solved explicitly after the SIMPLEC loop at the end of the time step. The ϕ values are then used to solve the reinitialisation equations. The solution steps are given below.

1. Initialise variables and $\phi(x,0)$ to be the signed normal distance to the free surface front

2. Update material properties

3. Begin time-step

   - Set $\boldsymbol{\tau}^o = \boldsymbol{\tau}, \boldsymbol{u}^o = \boldsymbol{u}, p^o = p$
   - SIMPLEC
     - Solve constitutive equation
     - Solve momentum equation
     - Solve pressure correction equation
     - Correct pressure and velocity fields
     - Calculate convection fluxes
     - Iterate until convergence
   - Solve advection & reinitialisation equations

4. End time-step

5. Repeat steps 2-4 for time-step advancement

4.5 Validation of the SEA and LSM Viscoelastic Free Surface Algorithms

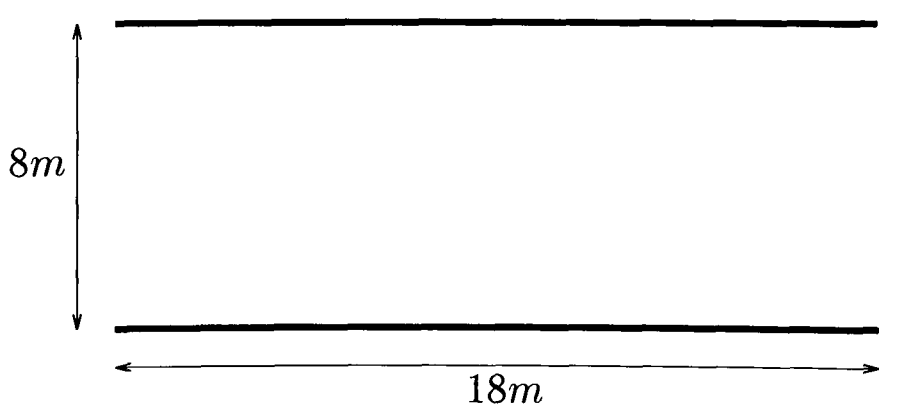

Figure 4.2: 2-D channel geometry.

a)

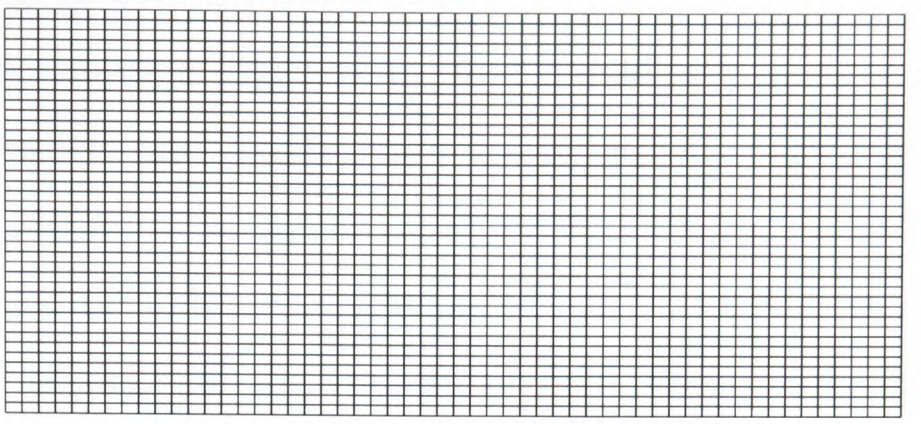

b)

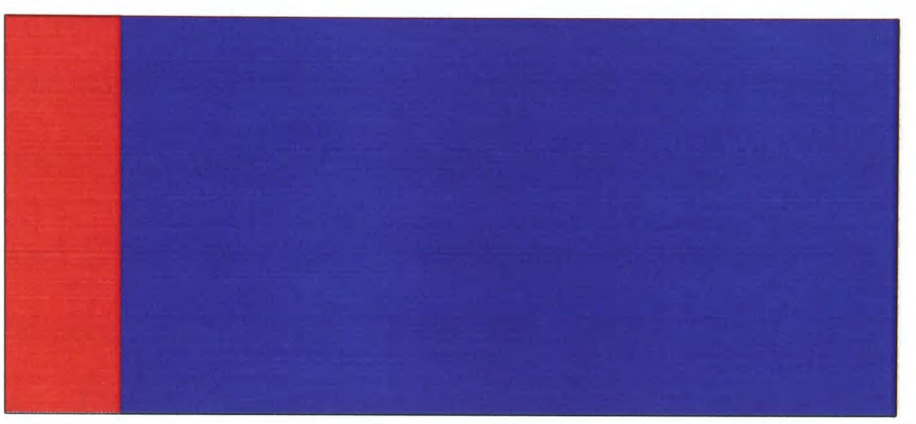

Figure 4.3: a) The mesh for the 2-D channel. b) The initial conditions where the viscoelastic material is represented by the red colour and the blue region represents air.

To validate the two algorithms for viscoelastic flow a validation technique similar to that used by Tomè et al. [79] is employed. This involves the comparison of shear and normal stress profiles at a cross section in a 2-D planar channel with that of the analytical solutions at steady state conditions.

To carry out the validation a 2-D planar channel as shown in Figure 4.2 with a channel width of $8m$ is considered. Fully developed flow is imposed at the inlet given by

$$u = \frac{3}{128}(16 - y^2), \quad v = 0, \tag{4.50}$$

No slip boundary conditions are imposed at walls for u and v velocities and Neumann boundary conditions are imposed at the outlet for the extra-stress. Pressure is set to zero at the outlet.

Initially a thin strip of fluid is defined close to the inlet ($0 \leq x \leq 2$). The mesh and the initial state are shown in Figure 4.3. Fluid is gradually injected into the channel until it reaches outflow and steady state is established. The material properties are set at $\rho_1 = 1300kgm^{-3}$(polymer) and $\rho_2 = 1.19kgm^{-3}$(air) for the mixture density (ρ_m) and for the mixture viscosity (μ_m) $\mu_1 = 4.0Pas$ (η_2 of polymer) and $\mu_2 = 1.819\text{E} - 5Pas$(air). For the viscoelastic fluid, due to difficulties in obtaining data, the dynamic viscosity of the polymer is taken as the dynamic viscosity of the Newtonian contribution η_2 and the dynamic viscosity of the viscoelastic contribution $\eta_1 = 1 - \eta_2/\rho$ (where η_2/ρ is the kinematic viscosity of the polymer with ρ being its density). The relaxation time of the polymer is taken to be $\lambda_1 = 0.14s$.

In both the SEA and LSM the van Leer differencing scheme is used to approximate ϕ_f. Figure 4.4 a) shows the progress of the viscoelastic fluid after 12 seconds using the SEA algorithm. Figure 4.4 b) shows the interface region $0 < \phi < 1$. Figure 4.5 a) shows the progress of the viscoelastic fluid using the LSM algorithm after 12 seconds. In Figure 4.5 b) the level sets of the flow are presented. In this case there is no interface region and therefore the position of the interface does not have to be guessed as with SEA. The CPU time for SEA is $7518s$ and for LSM it is $8247s$ on a 433Mhz Dec Alpha ev5.6 64-bit CPU. The interface profile from the LSM method compares well with that of SEA and the simulation time is only marginally larger than for SEA.

Once steady state is achieved the velocity field at the outlet must have the same profiles as the boundary conditions imposed at inflow given by Eqns(4.50) and the τ_1^{xx} and τ_1^{xy} stress profiles along a cross section should be similar to the analytical solutions given by

$$\tau_1^{xx} = 2\lambda_1(1 - \eta_2/\rho)\left(\frac{\partial u}{\partial y}\right)^2, \quad \tau_1^{xy} = (1 - \eta_2/\rho)\frac{\partial u}{\partial y}, \quad \tau_1^{yy} = 0. \tag{4.51}$$

In Figure 4.6 the velocity fields for both methods once steady state has been reached are plotted. The τ_1^{xx} normal stress and the τ_1^{xy} stress profiles along the cross section at $x = 10m$ ($0 \leq x \leq 18$), are given in Figures 4.7 and 4.8 for SEA and LSM respectively. The plots show that the numerical results are a very good match for the analytical results.

The relative l_2-norm of the errors are calculated using Eqn(3.29) and values for τ_1^{xx}

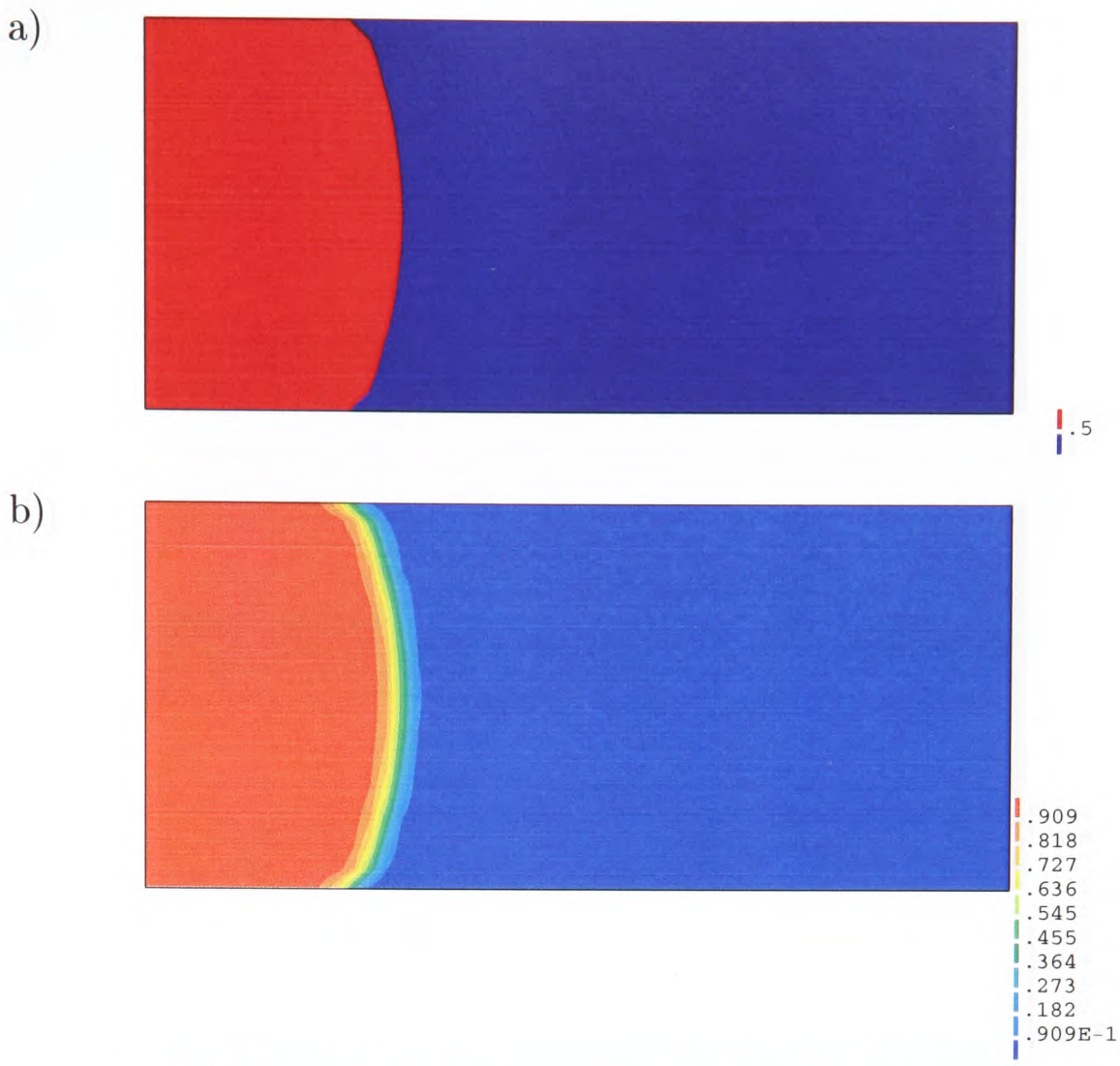

Figure 4.4: Interface dynamics with SEA at $t = 12s$.

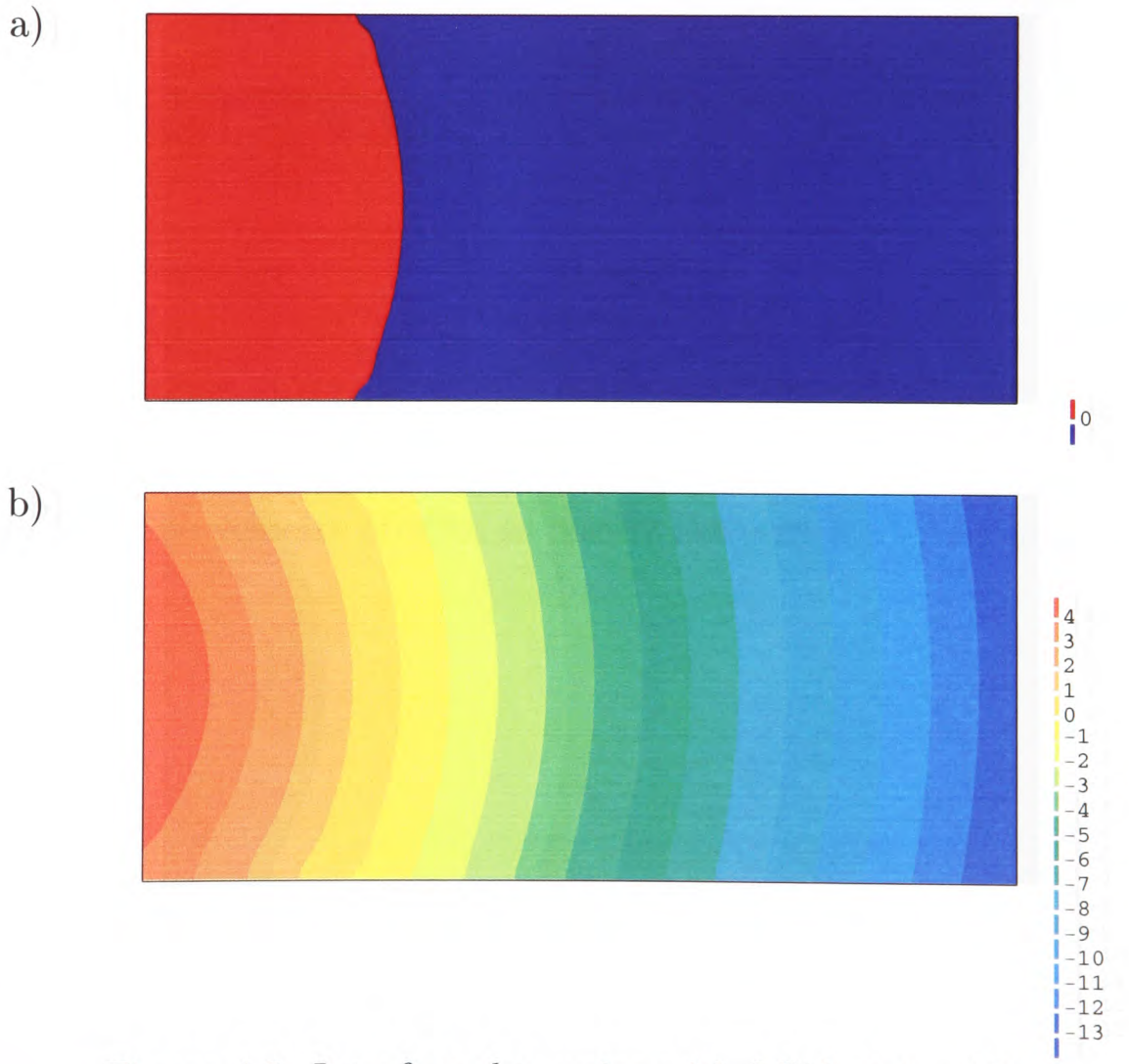

Figure 4.5: Interface dynamics with LSM at $t = 12s$.

a)

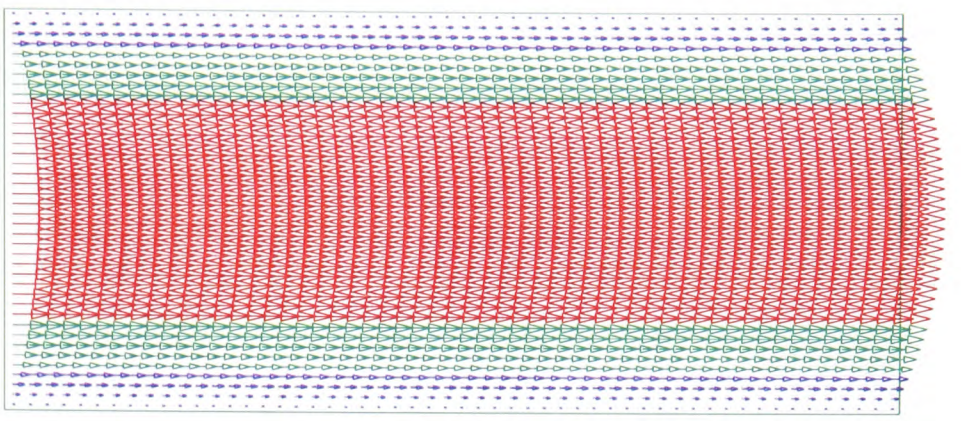

b)

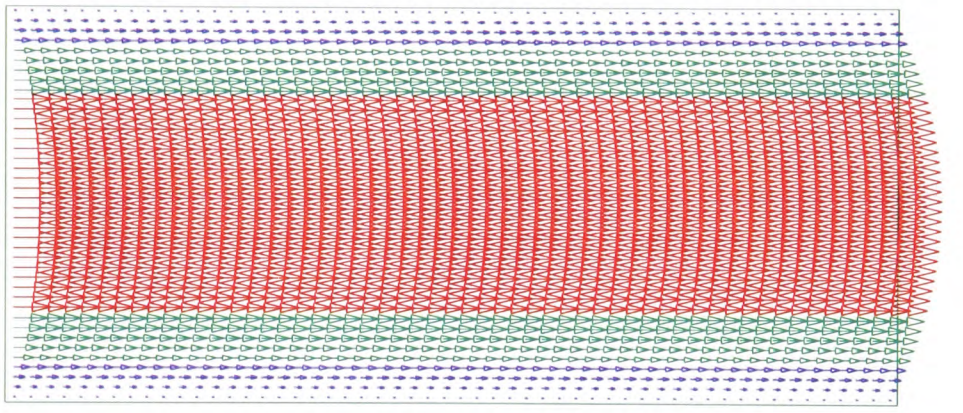

Figure 4.6: The velocity profiles at steady state with a) SEA and b) LSM.

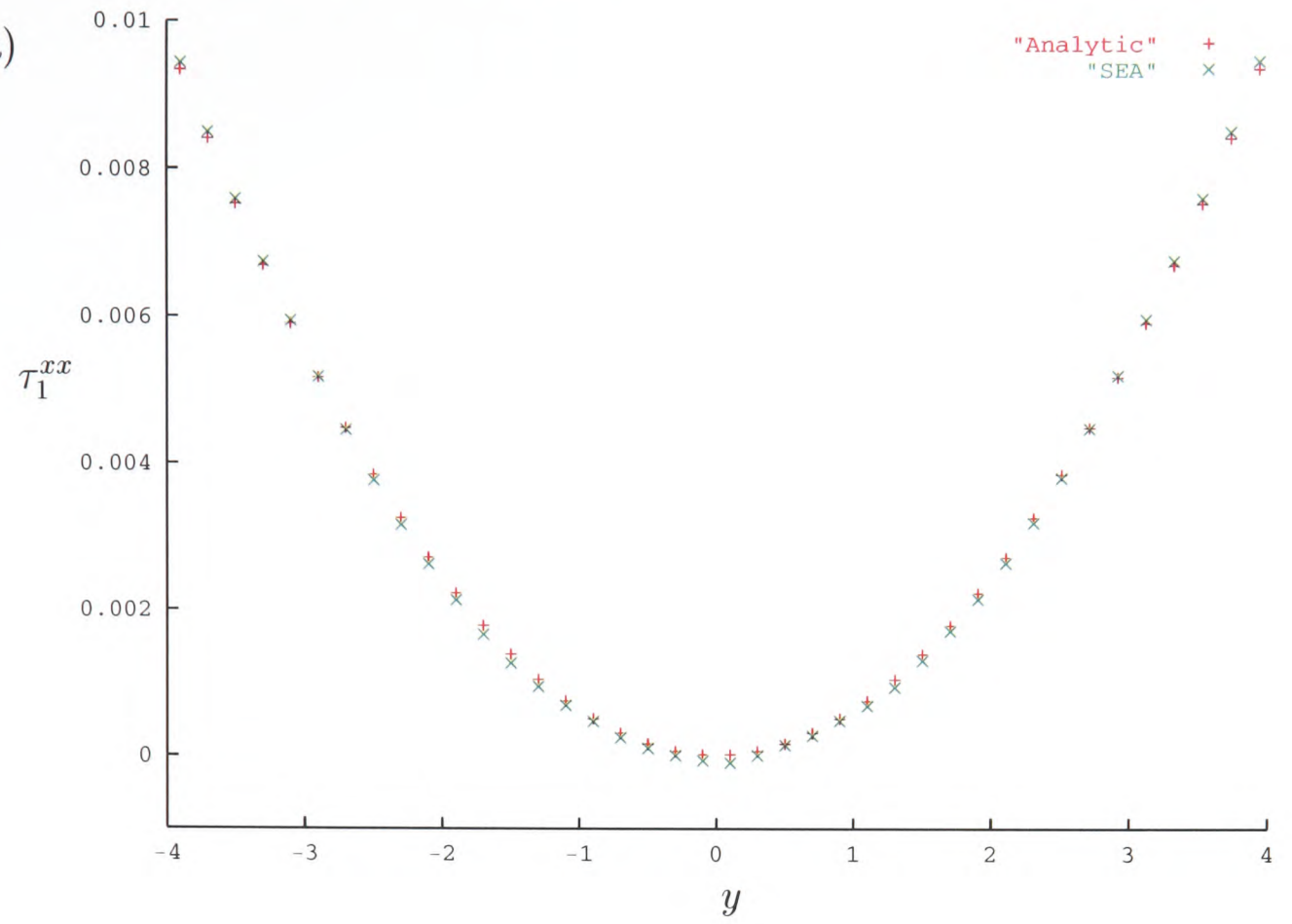

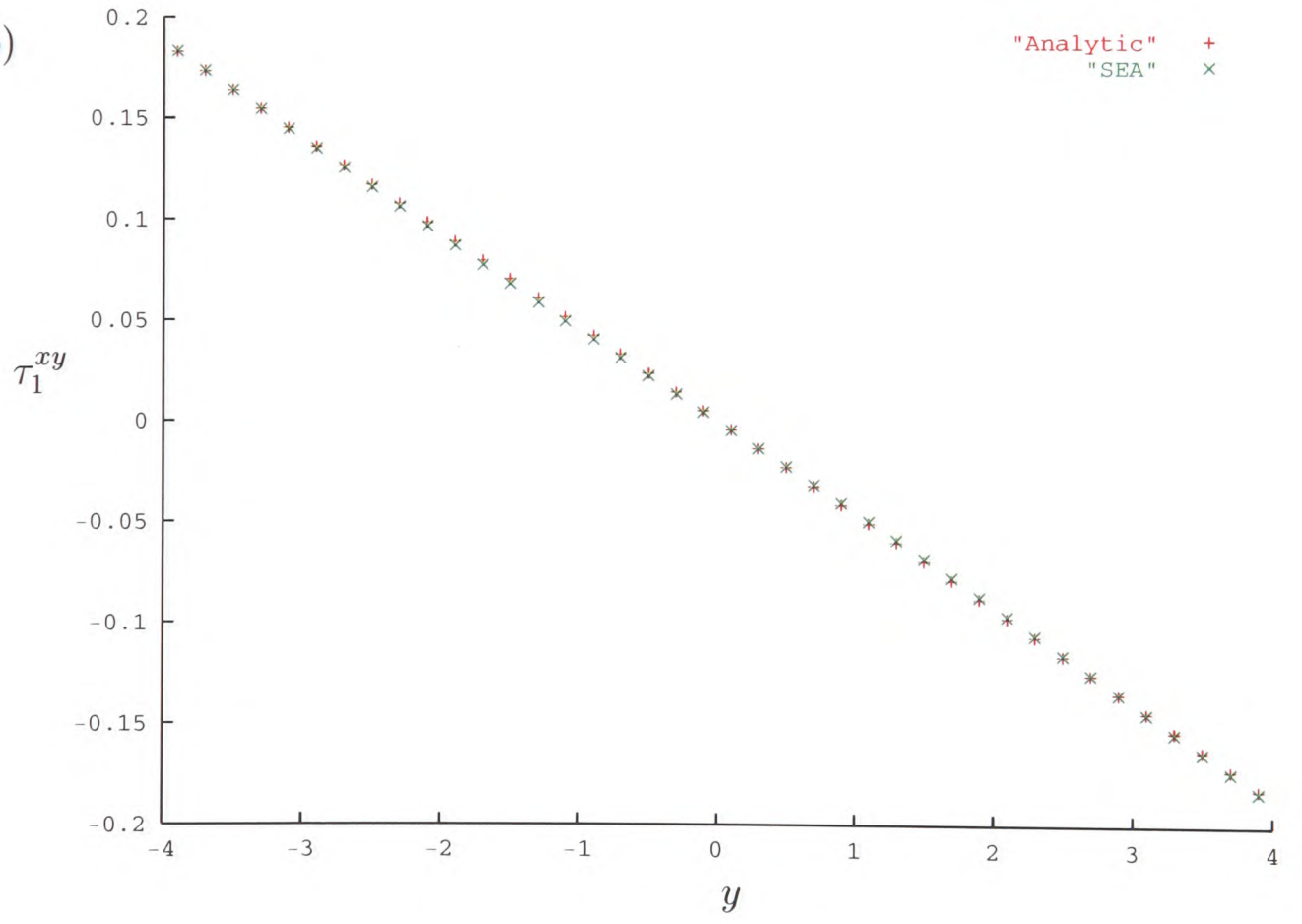

Figure 4.7: A comparison of steady state analytic and calculated values of a) τ_1^{xx}, and b) τ_1^{xy}, at $x = 10$ with SEA.

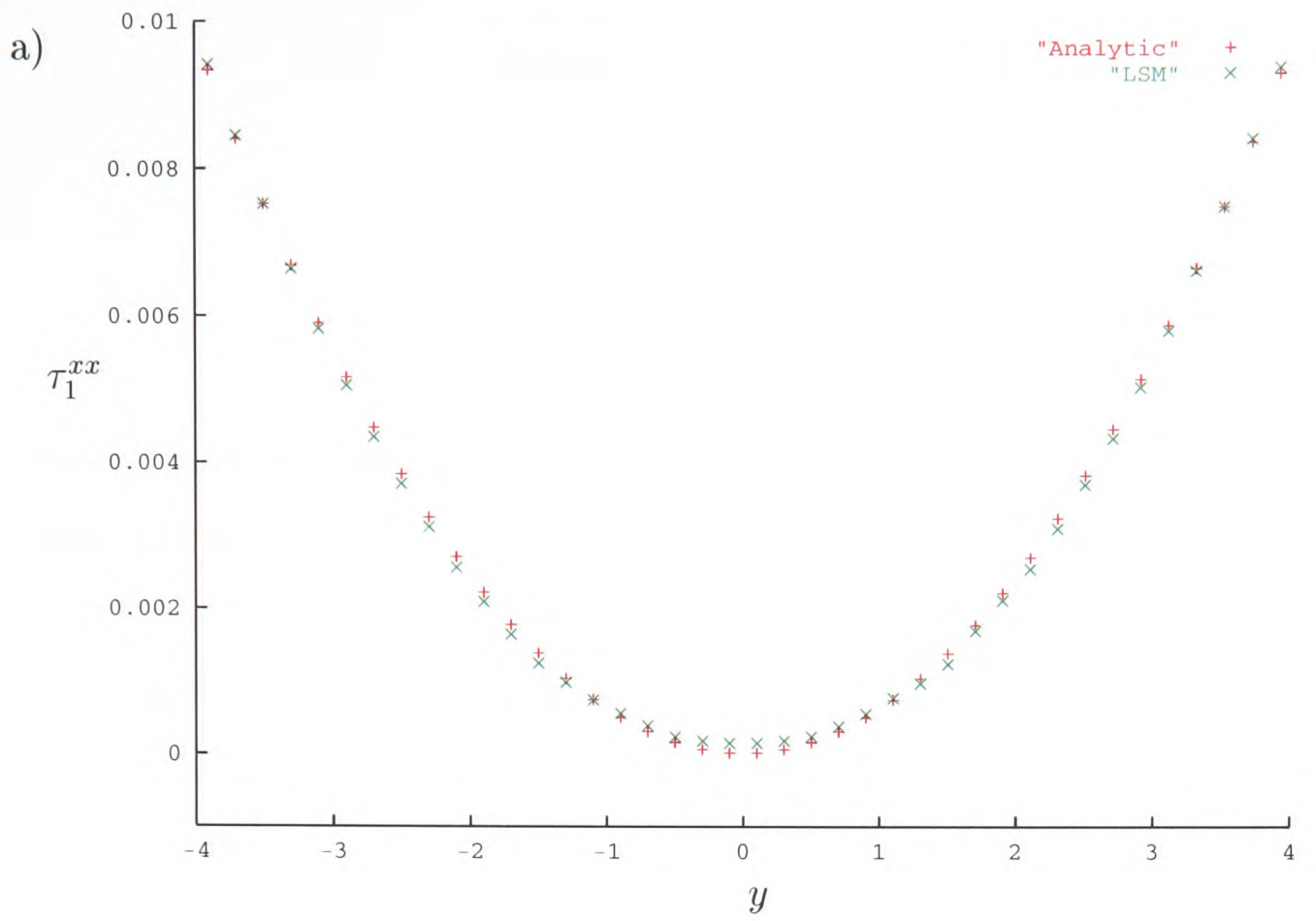

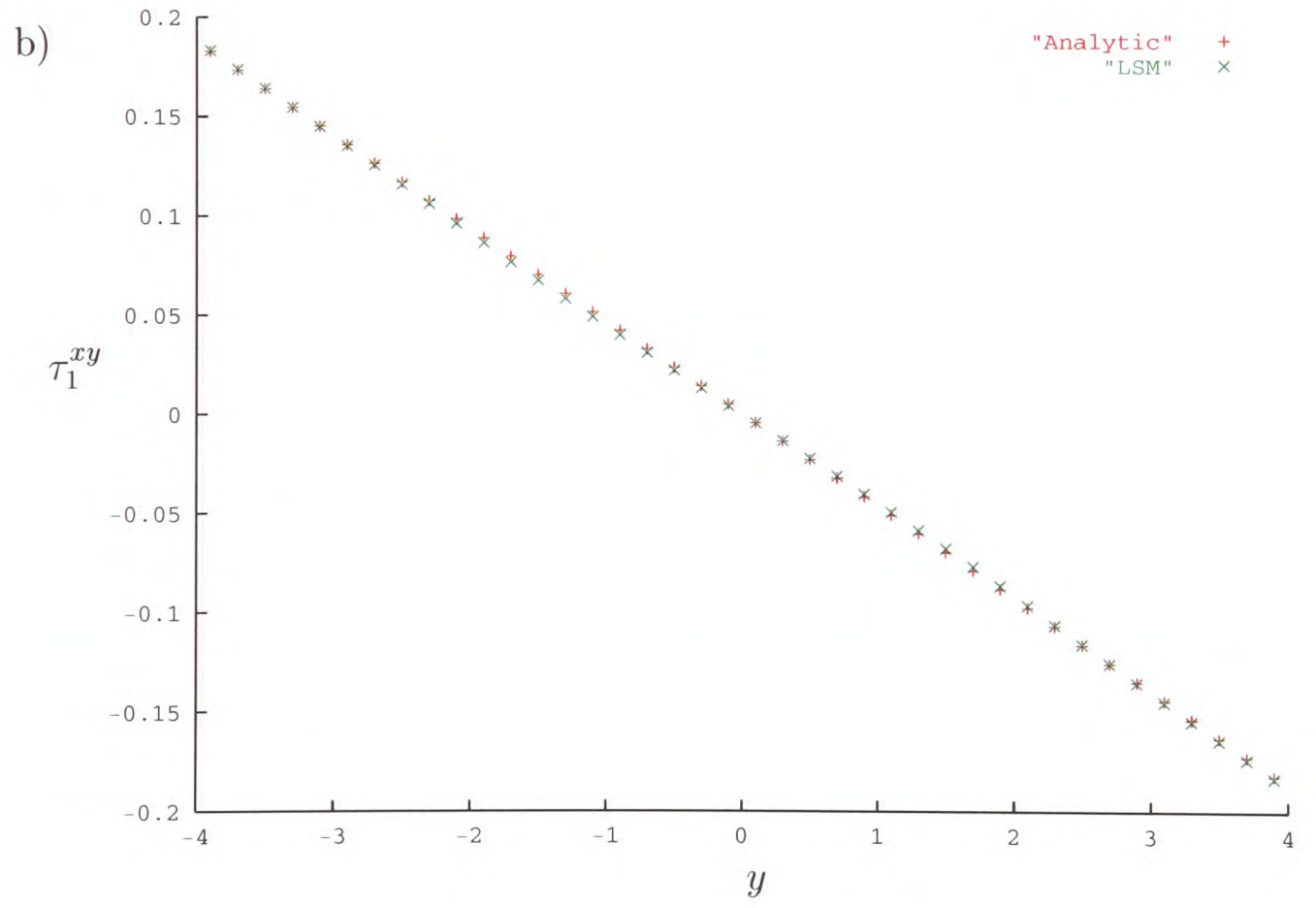

Figure 4.8: A comparison of steady state analytic and calculated values of a)τ_1^{xx}, and b)τ_1^{xy}, at $x = 10$ with LSM.

Stress	SEA	LSM
τ_1^{xx}	2.52E − 4	4.84E − 4
τ_1^{xy}	1.01E − 4	1.50E − 4

Table 4.1: The l_2 errors for the stresses.

and τ_1^{xy} with SEA and LSM are given in Table 4.1. The results presented above show that both methods predict similar flow behaviour based on which it can be concluded that the methods have been implemented correctly. Based on the CPU times for the two methods SEA is faster than LSM and l_2 errors of the stresses (see Table 4.1) show that SEA is more accurate than LSM. However with SEA the position of the interface had to be guessed whereas with LSM the exact position of the interface is known. This is an advantage especially when implementing surface tension effects since it enables the curvature of the interface to be calculated accurately. Therefore in the following section surface tension effects are implemented within the LSM algorithm.

4.6 Surface Tension Effects Within LSM

Surface tension effects are introduced into the PHYSICA+ solution algorithm through a source term in the momentum equation Eqn(4.2). The source terms are calculated through the level set method. If a 3-D space Ω is occupied by two fluids, Ω_1 and Ω_2 which is enclosed by surface areas Γ_1 and Γ_2 such that $\Gamma = \Gamma_1 + \Gamma_2$, then an interface area Γ_S exists between Ω_1 and Ω_2 with an associated surface tension γ. Figure 4.9 depicts this Ω space. The following sections describe the derivation of the surface tension source term and its implementation within PHYSICA+.

4.6.1 Edge Source Term

Assuming the interface Γ_S is smooth, and by neglecting other forces, the surface tension acting on Ω is given as

$$\boldsymbol{S}_{i\gamma} = \oint_{\partial\Gamma_S} \gamma m_i d(\partial\Gamma_S), \tag{4.52}$$

where m_i is the normal to Γ and tangent to Γ_S respectively [83].

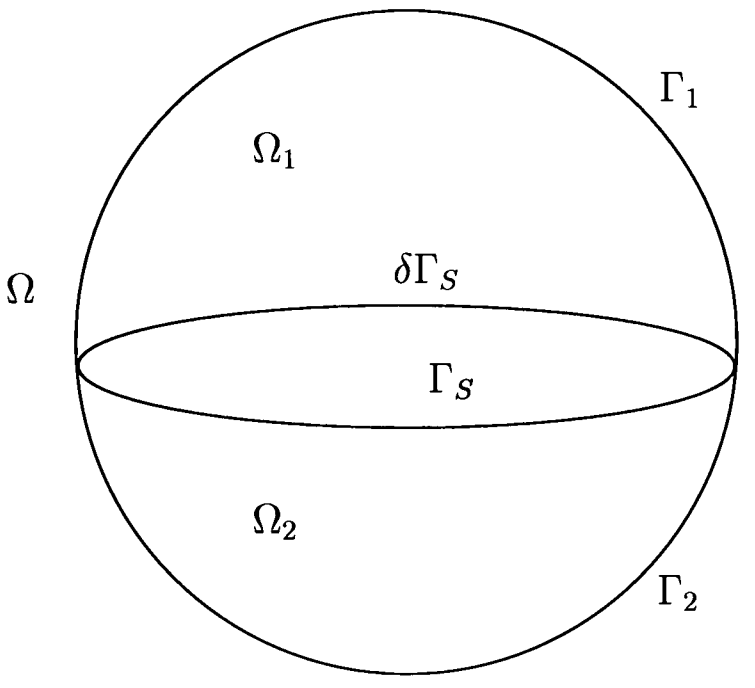

Figure 4.9: 3-D space Ω occupied by two fluids, Ω_1 and Ω_2.

4.6.2 Surface Source Term

By expressing the edge source term Eqn(4.52) as a surface integral we derive the surface source term

$$\boldsymbol{S}_{i\gamma} = \int_{\Gamma_S} \partial_i^S \gamma d\Gamma_S - \int_{\Gamma_S} \gamma n_i \partial_j^S n_j d\Gamma_S, \tag{4.53}$$

where ∂_i^S is the surface gradient in Cartesian coordinates given by

$$\partial_i^S = (\delta_{ij} - n_i n_j)\frac{\partial}{\partial x_j}. \tag{4.54}$$

In Eqn(4.54) δ_{ij} is the delta tensor. Details on the derivation of Eqn(4.53) can be found in Wheeler [83].

The second term in Eqn(4.53) includes the curvature of the surface because the divergence of the normal is equal to the negative of the curvature. Therefore

$$\partial_i^S n_i = -\boldsymbol{J}, \tag{4.55}$$

where $\boldsymbol{J}$ is the curvature of the surface. Thus Eqn(4.53) can be rewritten as

$$\boldsymbol{S}_{i\gamma} = \int_{\Gamma_S} \partial_i^S \gamma d\Gamma_S + \int_{\Gamma_S} \gamma n_i \boldsymbol{J} d\Gamma_S. \tag{4.56}$$

To include the surface tension source term in the LSM formulation Eqn(4.56) is rewritten as a volume integral given by

$$\boldsymbol{F}_{i\gamma} = \int_{\Omega} [\partial_i^S \gamma + \gamma n_i \boldsymbol{J}(\phi)] \delta(\phi) |\nabla \phi| d\Omega \tag{4.57}$$

The transformation of Eqn(4.56) to Eqn(4.57) in 3-D has been proved by Wheeler [83].

The result within the square bracket in Eqn(4.57) can be expanded as follows

$$\partial_i^S \gamma + \gamma n_i \boldsymbol{J}(\phi) = (\delta_{ij} - n_i n_j) \frac{\partial \gamma}{\partial x_j} - \gamma n_i (\delta_{kj} - n_k n_j) \frac{\partial n_k}{\partial x_j} \tag{4.58}$$

The normal $\boldsymbol{n}$ is related to the distance scalar ϕ such that

$$\hat{\boldsymbol{n}} = \frac{\nabla \phi}{|\nabla \phi|}. \tag{4.59}$$

Thus using Eqns(4.58) and (4.59) the surface tension source term can be expressed in terms of ϕ as

$$\boldsymbol{S}_{\gamma} = \delta(\phi) |\nabla \phi| \nabla \gamma - \frac{\delta(\phi)}{|\nabla \phi|} (\nabla \phi \cdot \nabla \gamma) \nabla \phi + \gamma \nabla \phi \boldsymbol{J}(\phi) \delta(\phi), \tag{4.60}$$

where

$$\int_{-\alpha}^{\alpha} \delta(\phi) d\phi = 1. \tag{4.61}$$

When the surface tension is constant the first two terms on the right hand side of Eqn(4.60) will be zero.

The curvature, in terms of ϕ is given by

$$\begin{aligned} \boldsymbol{J}(\phi) &= -\partial_j^S n_j \\ &= -(\delta_{jk} - n_j n_k)(n_j)_{x_k} \qquad (4.62) \\ &= -\left(\frac{\phi_{x_k}}{|\nabla \phi|} \right)_{x_j} + \frac{\phi_{x_j} \phi_{x_k}}{\phi_{x_l} \phi_{x_l}} \left(\frac{\phi_{x_j}}{|\nabla \phi|} \right)_{x_k}. \qquad (4.63) \end{aligned}$$

Although surface tension is normally associated only with the surface, in these equations it needs to be defined across the region $-\alpha < \phi < \alpha$.

4.6.3 Discretization of the Surface Tension Source Term

The source term $\boldsymbol{S}_{\gamma}$ is discretized using the finite volume technique. The curvature $\boldsymbol{J}$, the gradients $\nabla \phi$ and $\nabla \gamma$ and $\delta(\phi)$ are stored at the centre of the control volumes

and are the averages over each cell. The discretization of the components are as follows:

- Eqn(4.62) can be written as

$$\boldsymbol{J}(\phi) = -(\delta_{ij} - n_i n_j)\frac{\partial n_i}{\partial x_j}, \tag{4.64}$$

where

$$\boldsymbol{n} = \frac{\nabla\phi}{|\nabla\phi|}. \tag{4.65}$$

The terms n_i and n_j within the brackets in Eqn(4.64) are calculated directly from $\nabla\phi$ and $|\nabla\phi|$. The term outside the brackets is calculated using the divergence theorem which gives

$$\int_V \frac{\partial}{\partial x_j}\left(\frac{\phi_{x_i}}{|\nabla\phi|}\right) dV = \int_S \frac{n_j\phi_{x_i}}{|\nabla\phi|} dS. \tag{4.66}$$

The discretization of the curvature is therefore

$$\boldsymbol{J}(\phi) = -(\delta_{ij} - \frac{\phi_{x_i}\phi_{x_j}}{|\nabla\phi|^2}) \sum_f \frac{A_f (n_j)_f (\alpha_f (\phi_{x_i})_A + (1-\alpha_f)(\phi_{x_i})_P)}{V_P(\alpha_f |\nabla\phi|_A + (1-\alpha_f)|\nabla\phi|_P)}. \tag{4.67}$$

- To calculate the gradients $\nabla\phi$ and $\nabla\gamma$, they are expressed as in Eqn(4.35) and the arithmetic mean is used to calculate face values. The term $|\nabla\phi|$ is calculated directly from $\nabla\phi$ at each cell centre.

- The delta function, $\delta(\phi)$ ensures that the surface tension source term contributions to the momentum equations are only made for the control volumes near the interface and is given by

$$\delta(\phi) = \begin{cases} \frac{1}{2\alpha}\left(1 + \cos\left(\frac{\pi\phi}{\alpha}\right)\right) & \text{if } |\phi| \leq \alpha \\ 0 & \text{if } |\phi| > \alpha \end{cases} \tag{4.68}$$

4.6.4 The Wetting Angle

When an interface between two fluids is in contact with an external surface and the interface has surface tension then a force is exerted on the fluid interface by the external surface. The force balance at the contact points between interface and surface is modelled by Young's equation. This means that in the discretisation the

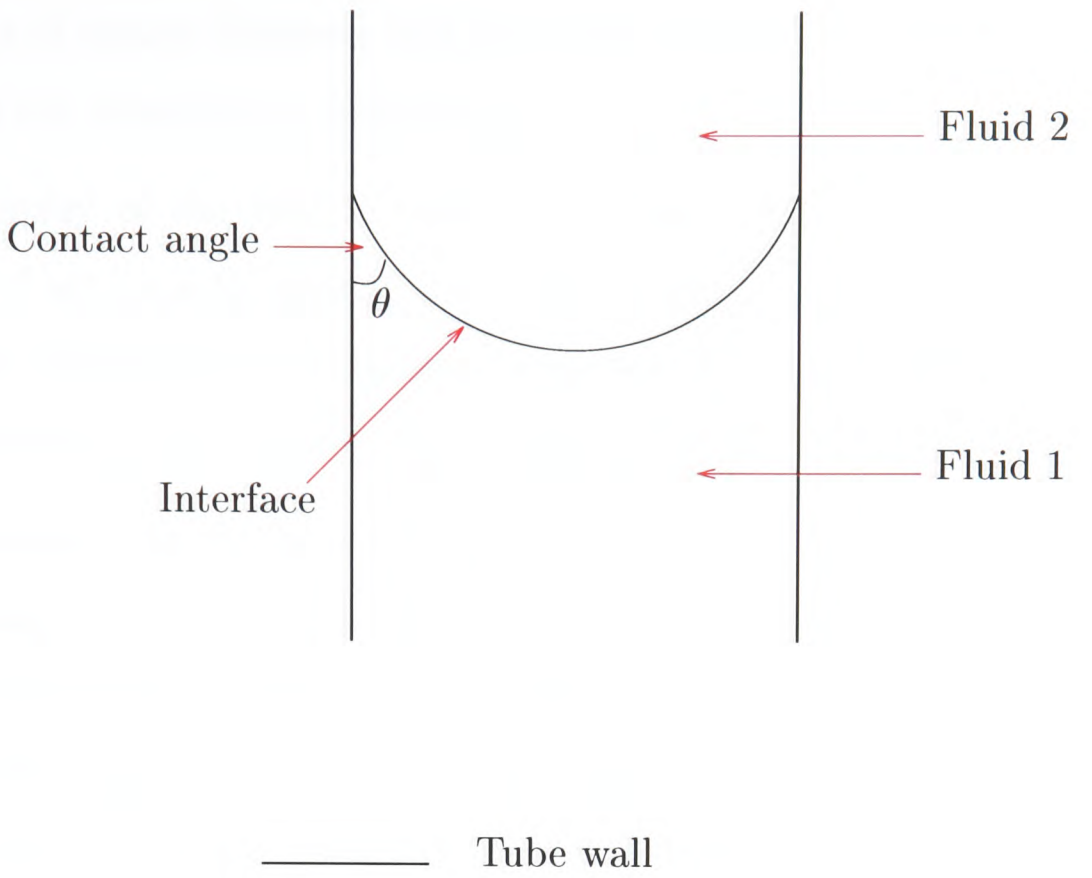

Figure 4.10: The contact angle.

boundary will have a certain equilibrium contact angle. To achieve this the curvature is amended in the cells adjacent to the boundary such that

$$\boldsymbol{J}(\phi) = \frac{1}{l}(\cos\theta - \boldsymbol{n}\cdot\nabla\phi), \tag{4.69}$$

where l is the grid-length, θ is the contact angle and $\boldsymbol{n}$ is the normal pointing into the boundary. When this contact condition is satisfied the third term in the source term (Eqn4.56) will be zero. This condition simulates a contact angle. If the condition is not satisfied the source term will force the fluid to move in the correct direction. Figure 4.10 shows the position of the contact angle in a two fluid system at equilibrium within a tube.

4.6.5 Viscoelastic Fluid Under Surface Tension

To demonstrate the effects of surface tension on a viscoelastic fluid the numerical example where a square gradually evolves into a circle is presented. The computational domain consists of one fluid. In the centre of the domain a square region is defined and surface tension is applied. With time the surface tension forces acting on the interface should change the shape of the interface from a square to a circle

to minimize the energy of the surface. Two meshes are used in this example. One consists of square elements and the other consists of triangular elements. The 2-D meshes are presented in Figure 4.11.

The density of the fluid is the same in both cases. The values $1300kgm^{-3}$, and $70Nm^{-2}$ are used for density and surface tension respectively. In addition, $\lambda_1 = 0.1$ and the Newtonian contribution of the viscosity $\eta_2 = 143Pas$ and the viscoelastic contribution of the viscosity $\eta_1 = 0.89Pas$ for the viscoelastic fluid.

Simulations were carried out using Mesh 1 for both Newtonian and viscoelastic fluids. In Figures 4.12 and 4.13 results are shown for a Newtonian fluid and a viscoelastic fluid respectively. The CPU time for the two simulations were $443s$ (Newtonian) and $734s$ (viscoelastic). For the viscoelastic fluid a further simulation was carried out on the mesh with triangular elements (Mesh 2) and these results are presented in Figure 4.14. The CPU time for the viscoelastic simulation on Mesh 2 was $3178s$. All simulations were carried out on a single CPU of a 5 Alpha server E545 system where each system contains four 1GHz CPUs and 4Gb of memory. In all three simulations with time the square is seen to evolve into a circle under the influence of surface tension. The circle for Mesh 2 appears to be slightly skew which may be due to the type of mesh elements used.

The analytical radius of the circles in all three cases is 0.225. The maximum level set value (ϕ_{max}) should be equal to the value of the radius. The numerical values of ϕ_{max} for each of the cases are 0.19418, 0.19418 and 0.14278 respectively. There is slight underprediction in the numerical values. The value for Mesh 2 may be lower because the shape is not completely circular due to the shape of the mesh elements. The values for both fluids on Mesh 1 is the same with the ϕ_{max} on Mesh 2 being the lowest.

From the Laplace-Young equation the pressure jump across the interface is equal to the surface tension divided by the radius of the circle. This gives a pressure jump of 311.111. The numerically calculated pressure jumps are 329.866, 329.920 and 331.819 for the three simulations respectively. For these material properties there is a over prediction of $6 - 7\%$ in the numerical values.

a)

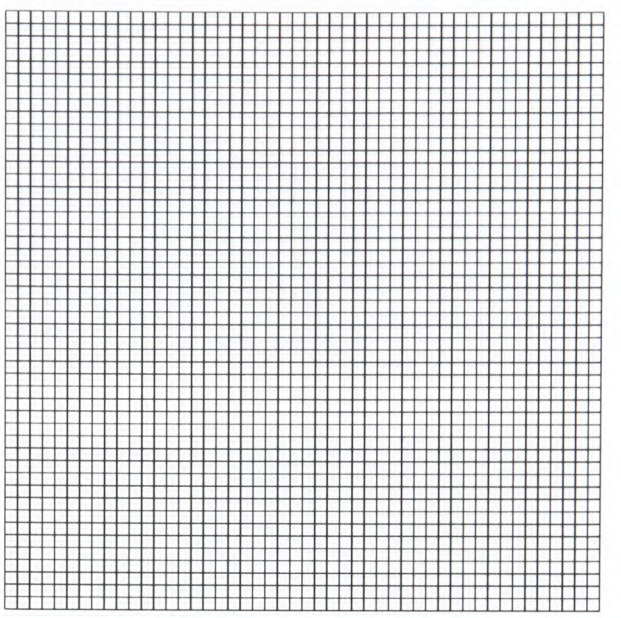

b)

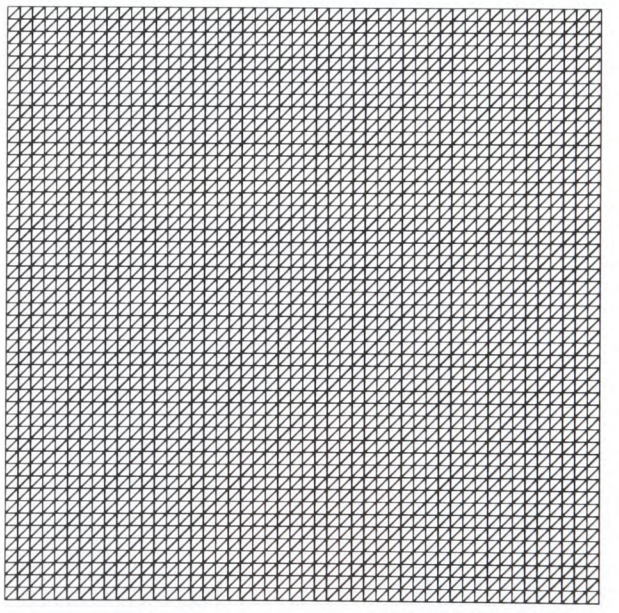

Figure 4.11: The meshes for the square to circle test case. a) Mesh 1 and b) Mesh 2.

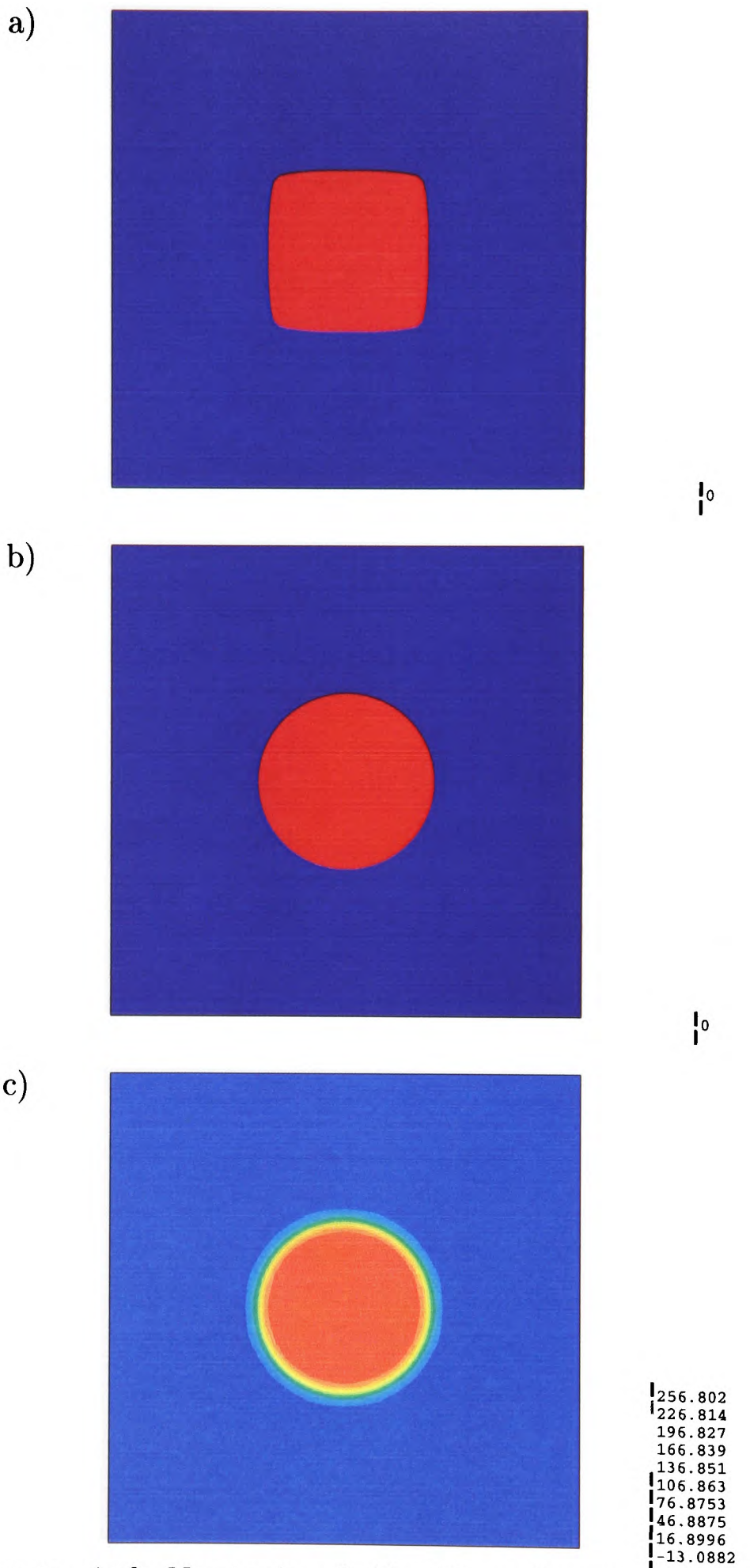

Figure 4.12: Square to circle Newtonian fluid with surface tension on Mesh 1. a) the initial shape of interface, b) shape of interface after $t = 16s$ and c) the pressure contours at $t = 16s$.

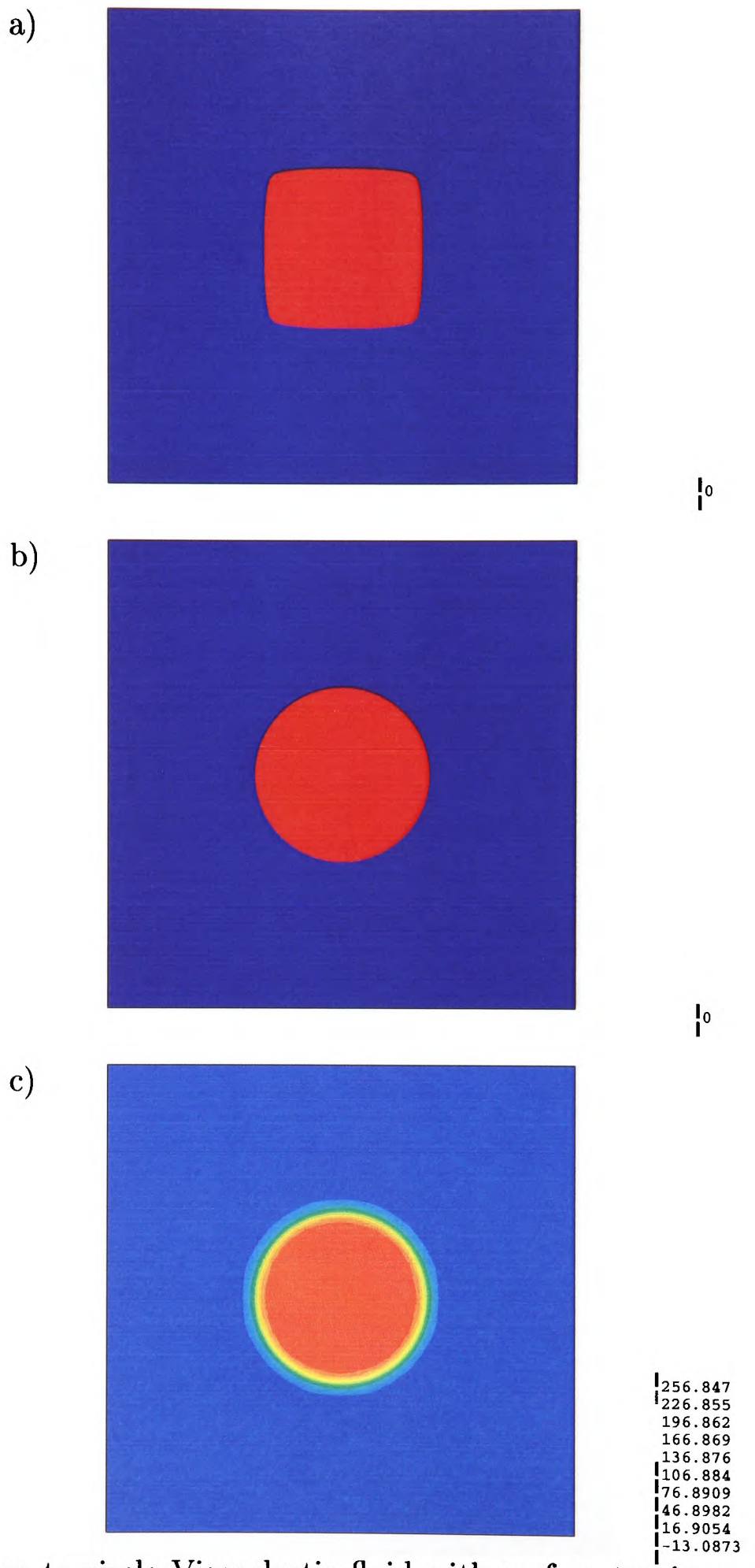

Figure 4.13: Square to circle Viscoelastic fluid with surface tension on Mesh 1. a) the initial shape of interface, b) shape of interface after $t = 16s$ and c) the pressure contours at $t = 16s$.

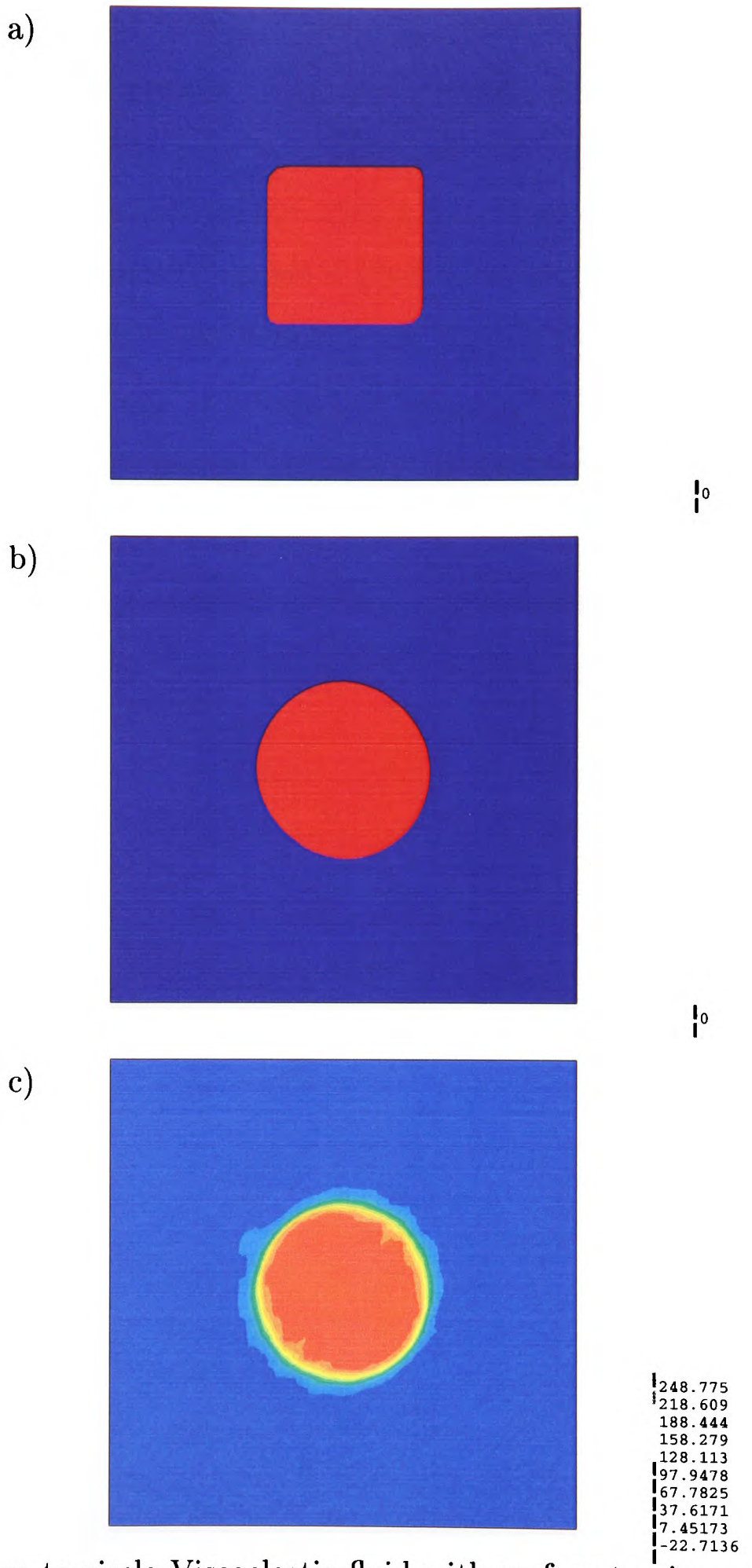

Figure 4.14: Square to circle Viscoelastic fluid with surface tension on Mesh 2. a) the initial shape of interface, b) shape of interface after $t = 16s$ and c) the pressure controus at $t = 16s$.

4.7 Conclusion

In this chapter two free surface algorithms, the Scalar Equation Algorithm (SEA) and the Level Set Method (LSM), have been described and implemented for viscoelastic flow. Simulations have been carried out using a 2-D planar channel test case in order to validate the numerical results against analytical results for a viscoelastic material and good agreement has been attained for both algorithms.

Taking advantage of the fact that interface smearing is minimal using the LSM, surface tension effects have been implemented in the LSM algorithm. A test case demonstrated the surface tension effects.

In the next chapter the SEA and LSM algorithms will be used to model two industrial processes which involve viscoelastic fluids and two-phase flow.

Chapter 5

Applications

In the preceding chapters two algorithms were presented to model two-phase viscoelastic flows. In the present chapter these algorithms are applied to two industrial processes which involve viscoelastic fluids to explore its potential as a predictive tool.

5.1 Electronic Packaging

Applications which involve viscoelastic materials are wide and varied ranging from biological applications such as arterial blood flow to industrial applications such as the forming of plastic bottles. The earliest successful attempt at computationally solving viscoelastic flow was by Perera and Walters in the late 70's. Since then, with the advent of fast computers with large memory capacity and advances in solution techniques, many of these processes have, to some extent, been investigated through computational modelling. This study focuses on two applications in the field of electronic packaging.

The advent of the silicon chip enabled large numbers of transistors to be fitted on to a small chip paving the way for much powerful machines. The size of the chip also reduced the dimensions of the circuitry. Therefore electronic circuits with embeded silicon chips (see Figure 5.1) found their way into numerous devices ranging from computers to household appliances. The quest today is to produce increasingly small lightweight electronic components. Therefore polymer materials have become popular in the electronic packaging industry since they form compounds which are

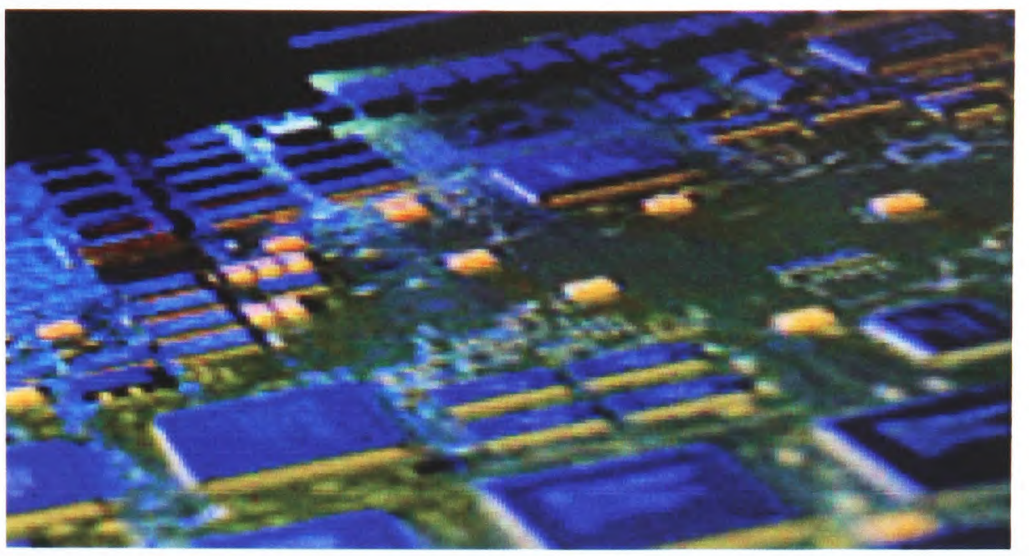

Figure 5.1: Electronic circuit board.

low in cost, meet the necessary material property requirements such as low dielectric constants and are much lighter in weight than materials such as glass or metal which were originally used for packaging. Some of the polymers used are viscoelastic materials.

5.2 Underfill

Polymers were first used in the electronic industry in the 1960s. A layer of organic resin was used to protect wirebonded semiconductor devices instead of producing hermetically sealed metal and glass packages in order to reduce cost. This technique came to be known as 'glob-topping' (see Figure 5.2).

With electronic devices getting increasingly small the next step was to reduce the size and height of the components and this was found to be possible through the direct mounting of silicon die on to circuit boards as shown in Figure 5.3. This method not only decreases the height but also reduces cost as it is possible to dispense with wirebonds. The direct attachment of chip on board is called 'Flip-chip' technology. When silicon die are flip-chip mounted electrically conductive bumps, usually made of solder, form an interface between the die pads and the board and a gap is formed between the interface joints. To protect the underside of the die and to strengthen the interface joints during thermal cycling, the gap between the joints are filled with 'underfill' encapsulants which have an epoxy resin base. Figure 5.4 shows the steps in

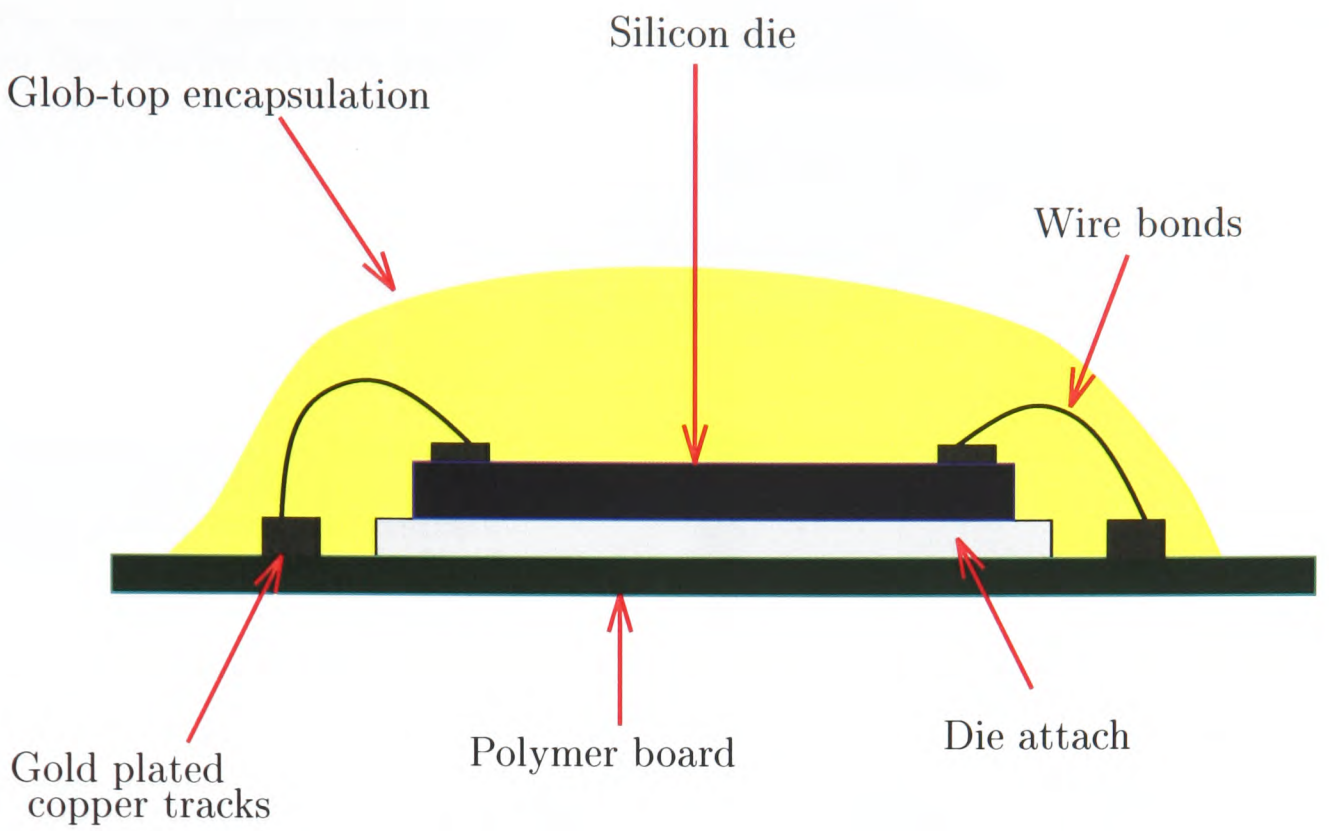

Figure 5.2: Glob-topped component.

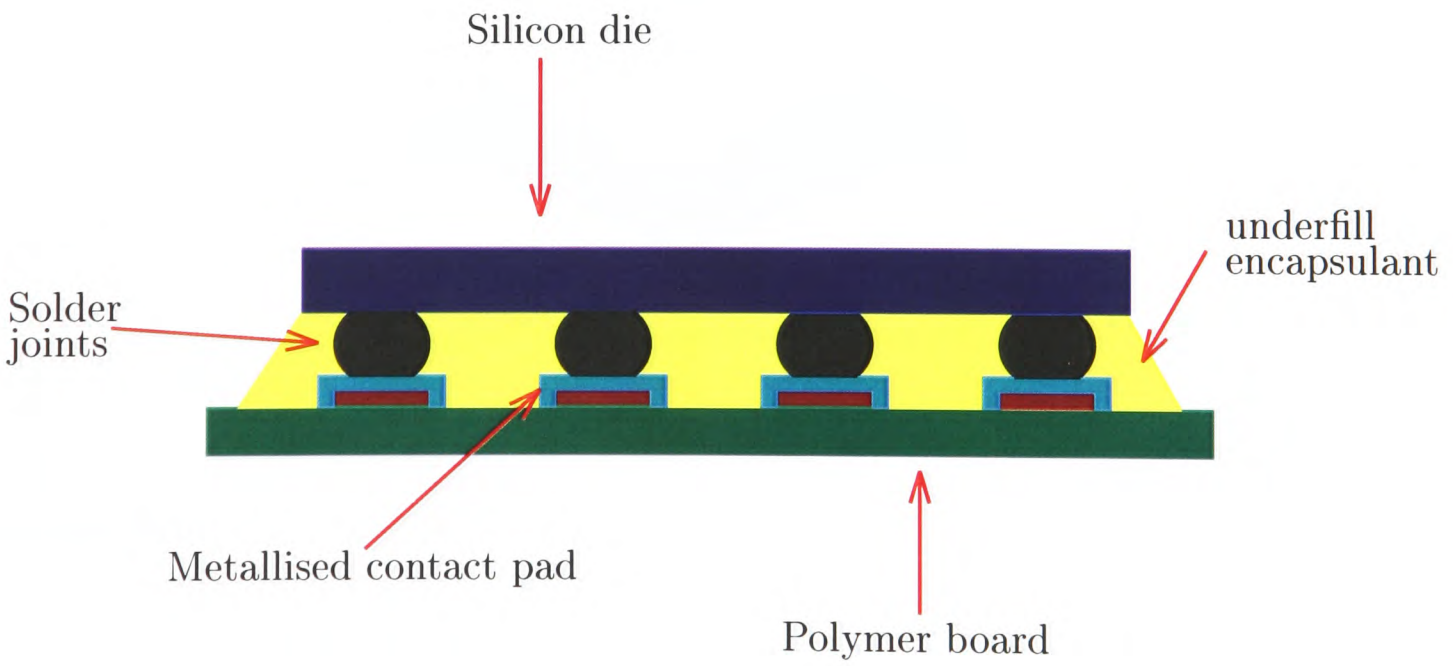

Figure 5.3: Flip-chip.

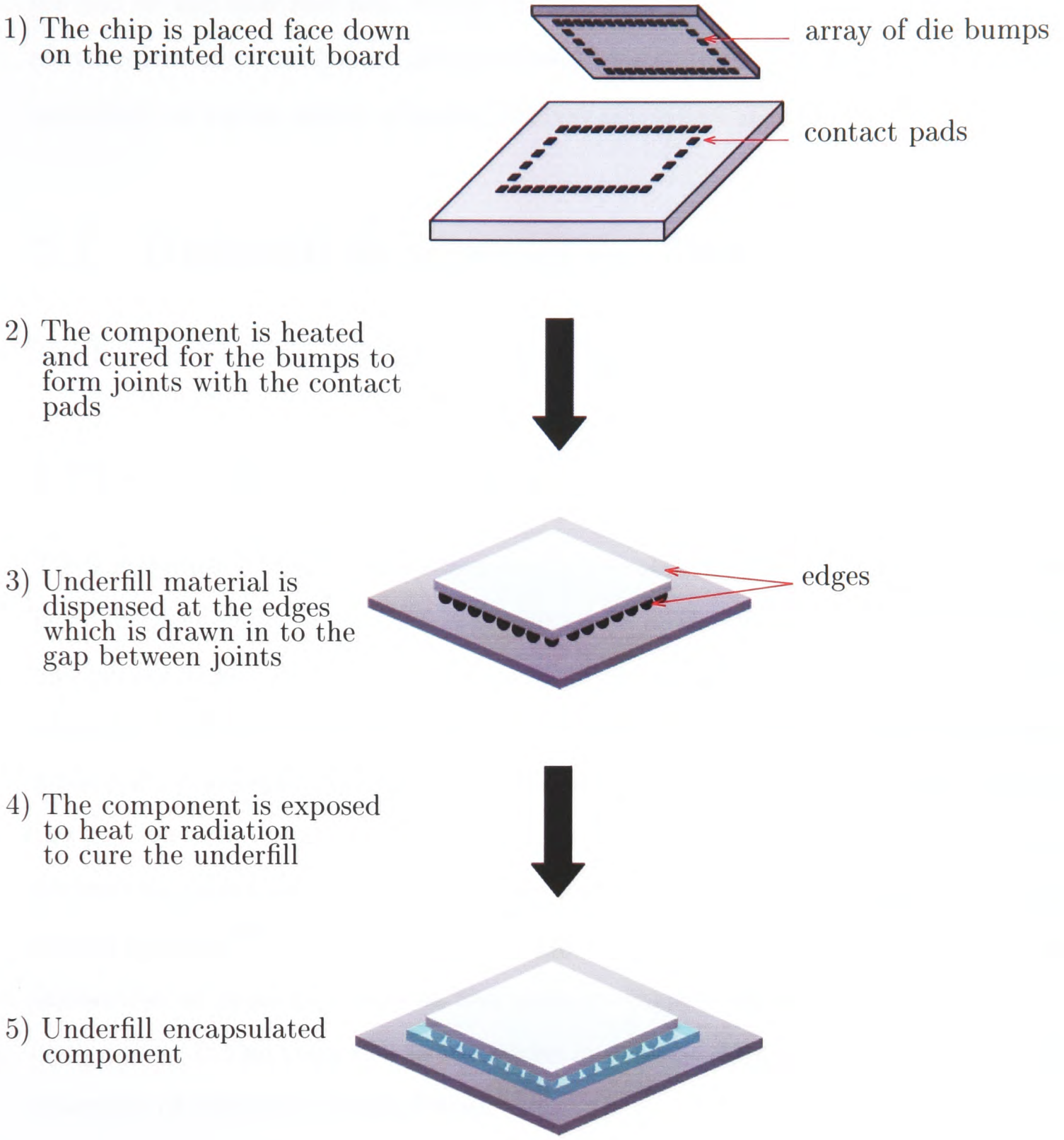

Figure 5.4: Underfilling Process.

the flip-chip process. The epoxy resins used for underfill encapsulants are viscoelastic materials [84].

5.2.1 Underfill Material

There are various types of underfill material commercially available to industry. A typical underfill material should have a high Young's modulus, a coefficient of thermal expansion matching that of the organic substrate with good adhesion to the organic substrate and the silicon chip. It should also flow well under low clearance

die and be fast flow and fast curing for optimum production. Most underfill materials therefore are a composite of a low-halide epoxy resin, a fused silica filler, an acid anhydride as curing agent, a latent catalyst and a wetting agent.

5.3 Underfill Encapsulation Techniques

The following sections describe three techniques for underfill encapsulation.

5.3.1 Capillary Driven Flow

The conventional method of encapsulating the solder joints is with capillary driven flow. In this technique the fluid is dispensed on to the heated circuit board at either one or two edges of the chip. The heat of the board reduces the viscosity of the underfill. The differing surface energies between the die surface, board and underfill gives rise to capillary action which results in drawing the low viscosity fluid into the gap between board and chip. Figure 5.5 a) shows the dynamics of capillary driven encapsulation. However this method has a tendency to capture air bubbles during the flow. This causes voids to be formed around the joints resulting in bump failure due to premature fatigue and thereby directly affecting the reliability of the component. It also gives rise to variations in density. The images in Figure 5.6 show examples of defective encapsulation.

5.3.2 Injection Flow

In injection flow underfill is injected into the substrate from an edge and the pressure at the inlet then drives the fluid into the substrate. The injection dynamics are shown in Figure 5.5 b). This method has shown to decrease underfilling times however it is limited by the maximum normal stress that the joints can withstand. Another drawback it is that the injection head has to stay in contact with the chip through out the flow process which prevents it from carrying out multiple dispensing. This results in a point to point processing limitation as the number of chips on the board increase which in turn affects the high throughput production rates. It also does not

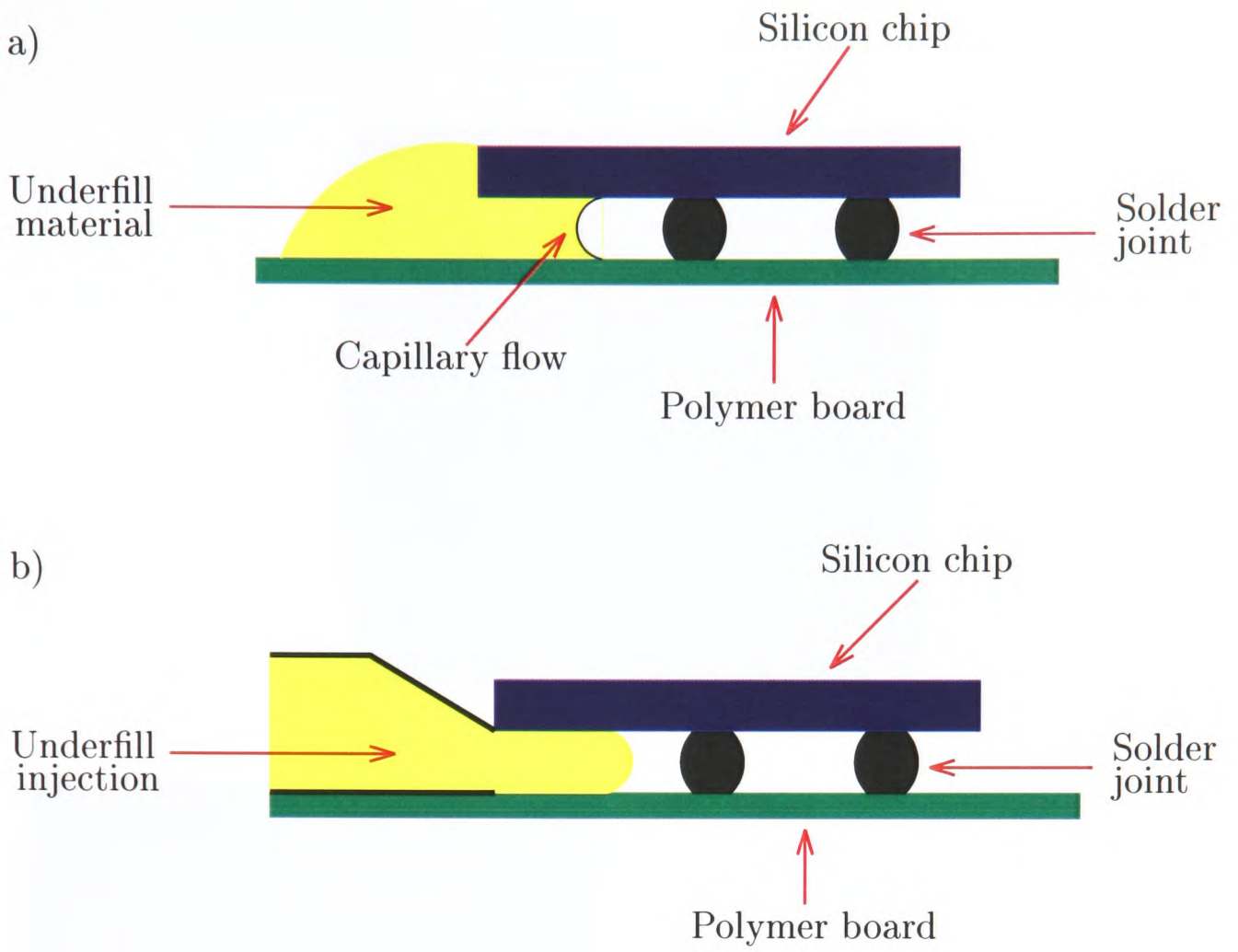

Figure 5.5: Underfilling techniques.

address the issue of the formation of voids.

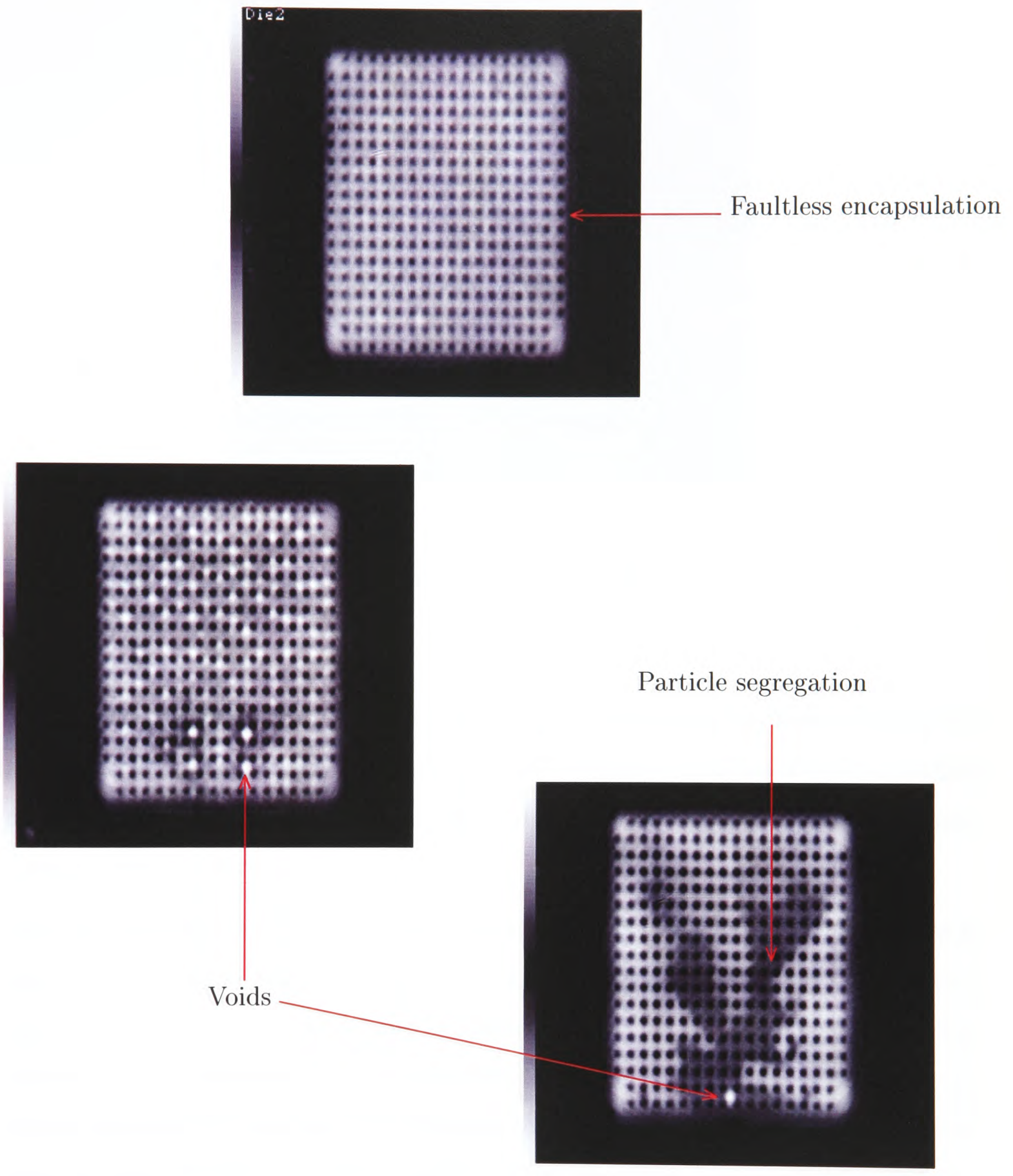

Figure 5.6: Process induced defects.

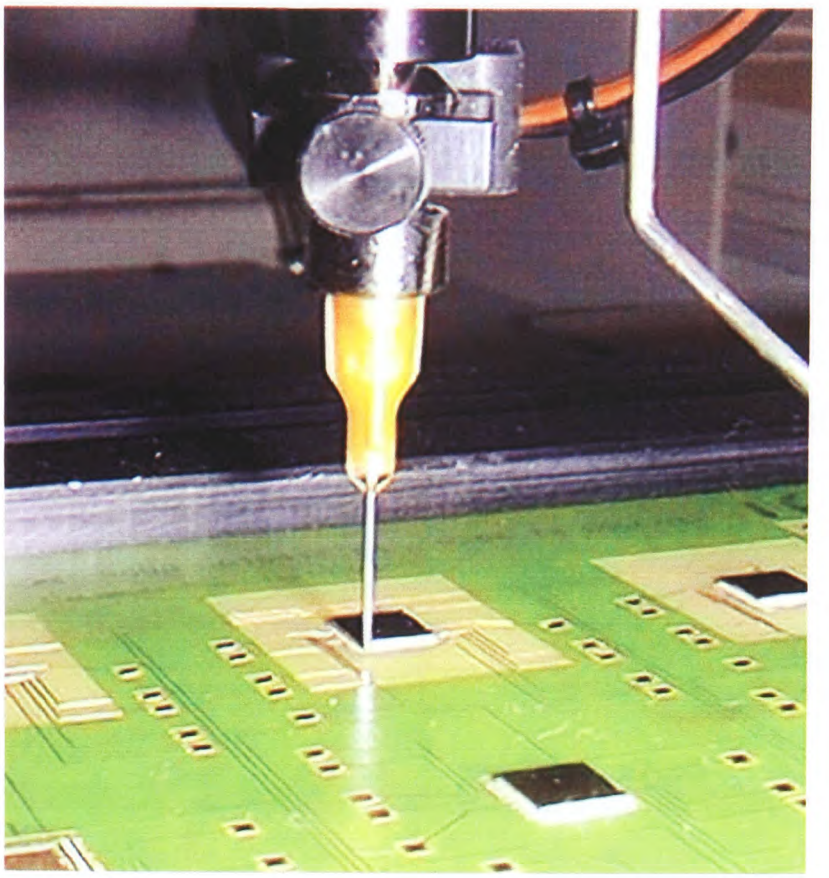

Figure 5.7: Jetting machine.

5.3.3 Jetting

Jetting is the selective dispensing of fluid without contact and has been in use in the packaging industry for various other processes. Figure 5.7 shows a type of jetting machine at work in this case dispensing underfill at the edges of chips which have already been mounted on to boards.

With the decrease in component sizes the height of the substrate is also decreasing and it is becoming increasingly difficult to encapsulate using techniques such as those described above. Therefore jetting of underfill on to printed circuit boards before silicon chips are mounted is being considered as a viable dispensing process. In the jetting process, the machines are calibrated to eject exact quantities of underfill dots onto the gaps between the contact pads on which the solder bumps sit when the chip is placed on the circuit board (see Figure 5.8). The silicon chip is then mounted and the component is cured. When the component is being cured the underfill dots which were dispensed melt and solidify around the joints.

In this technique precision is crucial as the dots have to maintain their shapes and fall on to exact locations which will ensure that the fluid on the board will have a specific diameter and height. Underfill is an abrasive fluid and causes the tip of the

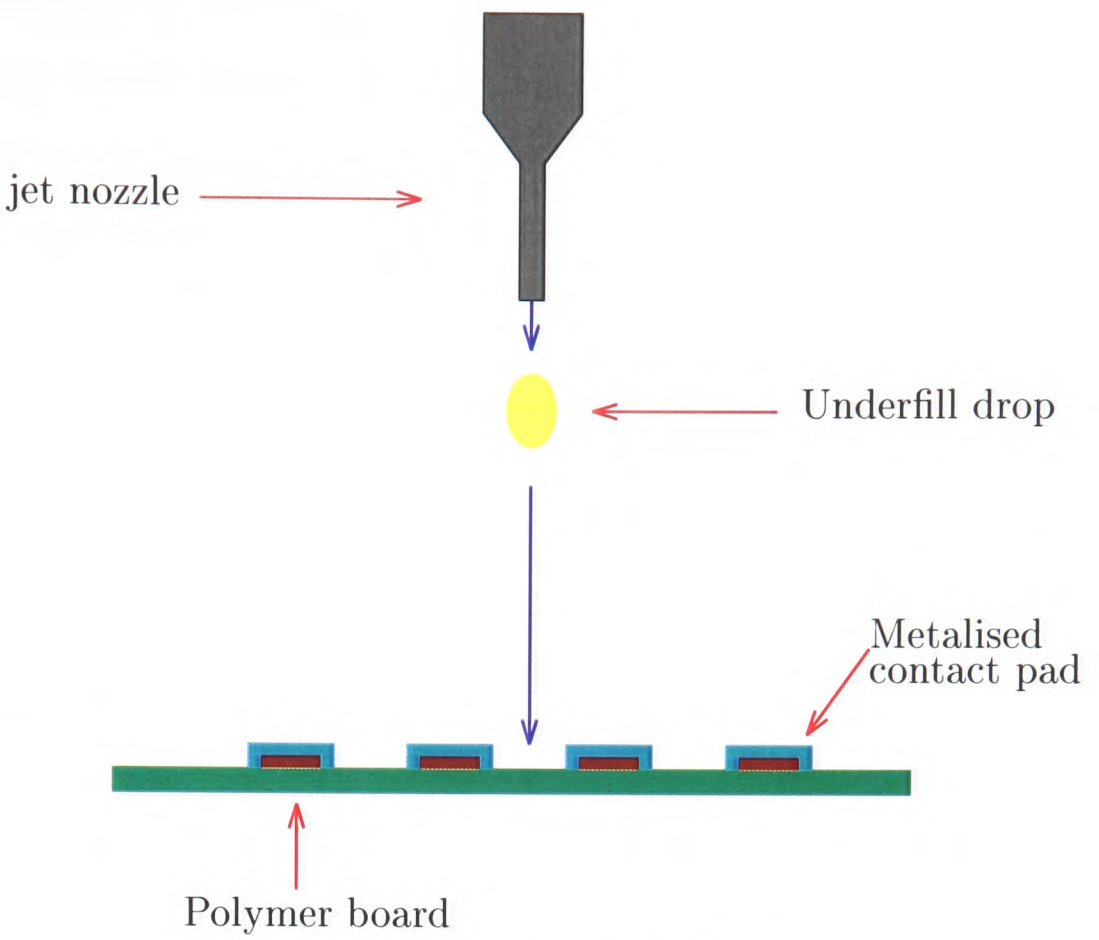

Figure 5.8: Jetting of underfill.

dispensing needle to wearout with extended use. It has been experimentally observed [85] that, with time, nozzle wearout affects the volume and shapes of the dispensed drops. Therefore this technique is still at the experimental stage.

5.4 Current Research

The bulk of the research in this area involves capillary driven flow as it is still the most widely employed technique in industry. Investigations into capillary driven flow have followed two main directions. The use of analytical models to predict mechanical properties of filled epoxies and the use of numerical modelling to develop predictive tools to capture process induced defects such as voids.

5.4.1 Analytical Models for Mechanical Properties

Flow times

The equation used to calculate underfill flow times is [86]

$$T = \frac{3\mu L^2}{h\gamma\cos\theta}, \tag{5.1}$$

where T is the time in seconds, μ is the viscosity of the fluid, L is the length of the die, h is the height between die and board, θ is the contact angle and γ is the surface tension of the liquid vapour interface. This equation takes into account the effects of differing surface energies which gives rise to capillary driven flow which is the conventional underfilling technique. From the equation it can be seen that the time for underfilling is proportional to the square of the length or width of the die. Therefore, if the underfilling times are to be minimised, the fluid should be dispensed at the longest side of the die.

The Mooney equation

This equation is used to estimate the increase of viscosity with filler content and is given by [87]

$$\ln\frac{\eta_c}{\eta_l} = \frac{k_E\phi_2}{1-\phi_2/\phi_m} \tag{5.2}$$

where η_c is the viscosity of the filled epoxy resin, η_l is the viscosity of the epoxy liquid, k_E is the Einstein constant ($= 2.5$), ϕ_2 is the volume fraction of filler and ϕ_m is the maximum volume the filler particle can have (it is around 0.632 for random close packing).

The Washburn Model

This equation models the effect of filler content on flow lengths (x) and is given by [87]

$$\frac{d(x_f)^2}{dt} = b\frac{\sigma}{6}(\cos\theta_0 + \cos\theta_s)\frac{s}{\mu_{eff}} \tag{5.3}$$

where x_f is the axial flow length, b is the flow parameter, σ is the liquid surface tension, θ_0 and θ_s are the contact angles at the lower and upper channel surfaces, s is the channel spacing and μ_{eff} is the effective viscosity. It is important to note that experimental measurements indicate that the contact angles and surface tensions are not strongly influenced by the filler content. Therefore, viscosity is the dominant factor in underfilling

The Kerner equation

Theoretically the equation for increase in modulus (Young's modulus) has been found to have the same form as that for increase in viscosity and the Mooney equation is used to predict increase in modulus. However, this method has proved to overestimate the modulus of filled epoxies [87]. Therefore the Kerner equation given by [87]

$$\frac{E_c}{E} = 1 + \frac{15(1 - v_1)\phi_2}{(8 - 10v_1)\phi_1}, \tag{5.4}$$

is used where E_c and E are the moduli of the filled and unfilled epoxy respectively, v_1 is the Poisson's ratio of the unfilled epoxy, ϕ_1 is the volume fraction of epoxy and ϕ_2 is the maximum volume the filler particle can take.

The effect of filler content on Coefficient of Thermal Expansion (CTE)

To study the CTE for polymers filled with spherical particles the linear equation given by [87]

$$\alpha_c = \phi_2\alpha_2 + (1 - \phi_2)\alpha_1, \tag{5.5}$$

is used, where α_c, α_1 and α_2 are the CTEs for the composite, matrix and filler respectively and ϕ_2 is the maximum volume the filler particle can take.

The effect of filler content on strength

The strength of the filled polymers are influenced considerably by particle-matrix adhesion and particle size. Therefore predicting the strength is difficult and the theory of Nicholais and Narkis is considered an adequate method to study the effect of filler content on strength. The equation has the form [87]

$$\sigma_c^* = \sigma^*(1 - 1.21\phi_2^{2/3}), \tag{5.6}$$

where σ_c^* and σ^* are the strengths of the composite and unfilled epoxy respectively and ϕ_2 is the maximum volume the filler particles can take. For untreated or debonding particles, the tensile stress decreases with increasing filler content and for well bonded filler particles it is independent of filler content and around 90% of the strength of the unfilled epoxy.

A model for fracture toughnes

The fracture toughness of a filled epoxy is controlled by a number of parameters among which filler particle size and filler content are the most important. Additionally the toughening mechanism is also important. Research on model epoxies have shown a micro-cracking mechanism induced by particles. This has been modelled by Evans et al. using the equation [87]

$$\frac{G_c}{G} = 1 - \phi_2 + 0.8\ln\left[\frac{E_c G_c}{4R(\sigma_c^*)^2}\right], \tag{5.7}$$

where G_c and G are the fracture toughness of the filled and unfilled epoxy respectively, E_c and σ_c^* are the modulus and strength of the filled epoxy, R is the radius of the filler particle and ϕ_2 is the maximum volume the filler particle can take.

5.4.2 Summary

These analytical models have been used extensively to improve underfill flow times, material properties etc. [88, 89, 87, 90, 91]. However the analytical solutions of these models cannot be used as a predictive tool which will for example give insight into the dynamics which cause defects such as formation of voids. With components becoming increasingly smaller such issues are becoming increasingly important as they have a direct impact on the reliability of components.

5.4.3 Numerical Modelling of Underfill

Computational modelling is a technique which can be used as a predictive tool. It can also be used as an alternative for physical testing thereby removing the need to produce large numbers of prototypes. It reduces the time-scale required for the design process and decreases costs. Therefore there is great demand for computational algorithms which can model the complex dynamics which govern the processes in electronic packaging. Numerical modelling has been used to investigate two aspects of the underfill process. These are the modelling of stress analysis in the cured underfill to predict crack propagation etc., and the modelling of the underfill flow encapsulation process.

The modelling of cured underfill has been carried out extensively using finite element algorithms where even the viscoelastic nature of the material has also been addressed through the use of constitutive models for viscoelastic solids [92, 93].

Work on the modelling of the encapsulation process has been limited as it involves complex flow mechanisms which are numerically challenging. Details of three areas of research are presented below to outline the current state of modelling of underfill flow.

Masunaga et al. [94] presented an analysis of polymer flow for flip-chip packaging based on capillary driven flow. They employed finite element techniques with the Simplified Marker and Cell (SMAC) method and the Volume of Fluid (VOF) method to discretize the Navier-Stokes equations, time integration and to track the free surfaces. The governing equations were the 2D Navier-Stokes equations for incompressible laminar Newtonian fluid given by

$$\frac{\partial \boldsymbol{u}}{\partial t} + \boldsymbol{u} \cdot \nabla \boldsymbol{u} = -\frac{1}{\rho}\nabla p + \frac{\mu}{\rho}\nabla^2 \boldsymbol{u} + \frac{\boldsymbol{r}}{\rho}, \tag{5.8}$$

and the continuity equation given by

$$\nabla \cdot \boldsymbol{u} = 0, \tag{5.9}$$

where $\boldsymbol{u}$ is the velocity vector, p is the pressure, ρ and μ are the density and viscosity of the fluid respectively and $\boldsymbol{r}$ is the flow resistance vector.

The x and y components of the flow resistance $\boldsymbol{r}$ were defined as

$$r_x = \frac{12\mu u_x}{h^2}, \qquad r_y = \frac{12\mu u_y}{h^2}, \tag{5.10}$$

where h is the height between the silicon chip and circuit board.

The pressure across the free surface was defined using the Laplace-Young equation given by

$$p = -\frac{2\Gamma\cos\theta}{h}, \tag{5.11}$$

where Γ is the surface tension of the liquid-vapor interface and θ is contact angle of the fluid at the surface of the chip and board.

This 2-D model ignored the effects of solder joints, surface roughness, other flow obstructions and end effects. It assumed a continuous supply of underfill at the inlet.

The results from the numerical simulations were compared against experimental results. In the experiments underfill materials with silica filler were used. A comparison of the filling times showed that the computed times were higher than experimental values. This was taken as an indication that a suspension cannot be modelled as a Newtonian fluid and therefore modifications were made to the flow resistance terms (Eqn 5.10) by multiplying the terms by a constant which was dependent upon underfill material properties. With this modification there was an improvement in the filling times obtained through modelling and the flow front profiles were in good agreement with the experimental results.

Han et al. [95] carried out both analytical and numerical work on underfill flow. The investigations started with simple analytical solutions similar to those presented in section 5.4, and then progressed to numerical modelling which allowed the complex dynamics of underfill flow. The numerical analysis was based on finite element techniques. A Hele-Shaw approximation was implemented where the viscosity was measured under comparable flow conditions. This is a simplified method of measuring viscosity of a material which is a suspension. This method is based upon the assumption that the space between the adjacent solder joints is large compared

to the height between chip and board. A power-law model was used to represent the constitutive behaviour of the fluid. Physical experimentation was carried out to validate the numerical work. A two-phase 3-D algorithm was presented by Yang et al.[96]. This algorithm was based on the VOF method for incompressible generalised Newtonian flow. A finite volume discretization was used with the SIMPLE solution algorithm. The governing equations used were the momentum conservation equations, the mass conservation equation and an advection equation for the transport of a scalar. The net normal force due to surface tension was calculated using the expression

$$\int \Delta p ds = \int \sigma \boldsymbol{n} x dx, \tag{5.12}$$

where Δp is the normal force per area, σ is the surface tension, $\boldsymbol{n}$ is the unit outward normal and x is the length of the line segment. The model was implemented into the algorithm as follows. After the liquid/gas interface was determined for each cell a unit normal of the interface was calculated and then Eqn(5.12) was used to calculate the net normal force. This was then introduced into the momentum equation as a body force. Results were presented on a 3-D geometry consisting of spheres which were truncated at the top and bottom. The underfill was modelled as a suspension by using a filler-particle model. The simulated results showed that the flow front moved in an uneven "leapfrog" manner [96] and was in agreement with experimental results. This fluid was modelled as a Newtonian fluid and a higher order surface reconstruction technique had to be used to overcome the smearing of the interface which occurs with VOF.

As mentioned in Section 5.3 interest in jetting as an alternative dispensing method is increasing. However the effect the abrasive nature of underfill has on the tip of the needle and variations in the shapes of the drops need to be better understood before it can be used in large scale packaging. Preliminary investigations have been carried out by Quinones et al. [85]. The modelling is based on a finite element calculation of the flow within the syringe and needle. This method does not have the capability to model the drop formation and to track the movement as it falls on to the surface. The technique also cannot model the erosion of the needle tip.

The flowchart in Figure 5.9 shows the various directions in which the research has

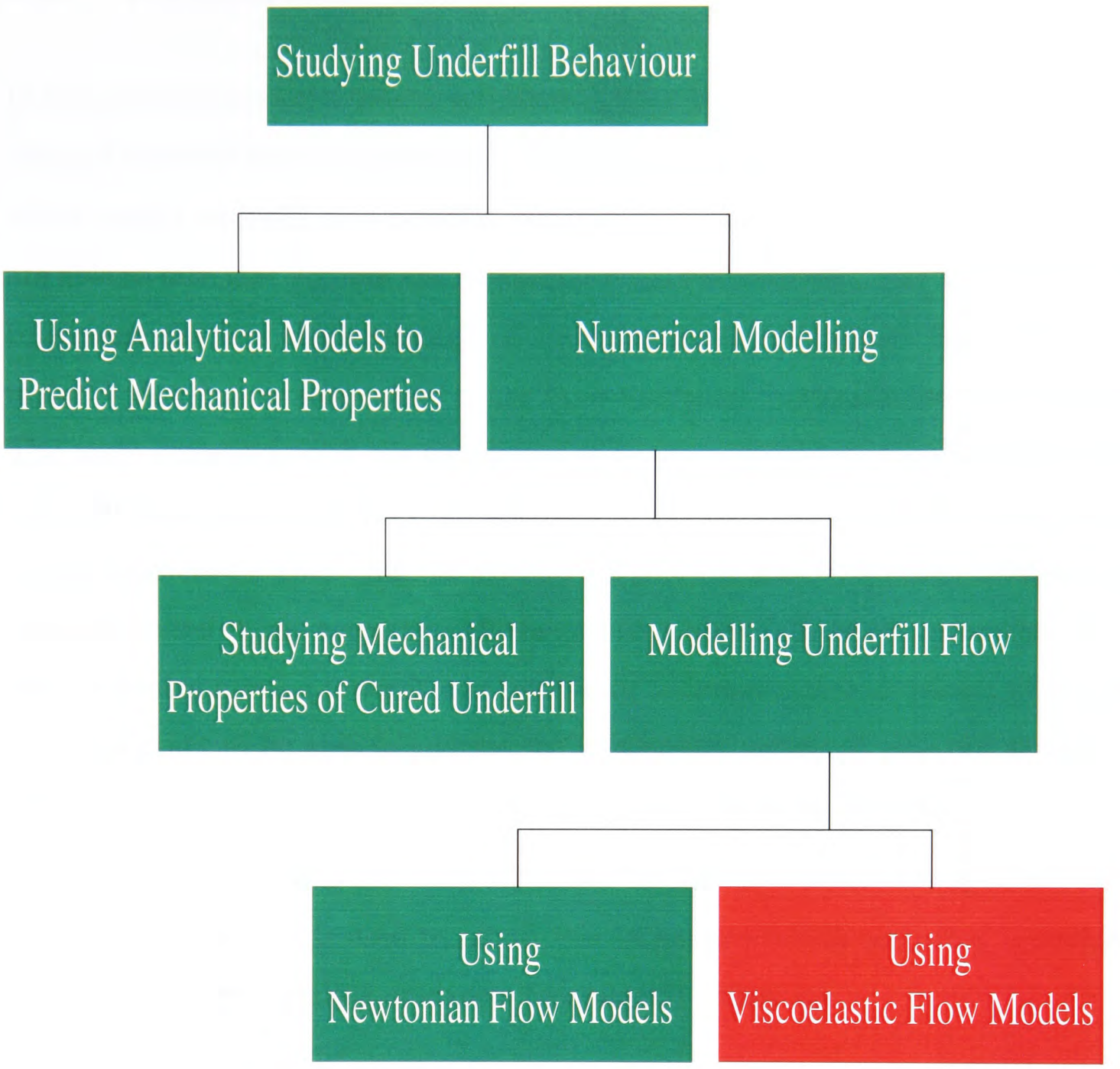

Figure 5.9: Flowchart.

developed in modelling of underfill flow. The green modules indicate research already carried out in this field. The red box indicates contributions from work undertaken in this PhD.

5.5 Numerical Tests

In the previous section a brief description of the current state of research on the modelling of underfill flow was presented. The existing techniques vary from 2-D methods which model underfill as a no-filler material to more advanced 3-D methods which are able to take into account the composite nature of underfill. The methods are able to capture the flow characteristics of the experimentally observed flow behaviour of underfill flow but in some cases it has been necessary to modify the flow equations. The main drawback with the techniques is in the constitutive representation of the underfill materials where they are assumed to be Newtonian when the materials are in fact viscoelastic fluids [84]. In instances where the non-Newtonian behaviour has been addressed it has been through the use of models such as the power-law model. With industry moving towards new packaging techniques such as jetting of underfill, it is important to be able to address the viscoelastic nature of underfill as there are obvious departures in behaviour from Newtonian behaviour [97, 98].

In the following sections the viscoelastic free surface algorithm developed during the course of this project is used to model two techniques which are being investigated as methods to encapsulate electronic components. They are

1. Injection flow
2. Jetting of underfill

Injection flow encapsulation is chosen instead of capillary driven flow since it can be modelled as pressure driven flow. A series of numerical experiments are carried out for each technique. The aim of these numerical experiments is to explore the predictive capability of the algorithm and to investigate the flow behaviour of viscoelastic flow in micro-scale geometries.

In the representation of material properties of the underfill fluid the following assumptions are made:

1. Underfill does not contain filler particles.
2. The no-filler underfill can be modelled using the constant viscosity Oldroyd-B viscoelastic constitutive model.

3. The contact angle between material and solid surfaces (ie. solder joint,interiror of jetting nozzle wall) is zero.

4. The material properties are not temperature dependent.

For the work presented in the following sections when the fluid is Newtonian the governing equations are Eqns(4.1)-(4.2) given in Chapter 4, section 4.2. The governing equations for the viscoelastic free surface algorithm are Eqns(4.22)-(4.24) as presented in Chapter 4, section 4.3.5. The definitions and notation for material properties used in the following sections will also be the same.

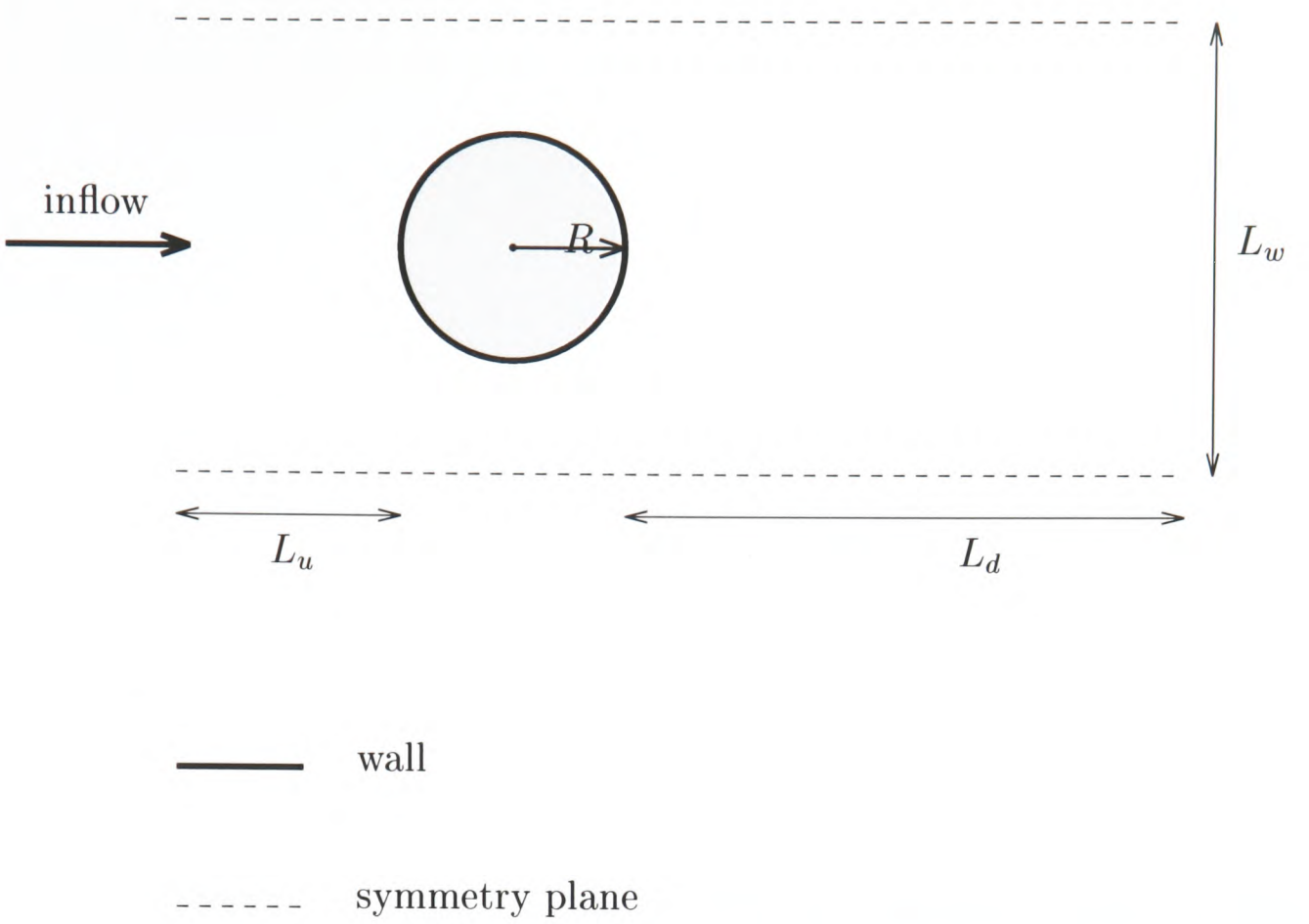

Figure 5.10: The flow past a solder joint geometry.

5.5.1 Viscoelastic Flow Past Solder Joints

The first experiment involves the pressure driven flow of an Oldroyd-B fluid past solder joints. This experiment consists of a series of tests beginning with the interface tracking of the fluid past one solder joint in 2-D which is then extended to 3-D geometries which include two solder joints.

A schematic of the geometry for the flow past one solder joint is given in Figure 5.10. The geometry consists of an entire solder joint and the symmetry planes are located on either side of the joint in order to be able to observe flow symmetry as the free surface moves around and past the joint. The flow is from left to right. The radius of the solder joint is R. The upstream and downstream channel lengths are defined as L_u and L_d respectively. The distance between the symmetry planes is L_w and $L_w = 4R$. The dimensional values used for the various meshes in this experiment are given in Table 5.1.

Mesh	Mesh 1	Mesh 2	Mesh 3	Mesh 4	Mesh 5	Mesh 6
$L_u(\mu m)$	150	150	150	150	150	150
$R(\mu m)$	100	100	100	100	100	100
$L_b(\mu m)$	-	-	-	-	200	200
$L_d(\mu m)$	150	900	900	190	850	1525
$L_w(\mu m)$	400	400	400	400	400	400
$L_h(\mu m)$	-	-	100	100	-	100
Elements	2688	4736	12288	15072	5760	41472

Table 5.1: Details of Meshes in Experiment 1.

Density of polymer	$1300 kgm^{-3}$
Newtonian contribution of viscosity of polymer (η_2)	$4.0 Pas$
Viscoelastic contribution of viscosity of polymer (η_1)	$0.996 Pas$
Relaxation time of polymer (λ_1)	$0.14s$
Surface tension of polymer (σ_1)	$42.66 \times 10^{-3} Nm^{-1}$
Density of air	$1.19 kgm^{-3}$
Viscosity of air	$1.819 \times 10^{-5} Pas$

Table 5.2: Material Properties for Experiment 1.

Test 1 - Newtonian flow past 1 solder joint 2-D: SEA algorithm

The first numerical test was carried out on a 2-D geometry using the SEA algorithm for Newtonian flow. The algorithm ignores surface tension effects. The simulation was carried out on Mesh 1 (see Table 5.1 and Figure 5.11) and the material properties used are given in Table 5.2. The density and viscosity of Fluid 1 were taken from a paper published by Evans et al.[68] and Fluid 2 is assumed to have the properties of air. A constant velocity of $0.05 ms^{-1}$ is imposed at the inlet. The pressure is set to zero at the outlet. No-slip condition was imposed on the joint wall.

Figure 5.12 shows the progress of the flow front with time. The fluid flows around and past the solder joint and captures an air bubble behind the joint. The shape of the void however is not smooth and this is believed to be due to the absence of surface tension effects in this model.

Using one CPU on a 5 Alpha server E545 system where each system contains four 1GHz CPUs with 4Gb of memory the total time for the above run was $1519s$.

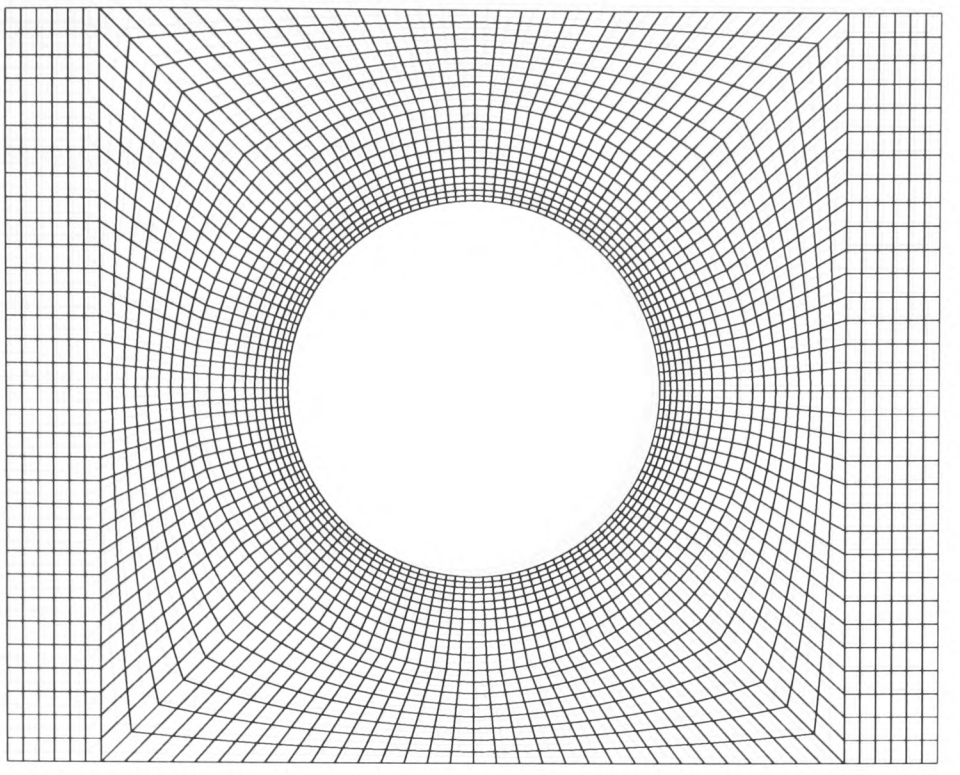

Figure 5.11: Mesh 1:2-D mesh for one solder joint.

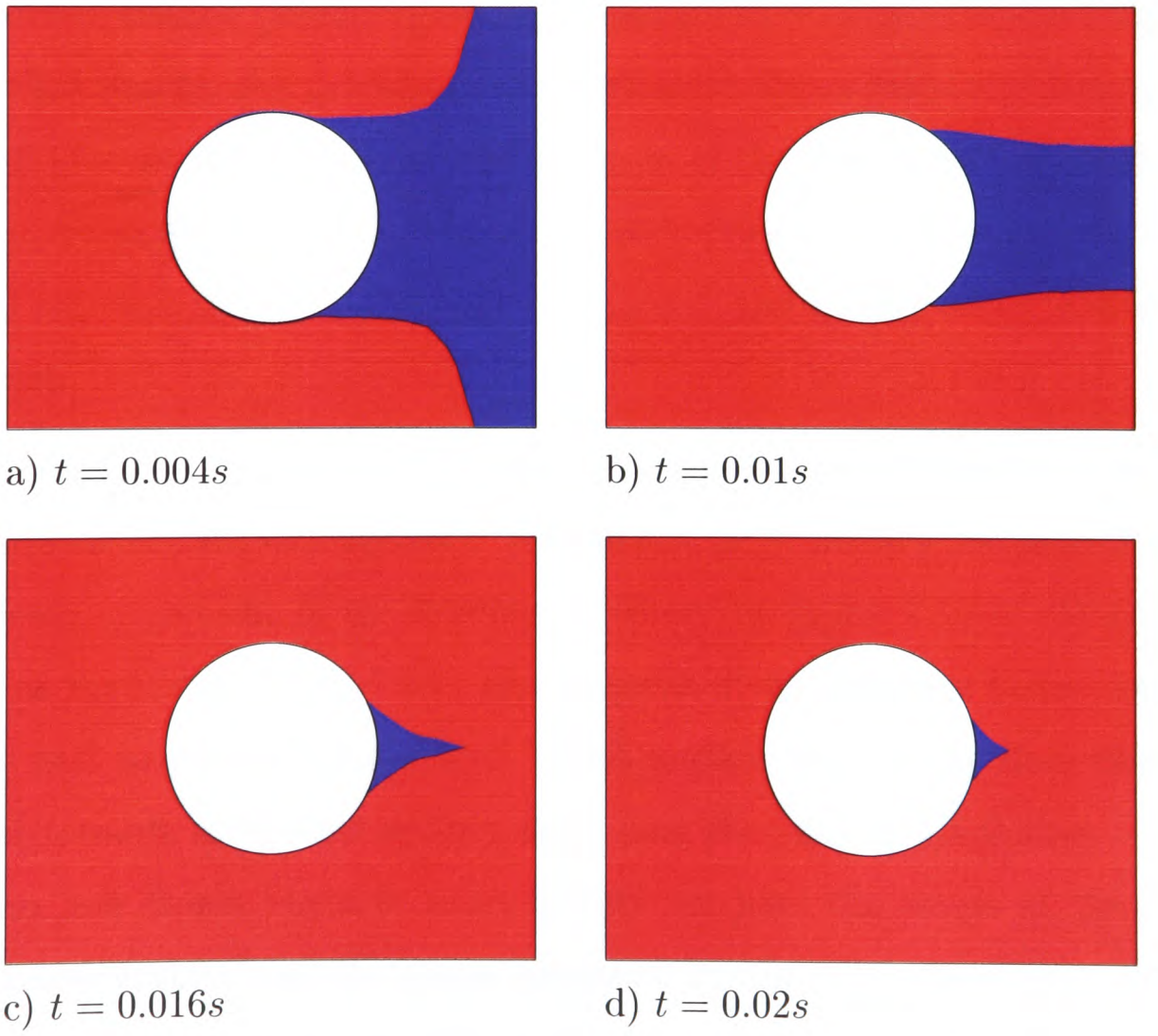

Figure 5.12: Free surface flow of a Newtonian fluid past a solder joint in 2D planar geometry with SEA.

Test 2 - Viscoelastic flow past 1 solder joint 2-D: SEA algorithm

In Test 2 the simulation was repeated for a viscoelastic material. The relaxation time, taken from Evans et al. [68], is given in Table 5.2. Figure 5.13 shows the movement of the interface over time. The time intervals at which the flow front has been captured are the same in both Figures 5.12 and 5.13. The pressure and stress contours at $t = 0.02s$ are shown in Figure 5.14. For the viscoelastic fluid the flow shows normal and shear stress development with high stress boundary layers appearing close to the solder joint wall. The Newtonian model does not have the capability to capture these features.

Using the same computational resources as in Test 1 the CPU time was $2275s$.

Test 3 - Newtonian flow past 1 solder joint 2-D: LSM algorithm

In this section Newtonian flow was simulated using the LSM technique in order to include surface tension effects. However, to be able to directly compare LSM results with the SEA results, the first simulation with LSM was carried out without surface tension effects. In this simulation the progress of the flow front appeared exactly like the SEA result in Figure 5.12 at $t = 0.004s$. For $t > 0.004s$ with LSM the flow fronts did not close in behind the joint as it moved past it, instead continued to flow straight out.

The next simulation was carried out with surface tension implemented. The contact angle at the solder joint wall was set to zero and at the symmetry planes to 90 degrees. The transient movement of the interface is shown in Figure 5.15 at the same time intervals as Figures 5.12 and 5.13. The progress of the interface in the first frame compares well to that of Figure 5.12. With surface tension the flow fronts show movement towards each other as they move past the joint at $t > 0.004s$. However as the two flow fronts begin to meet behind the joint the shape of the interface deviates considerably from the shape produced by the SEA algorithm. This is an erroneous result since both algorithms should produce similar flow fronts. In the level set method the flow front is at the zero level set which lies within the prescribed interface and the values of the scalar marker outside the interface are re-calculated

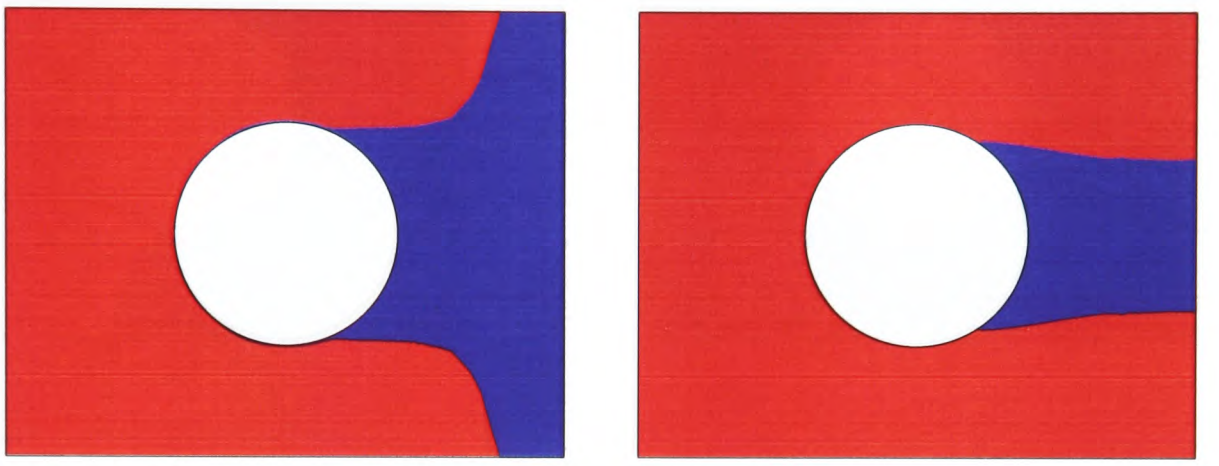

a) $t = 0.004s$ b) $t = 0.01s$

c) $t = 0.016s$ d) $t = 0.02s$

Figure 5.13: Free surface flow of a viscoelastic fluid past a solder joint in 2-D planar geometry with SEA.

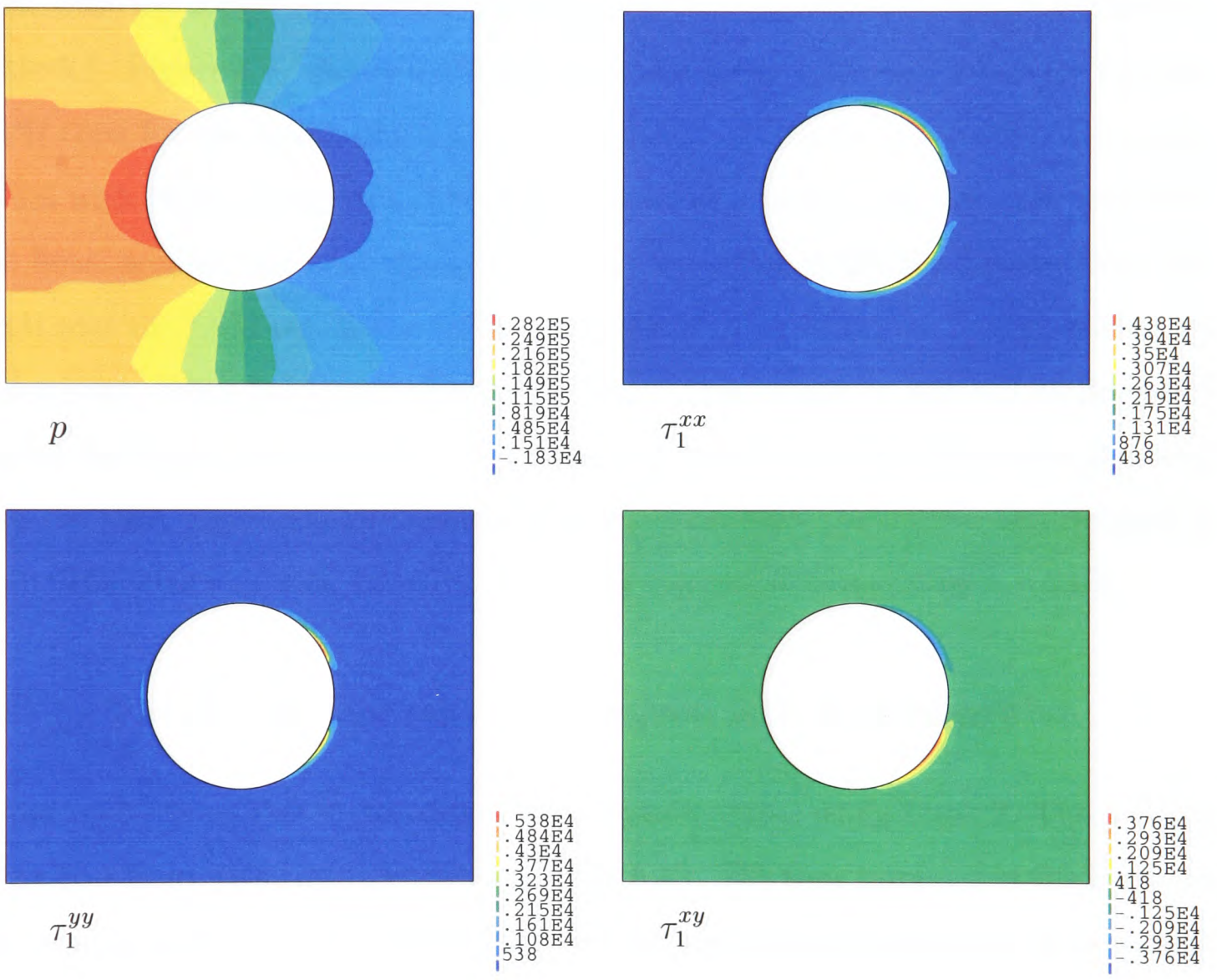

Figure 5.14: Pressure (p) and stress (τ_1^{ij}) contours of a viscoelastic fluid past a solder joint in 2-D planar geometry with SEA at $t = 0.02s$.

with respect to the zero level set. This geometry has a short downstream channel and at $t = 0.01s$ the flow front of the fluid has reached the outlet which places some parts of the zero level set outside the computational domain. This could be an explanation for the misshapen flow front with the LSM algorithm.

In order to test this hypothesis a further simulation was carried out by extending the downstream channel length (Mesh 2) from $150\mu m$ to $900\mu m$. Figure 5.16 shows the mesh with the longer downstream channel and the dimensional details are given in Table 5.1. Figure 5.17 shows a series of results showing the position of the interface (CPU time for the simulation up to $t = 0.04s$ was 42.62h on a 466 MHz Dec Alpha EV5.6 with 1Gb of memory). The shape of the flow front is smooth and symmetric and flows around and past the solder joint. A notable difference between the SEA result and the LSM result now is the time taken by the fluid to close in behind the solder joint. With the longer channel the fluid takes longer to isolate the air bubble behind the solder joint with the LSM technique than it took on the shorter geometry with the SEA algorithm for Newtonian flow. With SEA the bubble was isolated by $t = 0.016s$ where as with LSM on the longer channel it happens by $t = 0.02s$.

Test 4 - Viscoelastic flow past 1 solder joint 2-D: LSM algorithm

Following on from Test 3 viscoelastic flow was simulated using Mesh 2. The progress of the flow front with time is shown in Figure 5.18. The time intervals in the figure are the same as in Figure 5.17. When Figures 5.17 and 5.18 are compared the two flows appear to travel the same distance initially ($t \leq 0.1s$) and then the flow fronts of the Newtonian fluid closes in behind the solder joint faster than those of the viscoelastic fluid. Figure 5.19 shows the normal and shear stress buildup in the region of the joint wall. The contour plots indicate very high stress values with the τ_1^{xx} value being the highest.

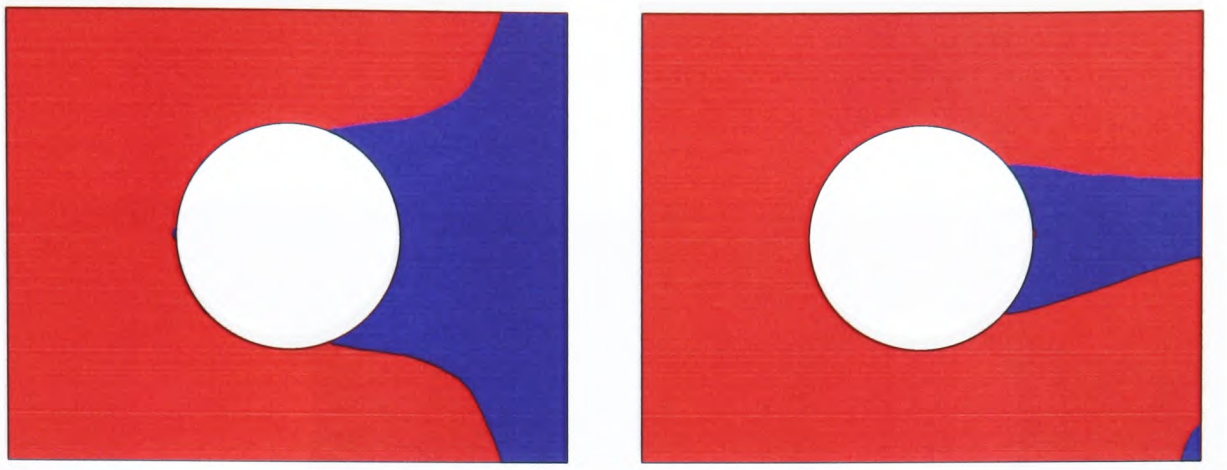

a) $t = 4E - 3s$ b) $t = 1E - 2s$

c) $t = 1.6E - 2s$ d) $t = 2E - 2s$

Figure 5.15: Free surface flow of a Newtonian fluid past a solder joint in 2D planar geometry with LSM.

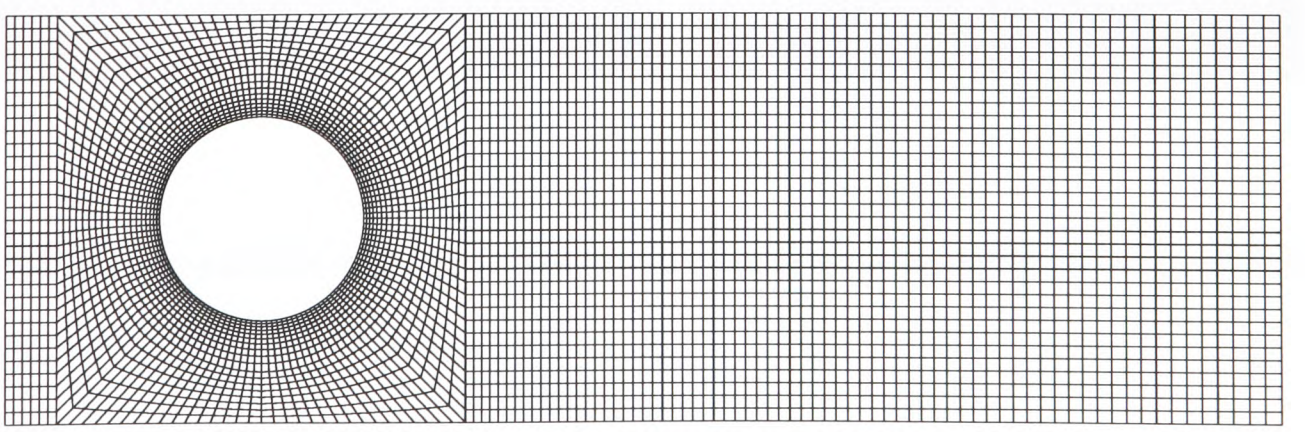

Figure 5.16: Mesh 2: 2-D mesh for one solder joint with extended exit channel length.

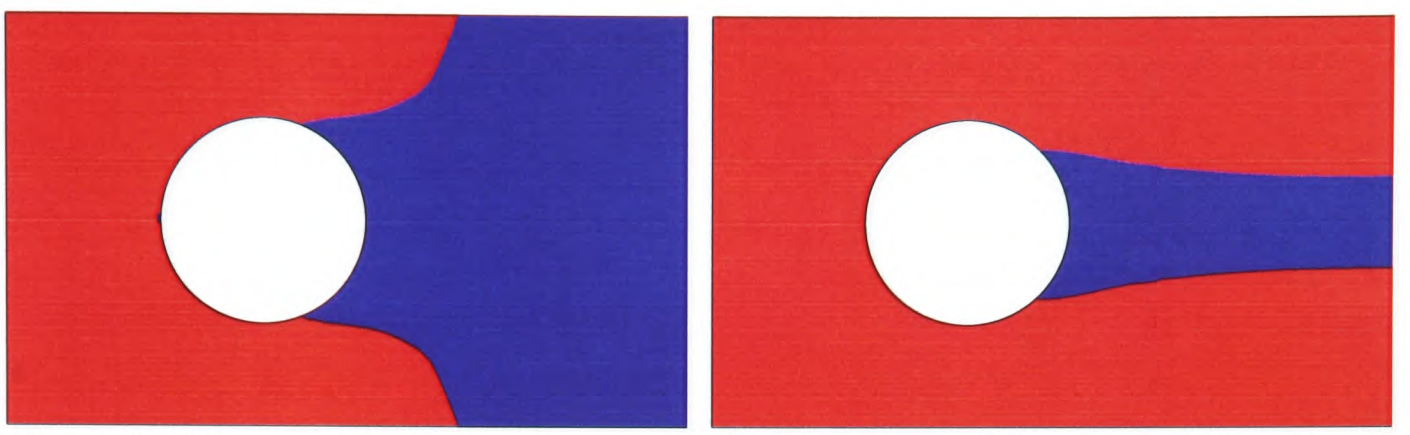

a) $t = 0.004s$ b) $t = 0.01s$

c) $t = 0.016s$ d) $t = 0.02s$

e) $t = 0.022s$ f) $t = 0.03s$

Figure 5.17: Free surface flow of a Newtonian fluid past a solder joint in 2D planar geometry with LSM on Mesh 2.

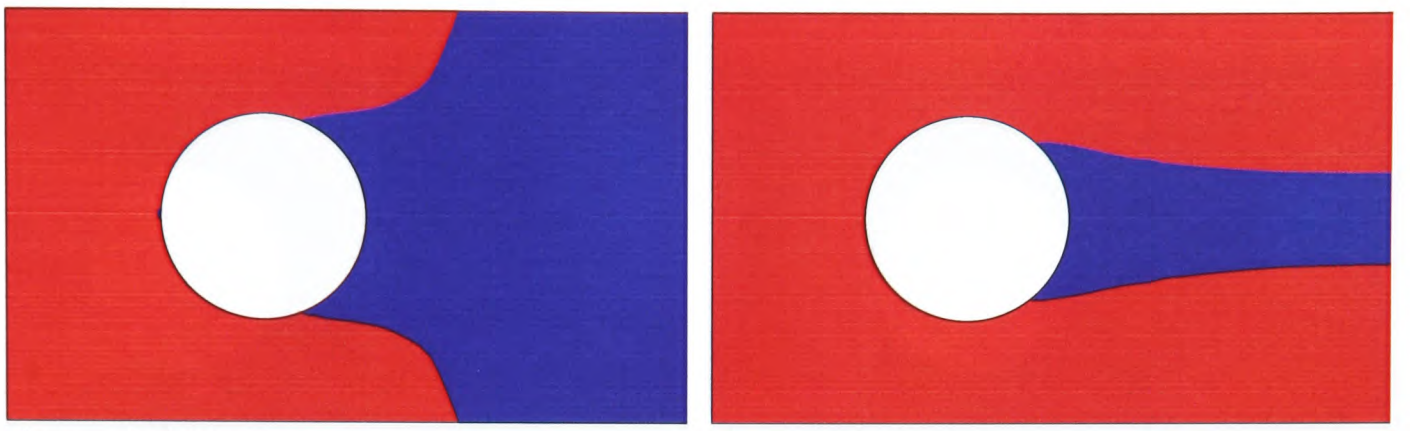

a) $t = 0.004s$ b) $t = 0.01s$

c) $t = 0.016s$ d) $t = 0.02s$

e) $t = 0.022s$ f) $t = 0.03s$

Figure 5.18: Free surface flow of a viscoelastic fluid past a solder joint in 2D planar geometry with LSM on Mesh 2.

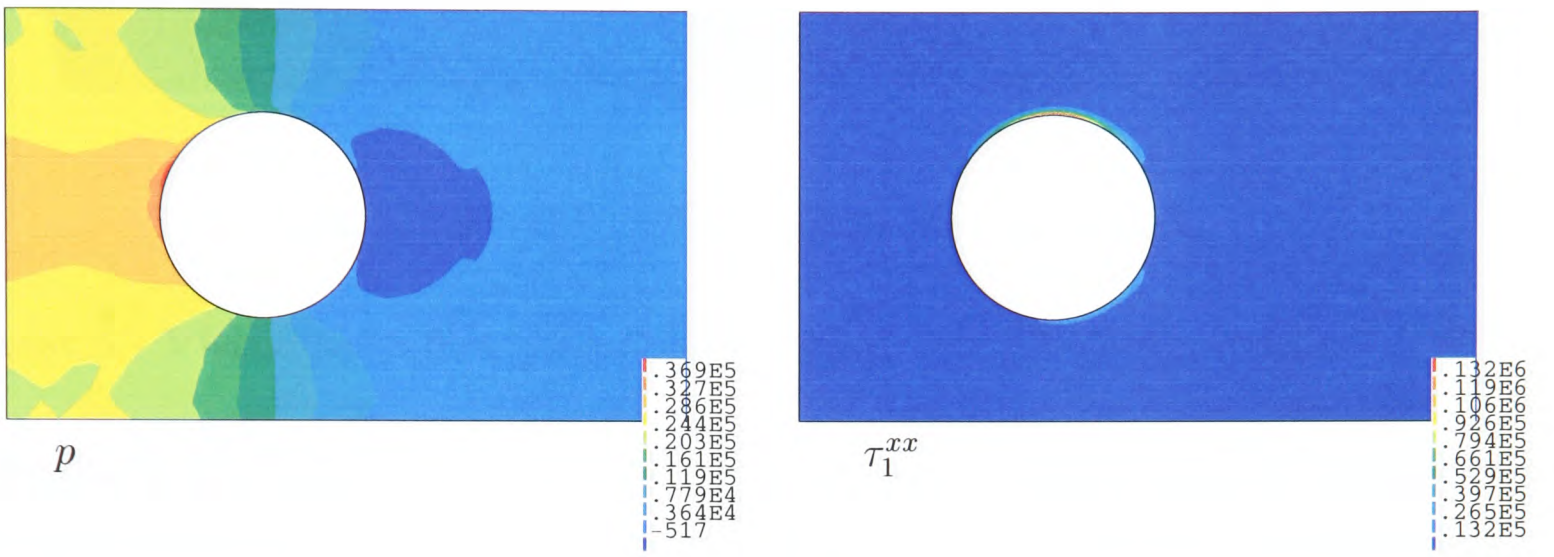

Figure 5.19: Pressure and stress of viscoelastic fluid past a solder joint in 2-D planar geometry with LSM on Mesh 2.

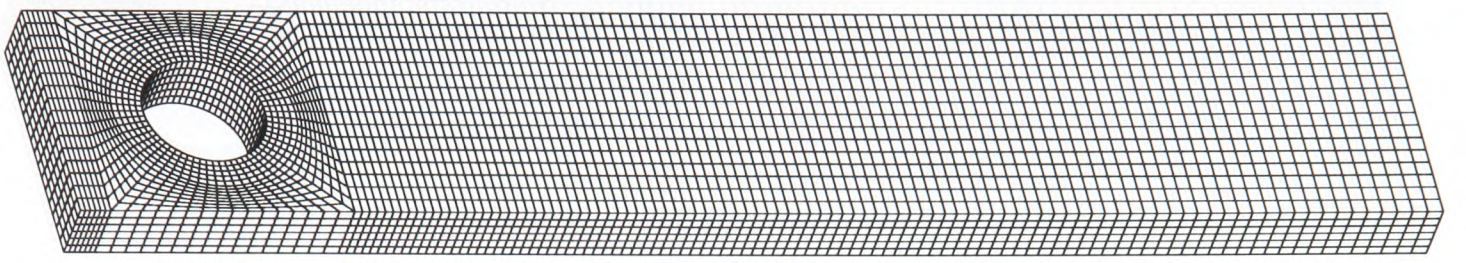

Figure 5.20: Mesh 4:3-D mesh for one solder joint.

Test 5 - Viscoelastic flow past 1 solder joint 3-D: LSM algorithm

Having simulated flow on 2-D geometries, the testing was extended to a 3-D geometry in this simulation. To carry out 3-D simulations the element density of Mesh 2 was reduced and the 2-D mesh was swept by $100\mu m$ (6 elements) in the direction of the third dimension creating a 3-D mesh which is referred to as Mesh 3. The details of the the new mesh are given in Table 5.1 along with the length of the geometry in the 3rd dimension (L_h). The inlet velocity u is set to $0.05ms^{-1}$. In this simulation the flow fronts reached the end of the channel before meeting up behind the solder joint. Since a shorter channel gave rise to a misshapen flow feature in Test 3 (see Figure 5.15) the channel length of the 3-D geometry was extended further by $1000\mu m$. This new 3-D mesh is Mesh 4 in Table 5.1 and is shown in Figure 5.20. A timestep of 1×10^{-5} was used for the simulation. The results are shown in Figure 5.21 at selected time intervals. The simulation took seven days on a 433MHz Dec Alpha EV5.6 64-bit CPU.

With this mesh it was possible to observe the meeting of the flow fronts behind the joint. In addition an important observation can be made from Figure 5.21 d). In the 2-D simulations the air bubble captured behind the solder joint clung to the wall with time. However in the 3-D case it can be seen that the air bubble captured behind the solder joint gradually gets detached from the wall and moves downstream with time. Figure 5.22 shows the pressure and stress contours at $t = 0.03s$. The stress contour plots show high stress build up on the joint wall. The τ_1^{xx} contours clearly indicate the build up of stress layers on the joint walls.

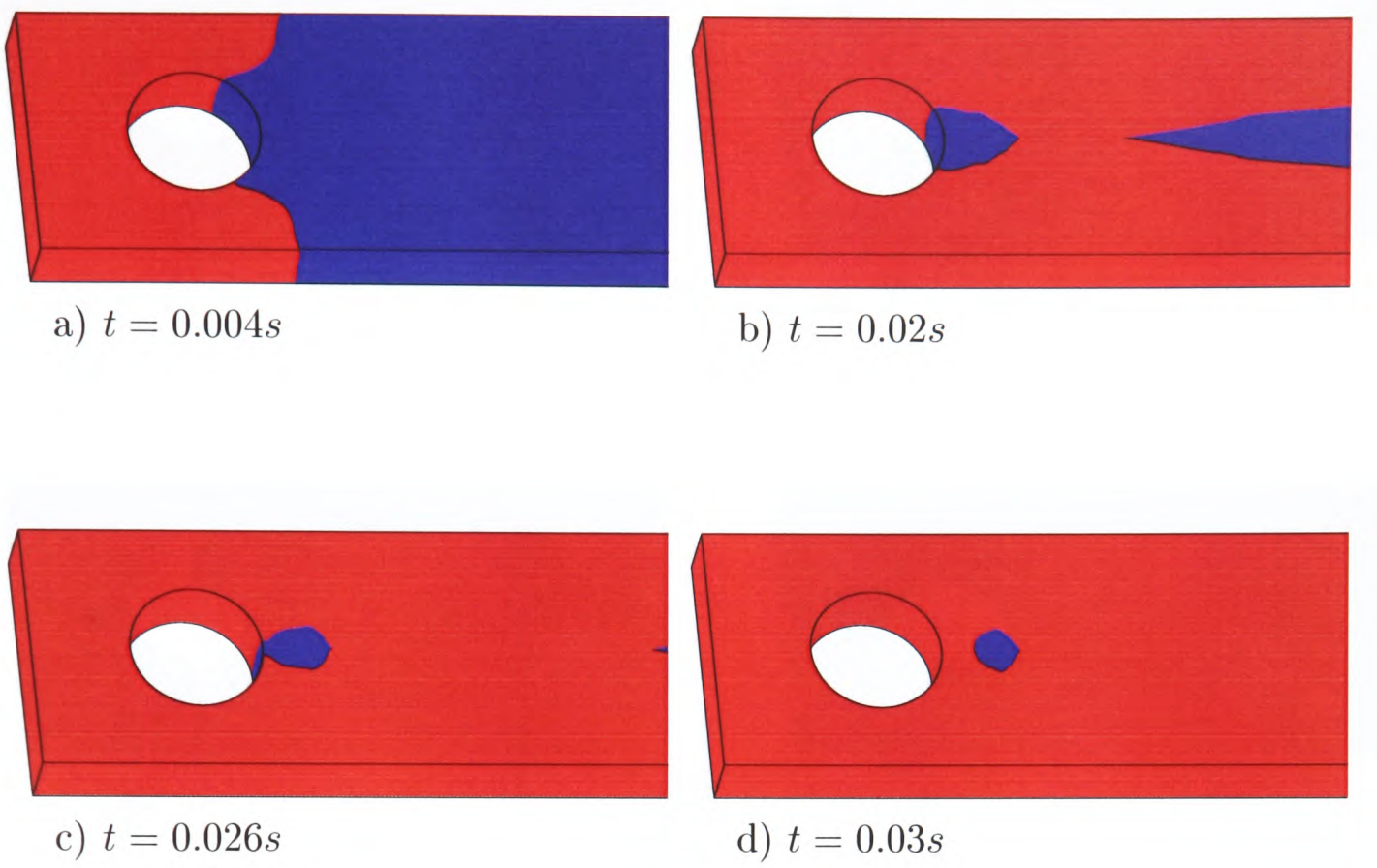

Figure 5.21: Viscoelastic fluid past a solder joint in 3-D geometry with LSM and $u = 0.05ms^{-1}$.

To investigate this result a further simulation was carried out with a higher inlet velocity of $0.1ms^{-1}$. A timestep of 1×10^{-7} had to be used in this case. The movement of the flow was similar to the previous case and as the two flow fronts met behind the joint it captured the void and with time the fluid continued to creep along the wall indicating that this void too would get pushed away from the wall as with the previous simulation. However the size of the void began to reduce in size before the fluid creeping along the joint wall could push the void away from the wall. This can be seen from Figure 5.23 which shows the movement of the flow front and the formation of the void at four consecutive time intervals at $u = 0.1ms^{-1}$. Even though there was some numerical diffusion with the first simulation it was not as significant as with the second simulation. The CPU time for the second simulation was four months on a 433MHZ Dec Alpha EV5.6 64-bit CPU.

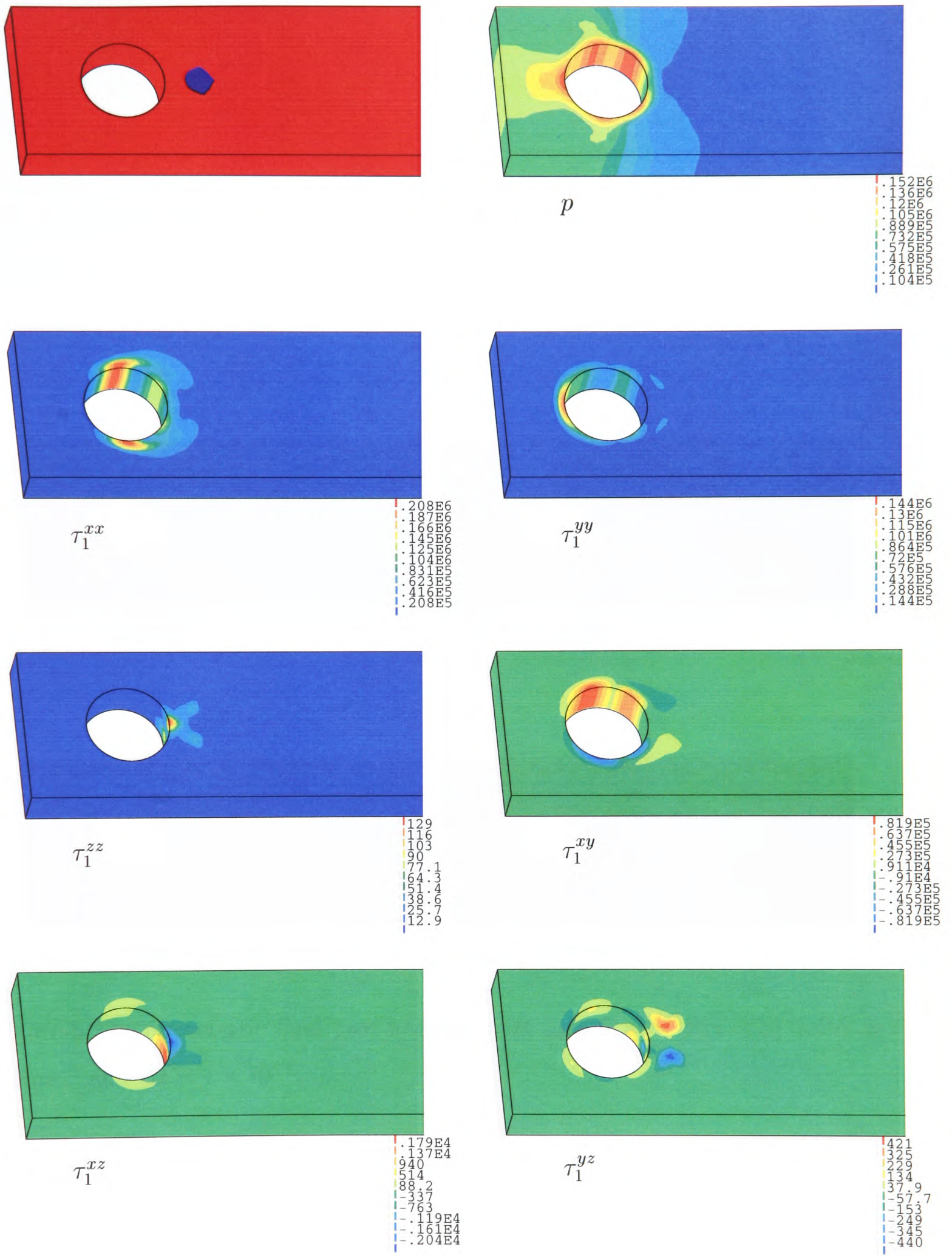

Figure 5.22: Viscoelastic fluid past a solder joint in 3-D geometry with LSM and $u = 0.05ms^{-1}$ at $t = 0.3E-1s$.

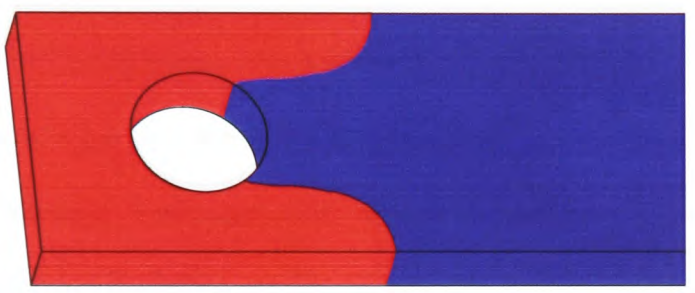

a) $t = 0.003s$

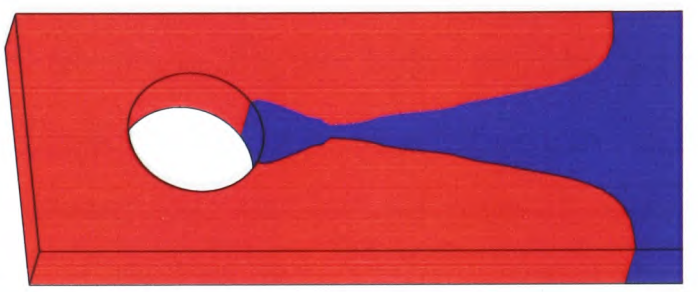

b) $t = 0.006s$

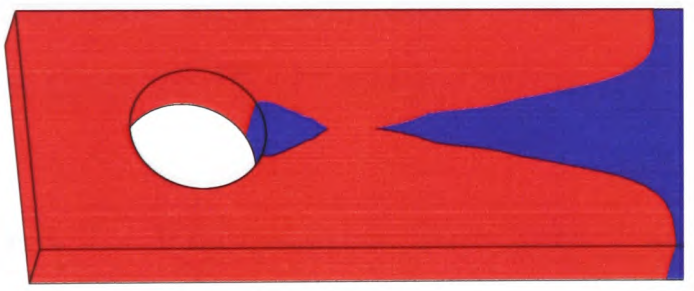

c) $t = 0.0066s$

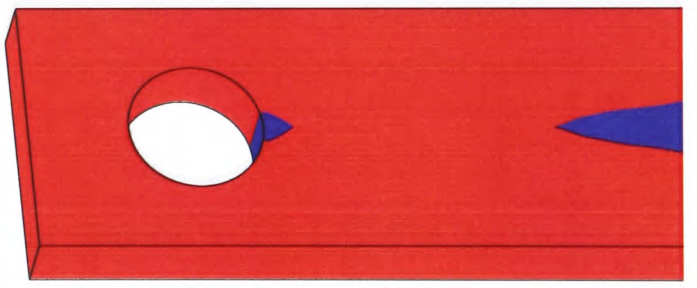

d) $t = 0.009s$

Figure 5.23: Viscoelastic fluid past a solder joint in 3-D geometry with LSM: $u = 0.1ms^{-1}$ and $\Delta t = 1 \times 10^{-7}$.

Test 6 - Viscoelastic flow past 2 solder joints 2-D: LSM algorithm

The underfill process involves the encapsulation of an array of solder joints. Therefore as a next step in this investigation the testing was extended to the simulation of flow past two solder joints in 2-D. The schematic of the flow domain is shown in Figure 5.24. The first simulation involved a 2-D geometry where the element configuration around each 2-D joint is similar to that of Mesh 1 (Figure 5.11). The downstream channel length was chosen to be sufficiently long enough for fully developed flow at the exit. The mesh used in this test, Mesh 5 is shown in Figure 5.25 (see Table 5.1 for details).

The transient viscoelastic flow results are shown in Figure 5.26. In this figure the flow can be seen to move past the first joint capturing an air bubble behind it whilst moving towards the second joint. As it moves past the second joint it captures a second bubble in front of the second joint and then finally a third bubble behind the second joint. The air bubbles continue to cling to the walls of the joints with time.

Figure 5.27 show the pressure and stress contours at $t = 0.036s$. As expected the plots show very high stress behaviour on the joint walls. The highest stress layers are those of the τ_1^{xx} normal stress.

Test 7 - Viscoelastic flow past 2 solder joints 3-D: LSM algorithm

To carry out 3-D simulations the 2-D mesh was swept in the third direction by $100\mu m$(Mesh 6). For 3-D simulations a longer downstream channel length of $1525\mu m$ was used. The mesh (Mesh 6 see Table 5.1) used for the simulation is shown in Figure 5.28.

This simulation diverged before it reached completion. An instability set in through the pressure when the fluid met the 1st joint. This was observed as the pressure residual began to fluctuate. This gradually affected the velocity fields and with time the instability in the velocities affected the stresses. The results obtained before divergence are shown in Figure 5.29.

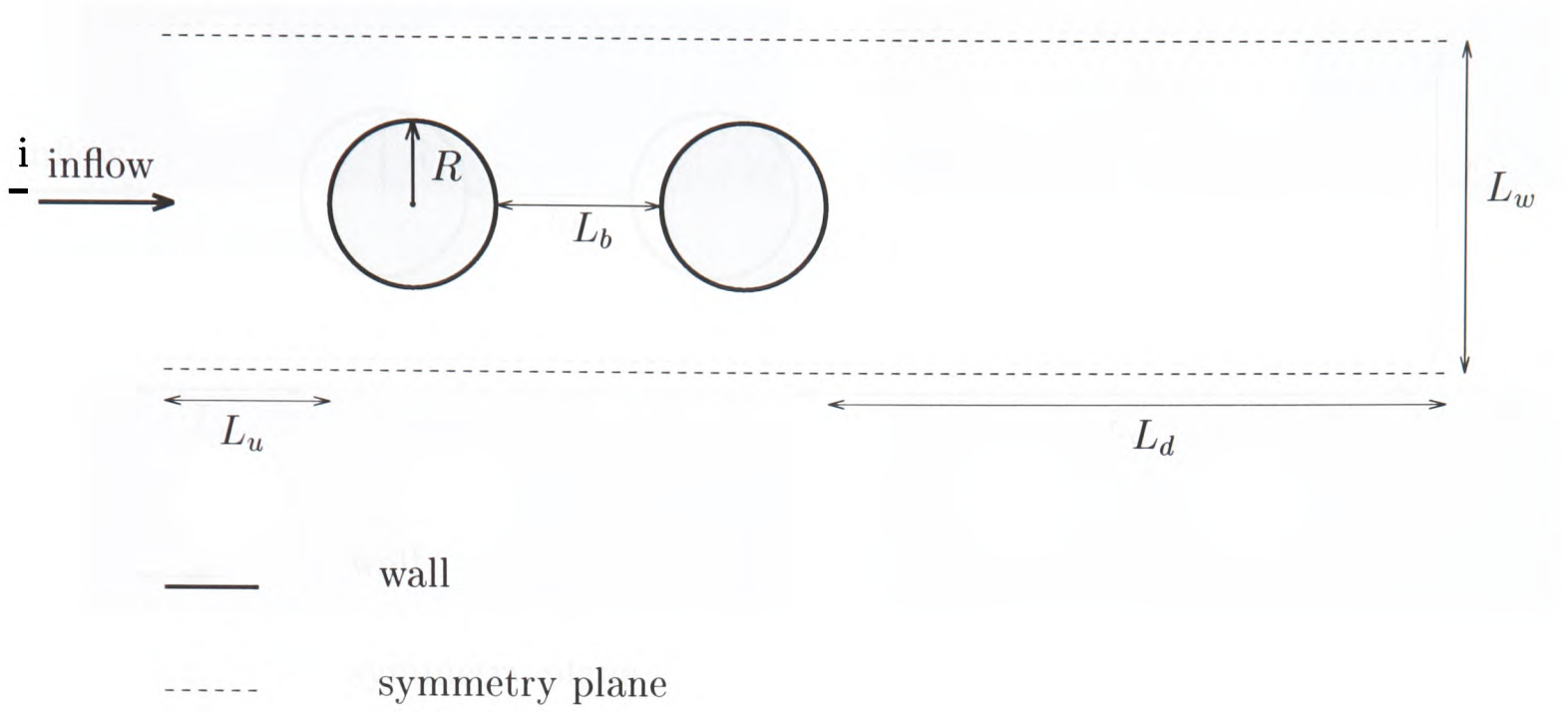

Figure 5.24: The flow past a two solder joints geometry.

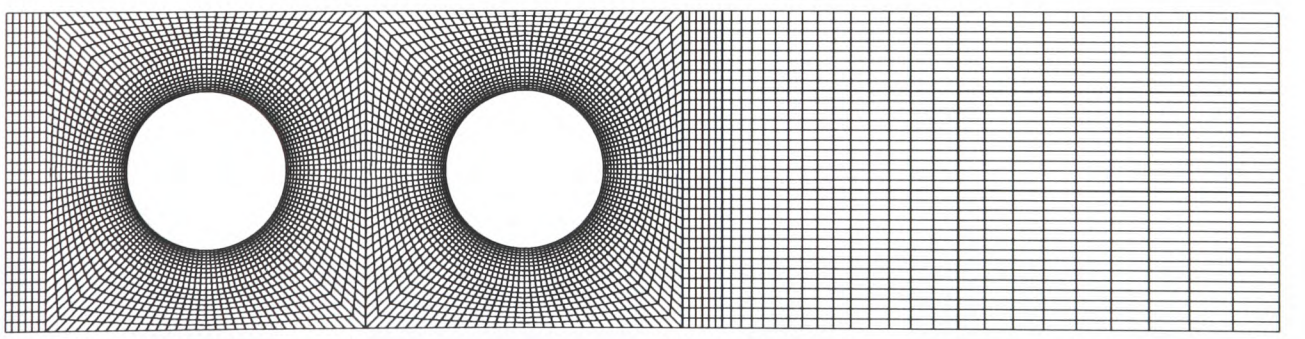

Figure 5.25: Mesh 5:2-D mesh for two solder joints.

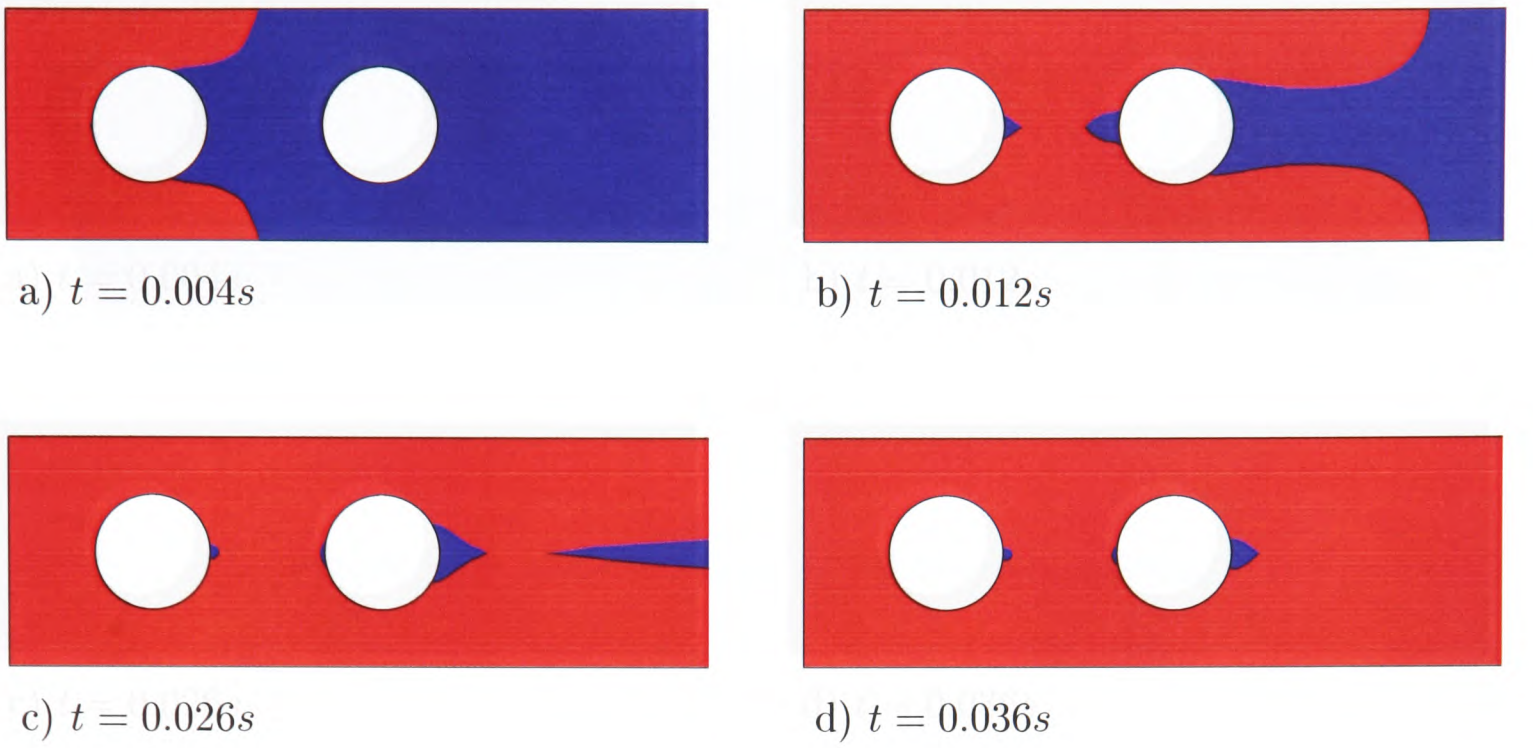

a) $t = 0.004s$ b) $t = 0.012s$

c) $t = 0.026s$ d) $t = 0.036s$

Figure 5.26: Viscoelastic flow past two solder joints in a 2D geometry with LSM and $u = 0.05ms^{-1}$.

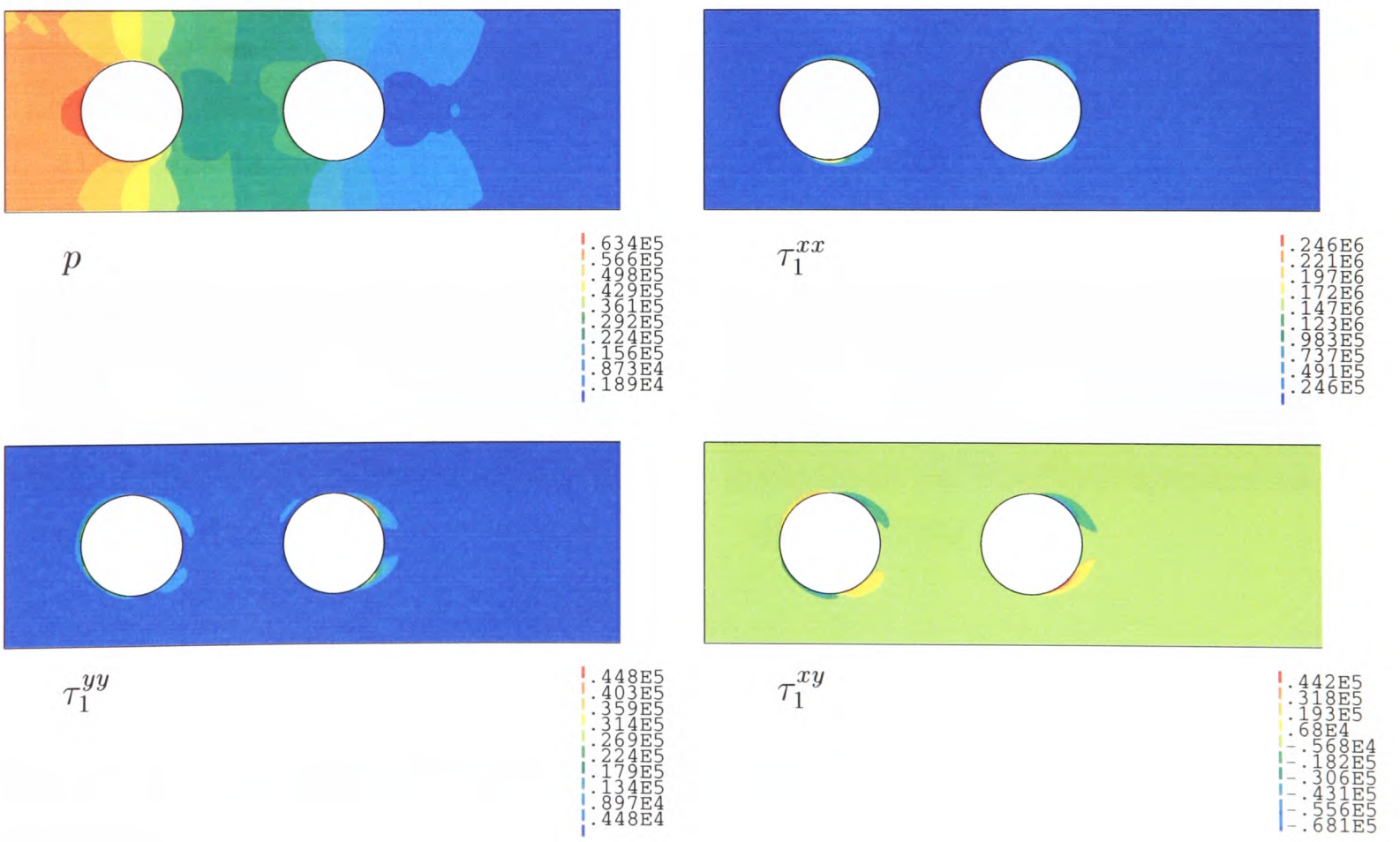

Figure 5.27: The pressure and stress contours at $t = 0.036s$.

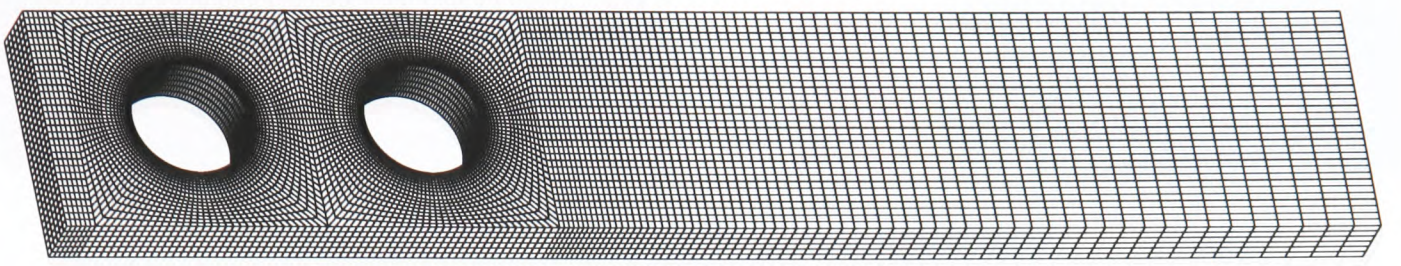

Figure 5.28: Mesh 6:3-D mesh for two solder joints.

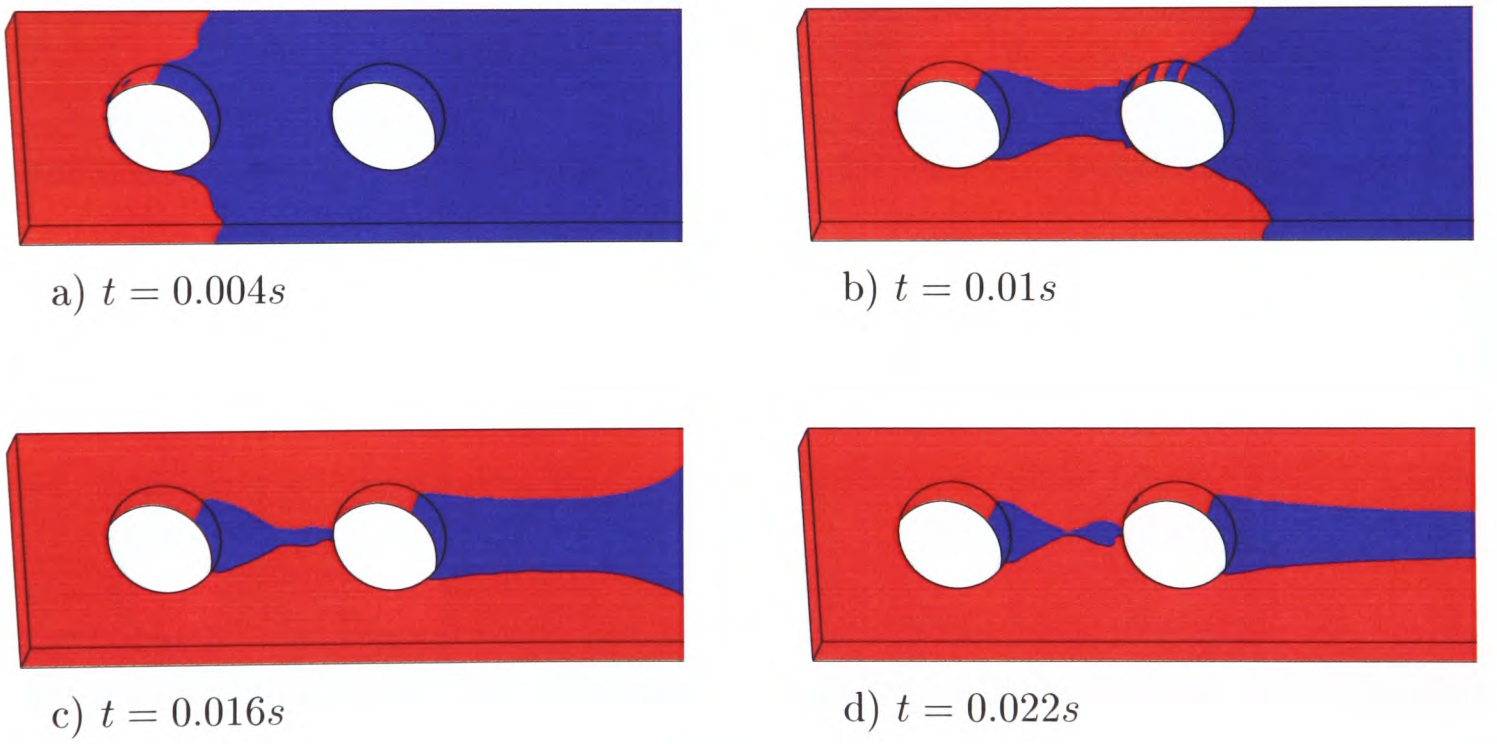

Figure 5.29: Viscoelastic flow past two solder joints in 3D geometry with LSM and $u = 0.05ms^{-1}$.

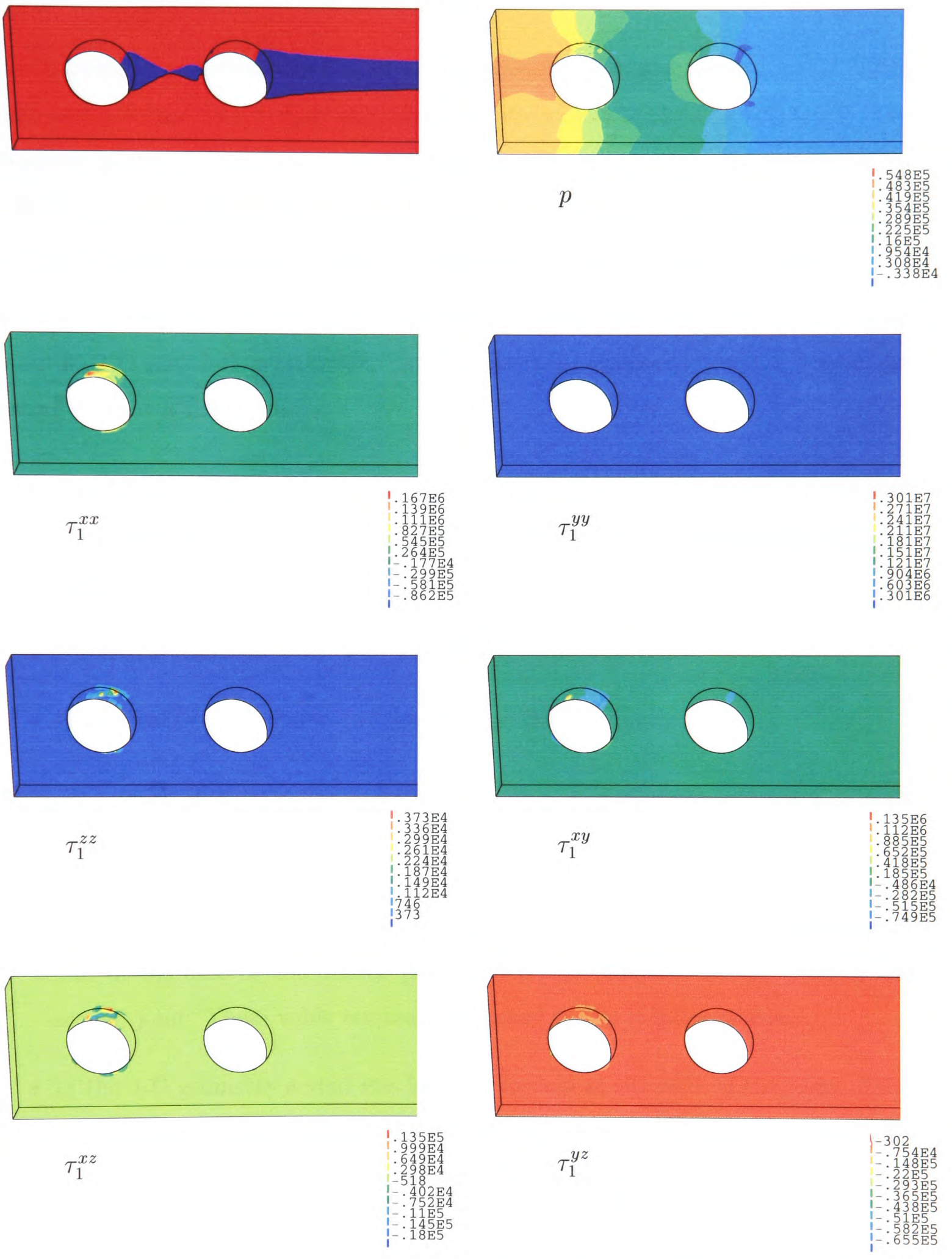

Figure 5.30: Pressure and stress contours at $t = 0.022s$ 3-D geometry with LSM and $u = 0.05ms^{-1}$.

5.5.2 Summary of Injection Flow

In the preceding sections results were presented for the flow around solder joints modelled with the free surface viscoelastic algorithms developed in this work. The objective of the exercise was to model injection flow and explore the predictive capability of the algorithm. For this experiment it was assumed that underfill material had no filler in it and that it could be represented by the Oldroyd-B model.

A series of tests were carried out which involved flow past single as well as double joints in 2-D and 3-D geometries. Some difficulties were encountered during the testing process which included:

- The LSM appeared to be more sensitive to channel length than the SEA and unrealistic flow fronts were obtained with LSM when the downstream channel length was too short.
- Numerical diffusion when very small time steps were used.
- Numerical divergence for 3-D flow past a double joint.

However, in each of the tests the algorithm was able to predict the formation of voids in the underfill material.

- In the 2-D geometries the voids were attached to the backs of the solder joints, and in the case of the double joint a void was detected on the front of the second joint. These voids remained attached to the joints over time.
- In the 3-D geometry a void was initially formed at the back of the joint. However the algorithm predicted the detachment of the void from the joint over time and this void was then observed to move downstream.

In addition the viscoelastic algorithm was able to predict the normal stress behaviour of the underfill material which would not have been possible with a Newtonian model. It was observed that high stresses occured on the solder joint wall.

Meshes	L_b (μm)	L_h (μm)	L_n (μm)	L_o (μm)	L_i (μm)	*elements*
Mesh 1	79.98	300	100	17.98	29.98	6880
Mesh 2	34.99	300	100	8.99	14.99	3440

Table 5.3: Meshes for the jetting experiment.

Density of water	$1000 kgm^{-3}$
Viscosity of water	$0.1137 \times 10^{-2} Pas$
Surface tension of water	$0.1 Nm^{-1}$
Density of air	$1.0 kgm^{-3}$
Viscosity of air	$0.1776 \times 10^{-4} Pas$

Table 5.4: Material properties for the water droplet.

5.5.3 Jetting of Viscoelastic Fluids

The second application that was investigated was the jetting of viscoelastic fluids. Once again a series of numerical experiments were carried out beginning with simulations on a 2-D geometry and extending to a 3-D axi-symmetric geometry.

Test 1 - Jetting of Newtonian material on a 2-D geometry

The geometry of the 2-D flow domain in 2-D is given in Figure 5.31.

The mesh (Mesh 1) used for the 2-D simulation is shown in Figure 5.32. The mesh

Density of polymer	$1300 kgm^{-3}$
Newtonian contribution of viscosity of polymer (η_2)	$4.0 Pas$
Viscoelastic contribution of viscosity of polymer (η_1)	$0.996 Pas$
Surface tension of viscoelastic fluid (σ_1)	$70 Nm^{-1}$
Relaxtion time of viscoelastic fluid (λ_1)	$0.1 s$
Density of air	$1.0 kgm^{-3}$
Viscosity of air	$0.1776 \times 10^{-4} Pas$

Table 5.5: Material properties for the viscoelastic droplet.

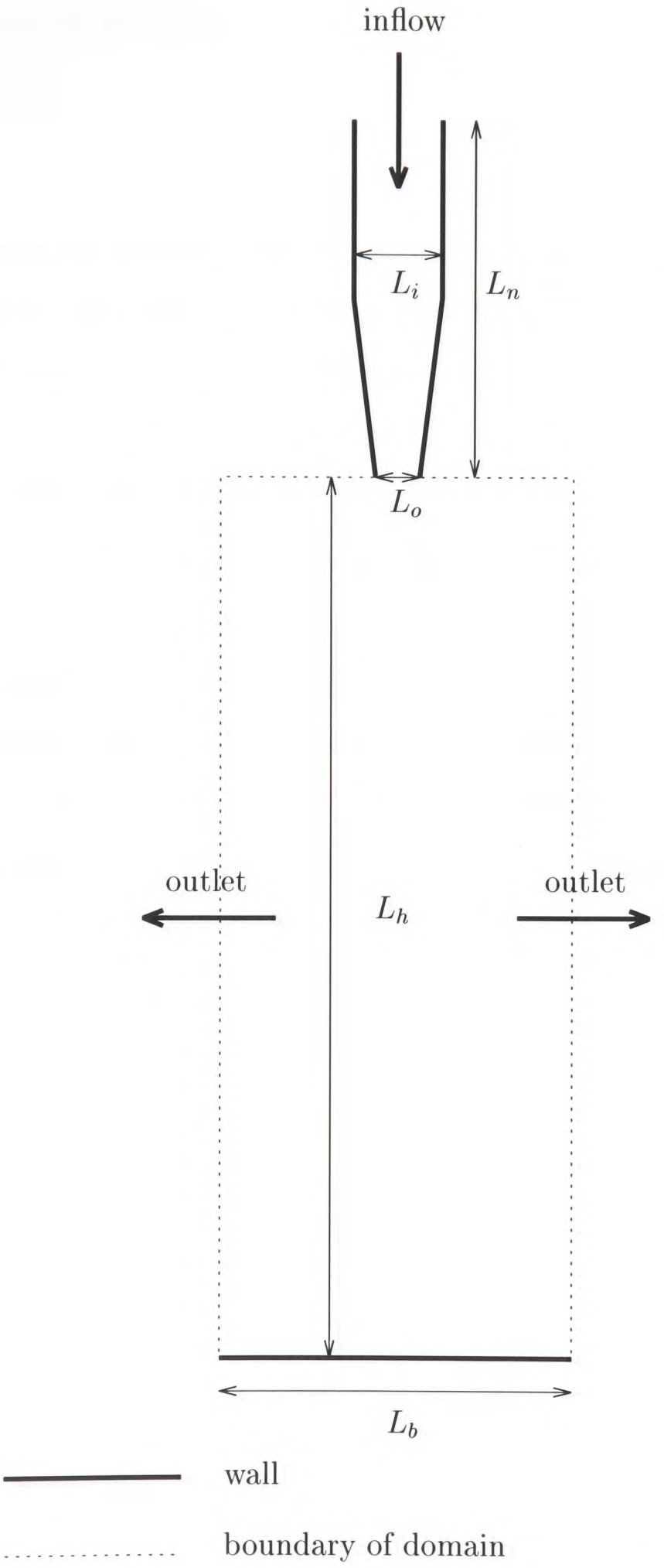

Figure 5.31: The 2-D geometry for the nozzle.

details are given in Table 5.3. The initial and boundary conditions for the simulation are as follows: At the inlet

$$\begin{aligned} u &= 0, \\ v &= a\cos\theta, \\ w &= 0. \end{aligned} \tag{5.13}$$

At the outlets the pressure was set to zero. No slip condition was imposed on the nozzle walls for the velocities. A value of 5 was used for a the amplitude of the cos wave and θ varies from zero to $\pi/2$ over a period of $10\mu s$. The velocity pulse was turned on for a period of $10\mu s$ and stopped. The fluid is Newtonian and the material properties used in this test are given in Table 5.4.

In Figure 5.33 the formation of the water droplet is shown at successive time intervals. In frame a) at $t = 2\mu s$ the fluid flows out of the nozzle and at $t = 10\mu s$ it has begun to neck giving shape to a drop. At $t = 15\mu s$ the necking continues with the neck getting slimmer while the bulb gets larger and finally at $t = 21\mu s$ a single drop is formed and is seen falling vertically down. A timestep of 1×10^{-7} was used and the CPU time was $4728s$. The simulation was carried out on one node of a 5 Alpha server E545 system where each system contains four 1GHz CPUs and 4Gb of memory.

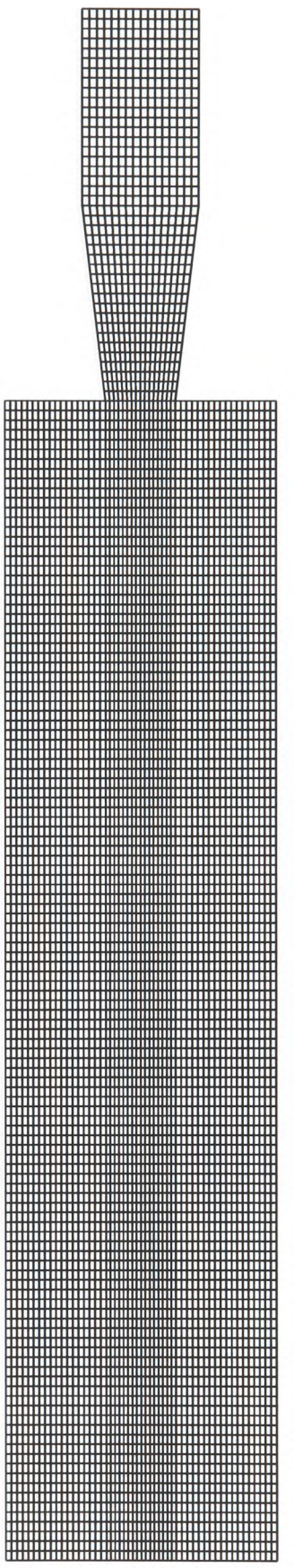

Figure 5.32: 2-D mesh for the jetting problem.

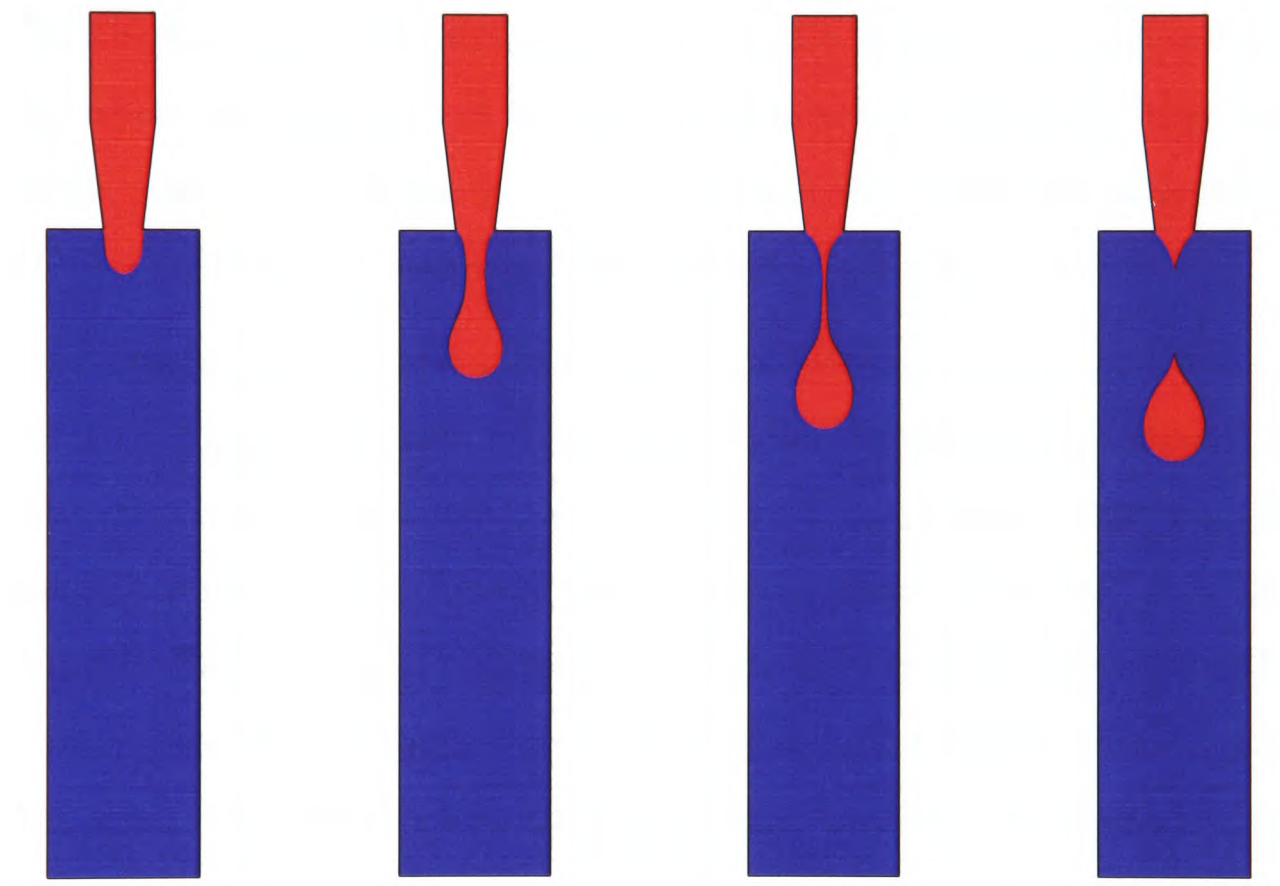

a) $t = 2\mu s$ b) $t = 10\mu s$ c) $t = 16\mu s$ d) $t = 22\mu s$

Figure 5.33: Droplet formation on a 2-D planar geometry.

Test 2 - Axisymmetric jetting of Newtonian material

In Test 2 the jetting simulation is carried out on an axi-symmetric 3-D geometry. A schematic of the axi-symmetric flow domain is shown in Figure 5.34. The dimensional lengths of the geometry are given in Table 5.3 (Mesh 2). Figure 5.35 shows the mesh used. The initial and boundary conditions are the same as in the previous test. Additionally symmetry conditions are imposed on the symmetry plane. The inlet velocity pulse of half a cosine wave with amplitude 5 is turned on for $10\mu s$.

The results are presented in Figure 5.36 using the same time intervals as in Figure 5.33. In the axi-symmetric simulation the results show the formation of satellite droplets which was not evident in the 2-D simulation. The CPU time was $2133s$ on a single node of a 5 Alpha server E545 system with each system containing four 1GHz CPUs with 4Gb of memory. The timestep used was 1×10^{-7}.

A further simulation was carried out using a quarter cosine wave (ie $\theta = \pi/4$) as the inlet velocity. Figure 5.37 shows the results of that simulation presented at the same time intervals. In this case there is a difference in the formation of the main drop and the satellites both with reference to time as well as shape. With half a cosine wave at $t = 16\mu s$ the main drop has separated from the ejected fluid where as with quarter cosine wave it is still necking. By $t = 22\mu s$ with half a cosine wave all the ejected fluid has separated into drops forming one main drop and two satellite droplets. In the case of the quarter cosine wave at $t = 22\mu s$ the main drop has separated but the satellite drops are still in the process of being formed and in this case the necking points to three satellites being formed. The difference in the two simulations may be attributed to the slightly larger quantity of fluid that is released with the quarter cosine wave inlet impulse velocity.

Test 3 - Axisymmetric jetting of low density viscoelastic material

In Test 3 a simulation was carried out using material properties similar to water, with the viscoelastic model turned on in the algorithm. The velocity at the inlet was half a cosine wave pulse. The results are shown in Figure 5.38. There is no noticeable difference in the formation of the droplets in comparison to the water droplets (Figure

5.36). However with the viscoelastic model the fluid displays normal in addition to shear stress behaviour. Figures 5.39 and 5.40 show the normal stresses along with the pressure contours and the shear stresses at time intervals $t = 10\mu s$ and $t = 22\mu s$. For both time intervals it can be seen that the highest stress value is associated with the τ_1^{yy} normal stress in the region of the tip of the needle, ie. at the nozzle outlet where a singularity occurs in the geometry. In addition stress boundary layers build up along the nozzle wall. The CPU time was $2377s$ on a single node of a 5 Alpha server E545 system with each system containing four 1GHz CPUs with 4Gb of memory. The timestep used was 1×10^{-7}.

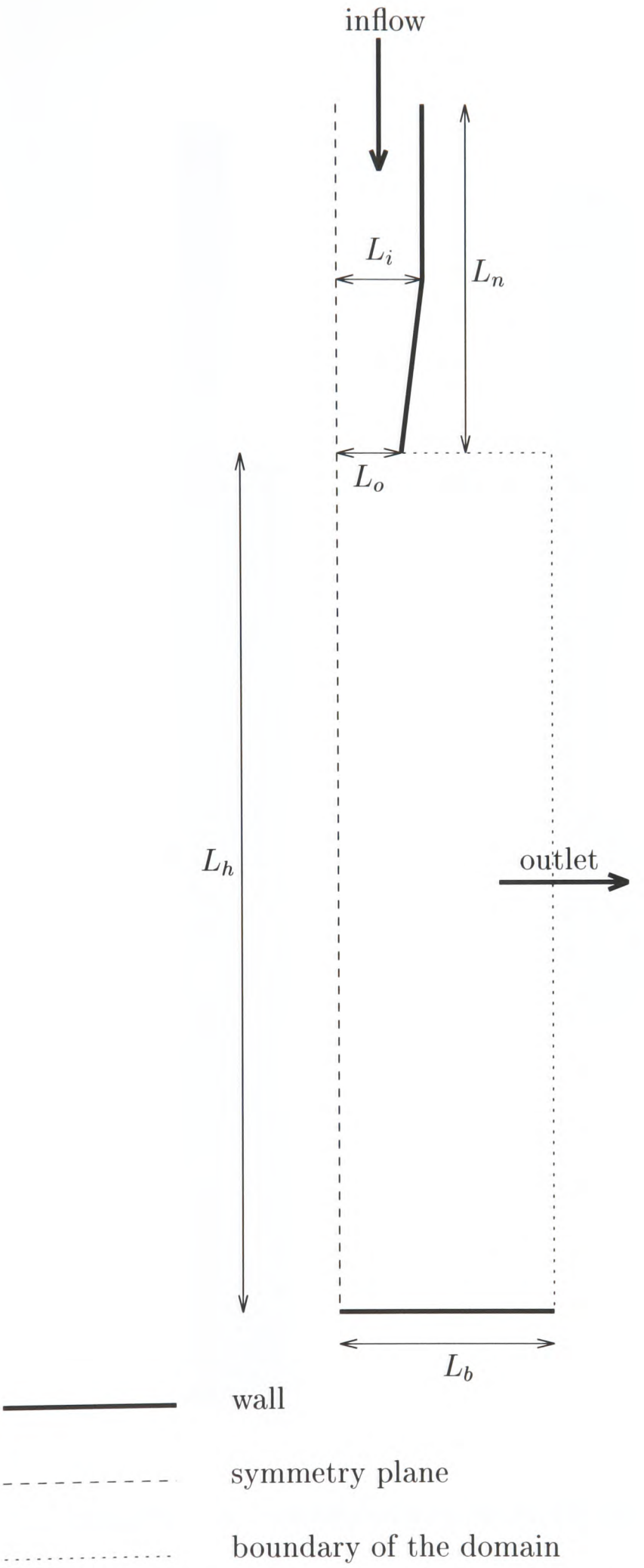

Figure 5.34: The axi-symmetric geometry for the nozzle.

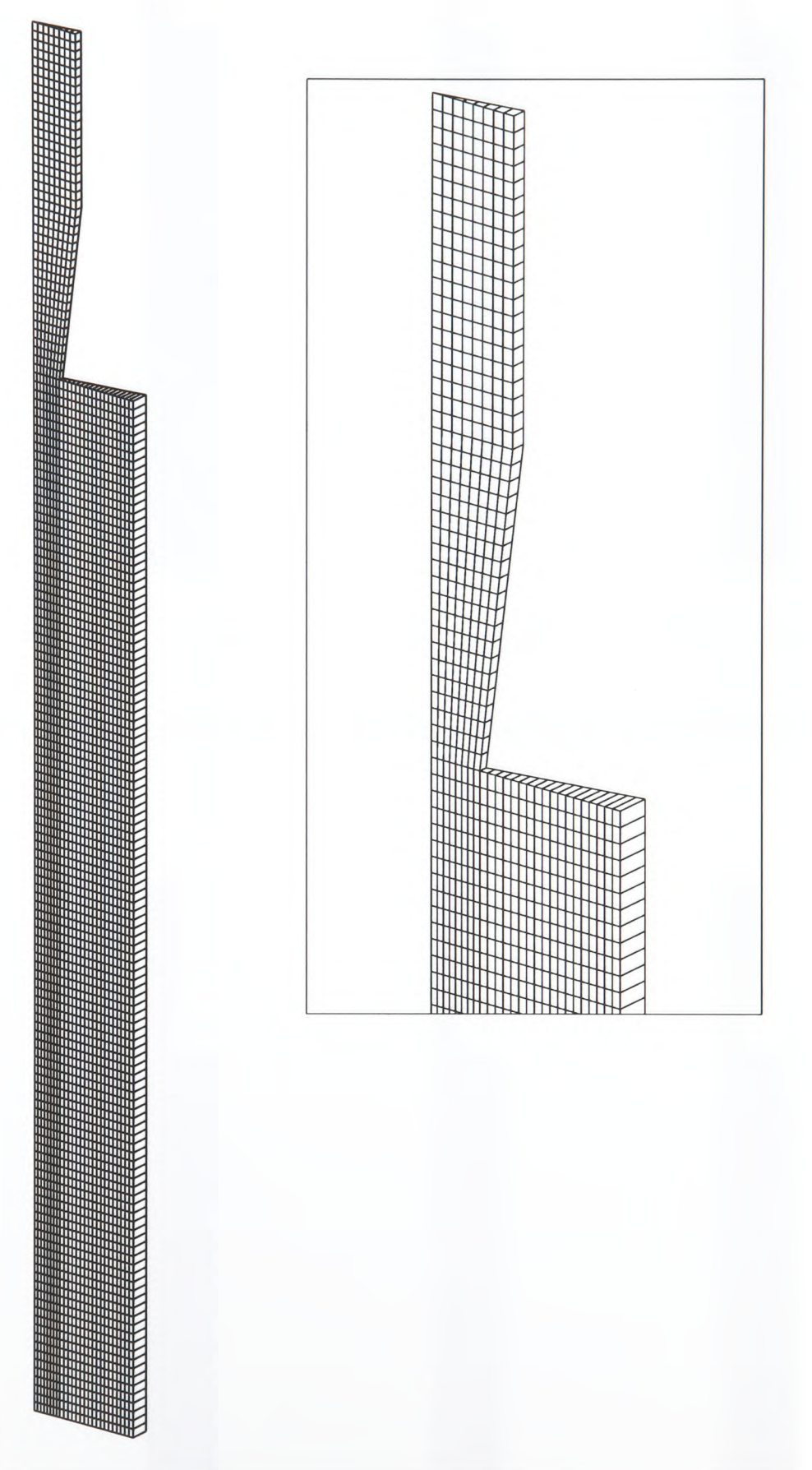

Figure 5.35: Axi-symmetric mesh for the jetting problem.

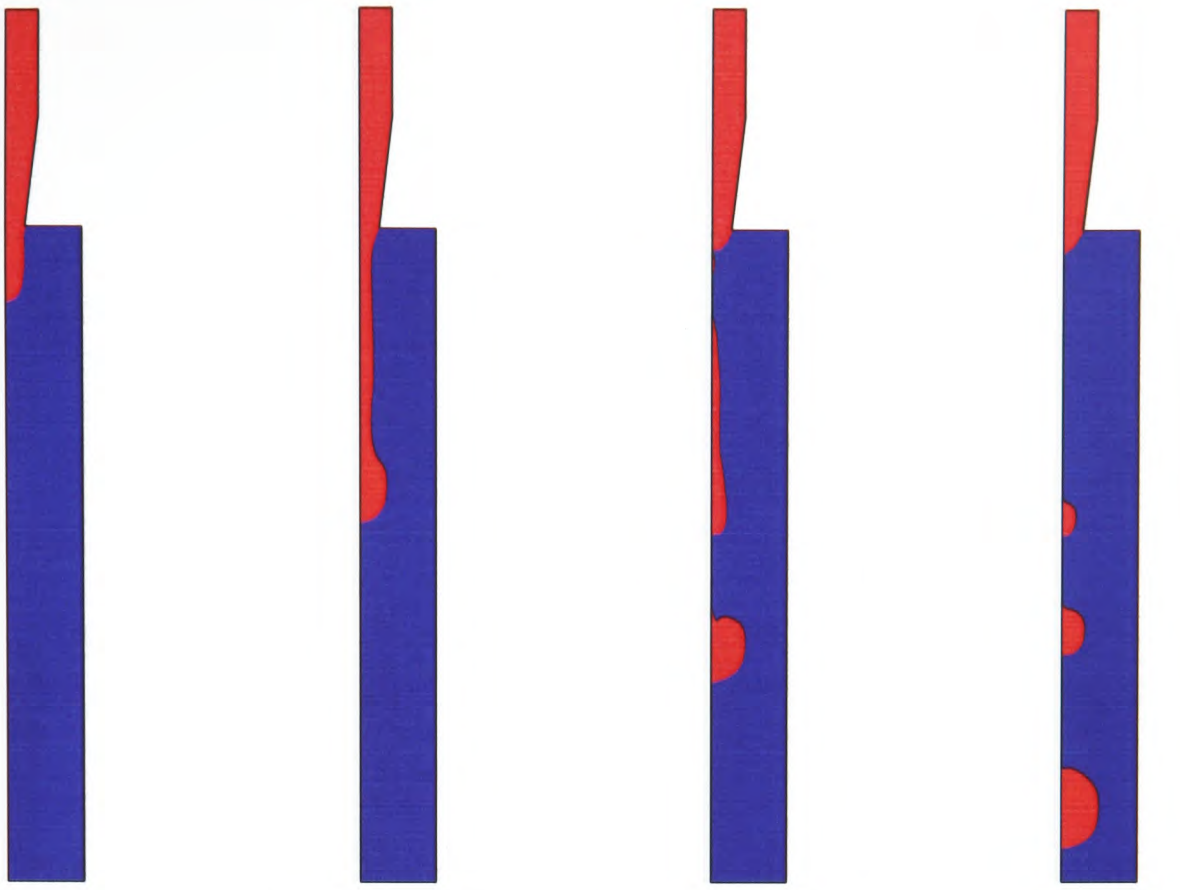

a) $t = 2\mu s$ b) $t = 10\mu s$ c) $t = 16\mu s$ d) $t = 22\mu s$

Figure 5.36: Water droplet formation on an axi-symmentric geometry inlet velocity 1/2 cosine wave.

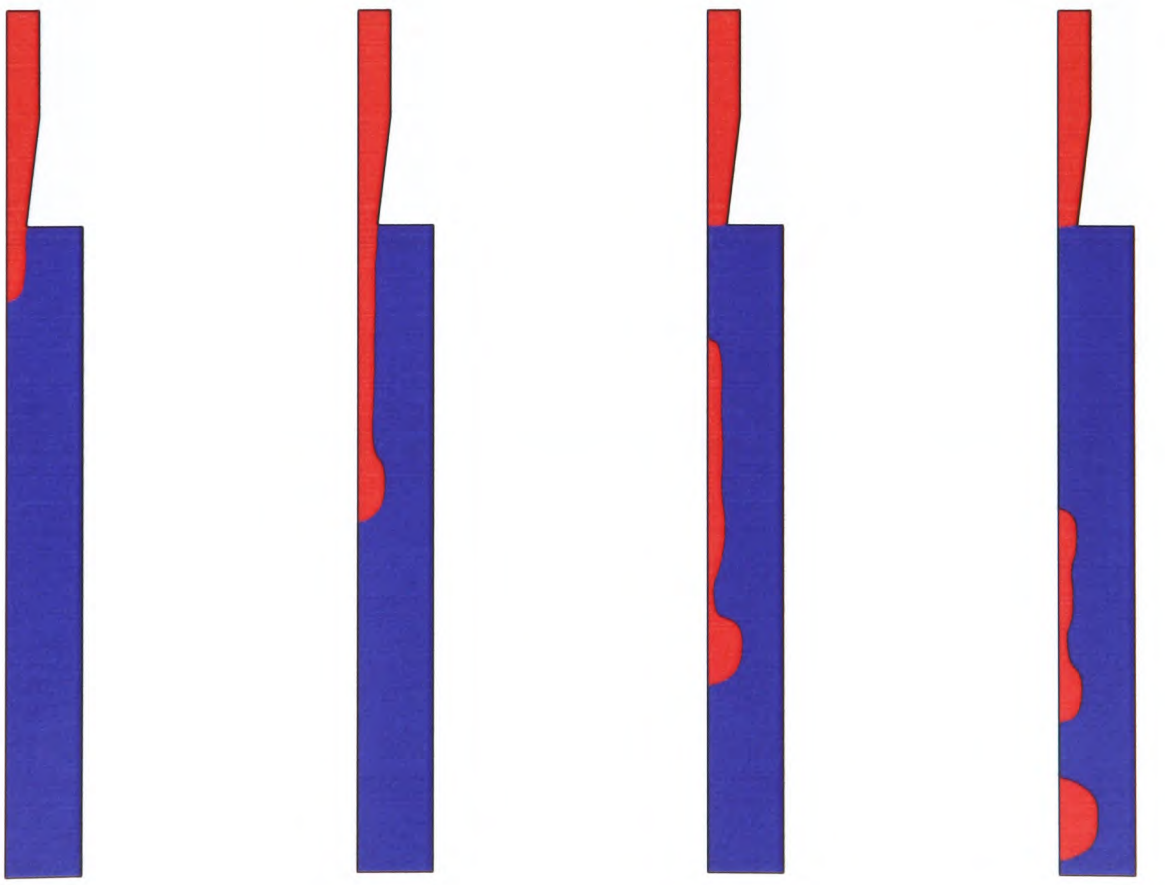

a) $t = 2\mu s$ b) $t = 10\mu s$ c) $t = 16\mu s$ d) $t = 22\mu s$

Figure 5.37: Water droplet formation on an axi-symmentric geometry inlet velocity 1/4 cosine wave.

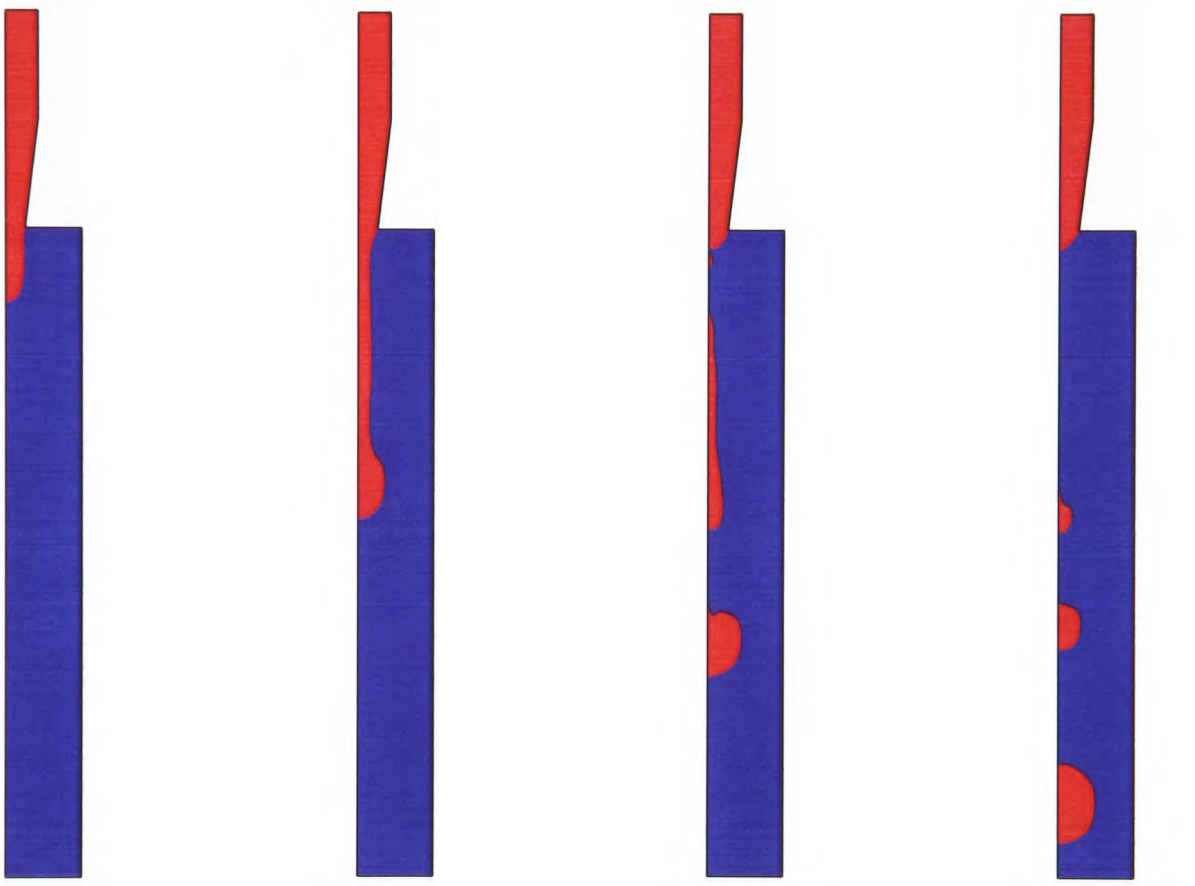

a) $t = 2\mu s$ b) $t = 10\mu s$ c) $t = 16\mu s$ d) $t = 22\mu s$

Figure 5.38: Viscoelastic fluid with material properties of water inlet velocity 1/2 cosine wave.

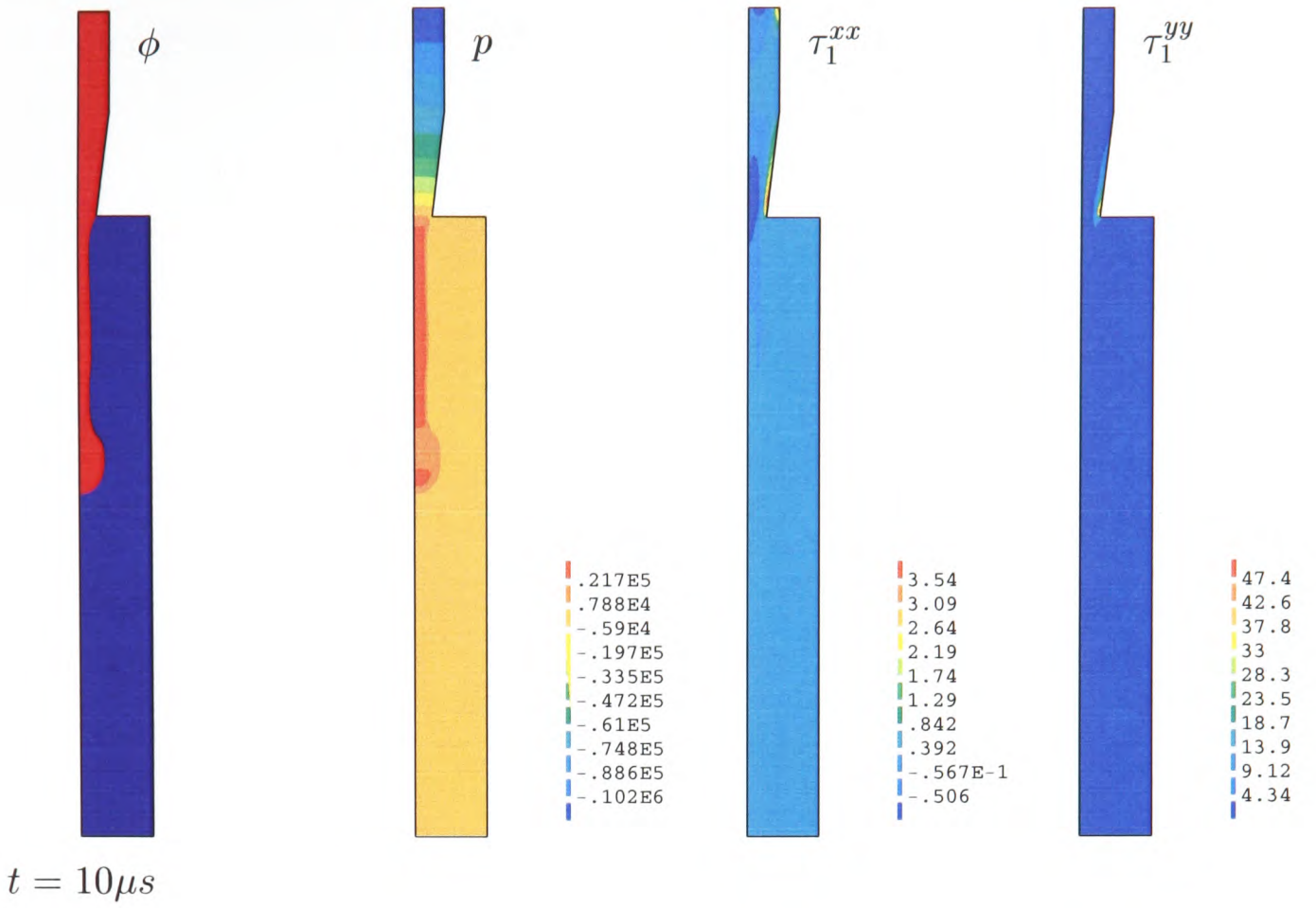

Figure 5.39: The pressure and normal stress contours in the region of the nozzle tip for test 2 at $t = 10\mu s$ and $t = 22\mu s$.

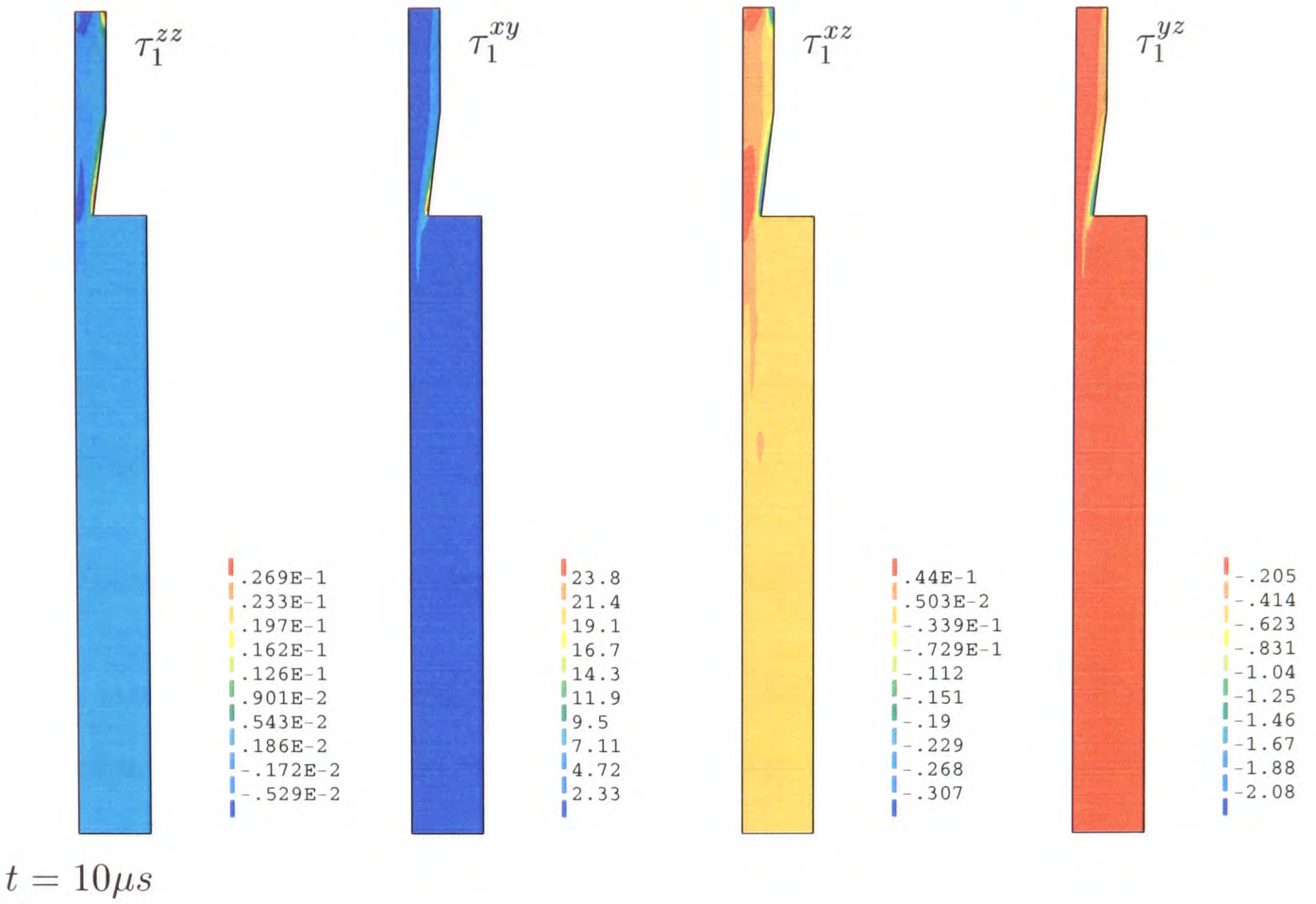

Figure 5.40: The shear stress contours in the region of the nozzle tip for test 2 at $t = 10\mu s$ and $t = 22\mu s$.

Density (kgm^{-3})	Dynamic Viscosity(Pas)	Kinematic Viscosity(m^2s^{-1})
1300	4.0	3.0769×10^{-3}
2000	4.0	2.0×10^{-3}
3000	4.0	1.3333×10^{-3}

Table 5.6: Constant Dynamic viscosity and corresponding kinematic viscosity for increasing densities.

Test4 - Axisymmetric jetting with viscoelastic material V2

The next simulation was carried out using material properties listed in Table 5.5. The initial and boundary conditions were the same as for Test 2. The velocity pulse is turned on for $10\mu s$ and then stopped. The results are presented in Figure 5.41. At $t = 2\mu s$ the fluid is seen emerging from the nozzle. At $t = 4\mu s$ instead of the necking which is expected it has begun to grow along the upper boundary.

The simulation was then carried out using a constant inlet velocity pulse of $5ms^{-1}$ over period of $20\mu s$. The results are shown in Figure 5.42. There is no discernible difference in the behaviour of the flow front.

The next test involved increasing the density whilst holding all other material properties constant including the dynamic viscosity. The density values used and the corresponding Dynamic and Kinematic viscosity values are shown in Table 5.6. With the density increased to $\rho = 2000kgm^{-3}$ there was no improvement in the results. Therefore a further test was carried out at $\rho = 3000kgm^{-3}$. This test also showed no change.

Simulations were then carried out for increasing densities whilst holding the kinematic viscosity constant (ie. the dynamic viscosity varied according to density as shown in Table 5.7).

With the density of the fluid increased to $\rho = 2000kgm^{-3}$ and the kinematic viscosity constant with the constant inlet velocity pulse the results showed a definite improvement. In Figure 5.43 the results are presented at four time intervals and as can be seen at $t = 4\mu s$ where previously the fluid had begun the creep along the symmetry plane necking can be observed. However further on in time the drop looses its shape

Density (kgm^{-3})	Dynamic Viscosity(Pas)	Kinematic Viscosity(m^2s^{-1})
1300	4.0	3.0769×10^{-3}
2000	6.154	3.0769×10^{-3}
3000	9.231	3.0769×10^{-3}

Table 5.7: Constant Kinematic viscosity and corresponding Dynamic viscosity for increasing Densities.

and begins to creep along the upper boundary.

A further simulation is carried out with the density increased to $\rho = 3000kgm^{-3}$ and the results can be seen in Figure 5.44. In this case the injected fluid behaves as expected displaying necking and the separation of the droplet with time. However there is no indication of satellite droplets. The CPU time was 11.659h on a single node of a 5 Alpha server E545 system with each system containing four 1GHz CPUs with 4Gb of memory. The simulation was carried out using a timestep of 1×10^{-8}.

Figure 5.45 shows the orientation of the velocity vectors for $\rho = 2000kgm^{-3}$ and $\rho = 3000kgm^{-3}$ at time intervals $t = 2\mu s$ and $t = 10\mu s$. At $t = 2\mu s$ both plots are fairly similar with the lower density fluid having a slightly higher region of re-circulation near the fluid/air interface. At $t = 10\mu s$ the plots are completely different. The velocities appear to have become diffused near the nozzle tip for $\rho = 2000kgm^{-3}$ whereas at $\rho = 3000kgm^{-3}$ they are aligned in the direction of the fluid droplet which is necking and moving vertically down. Figures 5.46 and 5.47 show the corresponding pressure and stress contours at $t = 10\mu s$. Figure 5.48 shows the pressure and stress contours at $t = 22\mu s$ for the $\rho = 3000kgm^{-3}$ fluid.

Additionally three tests using Newtonian flow were also carried out for density values $1300kgm^{-3}$, $2000kgm^{-3}$ and $3000kgm^{-3}$ with the kinematic viscosity held constant. The results proved to be similar to that observed with the viscoelastic model.

As a final test the flow is simulated using the cosine wave inlet velocity turned on for $10\mu s$ with a density of $\rho = 3000kgm^{-3}$, and the results are presented in Figure 5.49. The fluid displays signs of necking at $t \leq 6\mu s$. However by $t = 8\mu s$ the flow front has begun to creep along the upper boundary.

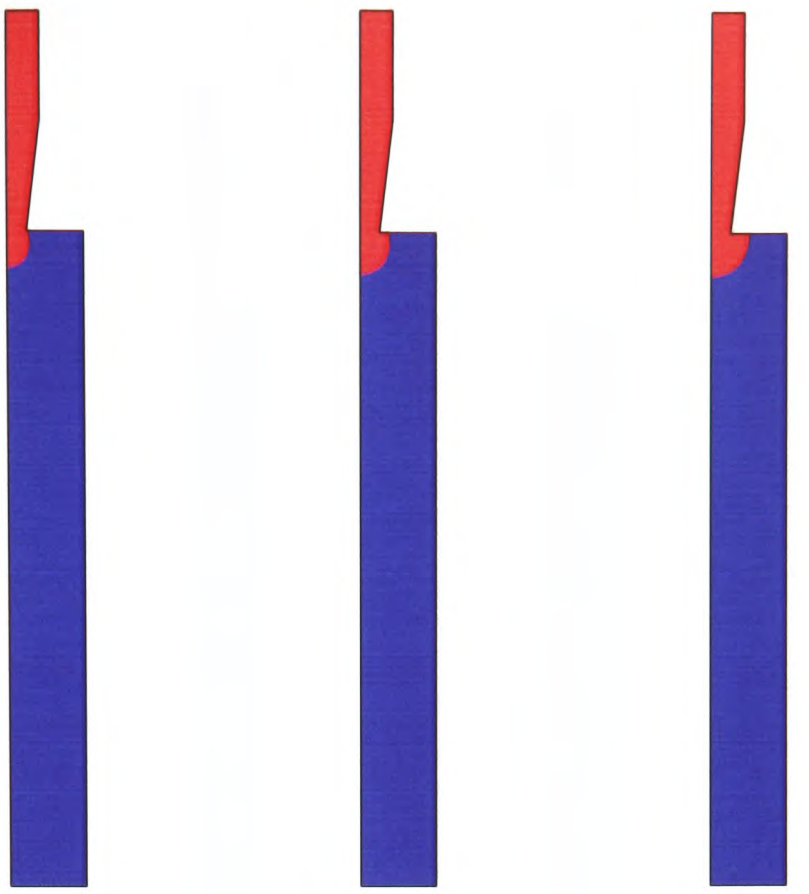

a) $t = 2\mu s$ b) $t = 4\mu s$ c) $t = 10\mu s$

Figure 5.41: Viscoelastic fluid with $\rho = 1300 kgm^{-3}$ and inlet velocity 1/2 cosine wave.

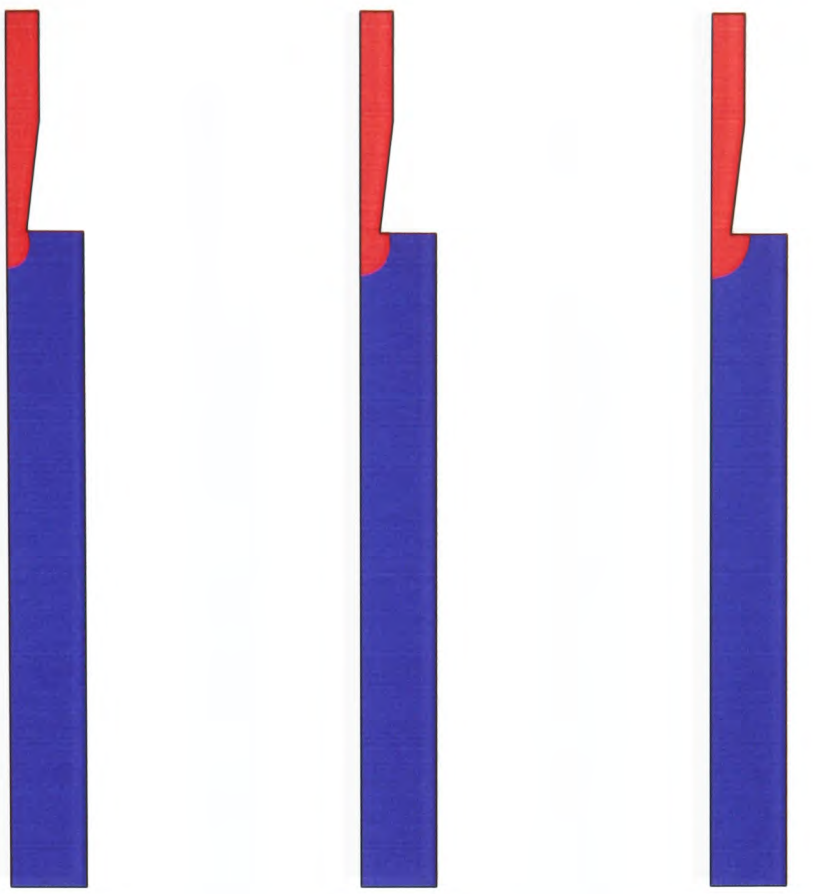

a) $t = 2\mu s$ b) $t = 4\mu s$ c) $t = 10\mu s$

Figure 5.42: Viscoelastic fluid with $\rho = 1300 kgm^{-3}$ and constant inlet velocity pulse.

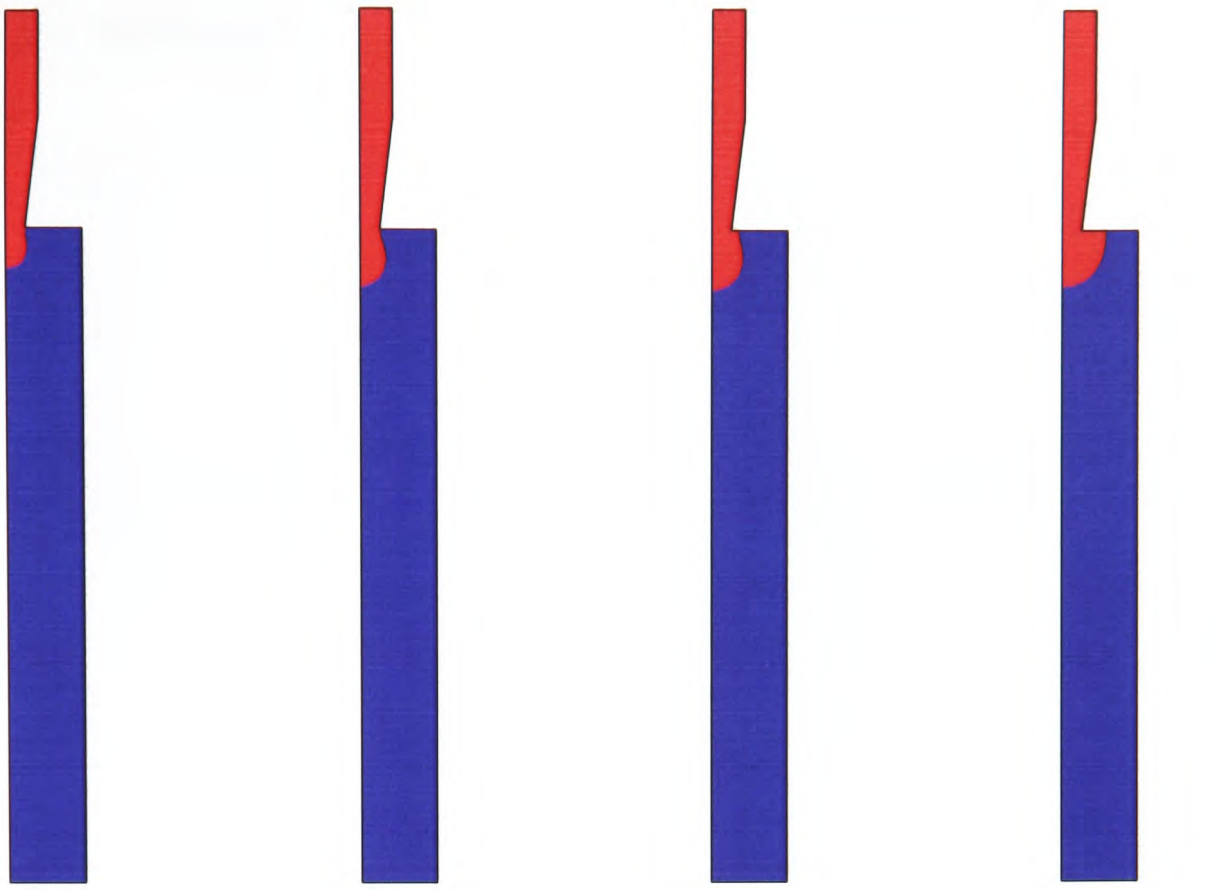

a) $t = 2\mu s$ b) $t = 4\mu s$ c) $t = 6\mu s$ d) $t = 10\mu s$

Figure 5.43: Viscoelastic fluid with $\rho = 2000 kgm^{-3}$ and constant inlet velocity pulse.

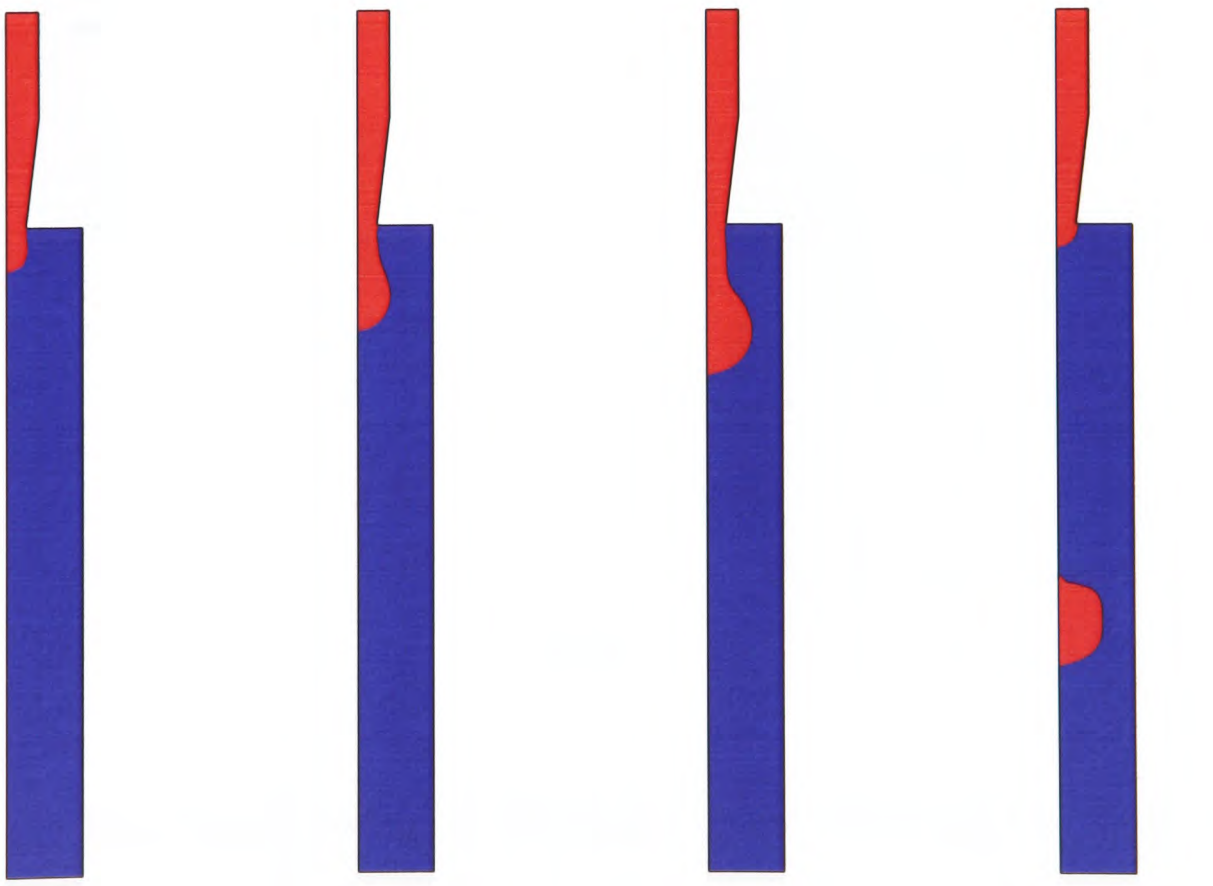

a) $t = 2\mu s$ b) $t = 10\mu s$ c) $t = 20\mu s$ d) $t = 26\mu s$

Figure 5.44: Viscoelastic fluid with $\rho = 3000 kgm^{-3}$ and constant inlet velocity pulse.

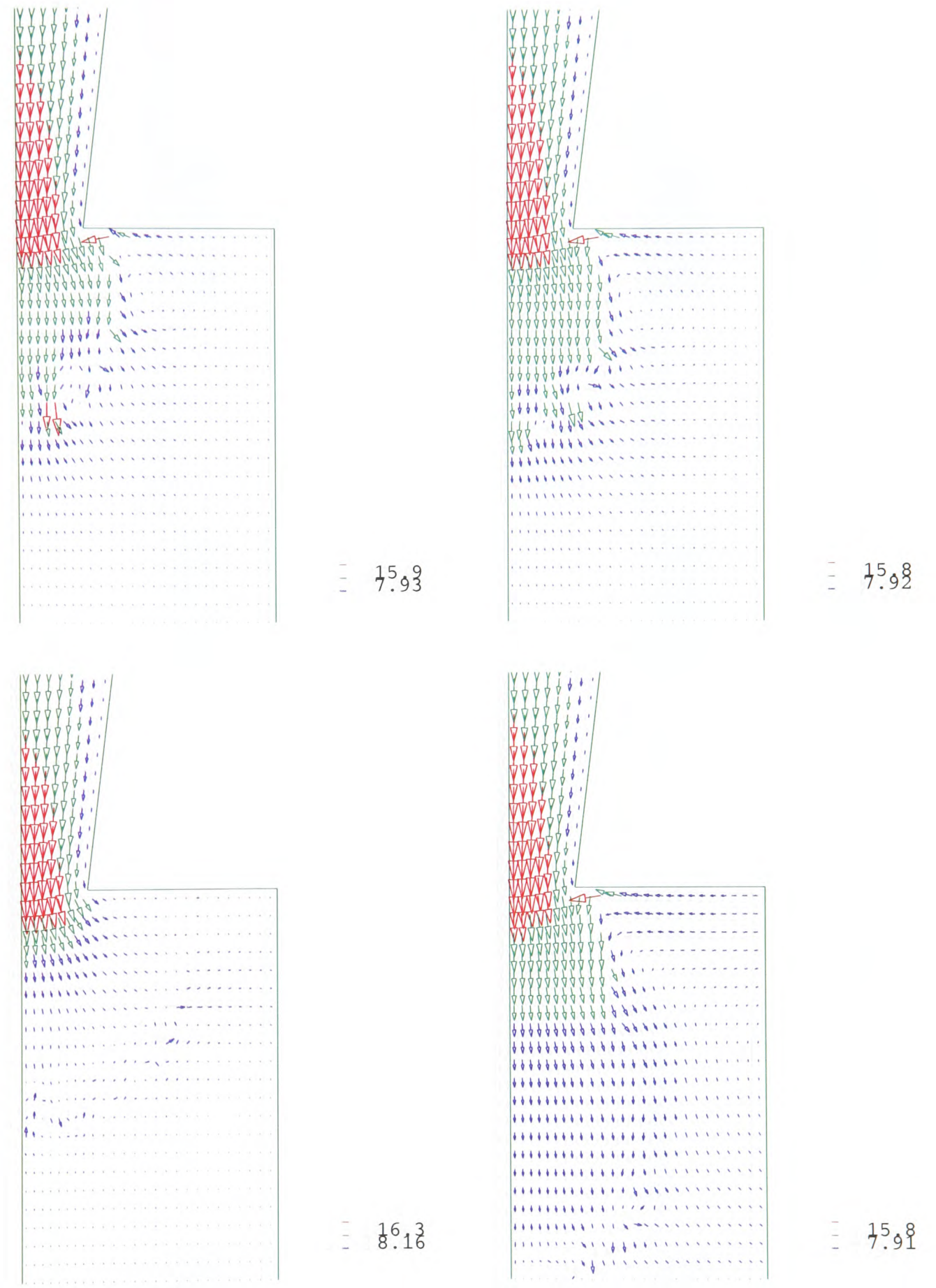

Figure 5.45: The velocity vectors in the region of the nozzle tip for $\rho = 2000kgm^{-3}$ and $\rho = 3000kgm^{-3}$ at $t = 2\mu s$(left) and $t = 10\mu s$(right).

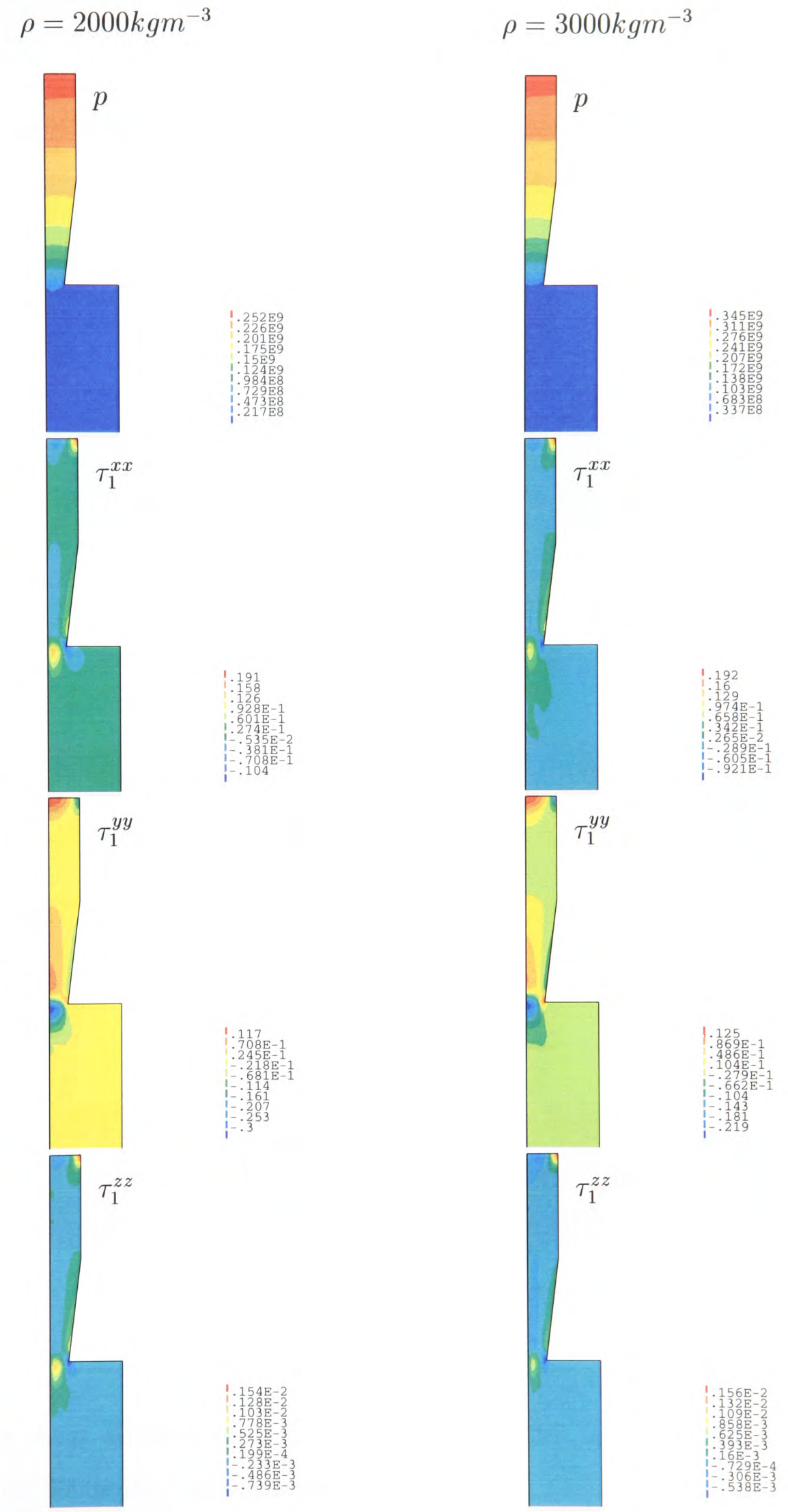

Figure 5.46: The pressure and normal stress contours in the region of the nozzle tip for $\rho = 2000$ and $\rho = 3000kgm^{-3}$ at $t = 10\mu s$.

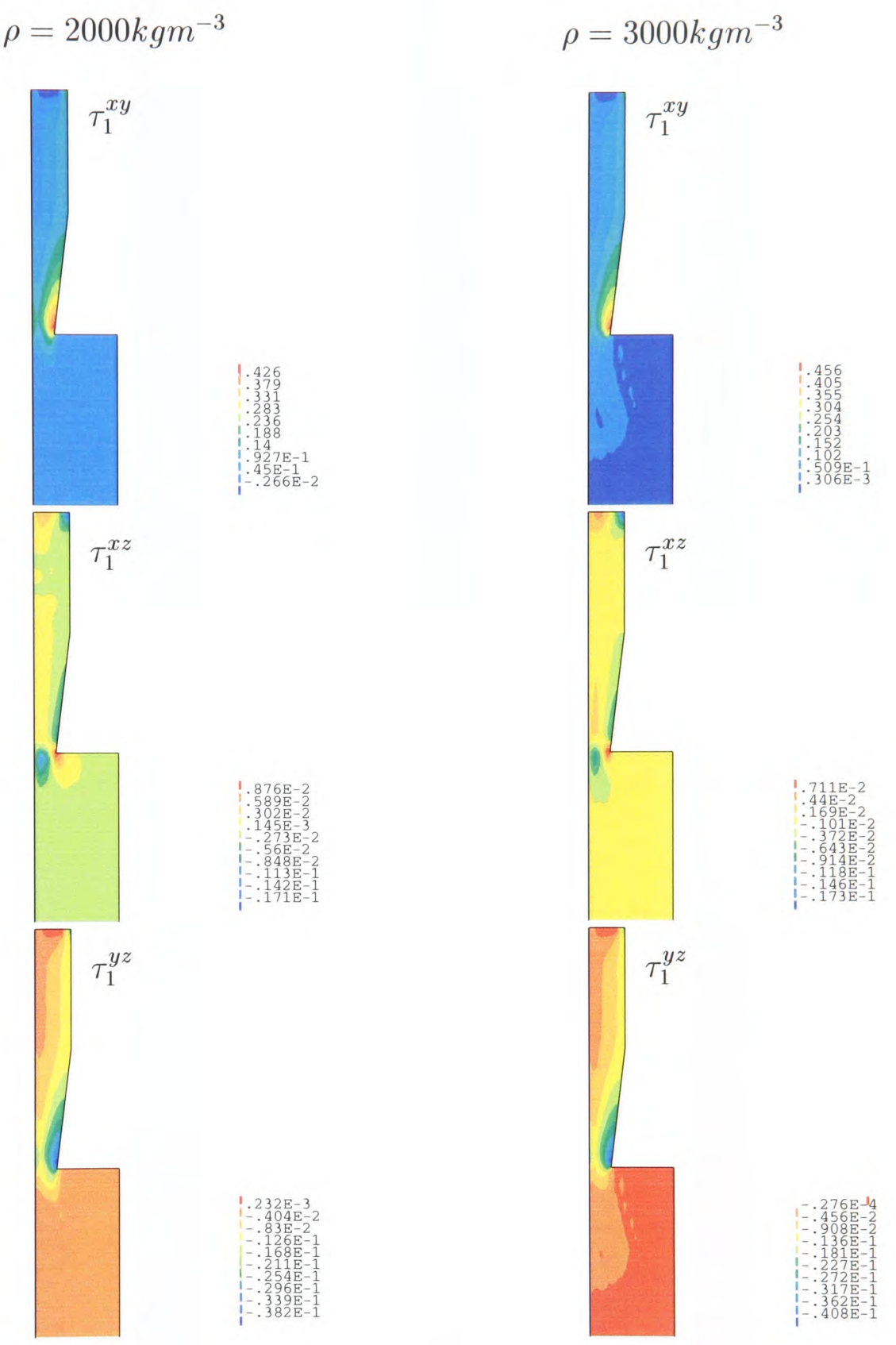

Figure 5.47: The shear stress contours in the region of the nozzle tip for $\rho = 2000kgm^{-3}$ and $\rho = 3000kgm^{-3}$ at $t = 10\mu s$.

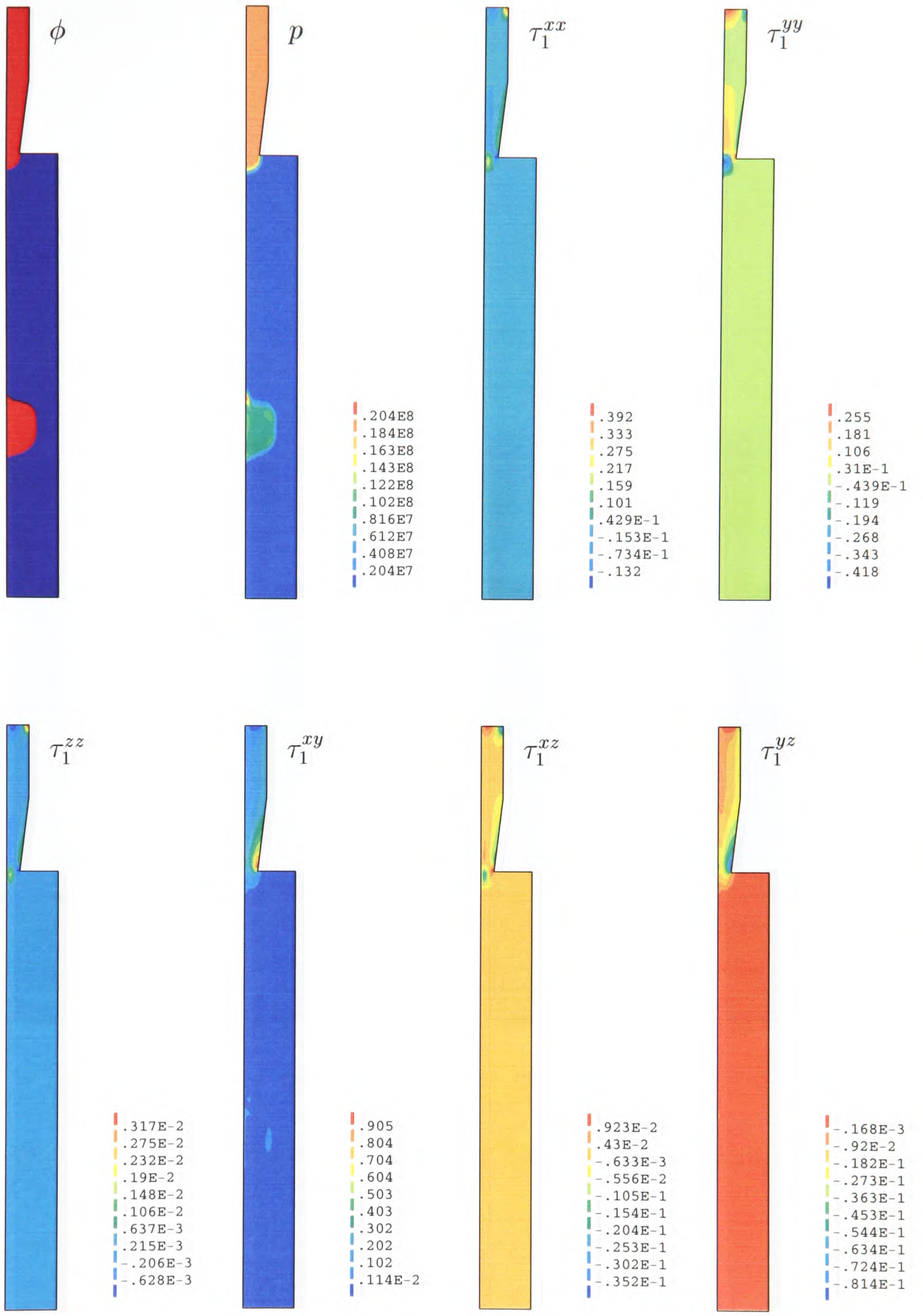

Figure 5.48: The pressure, normal and shear stress contours in the region of the nozzle tip for $\rho = 3000 kgm^{-3}$ at $t = 26\mu s$.

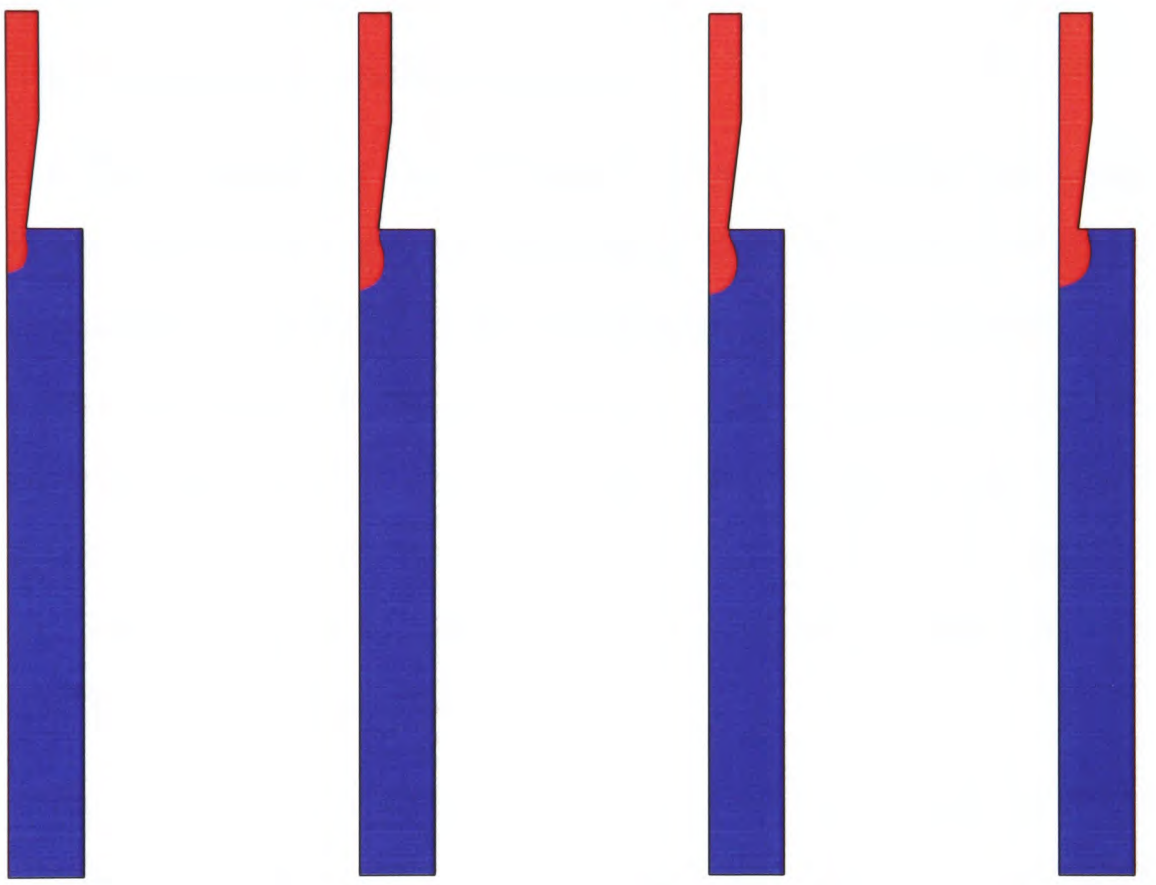

a) $t = 2\mu s$ b) $t = 4\mu s$ c) $t = 6\mu s$ d) $t = 8\mu s$

Figure 5.49: Viscoelastic fluid with $\rho = 3000 kgm^{-3}$ and $1/2$ cosine wave inlet velocity pulse.

5.5.4 Summary of Jetting

The numerical tests in the section above involved the jetting of fluid droplets. The first test was carried out on a 2-D geometry for water. The numerical results successfully predicted the necking and the subsequent separation of the fluid ejected from the nozzle.

The testing was then extended to an axi-symmetric geometry. The simulation results for water were once again able to predict the formation of a droplet due to necking of the fluid. Additionally on the axi-symmetric geometry the numerical results also predicted the formation of satellite droplets.

Following on from simulating the jetting of water, the testing was extended to viscoelastic fluids. For a low viscosity viscoelastic fluid the results on the formation of the droplet showed a similarity to the Newtonian case as expected. When material properties were increased the results indicated signs of necking initially as the fluid was ejected from the nozzle. However with time instead of the droplet breaking off as with the previous cases the fluid began to grow along the upper boundary of the domain. This appeared to indicate that the surface tension forces were able to overcome the gravitational pull on the drop.

The next stage of experimentation involved tests on the suitability of the boundary condition used for the inlet velocity. The principal velocity in the simulations was a cosine wave impulse which was turn turned on over a period of $10\mu s$ after which there was no outflow from the nozzle. The velocity at the inlet therefore gradually decreased towards the end of the impulse giving rise to a decreasing pressure gradient at the inlet. This diminishing force on the ejected fluid may have enabled the surface tension forces to overcome the gravitation pull on the ejected fluid.

Therefore in the next simulation the principal inlet velocity was changed to a constant velocity which was applied over a period of $20\mu s$. With the new inlet velocity pulse more fluid was ejected, however the behaviour of the fluid showed no noticeable difference.

The experimentation then focused on the density of the fluid whilst holding other material variables constant including the dynamic viscosity (which was held at the

same value used in previous simulations). Simulations were carried out for increasing densities of $\rho = 2000kgm^{-3}$ and $\rho = 3000kgm^{-3}$ respectively using the constant velocity pulse. The results did not show any improvment.

The testing then focused on keeping the kinematic viscosity constant and increasing the density along with a constant inlet velocity pulse. The results began to show a definite improvement. The necking of the ejected fluid continued for longer than before. However after a time the fluid began to grow along the upper boundary of the domain.

The increased necking indicated that the change in density whilst holding the kinematic viscosity constant aided the necking mechanism. Therefore an even higher density ($\rho = 3000kgm^{-3}$) was used for the next simulation. The results showed the necking of the fluid and the separation of the droplet. For this case there was no indication of satellite droplets. Clearly with this density the gravitational force was able to overcome the surface tension forces at the outlet of the nozzle. Corresponding tests using Newtonian flow showed similar behaviour to that observed with the viscoelastic model. This clearly indicated that the phenomena observed were related to the high surface tension of the polymer material and the geometry in question and not difficulties associated with the algorithm and its capability of solving viscoelastic flow.

Finally to investigate the response of this very high density fluid to the cosine wave inlet velocity pulse a further simulation was carried. With the cosine wave impulse velocity applied at the inlet the fluid failed to separate into a droplet instead it began to grow along the upper boundary of the domain. Clearly for jetting of viscoelastic fluids on this particular geometry with the type of higher material property values used the inlet velocity pulse should be a constant value.

5.6 Conclusion

The aim of this chapter was to investigate the predictive capability of the unstructured viscoelastic free surface algorithm developed during the course of this project.

The two processes chosen to carry out numerical experiments were

- Injection flow of underfill past solder joints.
- Jetting of underfill droplets.

The geometries considered were micro-scale in dimensions. Underfill material was assumed to have no filler particles in it. It was also assumed that underfill material which is a viscoelastic fluid can be modelled using the Oldroyd-B constitutive model.

Both processes have a significant relevance to the electronic packaging industry which uses viscoelastic fluids but have not addressed the viscoelasticity of the materials in research that has been carried out.

When simulating pressure driven flow past cylindrical obstacles, the dimensions of the cylinders were chosen to be that of solder joints. The algorithm was able to accurately capture flow features such as the formation of voids near joint walls observed during the underfill process.

The modelling of jetting was initially carried out for water using Newtonian flow. Simulations showed the necking of the ejected fluid and the subsequent formation of satellite droplets. Testing was then carried out using the viscoelastic model and material properties of water. The result on the formations of droplets was similar to that of the Newtonian model. However the viscoelastic model was able to predict stress buildup in the interior of the nozzle tip which is a point of singularity in the geometry. The modelling was then extended to polymeric fluids. Both Newtonian and viscoelastic models were used to investigate flow behaviour. Both models predicted similar behaviour with regard to the ejected fluid and the viscoelastic model was able to predict stress development especially in the interior of the nozzle tip. Additionally the numerical experiments gave insight into the differences associated with modelling such flow with high surface tension as opposed to fluids such as water.

The algorithm is clearly able to model viscoelastic flow involving diverse flow behaviour. Therefore it can be used to model industrial processes involving viscoelastic fluids in order to gain insight into complex flow mechanisms.

Chapter 6

Conclusion

Advances in technology have led to the use of polymer based materials which are viscoelastic fluids in various products including micro-scale electronic components. The sizes of these components make physical testing increasingly difficult. Therefore computational tools are being sought to replace physical experimentation. Predictive tools are also being viewed as a cost effective method of testing as they remove the need for large numbers of proto-types and decrease testing cycles.

In developing such a predictive tool the complex nature of viscoelastic materials are required to be addressed through use of special constitutive equations. The use of such constitutive models have been found to give rise to problems such as the "high Weissenberg number problem". The constitutive equations also add further complexity to processes which already require complicated governing equations. Therefore the process modelling that has been carried out in the electronic packaging industry for example have compromised in the physical representation of the model through the use of Newtonian or modified Newtonian models. Commercial codes such as Polyflow which provide for viscoelastic behaviour tend to be finite element based codes with mesh adapting techniques for free surfaces which are computationally costly.

The objective of this research was to develop a free surface viscoelastic algorithm including surface tension using unstructured finite volume techniques for use in complex geometries and processes. The main achievements of this research are the following:

- The implementation of a viscoelastic constitutive model within the multi-physics framework PHYSICA+ resulting in a new fully unstructured finite volume algorithm for viscoelastic flow.

- The solution of viscoelastic flow on the 4:1 planar contraction. The results obtained confirmed the latest numerical trends for this problem as reported by Alves et al. [22] and Aboubacar et al. [20].

- The coupling of the viscoelastic algorithm with two free surface algorithms - the Scalar Equation Algorithm and the Level Set Method. The latter does not suffer from interface smearing and allows surface tension effects to be implemented.

- The modelling of two underfill techniques - injection flow and jetting.

6.1 Chapter Summary

In Chapter 1 the complex nature of viscoelastic fluids was reviewed. Constitutive equations that have been developed to model the physical characteristics of such fluids were presented and their limitations were outlined. The chapter concluded with a look at the type of process modelling techniques currently avaible to industry and an outline of this research project.

Chapter 2 introduced an unstructured collocated finite volume algorithm for the solution of a generic scalar. The details of the discretization of the transient, convective, diffusive and source contributions for a general conservation equation were given along with techniques to overcome pressure checker board effects and geometries with skew elements. First and third order accurate differencing schemes based on upwinding techniques were also described.

The 3-D implementation of a non-linear viscoelastic model was presented in Chapter 3. The chapter began with a review of finite volume algorithms which have been employed for the solution of viscoelastic flow. The 3-D Oldroyd-B model was chosen for implementation within the collocated finite volume algorithm described in Chapter 2 and the implementation was validated based on laminar flow simulations

in a 2-D planar channel in the XY, YZ and ZX planes respectively. The numerical solutions for normal and shear stresses compared very well with the analytical solutions on each respective plane. Having tested the implementation the algorithm was then tested for its sensitivity to increasing elasticity using the 4:1 planar contraction bench mark test case in the XY plane. A detailed literature review was carried out on published work on this problem. Several meshes were used in the testing and, for each mesh, simulations were carried out for a series of We numbers under creeping flow conditions starting with Stokes flow.

In Chapter 4 the viscoelastic algorithm was coupled with two free surface algorithms to model two phase flow. The chapter began with a review of free surface algorithms that have been developed for viscoelastic flow simulations. The details of the Scalar Equation Algorithm and Level Set Method in PHYSICA+ were presented. Higher order differencing schemes for approximating the value of the scalar marker at the element faces were described and the coupling of the viscoelastic algorithm with the interface tracking methods were presented. The viscoelastic free surface algorithm was validated through simulations on a 2-D planar channel. The numerical solutions for the normal and shear stresses compared very well with their analytical solutions. The effect of surface tension was demonstrated using the square to circle test case. Structured as well as unstructured meshes were used in the tests.

The aim of the work presented in Chapter 5 was to test the viscoelastic free surface algorithm for its predictive capability. The chapter began with a look at developments in the use of polymer based materials in the electronic packaging industry with special relevance to the underfill process which is used to encapsulate the joints usually made of solder which fuse silicon chips on to printed circuit boards. A description of the process, the material composition and various types of encapsulation techniques were then presented followed by an in depth review of analytical and numerical work carried out in the field.

Based on the literature review it was observed that the most pressing problems in the underfill process are the formation of flow voids during both capillary as well as pressure driven flow encapsulation, and the difficulty of using mass transfer methods for encapsulation as the standoff height between chip and board decreases. Therefore

the first process chosen for simulation was injection flow which involves pressure driven flow in channels containing solder joints to test if the algorithm predicted the formation of flow voids. The second process tested was the jetting of fluids which is being experimented with as a viable underfilling method to replace mass transfer methods.

Flow simulations on the channel were carried out on 2 and 3-D goemetries with one and two cylindrical obstacles with dimensions of solder joints. In all tests flow was simulated under creeping flow conditions. The results showed the formation of voids in the vicinity of the joint walls. With LSM the flow fronts took longer to meet up behind the solder joint in the Newtonian case as was seen on simulation of flow past a solder joint test. With the viscoelastic flow the results showed high normal stress layers on the joint walls. In the 3-D experiments the results also showed the void detaching from the joint wall and moving downstream which was not detected in 2-D simulations. The 3-D simulations also showed high stress build up on the joint walls for viscoelastic flow.

The simulations on jetting were carried out on a 2-D and an axi-symmetric geometry. The simulation on the 2-D geometry was carried out for a Newtonian fluid. The initial simulation on the axi-symmetric geometry was also carried out for the same Newtonian fluid. The results for the two cases showed a notable difference. In the 2-D case the jetted fluid formed a single drop whilst in the axi-symmetric case the jetted fluid broke up to form a principal drop and several satellite droplets. Simulation of a low density viscoelastic fluid on the same axi-symmetric geometry displayed similar drop formation behaviour to the Newtonian fluid. However the viscoelastic model was able to predict additional features such as normal stress behaviour in the region of the nozzle tip.

In the case of the jetting of a high density polymer both Newtonian and viscoelastic models predicted similar results for the formation and the separation of the polymer drop. Once again the viscoelastic model predicted stress dynamics in the region of the interior of the nozzle and within the ejected fluid. This test was however proved to be more important in terms of the evaluation of surface tension effects relative to material properties and inflow boundary conditions when jetting such polymers

through nozzles of the sizes used.

6.2 Suggestions for Future Work

Future work can be categorised as follows

6.2.1 4:1 Contractions

On the 4:1 planar contraction problem further work could include flow simulations for $Re = 1.0$. Work also could be carried out on the 4:1 axi-symmetric contraction problem for creeping flow and $Re = 1.0$.

In this present study the algorithm was tested on several meshes with varying degrees of mesh intensities in the region of the point of singularity. On the most refined mesh which had a minimum element size of $\Delta x = 0.0057$, $\Delta y = 0.0085$ at the re-entrant corner, the algorithm produced converged solutions up to $We = 3.0$. This however may not be the We number limit for the algorithm since further simulations for consecutively higher Weissenberg numbers were not carried out due to time constraints. Therefore further work could include the testing of the Weissenberg number limit.

Additionally further tests could be carried out on mesh refinement in order to investigate the lower bound of the vortex lengths.

6.2.2 Underfill

For the underfill problem in addition to assuming that the fluid contained no filler particles it was also assumed that the material properties for a Boger fluid as given by Evans and Walters [68] could be used. The contact angle between the fluid and surfaces were assumed to be zero. Further work on this problem should include using more realistic material properties for underfill.

- Flow past solder joints

  Further work on the flow past solder joints could include flow with friction and contact angles imposed on channel walls.

A goemetry with longer upstream channel for the 3-D case with two solder joints which may help overcome simulation problems encountered during the work presently carried out.

Modelling of capillary driven viscoelastic flow in a planar channel with and without solder joints should also be considered.

- Work on jetting

  Suggestions for future work on the jetting problem include the jetting simulations using a wider nozzle. The dimensions of the nozzle used in the numerical experiments are those obtained from Rider and Kothe [99] who modelled the ejection of water through an ink jet printer nozzle where the diameter of the exit of the nozzle was $18\mu m$. In the physical experiments carried out by Quinones et al. [85] on underfill the diameter of the nozzle used were $101.6\mu m$ and $127\mu m$. Further simulations could be carried out using the dimensions used by Quinones et al.

6.2.3 Other Constitutive Models

In addition to the various suggestions presented above for the Oldroyd-B model, future work should also involve the implementation of more physically realistic models. This could include the shear thinning Phan-Thien–Tanner model which has been found to be better suited to model behaviour of industrial polymers.

Bibliography

[1] R.B. Bird, R.C. Armstrong, and O. Hassager. *Dynamics of Polymeric Liquids. Volume 1, Fluid mechanics.* John Wiley & Sons, USA, 1987.

[2] H.A. Barnes, J.F. Hutton, and K. Walters. *An Introduction to Rheology.* Elsevier, Amsterdam, 1989.

[3] M. Reiner. The Deborah Number. *Physics Today*, pages 17–62, 1964.

[4] R.G. Owens and T.N. Phillips. *Computational Rheology.* Imperial College Press, London, 2002.

[5] R.I. Tanner and K. Walters. *Rheology:An Historical Perspective.* Elsevier, Amsterdam, 1998.

[6] R.I. Tanner. *Engineering Rheology.* Oxford Science Publications, Oxford, 1988.

[7] B.D. Coleman and W. Noll. An approximation theorem for functionals, with applications in continuum mechanics. *Arch. Rat. Mech. Anal.*, 6:355–370, 1960.

[8] F.T.P. Baaijens, S.H.A. Selen, H.P.W. Baaijens, G.W.M. Peters, and H.E.H. Meijer. Viscoelastic flow past a confined cylinder of a low density polyethylene melt. *J. Non-Newtonian Fluid Mech.*, 68:173–203, 1997.

[9] G.D. Smith. *Numerical Solution of Partial Differential Equations.* Clarendon Press, Oxford, 1985.

[10] E.H. Twizell. *Computational Methods for Partial Differential Equations.* John Wiley & Sons, New York, 1984.

[11] O.C. Zienkiewicz and R.L. Taylor. *The Finite Element Method-Vol. 2:Solid and Fluid Mechanics.* McGraw-Hill, New York, 1991.

[12] D. Gottlieb and S.A. Orszag. *Numerical Analysis of Spectral Methods:Theory and Applications.* SIAM, Philadelphia, 1977.

[13] S.V. Patankar. *Numerical Heat Transfer and Fluid Flow.* McGraw-Hill, New York, 1980.

[14] T. Sato and S.M. Richardson. Explicit numerical simulation of time-dependent viscoelastic flow problems by a finite element/finite volume method. *J. Non-Newtonian Fluid Mech.*, 51:249–275, 1994.

[15] E.O.A. Carew, P. Townsend, and M.F. Webster. A Taylor-Petrov-Galerkin algorithm for viscoelastic flow. *J. Non-Newtonian Fluid Mech.*, pages 253–287, 1993.

[16] H. Matallah, P. Townsend, and M.F. Webster. Recovery and stress-splitting schemes for viscoelastic flows. *J. Non-Newtonian Fluid Mech.*, 75:139–166, 1998.

[17] J.M. Marchal and M.J. Crochet. A new mixed finite element for calculating viscoelastic flow. *J. Non-Newtonian Fluid Mech.*, 26:77–114, 1987.

[18] J.Y. Yoo and Y. Na. A numerical study of the planar contraction flow of a viscoelastic fluid using the simpler algorithm. *J. Non-Newtonian Fluid Mech.*, 39:89–106, 1991.

[19] T.N. Phillips and A.J. Williams. Viscoelastic flow through a planar contraction using a semi-Lagrangian finite volume method. *J. Non-Newtonian Fluid Mech.*, 87:215–246, 1999.

[20] M. Aboubacar and M.F. Webster. A cell-vertex finite volume/element method on triangles for abrupt contraction viscoelastic flows. *J. Non-Newtonian Fluid Mech.*, 98:83–106, 2001.

[21] P.J. Oliveira and F.T. Pinho. Plane contraction flows of upper convected Maxwell and Phan-Thien-Tanner fluids as predicted by a finite-volume method. *J. Non-Newtonian Fluid Mech.*, 88:63–88, 1999.

[22] M.A. Alves, F.T. Pinho, and P.J. Oliveira. Effect of high-resolution differencing scheme on finite-volume predictions of viscoelastic flows. *J. Non-Newtonian Fluid Mech.*, 93:287–314, 2000.

[23] M. Aboubacar, H. Matallah, and M.F. Webster. Highly elastic solutions for Oldroyd-B and Phan-Thien/Tanner Fluids with a Finite Volume/Element Method:planar contraction flows. *J. Non-Newtonian Fluid Mech.*, 103:65–103, 2002.

[24] H.-S. Dou and N. Phan-Thien. The flow of an Oldroyd-B fluid past a cylinder in a channel: adaptive viscosity vorticity (DAVSS-ω) formulation. *J. Non-Newtonian Fluid Mech.*, 87:47–73, 1999.

[25] J. Sun, M.D. Smith, R.C. Armstrong, and R.A. Brown. Finite element method for viscoelastic flows based on the discrete adaptive viscoelastic stress splitting and the discontinuous Galerkin method: DAVSS-G/DG. *J. Non-Newtonian Fluid Mech.*, 86:281–307, 1999.

[26] C.-C. Tsai, T.-J. Liu, Y.-H. Chang, and W.T.W. Tseng. Numerical simulation of an optical fiber-forming process. *Chemical Eng. Science*, 52:221–235, 1997.

[27] I. Mutlu, P. Townsend, and M.F. Webster. Simulation of cable-coating viscoelastic flows with coupled and decoupled schemes. *J. Non-Newtonian Fluid Mech.*, 74:1–23, 1998.

[28] H. Demir and F.T. Akyildiz. Unsteady thermal convection of a non-Newtonian fluid. *Int. J. Eng. Science*, 38:1923–1938, 2000.

[29] H. Demir. Thermal convection of viscoelastic fluid with Biot boundary condition. *Math. and Comp. in Simulation*, 56:277–296, 2001.

[30] L.E. Becker and G.H. McKinley. The stability of viscoelastic creeping plane shear flows with viscous heating. *J. Non-Newtonian Fluid Mech.*, 92:109–133, 2000.

[31] A. Wachs and J-R. Clermont. Non-isothermal viscoelastic flow computations in an axisymmetric contraction at high Weissenberg numbers by a finite volume method. *J. Non-Newtonian Fluid Mech.*, 95:147–184, 2000.

[32] S.B. Pillapakkam and P. Singh. A level-set method for computing solutions to viscoelastic two-phase flow. *J. Computational Physics.*, 174:552–578, 2001.

[33] R.E. Khayat. Transient free-surface flow inside thin cavities of viscoelastic fluids. *J. Non-Newtonian Fluid Mech.*, 91:15–29, 2000.

[34] Polyflow. http://www.fluent.com/worldwide/benelux/.

[35] Moldflow. http://www.moldflow.com.

[36] J. Sun, S. Subbiah, and J.M. Marchal. Numerical analysis of nonisothermal viscoelastic melt spinning with ongoing crystallization. *J. Non-Newtonian Fluid Mech.*, 93:133–151, 2000.

[37] P.W. McDonald. The computation of transonic flow through two-dimensional gas turbine cascades. *Paper 71-GT-89 ASME*, 1971.

[38] R.W. MacCormack and A.J. Paullay. Computational efficiency achieved by time splitting of finite difference operators. *AIAA paper 72-154, San Diego*, 1972.

[39] A.W. Rizzi and M. Inouye. Time split finite volume method for three-dimensional blunt-body flows. *AIAA*, 11, 1973.

[40] M. Thomadakis and M. Leschziner. Numerical simulation of viscous incompressible flows using a pressure-correction method and unstructured grids. *ECCOMAS '94 Conference*, 1994.

[41] D. Pan, C.-H. Lu, and J.-C. Cheng. Incompressible flow solution of unstructured triangular meshes. *Numerical Heat Transfer, Part B*, 26:207–224, 1994.

[42] P. Chow. *Control volume unstructured mesh procedure for convection-diffusion solidification processes.* PhD thesis, University of Greenwich,United Kingdom, 1993.

[43] T.N. Croft. *Unstructured Mesh - Finite Volume Algorithms for Swirling, Turbulent, Reacting Flows.* PhD thesis, University of Greenwich, United Kingdom, 1997.

[44] PHYSICA+. Multi-Physics Software Inc, 1945 South 1100 East, Suite 100, Salt Lake City, Utah 84106, USA. http://www.multi-physics.com.

[45] G.A. Taylor. *A vertex based discretization scheme applied to material non-linearity within a multi-physics finite volume framework.* PhD thesis, University of Greenwich, United Kingdom, 1996.

[46] C. M. Rhie and W. L. Chow. Numerical study of the turbulent flow past an airfoil with trailing edge separation. *AIAA Journal*, 21:1525–1532, 1983.

[47] D.B. Spalding. A novel finite-difference formulation for differential expressions involving both first and second derivatives. *Int. J. Numer. Meth. Engrg.*, 4:551–559, 1972.

[48] B.P. Leonard. A stable and accurate convective modelling procedure based on quadratic upstream interpolation. *Comput. Meth. Appl. Mech. Engrg.*, 19:59–98, 1979.

[49] S.V. Patankar and D.B. Spalding. A calculation procedure for heat, mass and momentum transfer in three dimensional parabolic flows. *Int. J. Heat Mass Transfer*, 15:1787–1806, 1972.

[50] J. P. van Doormal and G. D. Raithby. Enhancements of the SIMPLE method for predicting incompressible fluid flows. *Num. Heat Transfer*, 7:147–163, 1984.

[51] G.P. Sasmal. A finite volume approach for calculation of viscoelastic flow through an abrupt axisymmetric contraction. *J. Non-Newtonian Fluid Mech.*, 56:15–47, 1995.

[52] S.-C. Xue, N. Phan-Thien, and R.I. Tanner. Numerical study of secondary flows of viscoelastic fluid in straight pipes by an implicit finite volume method. *J. Non-Newtonian Fluid Mech.*, 59:191–213, 1995.

[53] M.S. Darwish, J.R. Whiteman, and M.J. Bevis. Numerical modelling of viscoelastic liquids using a finite-volume method. *J. Non-Newtonian Fluid Mech.*, 45:311–337, 1992.

[54] G. Mompean and M. Deville. Unsteady finite volume simulation of Oldroyd-B fluid through a three-dimensional planar contraction. *J. Non-Newtonian Fluid Mech.*, 72:253–279, 1997.

[55] M. Gerritsma. *Time Dependent Numerical Simulations of a Viscoelastic Fluid on a Staggered Grid.* PhD thesis, University of Groningen, The Netherlands, 1996.

[56] M.G.N. Perera and K. Walters. Long-range memory effects in flows involving abrupt changes in geometry, Part I. *J. Non-Newtonian Fluid Mech.*, 2:49–81, 1977.

[57] P.H. Gaskell and A.K.C. Lau. Curvature-compensated convective transport: SMART, a new boundedness-preserving transport algorithm. *Int. J. Num. Methods Fluids*, 8:617–641, 1988.

[58] C.R. Maliska and G.D. Raithby. Calculating 3D fluid flows using orthogonal grids. Proc. Third Int. Conf. Num. Methods in Laminar and Turbulent Flows, Seattle, WA, 1986.

[59] J.S. Scroggs and F.H.M. Semazzi. A conservative semi-Lagrangian method for multidimensional fluid dynamics applications. *Numer. Meth. Partial Differential Equations*, 11:445–452, 1995.

[60] K.A. Missirlis, D. Assimacopoulos, and E. Mitsoulis. A finite volume approach in the simulation of viscoelastic expansion flows. *J. Non-Newtonian Fluid Mech.*, 78:91–118, 1998.

[61] X. Huang, N. Phan-Thien, and R.I. Tanner. Viscoelastic flow between eccentric rotating cylinders: unstructured control volume method. *J. Non-Newtonian Fluid Mech.*, 64:71–92, 1996.

[62] P.J. Oliveira, F.T. Pinho, and G.A. Pinto. Numerical simulation of non-linear elastic flows with a general collocated finite-volume method. *J. Non-Newtonian Fluid Mech.*, 79:1–43, 1998.

[63] R.B. Bird, W.E. Stewart, and E.N. Lightfoot. *Transport Phenomena.* John Wiley & Sons, USA, 1960.

[64] D.V. Boger, D.H. Hur, and R.J. Binnington. Further observations of elastic effects in tubular entry flows. *J. Non-Newtonian Fluid Mech.*, 20:31–49, 1986.

[65] S.A. White and D.G. Baird. Flow visualization and birefringence studies on planar entry flow behavior of polymer melts. *J. Non-Newtonian Fluid Mech.*, 29:245–267, 1988.

[66] C.D. Eggleton, T.H. Pulliam, and J.H. Ferziger. Numerical simulation of viscoelastic flow using flux difference splitting at moderate Reynolds numbers. *J. Non-Newtonian Fluid Mech.*, 64:269–298, 1996.

[67] M.A. Alves, P.J. Oliveira, and F.T. Pinho. Benchmark solutions for the flow of Oldrod-B and PTT fluids in planar contractions. *J. Non-Newtonian Fluid Mech.*, 110:45–75, 2003.

[68] R.E. Evans and K. Walters. Flow characteristics associated with abrupt changes in geometry in the case of highly elastic liquids. *J. Non-Newtonian Fluid Mech.*, 20:11–29, 1986.

[69] R.E. Evans and K. Walters. Further remarks on the lip-vortex mechanism of vortex enhancement in planar-contraction flows. *J. Non-Newtonian Fluid Mech.*, 32:95–105, 1989.

[70] C.W. Hirt and B.D. Nichols. Volume of fluid (VOF) method for the dynamics of free boundaries. *J. Computational Physics.*, 39:201–225, 1981.

[71] J. Ramshaw and J. Trapp. A numerical technique for low speed homogeneous two-phase flow with sharp interfaces. *J. Computational Physics.*, 21:438, 1976.

[72] D.B. Spalding. Developments in IPSA procedure for numerical computation of multi-phase flow. 2nd National Symposium on Numerical Properties and Methodologies, 1981.

[73] L.Jun and D.B. Spalding. Numerical simulation of flows with moving interfaces. *Phy. Chem. Hydrodynamics*, 10:625–637, 1988.

[74] M. Sussman, P. Smereka, and S. Osher. A level set approach for computing solutions to incompressible two-phase flow. *J. Computational Physics.*, 114:146–159, 1994.

[75] E. Mitsoulis. Three-dimensional non-Newtonian computations of extrudate swell with the finite element method. *Comput. Meth. Appl. Mech. Engrg.*, 180:333–344, 1999.

[76] A.G. Lee, E.S.G. Shaqfeh, and B. Khomami. A study of viscoelastic free surface flows by the finite element method:Hele-Shaw and slot coating flows. *J. Non-Newtonian Fluid Mech.*, 108:327–362, 2002.

[77] R.E. Khayat. Boundary element analysis of planar drop deformation in confined flow. Part II. Viscoelastic fluids. *Eng. Anal. with Boundary Elements*, 22:291–306, 1998.

[78] A.J. Wagner, L. Giraud, and C.E. Scott. Simulation of a cusped bubble rising in a viscoelastic fluid with a new numerical method. *Computer Physics Communications*, 129:227–232, 2000.

[79] M.F. Tomè, N. Mangiavacchi, J.A. Cuminato, A. Castelo, and S. McKee. A finite difference technique for simulating unsteady viscoelastic free surface flows. *J. Non-Newtonian Fluid Mech.*, 106:61–106, 2002.

[80] L. Jun and D.B. Spalding. Numerical simulation of flows with moving interfaces. *Physica-Chemical Hydrodynamics*, 10:625–637, 1988.

[81] D.B. Spalding. A method for computing steady and unsteady flow possessing discontinuities of density. Technical report, CHAM Report 910/2, 1974.

[82] B. van Leer. Towards the ultimate conservation difference scheme IV, a new approach to numerical convection. *J. Computational Physics.*, 23:276–299, 1977.

[83] D. Wheeler. *Computational modelling of surface tension phenomena in metals processing.* PhD thesis, University of Greenwich, United Kingdom, 2000.

[84] S. Michaelides and S. Sitaraman. Role of underfilling imperfections on flip-chip reliability. In *Advances in Electronic Packaging, INTERPACK Conference*, volume EEP-Vol.19-2, pages 1487–1493. ASME, 1997.

[85] H. Quinones, A. Babiarz, L. Fang, and C. Deck. Jetting technology for micro-electronics. The Fifth International IEEE Symposium on High Density Packaging and Component Failure Analysis in Electronics Manufacturing, Shanghai, China, June/July 2002.

[86] M. Bartholomew. *An Engineer's Handbook of Encapsulation and Underfill Technology.* Electrochemical Publications LTD, England, 1999.

[87] R.A. Pearson, A. Ayhan, and H.F. Nied. Modeling the mechanical behavior of underfill resins and predicting their performance in flip-chip assemblies. *2000 International Symposium on Advanced Packaging Materials*, pages 63–67, 2000.

[88] Y.C. Chia, S.H. Lim, K.S. Chian, S. Yi, and W.T. Chen. A study of underfill dispensing process. *The International Journal of Microcircuits and Electronic Packaging*, 22:345–352, 1999.

[89] Y.C. Chia, S.H. Lim, K.S. Chian, S. Yi, and W.T. Chen. An optimisation study of underfill dispensing process. In *Advances in Electronic Packaging, INTERPACK Conference*, volume EEP-Vol.26-2, pages 1545–1549. ASME, 1999.

[90] P. Li et al. Metrics for the underfill flow process. In *Advances in Electronic Packaging, INTERPACK Conference*, volume EEP-Vol.26-2, pages 1377–1379. ASME, 1999.

[91] D.F. Baldwin and N.W. Pascarella. Manufacturing analysis of underfill processing for low-cost flip chip assembly. *Journal of Electronic Manufacturing*, 8:39–50, 1998.

[92] K.-L.B. Wun and G. Margaritis. The evaluation of fast-flow, fast-cure underfills for flip chip on organic substrate. *IEEE Trans. on Comp. and Manuf. Tech. - Part A*, 21:13–17, 1998.

[93] D.G. Yang, L.J. Ernst, C. van 't Hof, M.S. Kiasat, J. Bisschop, J. Janssen, F. Kuper, Z.N. Liang, R. Schravendeel, and G.Q. Zhang. Vertical die crack

stresses of flip chip induced in major package assembly processes. *Microelectronics Reliability*, 40:1533–1538, 2000.

[94] T. Masunaga, T. Nishimura, and T. Nakazawa. Analysis of polymer flow due to capillary forces for flip-chip package designs. In *Advances in Electronic Packaging, INTERPACK Conference*, volume EEP-Vol.19-1, pages 1059–1064. ASME, 1997.

[95] S.Han and K.K. Wang. Analysis of the flow of encapsulant during underfill encapsulation of flip-chips. *IEEE Transactions on Components, Packaging and Manufacturinng Technology-Part B*, 20:424–433, 1997.

[96] H. Yang, S. Bayyuk, A. Krishnan, A. Przekwas, L. Nguyen, and P. Fine. Computational Simulation of Underfill Encapsulation of Flip-Chip ICs Part I:Flow Modeling and Surface-Tension Effects. 48th Electronic Components and Technology Conference, Seattle, Washington, May 1998.

[97] J.J. Cooper-White, J.E. Fagan, V. Tirtaatmadja, D.R. Lester, and D.V. Boger. Drop formation dynamics of constant low-viscosity, elastic fluids. *J. Non-Newtonian Fluid Mech.*, 106:29–59, 2002.

[98] R. Crooks, J. Cooper-Whitez, and D.V. Boger. The role of dynamic surface tension and elasticity on the dynamics of drop impact. *Chemical Engineering Science*, 56:5575–5592, 2001.

[99] W.J. Rider, D.B. Kothe, E.G. Puckett, and I.D. Aleinov. Accurate and robust methods for variable density incompressible flows with discontinuities. In *Barriers and Challenges in Computational Fluid Dynamics*. Kluwer Academic Publishers, 1998.